Title

ATOMIC MECHANISMS OF OXIDE NUCLEATION AND GROWTH AT THE ALUMINUM/OXIDE INTERFACE: A HIGH-RESOLUTION TRANSMISSION ELECTRON MICROSCOPY STUDY

Author

Lee, J.Y.

Publication Date

1986-05-01

Lawrence Berkeley Laboratory
UNIVERSITY OF CALIFORNIA

Materials & Molecular
Research Division

ATOMIC MECHANISMS OF OXIDE NUCLEATION AND GROWTH AT THE ALUMINUM/OXIDE INTERFACE: A HIGH-RESOLUTION TRANSMISSION ELECTRON MICROSCOPY STUDY

J.Y. Lee
(Ph.D. Thesis)

May 1986

Prepared for the U.S. Department of Energy under Contract DE-AC03-76SF00098

DISCLAIMER

Atomic Mechanisms of Oxide Nucleation and Growth at the Aluminum/Oxide Interface: A High-Resolution Transmission Electron Microscopy Study

Jeong Yong Lee

Ph.D. Thesis

May 1986

Materials and Molecular Research Division

Lawrence Berkeley Laboratory

and

Department of Materials Science and Mineral Engineering

University of California

Berkeley, California 94720

TABLE OF CONTENTS

Atomic Mechanisms of Oxide Nucleation and Growth at the Aluminum/Oxide Interface: A High-Resolution Transmission Electron Microscopy Study

Jeong Yong Lee

ABSTRACT

Highly detailed analyses of the crystallographic aspects required for nucleation and growth of aluminum oxide at the metal/oxide interface were carried out using high-resolution transmission electron microscopy. These analyses led to the modelling of the mechanisms of nucleation and growth at the atomic level. The oxides were formed by oxidizing aluminum in 1 atm air at either 500 °C or 600 °C for times from 0.5 hr to 4 weeks. In conjunction with computer simulation comparisons, the cross-sectional high-resolution transmission electron microscopy images reveal directly the atomic structure of the oxide, the base metal, and all internal interfaces.

Results indicate that hemispherical crystalline oxide nuclei, less than 25 Å thick, protrude into the amorphous oxide from the macroscopically flat aluminum/crystalline oxide interface. In addition, the crystalline γ–Al_2O_3 forms in two major crystallographic relationships with the aluminum matrix: parallel and twinned. The parallel orientation interface is a {111} plane of the aluminum and the oxide. The twin orientation interface is also a {111} plane of the aluminum and the oxide. Comparison between experimental high-resolution electron microscopy images and simulated images leads to models of these interfaces, and complete models for these transformations have been proposed. In the later stages of oxidation, the crystalline oxide itself is characterized by parallel or nonparallel multiple internal twins which comprise the

polycrystalline nature of the oxide. If the aluminum/oxide interface is neither a parallel nor a twin orientation, the aluminum/oxide interface is comprised of a {111} oxide plane and a random plane of the aluminum. Models for these transformations have also been proposed.

It is concluded that the crystalline γ–Al_2O_3 nucleates by the structural rearrangement of the atoms within the amorphous oxide into the crystalline phase at the aluminum/amorphous oxide interface, and grows into the matrix parallel to the {111} octahedral planes of the oxide often by a ledge mechanism, and the growing oxide nucleates new grains by twinning. In addition, for the parallel orientation interface, aluminum transforms to the oxide structure by shuffling one quarter of the Al sites, by absorbing vacancies for one third of the Al sites, and by diffusion of oxygen, with reference to the $\Sigma = 1$ coincidence site lattice. For the twin orientation interface, aluminum transforms to the oxide structure by a twinning shear, followed by shuffling one quarter of the Al sites, by absorbing vacancies for one third of the Al sites, and by diffusion of oxygen, with reference to the $\Sigma = 3$ coincidence site lattice. For the random orientation interface, based on the assumption that the oxygen atoms must attach to the oxide by completing the coordination of the aluminum atom, the {111} habit planes of the crystalline oxide can be predicted.

Ronald Gronsky

Ronald Gronsky, Chairman of Committee

CHAPTER 1

INTRODUCTION

Virtually all engineering materials are utilized in the multiphase form and their properties are largely influenced by the presence of interfaces. Thin oxide films are often utilized as dielectric layers in electronic devices, and as protective layers for the application of the metals at high temperatures. For these applications, the study of the metal/oxide interface is essential to understand the properties of thin oxide films.

At the metal/oxide interface, microstructural features at the atomic level play an important role in the nucleation and growth of the oxide,[1] but little is known about the atomic mechanisms of nucleation and growth of the oxide at high temperatures. Furthermore, the following crystallographic aspects of nucleation and growth of the oxide at the metal/oxide interface have not been studied: 1) the local crystallography of the metal/oxide interface including microscopic habit planes, role of defects and growth directions, 2) interfacial roughness, role of faceting, and morphological evolution during oxide growth, 3) atomic structure of the metal/oxide interface. In view of the above questions, the purpose of this research is to perform highly detailed analyses of the crystallographic aspects and the atomic mechanisms required for nucleation and growth of the oxide, so that the atomic mechanisms of nucleation and growth can be modelled on an atomic level. In order to accomplish this at the atomic level, high-resolution transmission electron microscopy (HRTEM) of cross-sectional specimens of the aluminum/oxide interface and computer simulation of the images have been conducted.

The aluminum/aluminum oxide system was chosen for this study primarily because high-resolution lattice imaging of the aluminum and the oxide on an atomic

level has become available in current generation transmission electron microscopes.[2] Furthermore, aluminum shows most of the features of oxide nucleation and oxide growth shown by most other metals; but is exceptional in that these processes occur slowly at high temperatures. Thus, a study of nucleation and growth of aluminum oxides at the metal/oxide interface may well be useful as a model system to study the initial oxidation including amorphous oxide growth and nucleation and growth of a crystalline oxide. A study of the oxidation of aluminum and the factors affecting the establishment of its highly protective oxide films may be useful in its own right, as aluminum is frequently added to alloys.

The nucleation and growth of oxides at the aluminum/oxide interface has been extensively studied[3]-[26] by conventional replica techniques, stripped oxide methods, or hot-stage electron microscopy. Aluminum forms a highly protective amorphous oxide at room temperature which continues to grow at high temperatures up to the melting point of aluminum. A crystalline γ-Al_2O_3 nucleates at the metal/amorphous oxide interface and grows into the metal from this interface by inward diffusion of oxygen through the overlying amorphous oxide film.[12],[14],[18] The amorphous oxide does not crystallize and both oxides continues to grow at the same time.[5],[7],[12],[13],[18] A major crystallographic relationship between the aluminum and the oxide is a parallel orientation relationship.[5],[11],[14],[19] Very recently, Lee[27] has shown by high-resolution transmission electron microscopy that the crystalline oxide grows parallel to the {111} octahedral planes of the oxide, often by a ledge mechanism,[28] and the polycrystalline oxide is composed of multiple twin related grains.

Since many different aspects of nucleation and growth of the oxide are considered in this study, a background and summary of previous work on aluminum oxidation

and crystallographic aspects of the decomposition of aluminum solid solutions are given in the next chapter (CHAPTER 2). This summary is followed by brief reviews of crystal structure and defects in the Al-O system (CHAPTER 3) and theories of interfacial structure (CHAPTER 4) which are relevant to this investigation. Brief reviews of high-resolution transmission electron microscopy and computer image simulations (CHAPTER 5) are included in order to provide an unfamiliar reader with most of the background necessary to understand and interpret the experimental procedures and results which are given in the later chapters (CHAPTER 6 and CHAPTER 7). The experimental results are generally organized into a progression which considers the high-resolution images, the atomic models and computer image simulations. This information is subsequently combined to obtain the final atomic mechanisms. These results are summarized (CHAPTER 8) and the main conclusions are then given (CHAPTER 9).

CHAPTER 2

ALUMINUM OXIDATION

2.1 Introduction to High Temperature Oxidation

Corrosion is the destruction or deterioration of materials by a chemical or electrochemical reaction with the environment. At temperatures where water is liquid, the predominating corrosion process is electrochemical: that is, material wastage occurs by anodic dissolution. Water provides the solvent and connecting electrolyte needed for electrochemical corrosion.

Few materials, particularly those in common technological applications, are stable when exposed to the atmosphere at both high and low temperatures. When materials are subjected to high temperature they may deteriorate through a reaction with a gaseous environment. As for interaction with an oxidizing gaseous environment, it is usually an oxidation reaction.

2.1.1 Thermodynamic Considerations

The overall driving force of metal/oxygen reactions is the free energy change associated with the formation of the oxide from the reactants. The Gibbs free energy change ΔG of the oxidation reaction:

$$2Al_{(s)} + \frac{3}{2}O_{2(g)} \rightarrow Al_2O_{3(s)}$$

is, of course, composed of an enthalpy term and an entropy term

$$\Delta G = \Delta H - T\Delta S,$$

where T is the absolute temperature, S is the entropy, and H is the enthalpy. Often, a determination of the conditions under which a given oxidation product is likely to

form is required. In this regard, Ellingham diagrams, i.e. plots of the standard free energy of formation (ΔG) versus temperature for an oxide are useful in that they allow comparison of the stabilities of the oxide.[29] Note that the driving force of the above reaction is decreased as the temperature increases, since the entropy change in such reactions, where there is net decrease in the number of gas molecules, is negative.[30]

When a metal reacts with a gas containing more than one oxidant, a number of different phases may form depending on both thermodynamic and kinetic considerations. Isothermal phase stability diagrams, usually constructed with the logarithmic values of the partial pressures of the two non-metallic components, for example, log P_{O_2} and log P_{N_2}, as the coordinate axes, are useful in interpreting the condensed phases which form. A phase stability diagram for the Al-O-N system at 600 °C constructed from the data in the JANAF Thermochemical Tables[31] is shown in Fig. 1. The heavy lines denote the boundaries of condensed phases at unit activity and the equivalences of P_{O_2} to P_{H_2}/P_{H_2O} and P_{N_2} to P_{NH_3}/P_{H_2} are also indicated on the coordinate. In this diagram, the full circle in the upper-right corner, which represents the point corresponding to the partial pressures used in this experiment, clearly shows that the stable phase in the reaction of aluminum with air at 600 °C is Al_2O_3. However, thermodynamic phase stability diagrams should be regarded primarily as an analytical tool to aid in the understanding of phases to be formed in oxidation processes. Care should be taken in using them to predict the oxidation products, since these may be significantly displaced from equilibrium. The exact oxidation products also depend on the kinetics of various nucleation, diffusion and growth processes.

2.1.2 The Initial Fast Oxidation

When a metal is exposed to an oxidizing atmosphere at high-temperatures the initial reaction is expected to be very rapid since the oxide layer is very thin. However, if the parabolic rate law is extrapolated to zero scale thicknesses, an infinite rate is predicted. Clearly this is not so and the initial stage of oxidation must be controlled by some process other than ionic transport through thin oxide scales, e.g. the processing of gas molecules on the oxide surface according to

$$O_{2(g)} = O_{2(ad)} = 2O_{(ad)} = 2O^{-}_{(chem)} + 2h \rightarrow 2O^{2-}_{(latt)} + 2h.$$

This describes the adsorption, dissociation, chemisorption, and ionization of oxygen and would lead to a constant reaction rate if rate controlling. However, these processes are so rapid that the oxidation period over which they control the reaction rate is rarely observed.

2.1.3 Transport Mechanisms

With the progression of the oxidation reaction, it is obvious that the solid oxidation product will separate the two reactants, i.e. the metal and the oxygen.

Since the aluminum oxide is an n-type semiconductor,[32] the excess electron defect is an electron in the conduction band, so the corresponding excess lattice defect must be either an interstitial aluminum atom or an oxygen vacancy. In this discussion, the main defect is assumed to be the doubly charged oxygen vacancy $V_{\ddot{O}^{2-}}$ since this assumption leads to the growth of the crystalline oxide into the metal matrix.

As shown in Fig. 2, the oxide forming reaction and defect-injecting reaction both take place at the Al/oxide interface;

$$2Al \rightarrow Al_2O_3 + 3V_{\ddot{O}^{2-}} + 6e^{-}.$$

It follows, therefore, that since the oxide formation takes place at the Al/oxide

interface, an inert marker initially on the metal surface remains on the oxide/oxygen interface. In the oxide phase there is an oxygen activity gradient sufficient to provide the necessary reactant flux through the oxide layer. The defects diffuse to the oxide/oxygen surface and are eliminated;

$$3V_{\ddot{O}^{2-}(\text{metal/oxide})} \rightarrow 3V_{\ddot{O}^{2-}(\text{oxide/oxygen})},$$

$$3V_{\ddot{O}^{2-}(\text{oxide/oxygen})} + \frac{3}{2}O_2 + 6e^- \rightarrow 3O^{2-}_{(\text{oxide/oxygen})}.$$

The concentration of O^{2-} vacancies at the oxide/oxygen interface is very small, provided that the oxygen partial pressure exceeds the equilibrium pressure.

If the rate controlling step is the transport of the material across the oxide layer, then since this layer becomes proportionally thicker as the material is transported, the rate of transport, and hence the overall reaction rate, decreases with time. If, furthermore, it is assumed that the transport process is the same throughout the material, and does not depend on time, then plainly the rate of transport is inversely proportional to the thickness of the layer. This parabolic rate law is found to hold over a period whose duration depends upon factors such as specimen geometry and scale mechanical properties.

If the transport of the oxygen through this layer is the controlling step in determining the overall rate of the oxidation reaction, this is known as diffusion controlled growth. If the transport rate of the reactant from one phase to another phase is much slower than the transport rate of the reactant through one phase layer, growth is said to be interface controlled. It is also possible that the interface reaction and diffusion process occur at similar rates in which case the interface is said to grow under mixed control.

2.2 The Growth of Thin Oxide Films

Deville[33] (1859) was aware of the unusual resistance of aluminum to oxidation but did not associate it with an ever-present oxide film. It was not until attempts were made to solder the metal that the presence of a surface film was realized.[34]

One of the first attempts to determine the oxidation rate of aluminum in air at room temperature was by Vernon (1927).[35] His results showed that nearly all film growth occurred during the first few days' exposure, after which the curve of weight increase against time became almost asymptotic to the time axis. Hart[36] studied the oxidation of aluminum single crystal surfaces, presenting (100), (110) and (111) surfaces, in dry oxygen at 20 °C. He confirmed that film growth was at first rapid and then slow, the growth rate being inverse logarithmic, but could not experimentally verify anisotropy in the growth rate of amorphous films on differently oriented metal faces. Eley and Wilkinson[37] studied oxygen adsorption and oxide formation on aluminum films, and showed that the first two monolayers were taken up too rapidly for kinetic measurements.

There are two principal mechanisms that have been used to describe the low temperature kinetics of oxygen uptake in the formation of very thin oxide films on aluminum. The first of these, due to Mott,[37],[38] assumes that electrons tunnel from the metal through the thin oxide film to suitable acceptor levels provided by the chemisorbed oxygen producing O^- or O_2^- ions on the surfaces. The electrostatic field which arises in the oxide layer as a result of the oxygen ion production serves to assist in the transport of aluminum ions from the metal surface through the oxide film to the oxide surface where they combine with the oxygen ions to form the oxide. The second mechanism, due to Lanyon and Trapnell[40] and adapted to the case of alumi-

num by Eley and Wilkinson,[41] assumes that a neutral species of oxygen is chemisorbed on the oxide surface. Then, by a subsequent site exchange with underlying aluminum atoms, the chemisorbed oxygen combines with these atoms to form the oxide. The first of these two oxidation mechanisms predicts a pressure independent, inverse logarithmic time law for oxide growth which has been found to hold experimentally at atmospheric pressure. The second mechanism yields an oxide growth law which is pressure dependent and logarithmic in time and has been observed experimentally at low oxygen pressure in the range of from 10^{-1} to 1 Pa.

Huber and Kirk[42],[43] showed that the low pressure (10^{-1} to 10^{3} Pa) dry oxidation of aluminum at room temperature appears to be a two-stage reaction during which an intermediate product forms on the growing oxide surface. The first stage is an activated chemisorption of the oxygen on to the oxide surface which goes to completion by the formation of a polar (negative outward), chemisorbed oxygen-oxide surface complex. The second stage is an activated metal-oxygen place exchange which converts the chemisorbed oxygen-oxide surface complex to the bulk metal oxide and causes the film to grow. This two-stage oxidation reaction accounts for the observed increase and decrease in their work function study of the oxidizing aluminum film with changes in the oxygen gas pressure while simultaneously accounting for the observed irreversible uptake of oxygen by the film.

Biaconi *et al.* [44] studied the initial oxidation of Al(111) with surface Extended X-ray Absorption Fine Structure (EXAFS) for single crystal surfaces, and proposed a model for the oxidation stages characterized in their work. They showed that at low pressure (below 2×10^{-5} Pa) molecular oxygen chemisorbs, whereas previous studies have concluded that the initial oxidation is always dissociative. The chemisorption ini-

tiates through a non-dissociative molecular phase even at room temperature with the molecule approximately 1.33 Å from the surface. In the second stage, the molecular oxygen dissociates, and sits in the three fold hollow site. The third stage marks the transition to the oxide where the oxygen moves beneath the surface and a configuration approaching aluminum oxide is obtained.

Norman *et al.* [45] reported results for EXAFS of oxygen on Al(111) at submonolayer coverages. For the chemisorbed state they found strong support of the (1×1) oxygen overlayer structure suggested previously by low energy electron diffraction (LEED). As usually found with chemisorption systems, the adsorbate (O) atoms are located in positions which are a continuation of the face-centered cubic (fcc) stacking of the bulk (Al) lattice. For the initial oxide phase they suggest the geometry for this phase, in which an O atom is bonded to four Al atoms as in α-aluminum oxide and γ-aluminum oxide and each surface Al atom is bonded to three O atoms. This site can be occupied simultaneously with the chemisorption site, producing no distortion of the lattice, and both chemisorbed and oxide-like phases have been observed together. For both phases the O atoms form a (1×1) configuration with respect to the clean Al(111) surface. This can explain why a sharp (1×1) LEED pattern persists after relatively high exposures corresponding to more than monolayer coverage.

2.3 Kinetic Studies

Pilling and Bedworth (1923)[46] studied the rate of oxidation of aluminum in oxygen at 200 to 600 ° C and found that the oxidation came practically to a standstill after a certain film thickness had been reached.

The oxidation kinetics of pure aluminum vary considerably with temperature. From 350 to 425 ° C the oxide film thickens according to a parabolic rate law.[47],[48] At

higher temperatures the kinetics become much more complex and higher weight gains are observed than would be expected from an extension of the lower temperature growth laws.[12],[49],[50]

Smeltzer[47] attempted to explain the complex kinetics on the basis of two consecutive rates of parabolic oxidation; this treatment failed to account mathematically for the terminal stages of the oxidation kinetics. Aylmore *et al.* [49] also showed that the toe of the sigmoid curve fit a parabolic growth law; the rapidly rising portion of the weight gain-time curve was treated as a transition from the parabolic to a linear growth law. Neither of these models provided a particularly good fit with the experimental data and neither explanation appeared to have well defined physical significance.

Beck *et al.* [12] studied the oxidation behavior of high purity Al at temperatures from 450 to 575 °C in dry oxygen. Their results indicate that the sigmoidal oxidation behavior is due to two processes which are mutually independent. These processes, which occur simultaneously, are first the formation of a layer of amorphous γ–Al_2O_3 with poorly developed long range order, and second the nucleation and growth as expanding cylinders of crystalline γ–Al_2O_3 at the amorphous oxide/metal interface. Beck *et al.* [12] were able to separate the kinetics of growth of the amorphous oxide from the overall film growth by determining local amorphous film thicknesses between crystals of γ–Al_2O_3 from electron opacity measurements. In this way they showed that the amorphous oxide forms according to a simple parabolic rate law, probably by the egress of aluminum ions and electrons to the amorphous oxide/gas interface and their reaction with oxygen to form amorphous γ–Al_2O_3. This analysis was in agreement with an observation by Brock and Pryor[18] that the amorphous film, growing by out-

ward diffusion of metal ions, forms between the crystals of γ–Al_2O_3 with accurately parabolic kinetics throughout the temperature and aluminum-copper alloy composition range.

Beck *et al.* [12] showed that the growth of the amorphous oxide is completely independent of the presence of underlying crystals of γ–Al_2O_3. Accordingly, the crystalline oxide must offer negligible resistance to the passage of aluminum ions. However, Brock and Pryor[18] thought that above the crystalline phase the amorphous oxide forms at a lower rate because of the additional resistance conferred to the cation egress afforded by the crystalline oxide.

Beck *et al.* [12] showed that the crystalline oxide was not a recrystallization product from the amorphous oxide but that it was instead formed by the inward diffusion of oxygen ions to the metal/oxide interface and their reaction at that interface. They showed that the overall weight gain-time curves could be expressed by the direct summation of the parabolic rate equation for amorphous oxide formation and the sigmoidal equation for crystalline oxide formation.

Dignam and Fawcett[51] presented weight gain data for the oxidation of electropolished aluminum in the temperature range 475 ° to 600 ° C and analyzed in terms of the following model. The γ–Al_2O_3 crystallites, which nucleate beneath the amorphous oxide film, rapidly achieve a terminal thickness, which is approximately 150 Å, and grow radially at a linear velocity until the crystallites impinge on one another. The reduction in the growth rate which takes place at increasing times is thought to be due either to crystal impingement[12] or an increased oxygen diffusion path.[14]

Hunt and Ritchie[32] carried out resistance marker measurements to study the oxidation of evaporated aluminum films between 230 and 400 ° C and concluded that

the amorphous oxide grows by metal transport. From the sign of its Seebeck coefficient, the oxide was deduced to be n-type. The effect of applying an electric field across the growing oxide layer on aluminum was also investigated. When the oxygen/oxide interface was biased negatively with respect to the aluminum, an enhancement of the oxidation rate was achieved. These results were interpreted in terms of the Mott-Cabrera theory.[52]

2.4 Transmission Electron Microscopy Studies

2.4.1 The Growth of Amorphous and Crystalline Oxides

Raether[54] and Steiner[55] obtained diffuse halo electron diffraction patterns from the oxide on aluminum. These authors described the oxide film as being amorphous because of the diffuse nature of the diffraction yielded by it. After a detailed X-ray examination Verwey[56],[57] concluded that these diffuse patterns are yielded by a film substance γ' $-Al_2O_3$ which has a structure intermediate between the amorphous state and completely arranged state of γ–Al_2O_3. Preston and Bircumshaw,[58] on the other hand, concluded that these films are amorphous and not composed of very small γ–Al_2O_3 crystals. Belwe,[59] however, evaluated the size of the individual crystals which gave rise to these halo patterns to be equal to about one elementary cell of γ–Al_2O_3. Belwe considered that the diffuse ring diffractions are due to the (220) and (440) lattice planes. Wilsdorf[60] investigated the structure of this amorphous alumina by assuming that it consists of totally disordered, uniformly built, molecular groups, and then determined its structure as an aggregate of groups of two molecules of Al_2O_3, an atomic arrangement which does not occur in the γ–Al_2O_3 lattice.

Harrington and Nelson[61] first found a variety of crystalline patterns after heat-

ing aluminum in air at 550 to 650 ° C. De Brouckère[62] showed that this crystalline phase is γ–Al_2O_3 after heating aluminum in air at 400 to 700 ° C. The lattice parameter of the γ–Al_2O_3 cubic lattice was measured to be 7.9 Å for crystalline oxide formed on an aluminum substrate at 500 ° C.[63] Hunter and Fowle[3] studied growth of oxide films on aluminum in dry atmosphere at temperatures from 75 to 600 ° C, using electron microscopy and electron diffraction. They considered that these films might be either amorphous or crystalline, depending on whether they are formed below or above the temperature required to form crystalline oxide.

However, later, it has been established[12],[18] that below about 450 ° C the only oxidation product is a thin film of amorphous oxide, and at temperatures above 450 ° C the morphology of the oxide film changes considerably and discrete crystals of γ–Al_2O_3 are formed together with the amorphous oxide.

Above 400 ° C the crystalline oxide formed by nucleation at the aluminum/amorphous oxide interface,[4] and significant growth of crystallites of γ-alumina oxide began after a temperature dependent induction period.[6]

Doherty and Davis[5] have shown that the low temperature amorphous oxide grown by transport of cations is smooth at the metal/oxide interface whereas a high temperature crystalline oxide grows by the transport of anions. It has been established[5],[7],[12],[13],[18] that the amorphous oxide film which grows up to approximately 200 Å does not crystallize during the growth of the crystalline oxide and the amorphous oxide continues to grow up to the melting point of aluminum, but the growth rate is very slow below 200 ° C.

Natesh and Ansell[10] observed the oxidation of Al foils containing a dispersion of 2 wt% Al_2O_3 particles by hot stage transmission electron microscopy, and found that

the crystalline oxide could grow as an oriented layer in a $\{110\}<221>$ fashion.

Beck *et al.* [12] showed that the crystal nuclei first rapidly grew to a fixed and only slightly temperature dependent depth into the underlying metal. Subsequent oxidation results in only lateral growth of these crystals until they coalesce, whereupon crystalline oxide formation ceases. These observations are in agreement with the findings of Doherty and Davis[5] and Randall and Bernard[7] who previously had shown that the crystalline oxide grew into the metal as well as growing laterally.

However, the formation of a continuous crystalline film was not necessarily the result of islands increasing in size until they joined together. This process did occur but the growth of many islands had essentially stopped before join-up.[14] Filling in between islands was observed to be due to two processes.[14] One was the creation of small second generation islands which grew from about one fifteenth the size of existing islands, and the other was accelerated growth in certain crystallographic directions, with reference to the metal lattice.

Brock and Pryor[18] studied the oxidation behavior of aluminum-copper alloys at temperatures from 475 to 575 °C in dry oxygen. The oxidation product was found to be duplex in nature consisting of both amorphous and crystalline γ–Al_2O_3. Roughly cylindrical crystals of γ–Al_2O_3 of constant thickness, at any given temperature and alloy content, grew into the metal from the amorphous oxide/metal interface by inward diffusion of oxygen through the overlying amorphous film.

Scamans and Butler[19] carried out an *in situ* morphological study of the oxidation of aluminum and aluminum alloys containing zinc and magnesium in the temperature range 400 to 520 °C using the hot stage of a 1 MeV transmission electron microscope. They confirmed that in pure aluminum, oxidation takes place after a tem-

perature dependent induction period, by the nucleation of crystalline γ–Al_2O_3 at the amorphous oxide/metal interface. This process is delayed by additions of zinc which modifies the structure of the oxide.

Corkish[20] studied the oxidation of aluminum, aluminum-0.5% copper and various aluminum-silicon alloys and examined the effect of orientation and the role of the initial room temperature oxide on the nucleation and growth of a crystalline oxide. He showed that the average nucleation density on aluminum of γ–Al_2O_3 was 1.5×10^9 cm^{-2} and the average density decreased with increasing alloying additions of copper and particularly silicon. The orientations with the low index planes showed a higher nucleus density than the orientations of planes in the center of the unit triangle. The density varied by approximately a factor of 45 with (111) > (100) > (110) > (120) > (113) > (135). He also showed that the majority of scratches on the surface acted as nucleation sites along much of their length, whereas there was a minor tendency for grain boundary nucleation. The crystalline oxide islands grew laterally up to 15 μm across which was a factor of 500 to 1000 greater than the island thickness.

2.4.2 Morphologies of the Oxides

There are three different kinds of oxides formed on aluminum films by thermal oxidation in air in addition to normal amorphous oxide forming the surface layer:[11] (a) Type A is a flower-like amorphous oxide, which nucleates and grows preferentially at the grain boundaries of aluminum at 400 ° C. By exposure to high electron beam intensity it crystallizes to γ–Al_2O_3.[11] This type oxide is so porous that aluminum might be successively eroded by air which comes through the pores. (b) Type B is a plate of a single crystal γ–Al_2O_3. These oxide crystals are observed to be formed into well defined crystallographic shapes.[14] The crystal orientation of the oxide is

associated with that of the aluminum crystal beneath it. On the surface of an aluminum grain with its (111) plane parallel to the film plane, the oxide whose shape is trigonal or hexagonal grows with a parallel orientation; $(111)_{Al} \,||\, (111)_{oxide}$ and $[1\bar{1}0]_{Al} \,||\, [1\bar{1}0]_{oxide}$.[11],[22],[23] (c) Type C is composed of many dendrite crystals of γ–Al_2O_3, which are often observed at the grain boundaries of aluminum at 600 ° C, and the formation of these oxides is supposed to occur in cracks of the protective surface oxide layer.[11] The agglomeration of particles (Type C) comprising each island is mosaic textured about a common fiber axis,[14] and occurs on surfaces with orientations near the center of the unit triangle and near (100).[13] It was suggested from electron diffraction studies[20],[64],[65] that these polycrystalline oxides might contain a high concentration of faults that are {111} twins or stacking faults.

However, Csanady *et al.* [21] studied the oxidation of thin aluminum films *in situ* prepared by evaporation directly in the electron microscope under ultra-high-vacuum conditions. They showed that the oxide crystals formed above 350 ° C exhibited a needle-like morphology[4] and those formed at higher temperature (about 450 ° C) were mostly hexagonal platelets.

2.5 Atomic Mechanisms of the Decomposition of Aluminum Solid Solutions

In this section crystallographic aspects of the decomposition of supersaturated aluminum solid solutions are briefly reviewed since no atomic mechanism of nucleation and growth of the oxide at the metal/oxide interface in crystallographic aspects has been proposed.

The atomic interaction in the crystal lattice of an alloy is governed by the interaction of electrons in the outer shells. One of the factors determining the structure of a stable lattice, that is, its coordination polyhedra, is the electron

concentration.[66] Any change in the parameters of the coordination polyhedra and, in particular, a change in the kind of atoms in supersaturated solid solutions, increases the free energy of the crystal. It is possible to reduce this energy by replacing the alien atom by an atom characteristic of the given structure. Therefore the lattice of the matrix crystal tends to push away the atoms of the dissolved element in the initial stages of decomposition of the supersaturated solid solution and as a result, alloying atoms cluster in small regions of the crystal.

As the concentration of dissolved atoms in these regions increases, the rules for the construction of a lattice based on a different electron concentration begin to operate. There is a tendency for new coordination polyhedra to be created, that is, for the crystal lattices to be rearranged, which gradually intensifies as the content of alloying atoms grows. This leads to successive rearrangement of the lattices, finally creating the structures of stable precipitate phases. The reason for rearrangement of the lattices lies in the change of atomic interactions when the atomic composition changes. The kinds of rearrangement are governed by the types of initial and final crystal lattices.

Shchegoleva[67] reviewed the literature concerning the study of aging mechanisms in aluminum alloys, and proposed that aging mechanisms in aluminum alloys are governed by the ways in which the perfect crystal lattice of the matrix can be rearranged into lattices of stable precipitate phases. The methods whereby the initial perfect lattice is transformed into the lattice of a stable precipitate phase determine the specific decomposition mechanisms of supersaturated solid solutions. Metastable precipitate phases appear in the intermediate stages of lattice rearrangement. If one knew how the lattices rearranged one could understand the aging processes of alloys, eluci-

date features of the structural components, and direct those processes.

The major premise of the study of aging mechanisms in a series of aluminum alloys has been the decisive role of the sequence of lattice rearrangements from the initial crystal to the stable precipitate phase which secure a succession of structural components.[67] The possibility of creating lattices of precipitating phases from the defect-free lattice of the matrix by means of shears of a minimum number of atoms by the least possible distances without the atoms changing places is determined by crystallographic analysis. One criterion for the feasibility of the resulting rearrangement mechanism is the coincidence of orientation relations between the initial and final lattices with the experimentally observable relations between the matrix and precipitate phase.

For example, decomposition of supersaturated solid solution in alloy Al-Cu-Mg of composition[68] corresponding to section Al-S on the constitution diagram results in the formation of stable phase S (Al_2CuMg). The lattice is orthorhombic (space group $Cmcm$) with parameters: $a = 4.01$ Å, $b = 9.25$ Å, $c = 7.15$ Å. The orientation relationship with matrix is: $[100]_S \,||\, [210]_{Al}$; $[010]_S \,||\, [120]_{Al}$; $[001]_S \,||\, [001]_{Al}$.

According to the hypothesis of Bagaryatskiy,[68] the stable phase S is preceded by an S' phase which in turn is preceded by an $S*$ phase. S' is elastically-deformed, coherent with the S-phase matrix. $S*$ is a phase which includes elements of S' and S''. Bagaryatskiy has suggested that the atomic arrangement of S'' is the same as in the S phase but that the orientation relations are different: $[100]_{S''} \,||\, [17.\bar{7}.0]_{Al}$; $[010]_{S''} \,||\, [5.13.0]_{Al}$; $[001]_{S''} \,||\, [001]_{Al}$. Quite small displacements of the atoms from their positions in the aluminum lattice are required to form S''. It has been proposed that the aging mechanisms of alloy Al-Cu-Mg consist of the following

stages.[67] 1) Formation of cylindrical particles of an S'' phase from clusters of atoms of the alloying elements by means of rearrangement of the face-centered cubic matrix lattice into the S'' phase. 2) Reorientation of particles resulting in the appearance of an S' phase. 3) Growth of S' particles, and destruction of coherence with the matrix signifying the appearance of particles of a stable S phase. The diffuse scattering arcs in the reciprocal lattice of the alloys arise due to gradual rearrangement of the precipitate phase sites from positions typical of S'' to positions in S. They are analogous to the streaks which arise during the fcc-hcp (hexagonal close packing) rearrangement. The shape of the diffuse scattering regions suggests that reorientation proceeds without any particular change in the interplanar spacing in the precipitate phase.

The S phase has the same density as the aluminum phase: there are 16 atoms in one unit cell (volume 263.6 $\mathring{A}^3$), that is, as many as in four unit cells of aluminum (volume 263.76 $\mathring{A}^3$). This fact, as well as the way in which its predecessor S'' was formed, shows that a defect-free lattice of the precipitate phase is formed from the perfect matrix lattice. One can conclude from the experimental results obtained during aging of alloy Al-Cu-Mg and results of crystallographic analysis that aging of the alloy after the appearance of clusters of alloying atoms is determined by rearrangement of the lattice into that of the final precipitate phase.

CHAPTER 3

CRYSTAL STRUCTURE AND DEFECTS IN Al-O SYSTEM

3.1 The Al-O System

Figure 3 shows the phase diagram[69] of the Al-O system in the composition range between 0 and 60 atomic % O. The equilibrium phases are: (1) the liquid, L, which exists as two immiscible liquids, here termed "L_1," an Al-rich liquid, and "L_2," an O-rich liquid Al_2O_3; (2) the face-centered cubic Al terminal solid solution, in which the solubility of O is unknown but small; (3) the trigonal aluminum oxide α–Al_2O_3 (α-alumina, sapphire, or corundum), for which the deviations from stoichiometric composition are unknown but small; and (4) the gas. Previously published diagrams[69],[70] for the condensed phases show no solid solubility of O in solid Al or deviation from stoichiometry in Al_2O_3. There is general agreement that no stable condensed phase exists that is richer in O than Al_2O_3. Recent work[71] on structural transformations in aluminum oxide films grown on (111) Al has revealed that the films retain the Al_2O_3 stoichiometry down to the thicknesses as small as 5 Å.

3.1.1 Terminal Solid Solution, Al

Solid aluminum exhibits the face-centered cubic (fcc) structure (Table 1) as shown in Fig. 4 (a). The lattice constant is 4.0496 Å at 0 °C and the radius of an atom at 0 °C is 1.42 Å.[72] Interstitial sites have a radius of 0.585 Å for the octahedral site and 0.32 Å for the tetrahedral site.[72] The atomic radius of the oxygen atom is 0.65 Å.[72]

The solid aluminum phase is stable only at O_2 fugacities less than or equal to

2.5×10^{-47} Pa at 660 °C as shown in Table 2.[73] No credible measurement of solubility of O in solid aluminum has been reported. Numerous determinations of O in Al that were reported fail to distinguish between dissolved O and O present as oxide.[69]

3.1.2 Solid Oxide Phases

In addition to α–Al_2O_3, there are many polymorphic forms with the same stoichiometry. These types of transition Al_2O_3 may develop by oxidation of aluminum followed by heating the stripped oxide,[74] decomposition of compounds containing Al and O,[75],[76],[77] or heat treatment of other Al_2O_3 varieties in transition to α–Al_2O_3.[78]

For example, amorphous alumina films are formed on oxidized bare aluminum, etched surfaces and electropolished surfaces. Cubic γ–Al_2O_3 is produced from oxidation of aluminum or from the decomposition of boehmite.[75],[76] χ–Al_2O_3 and κ–Al_2O_3, which have a structure composed of hexagonal close-packed oxygen atoms, resembling the final term of transition aluminas (α–Al_2O_3), are produced from hydrargillite.[76] Certain so-called *aluminas*, notably β and ς, are not strictly binary compounds,[79] while other types, such as μ, ν, and ξ, occur as thin films on Al.[80]

All the crystalline forms of Al_2O_3 are constructed of stacked, closed-packed layers of O ions, with Al ions and vacancies distributed on the tetrahedral and octahedral sites among these O ions. Polymorphism arises from the possibilities for different O-layer stacking sequences and disorder therein, from variations in the distribution of Al ions on their two types of sites, and ordering among the Al ions and vacancies on those sites. Because of these possibilities, not only are cubic, hexagonal, and tetragonal structures formed, but also others of lower symmetry. Confusion stems from the multiplicity of variations, because small-step changes may be manifested in specimens with different histories. Table 1 contains information on crystal structures and lattice

parameters of well documented and widely accepted oxide phases.

Amorphous Oxide

The amorphous oxide is amorphous in the sense that no crystalline nature is detectable by electron diffraction or X-ray diffraction; this does not rule out the possibility of very small crystalline aggregates. A model based on a disordered glassy γ–Al_2O_3 analogue shows a good fit with the X-ray scattering pattern.[81] The diffuse electron diffraction rings[82] from the oxide are also interpreted in terms of γ–Al_2O_3 structure, but the line broadening is not believed to be from very small crystallites because the amorphous films have a much higher resistivity than crystalline γ–Al_2O_3.

However, Forty and El-Mashari[83] suggested from the analysis of the diffuse electron diffraction rings that the amorphous oxide has two molecules of Al_2O_3 arranged in sheets which, if stacked, give the appropriate admixture of octahedral and tetrahedral sites occupied by Al^{3+}.

Evaporated amorphous oxide films become poorly crystalline at 600 ° C and at higher temperatures they transform to α–Al_2O_3.[78] Amorphous anodic films stripped from aluminum transform to α–Al_2O_3 at 700 to 800 ° C when heated in a furnace.[84] However, amorphous thermal oxide films on aluminum do not crystallize below 660 ° C.[7],[12]

γ Phase

This phase has a defect spinel structure with the oxygen ions in face-centered cubic close packing and the aluminum ions in certain interstices. The lattice parameter of γ–Al_2O_3 is 7.9 Å[63] and the atomic radius of Al^{3+} is 0.51 Å while that of O^{2-} is 1.40 Å.[85]

As shown in Fig. 4 (b), for an elementary cell of this spinel structure there are four oxygen atoms, four octahedral interstices, and eight tetrahedral interstices. This makes a total of twelve intersticies to be filled by three cations. In each elementary cell two octahedral sites are filled and one tetrahedral. Eight of these elementary cells are arranged so as to form a unit cell containing 32 oxygen ions, 16 octahedral cations, and 8 tetrahedral cations as illustrated in Fig. 4 (b).

In γ–Al_2O_3, there are $21\frac{1}{3}$ aluminum cations in the unit cell of 32 oxygen ions to maintain charge balance, so $21\frac{1}{3}$ aluminum ions are distributed among the 24 cation sites. There is considerable disagreement[86],[87],[88] as to the distribution of aluminum ions in the cation sites of the spinel structure. Generally the distribution depends significantly on the history of the preparation of the sample.

Noncubic γ–Al_2O_3 with a tetragonal distortion was found only in the case of decomposition of aluminum hydrates.[77]

δ Phase

This oxide has a tetragonal superstructure of the spinel lattice with one unit cell parameter tripled: the oxygen ion sublattice is still a slightly distorted face-centered cubic lattice but the rearrangement of the aluminum ions differs from that of γ–Al_2O_3 structure giving a c-lattice parameter which is 2.9 times that of γ–Al_2O_3. By analogy with the similar phase γ-Fe_2O_3, the vacancies in δ–Al_2O_3 are thought to be ordered on octahedral sites of the spinel structure with an arrangement governed by a screw tetrad parallel to the c-axis.[86]

θ Phase

This phase is monoclinic and has the structure of β-Ga_2O_3. This structure can be regarded as a superstructure of the basic spinel unit cell, similar to that of δ–Al_2O_3, and they both share the same tripled spinel c parameter. Thus the pseudo-orthorhombic cell of θ–Al_2O_3 has $a = 5.619$ Å, $b = 2.907$ Å, $c = 22.89$ Å.[77]

α Phase

A broad consensus holds that α–Al_2O_3 is the only stable form of Al_2O_3.[89] Deviations from the stoichiometric composition in α–Al_2O_3 were not determined or even detected chemically. This phase has a trigonal structure, which may be described alternatively as hexagonal (Table 1). This is achieved by nearly hexagonal close packing of the oxygen ions with aluminum ions filling two-thirds of the octahedral sites.

3.1.3 Phase Transition of Aluminum Oxide

One basic sequence of phase transition of aluminum oxide is generally given as

$$\gamma\text{–}Al_2O_3 \rightarrow \delta\text{–}Al_2O_3 \rightarrow \theta\text{–}Al_2O_3 \rightarrow \alpha\text{–}Al_2O_3,$$

although there are considerable disagreements as to the transformation path and temperature between them.[77] Transformation of the metastable varieties to α is slow, even at temperatures well above 1000 ° C.

Wilson[77] discussed the close crystallographic relationship between the different forms of alumina, in a study based on the transformation from boehmite to γ–Al_2O_3 and other metastable aluminas. This γ phase possesses a structure based on cubic packing of oxygen anions. The transformation to hexagonal α–Al_2O_3 requires reorganization of the oxygen network.

The first step is growth of the cubic network and formation of a tetragonal structure (δ–Al_2O_3). The close relationship of these forms of alumina needs to be emphasized for understanding the transition mechanisms. For example, the a and b parameters for γ- and δ–Al_2O_3 are reported to be the same,[75] and the d-spacings reported for the two forms reinforce this close relationship:[75] d_{400} for γ–Al_2O_3 is reported to be 1.990 Å, while that for δ–Al_2O_3 is 1.986 Å. The d_{440} value reported for both forms is 1.407 Å.

An intermediate monoclinic structure then appears (θ–Al_2O_3) at 1000 ° C, which is transformed into α–Al_2O_3 around 1100 ° C.[76] Although monoclinic θ–Al_2O_3 seems to be a drastic change from tetragonal δ–Al_2O_3, the close relationship[90] between these structures is indicated by the fact that a $(\bar{4}40)$ spinel plane would be represented by $(20\bar{4})$ plane in the monoclinic system for θ–Al_2O_3. The $(\bar{4}40)$ planes for both γ- and δ–Al_2O_3 have a d-spacing of 1.407 Å while the $(20\bar{4})$ plane of θ–Al_2O_3 has a spacing of 1.4062 Å. θ–Al_2O_3 can be alternatively described to have aluminum cations in the same configuration as in α–Al_2O_3 but inscribed in a nearly face-centered cubic oxygen network instead of the hexagonal oxygen network of α–Al_2O_3.

3.1.4 Solid Aluminum Oxides that are not Al_2O_3

At least eight varieties of aluminum oxide in this class were reported:[91] Al_2O; Al_4O_3; AlO; Al_2O_2; Al_8O_9; Al_3O_4; Al_4O_6 and AlO_2. It is possible that none of these phases exists, even metastably. In many instances, the substances reported were produced in systems involving other elements, for example, with C or Si present.[92] This raises the possibility that the products were not pure compounds of Al and O. Sometimes, there was insufficient product for chemical analysis or even for X-ray diffraction in stress-free, isolated conditions. Therefore, identifications with a particular

stoichiometry were often weak.

Yamaguchi[93] reported that Al_2O and AlO were formed at the boundary between γ–Al_2O_3 and the metal in oxidizing Al foil at 300 ° C. The presence of suboxides was inferred from certain reflections in the X-ray diffraction patterns or electron diffraction patterns but the source of the reflections was not isolated chemically and analyzed.

A possible spinel-type oxide, Al_3O_4, was reported to have formed when aluminum reacted with air by Rhodin.[94] Claims that this oxide formed in the reaction of Al_2O_3 with C at high temperature[95] and in Fe-rich Fe-Al-O melts[96] were also made. Other investigators who made these types of experiments did not report finding Al_3O_4.[69]

3.2 Defects in Al and Spinel Oxide

3.2.1 Defects in Al

Quenching experiments on pure aluminum[97],[98] have shown that the concentration of vacancies is 10^{-4} after quenching from 550 ° C. Other quenching experiments on binary aluminum alloys[99] have shown that the concentration of the quenched-in vacancies actually increases with alloying. For example, in dilute Al-Cu alloys concentrations of 10^{-3} were found.[99]

For the face-centered cubic structure, perfect dislocations exhibit a Burgers vector of $\frac{a}{2}<110>$. The partials bounding a stacking fault either have Burgers vectors of type $\frac{a}{6}<112>$ (Shockley partials) or of type $\frac{a}{3}<111>$ (Frank partials). Shockley partials are glissile and the type encountered in dislocation dissociation whereas Frank partials may only move via climb, forming usually by the precipitation of vacancies or interstitials. Referring to the Thompson tetrahedron construction (Fig. 5), one finds

three possible Burgers vectors for Shockley partial in a {111} glide plane. For a partial dislocation lying along a <110> direction, two of these are 30° partial dislocations whereas the other is a 90° edge partial.

The most obvious kind of defect that could be formed by agglomeration of vacant lattice sites is found when an aluminum crystal is quenched relatively slowly. Voids are nucleated which grow large enough to be observed by transmission electron microscopy.[100] They take the shape of an octahedron because this allows all the surfaces to be parallel to {111} which is the face of lowest surface energy for the face-centered cubic structure. If an aluminum crystal is quenched at a slightly faster rate, most vacancies collect in planar clusters. A group of atoms in a single {111} layer is removed. Collapse of the lattice over the area of the resulting pancake-shaped void results in an intrinsic stacking fault bounded by an imperfect dislocation of Burgers vector $\frac{1}{3}\{111\}$. After collapse, the loop grows by absorbing additional vacancies at jogs. Large stacking fault loops can grow in aluminum only because their conversion to perfect dislocation loops is associated with a large activation energy.[101] Above a size of about 50 Å in diameter, the total energy of the defect is reduced if the stacking fault is removed and the dislocation converted from $\frac{1}{3}<111>$ to $\frac{1}{2}<110>$.[102] In aluminum, which has a high stacking fault energy ($\sim$150 ergs/cm^2),[103] the total energy of a large faulted loop can be decreased by eliminating the stacking fault even though the elastic strain energy is increased by increasing the magnitude of the Burgers vector of the surrounding dislocation. Further growth changes the loop shape from hexagonal to rhombus shape.[102]

3.2.2 Dislocations in Spinel Oxide

In Fig. 6, the lattice of spinel is projected on the (110) plane, as indicated in the accompanying legend in the bottom-left of this figure. The height of the ions above the plane of projection is expressed in multiples of $\frac{\sqrt{2}}{8}a$, where a is the lattice constant, in order to obtain whole numbers.

Along <111> directions, the spinel can be considered as consisting of a 24-layer stacking of cations and anions with an interlayer spacing of $\frac{\sqrt{3}}{24}a$ as shown in Fig. 6 and Table 3. In discussions about close-packed lattices it is customary to denote the stacking order in the <111> direction of a cubic close-packed lattice by

$$\cdots \text{ABCABCABC} \cdots .$$

This notation can be directly applied to the oxygen ions of the spinel lattice. Since the projections of all cations coincide with the projections of oxygen ions, cations sites can also be described by this notation.

However, not all octahedral and tetrahedral interstices are occupied by cations. Therefore, the sites of each layer have to be divided into four groups: 1,2,3,4. As illustrated in the bottom-right corner of Fig. 6 the stacking sequence in the [111] direction can be denoted by

$$\cdots /b_{1,2,3,4}/a_1/c_1/b_1/a_{1,2,3,4}/-/b_{2,3,4}/-/c_{1,2,3,4}/b_1/a_1/c_1/b_{1,2,3,4}/ \cdots .$$

As shown in Fig. 6, of all octahedral interstices at the cation layer corresponding to the $b_{2,3,4}$ layer, only three quarters are occupied. The cations at this stacking height form a layer structure which has been called a kagome-structure.[104] Between the oxygen layers corresponding to $b_{1,2,3,4}$ and $a_{1,2,3,4}$, cations of both kinds of sites are found. Although these cations are at different stacking heights corresponding to a_1, c_1 and b_1

layers, this composite layer has been called a mixed layer.[104] Between the oxygen layers in the <111> direction, alternatively kagome layers and mixed layers are found.

The tetrahedral ions nearest to a kagome layer occupy sites above and below the empty sites at the centers of the hexagon of the kagome layer. In all directions, there is always an empty octahedral site between two neighboring tetrahedral cations. Every oxygen ion in the spinel lattice is surrounded by four cations, one at a tetrahedral site and three at octahedral sites. It is useful to consider the spinel structure as a stacking of coordination polyhedra with cations in the centers and oxygen ions at the corners. In the perfect spinel structure, the octahedra share edges with four other octahedra and share corners with six tetrahedra. The tetrahedra do not touch each other.

A {111} plane of oxygen ions is shown in Fig. 7, together with the projection of the next kagome cation layer. Because the spinel structure belongs to the face-centered cubic lattice, the shortest translation vector for the spinel structure, and hence a perfect Burgers vector,[105] is $\mathbf{b} = \frac{a}{2}<110>$, represented by vector AB in Fig. 7. However, the oxygen ions form almost a cubic close-packed lattice with an oxygen-oxygen distance of $\frac{\sqrt{2}}{4}a$. If the cations were disregarded, the Burgers vector would be of this length. Thus, a dislocation with Burgers vector **b** can dissociate into collinear partial dislocations, each having the same $\frac{a}{4}<110>$ Burgers vector.[106] The dissociation reaction:

$$\frac{a}{2}[110] \rightarrow \frac{a}{4}[110] + \frac{a}{4}[110]$$

$$\mathrm{AB} \rightarrow \mathrm{A}\gamma + \gamma\mathrm{B}$$

produces a stacking fault in the cation sublattice only.

Dissociation on a {111} plane, into four partial dislocations or *quarter-partials* has been proposed by Hornstra[107],[108] to follow the reaction:

$$\frac{a}{2}[110] \rightarrow \frac{a}{12}[21\bar{1}] + \frac{a}{12}[121] + \frac{a}{12}[21\bar{1}] + \frac{a}{12}[121]$$

$$\mathrm{AB} \rightarrow \mathrm{A}a + a\gamma + \gamma b + b\,\mathrm{B}.$$

Each quarter partial dislocation has a Burgers vector $\frac{a}{12}<112>$ and is equivalent to a Shockley dislocation in the anion lattice. A stacking fault in both the cation and the anion sublattice is created by this dissociation. The two outer pairs of partials bound a stacking fault in the oxygen sublattice in which concurrently the cations would have moved to their favored crystal coordination. This process is called *synchro-shear* by Kronberg.[109] The two inner partials bound a fault in the cation stacking only. Hornstra's arguments are based on the requirement of local electron neutrality and on the observation of twinning on {111} planes. This last dissociation may occur only on {111} planes, the first reaction being possible in different planes. The synchro-shear process obviously acts during the glide of the split dislocation. In Fig. 7, the upper layer of oxygen ions is displaced by Aa . The cations are displaced to a new octahedral interstice. It is possible that the free energy of one or more of these stacking faults[110],[111] is so high that the width of the faulted region becomes very small, so that two quarter dislocations nearly coincide and almost form one half dislocation with Burgers vector $\frac{a}{4}[110]$.[112]

A third type of dissociation has been proposed by Doukhan and Escaig.[113] It is a glide dissociation given by

$$\frac{a}{2}[110] \rightarrow \frac{a}{6}[21\bar{1}] + \frac{a}{6}[121]$$

$$\mathrm{AB} \rightarrow \mathrm{AO} + \mathrm{OB}$$

This dissociation also produces a stacking fault in both sublattices.

3.2.3 Stacking Faults in Spinel Oxide

As discussed in the previous section, a dislocation with a {111} slip plane consists of four partials and three stacking faults. Of the three stacking faults the middle stacking fault has a cubic stacking of the oxygen ions, whereas the outer ones have a hexagonal stacking. The two outer stacking faults are similar; the detailed structure of the left one is presented in Fig. 8. It consists of two stacking faults which are called type I.[107] A characteristic for this type is the occurrence of octahedral ions at short distances from each other, namely in octahedra with one face in common. This would be an unfavorable combination I-I, although a similar configuration does occur in the structure of some hexagonal ferromagnetic oxides.[114]

The structure of the stacking fault bounded by the two inner partial dislocations is called type II.[107],[108] In this fault, there is a fault in the cation sublattice stacking only, the anion sublattice being undisturbed across the fault. A characteristic of this stacking fault is the occurrence of cations in tetrahedra and octahedra with one face in common. In both stacking faults Pauling's rule is not obeyed for some oxygen ions. This deviation from Pauling's rule occurs in some unfaulted spinels and also in complicated compounds.[107] Therefore, this deviation is no reason for considering stacking faults as very unfavorable configurations.

The two stacking faults discussed so far are sufficient to describe the extended dislocation, but still another type is possible (type III).[107],[108] The structure of this stacking fault is shown in Fig. 56. It has a hexagonal close-packed oxygen lattice like type I, but it cannot be formed from the spinel structure by the passage of one quarter dislocation, except when the slip plane coincides with a mixed cation layer and free interchange of octahedral and tetrahedral cations is possible. Whereas stacking fault II

can occur alone, I and III are always found in pairs or in the combination I-III. If I and III occur alone, the lattice is changed to the twin orientation.[107],[108] Therefore I and III represent two possible structures of the (111) twin plane, as will be discussed in the following section.

However, in a flux grown spinel crystal, there are some other types, $\frac{a}{4}[110](100)$[115] and $\frac{a}{4}[110](110)$[115],[116], of stacking faults through a relative displacement of cation packing within the perfect anion sublattice. Since these defects in grown spinel crystals are characterized by a fault in cation stacking, whereas the anion sublattice is undisturbed across the fault, they are best described as anti-phase boundaries. Two probable mechanisms[117],[118] for their formation were suggested: (a) impingement during solidification of domains in which the partial filling of interstices by cations is nucleated differently in adjacent domains, (b) introduction of a dislocation in the anion lattice during crystal growth which may nucleate an anti-phase boundary when the domain impinges on it.

3.2.4 Twins in Spinel Oxide

The spinel structure is well known for its (111) twins. These twins are so common that (111) twins occurring in other cubic crystals are also called spinel twins. Macroscopically this twinning may be described either as a reflection with respect to a (111) plane or as a rotation about [111] by 60° or 180°, or even as a rotation of 180° about a <112> axis. Microscopically the mirror plane may be a glide plane and the twin axis need not coincide with a threefold axis. There is a close relationship between stacking faults and twins as stacking faults may often be considered as extremely thin twin lamellae. This is not true for the stacking fault of type II, but only for those of type I and III.

Type III is shown in Fig. 56 as forming a twin plane. In this type of stacking fault Pauling's rule is obeyed, all oxygen ions having four cation neighbors. In addition, there are no cations very close to one another in polyhedra with one face in common as there are in stacking faults I and II. The energy difference between this defect and the perfect structure will therefore be small, and it is not surprising that a lattice similar to that of stacking fault III occurs in nature: the olivine lattice.[107] Thus, when twins are formed during crystal growth, a twin plane of type III is most likely.

Deformation twinning is known to be related to plastic deformation; it takes place when a partial dislocation (in this case a quarter dislocation) passes between every pair of successive oxygen layers.[119] However, by this deformation twinning mechanism, only twins with twin planes of type I can be formed. A twin plane of type III, which is more favorable, may be formed afterwards by the passage of two quarter dislocations with appropriate Burgers vectors along the twin plane.

CHAPTER 4

STRUCTURE AND CRYSTALLOGRAPHIC MODELS OF THE INTERFACE

4.1 Interfacial Structure

4.1.1. The Free Surface of a Crystal

To a first approximation the structure of solid surfaces can be discussed in terms of a hard sphere model. If the surface is parallel to a low-index crystal plane, the arrangement will be the same as in the bulk, apart from perhaps a small change in the lattice parameter, assuming the surface is not contaminated. The origin of the surface free energy is that atoms in the layers nearest the surface are without some of their neighbors. Therefore, every surface atom with *broken bonds* has an excess internal energy E_{SV} over that of the atoms in the bulk. In the broken bond model, different crystal surfaces should have different values for E_{SV} depending on the number of broken bonds. It might be expected that the surface atoms will have more free movement and therefore a high thermal entropy compared to atoms in the bulk.

The number of broken bonds at the surface for the face-centered cubic crystal will increase through the series {111}, {200}, {220}. When the macroscopic surface plane has a high or irrational {hkl} index the surface will appear as a stepped layer structure where each layer is a close-packed plane. A convenient method for plotting the variation of the surface energy, γ, with surface orientation in three dimensions is to construct a surface about an origin such that the free energy of any surface plane is equal to the distance between the surface and the origin when measured along the normal to the plane in question. This type of polar representation of γ is known as a γ-

plot. The equilibrium shape of a γ-plot has the property that total surface energy is a minimum and the shape that satisfies this condition is given by the Wulff construction. When the γ-plot contains sharp cusps the equilibrium shape is a polyhedron with the largest facets having the lowest interfacial free energy.

4.1.2. Crystalline/Amorphous Interface

Many of the ideas discussed with regard to crystalline/vapor interfaces can be carried over to crystalline/amorphous interfaces, only the low density vapor phase is replaced by a high density amorphous phase, and this is important for the structure and energy of the interfaces. There are basically two types of atomic structure for crystalline/amorphous interfaces. One is essentially the same as the free surface described in the previous section. In this case the transition from amorphous to crystalline phase occurs over a rather narrow transition zone approximately one atom layer thick. Such interfaces can also be described as smooth, faceted, or sharp. The other type is an atomically diffuse interface, in which the transition from amorphous to crystalline phase occurs over several atom layers. Diffuse interfaces are rough or non-faceted; there is a gradual weakening of the interatomic bonds and an increasing disorder across the interface into the bulk amorphous phase; in thermodynamic terms, enthalpy and entropy gradually change from bulk crystalline phase to bulk amorphous phase across the interface. For the crystalline phase and the amorphous phase to be in equilibrium it would be required that the high enthalpy of the amorphous phase be balanced by a high entropy so that both phases have the same free energy. But entropies of amorphous solids seem never to be high enough to make them equilibrium phases. Furthermore, in the interfaces, the balance is disturbed by an excess free energy, γ_{SL}. The type of structure chosen by a particular system will be that which

minimizes the interfacial free energy.

According to a simple theory developed by Jackson[120] the optimum arrangement depends mainly on the latent heat of fusion (L_f) relative to the melting temperature (T_m). This theory predicts that there is a critical value of $L_f/T_m \simeq 4R$ (R is the gas constant) above which the interface should be flat and below which it should be diffuse. Most metals have $L_f/T_m \simeq R$ and are therefore predicted to have rough interfaces. On the other hand the oxides and elements such as Si, Ge, and Sb have high values of L_f/T_m and generally have flat close-packed interfaces. If the model is applied to the free surface of a crystal, the heat of sublimation should be used instead of L_f and then flat surfaces are predicted for metals, in agreement with observation.

4.1.3. Interphase Interfaces in Solids

Coherent interfaces

A coherent interface results when the two crystals match perfectly at the interface plane so that the two lattices are continuous across the interface. This can only be achieved if, disregarding chemical species, the interfacial plane has the same atomic configuration in both phases and this requires the two crystals to be oriented relative to each other in a special way.

Within the bulk of metal or oxide, every atom has an optimum arrangement of nearest neighbors that produce a low energy. At the interface, however, there is usually a change in composition so that each atom is partly bonded to *wrong* neighbors across the interface. This increases the energy of the interfacial atoms leading to a chemical contribution to the interfacial energy (γ_{ch}). For a coherent interface, this is the only contribution to the interfacial energy, i.e.

$$\gamma_{(\text{coherent})} = \gamma_{ch}.$$

In terms of a metal/oxide system, if the atoms in the metal are at positions $(n_1 a_1,\ n_2 a_2)$ on the interface (assuming a planar interface) and the metal atoms in the oxide at the positions $(n_1'\ a_1'\ ,\ n_2'\ a_2'\ )$, then the interface is coherent if the a's are such that sets of n can be chosen satisfying the equation

$$(n_1'\ a_1'\ ,\ n_2'\ a_2'\ ) = (n_1 a_1,\ n_2 a_2)$$

for all $n_1'\ ,\ n_2'$.

This definition does not require that all the atoms in the metal be matched in the oxide, but it does require that all the metal atoms in the oxide plane be matched in the metal. Some relaxation of this condition can be permitted. For example, if

$$(N_1 n_1'\ a_1'\ ,\ N_2 n_2'\ a_2'\ ) = (n_1 a_1,\ n_2 a_2),$$

where N_1 and N_2 are small integers, then the interface can still be regarded as effectively coherent.

When the unit vectors on the interface plane in the oxide $a_1'\ ,\ a_2'$ are not necessarily the same length as the corresponding vectors in the free oxide, it is still possible to maintain coherency by straining one or both of the two lattices. The resultant lattice distortions are known as coherency strains. When the oxide is strained with coherency strain $\epsilon_1'\ ,\ \epsilon_2'$, the coherency condition is satisfied:

$$\left\{N_1 n_1'\ a_1'\ (1+\epsilon_1'\ ),\ N_2 n_2'\ a_2'\ (1+\epsilon_2'\ )\right\} = (n_1 a_1,\ n_2 a_2).$$

Finally, the metal can also be strained with coherency strain $\epsilon_1,\ \epsilon_2$:

$$\left\{N_1 n_1'\ a_1'\ (1+\epsilon_1'\ ),\ N_2 n_2'\ a_2'\ (1+\epsilon_2'\ )\right\} = \left\{n_1 a_1(1+\epsilon_1),\ n_2 a_2(1+\epsilon_2)\right\}.$$

However, the magnitude of strains must be insufficient to nucleate dislocations in the metal or the oxide at the interface. This problem has been treated by a number of

authors, and reviewed by Gretz[121] for the case of a nucleus on the metal substrate. It seems generally, however, that the combined strains in the oxide and the metal cannot exceed 10 %.

In reality one cannot discuss oxide/metal orientations on the assumption that the forming oxide freely chooses its lowest energy plane. To some extent, the orientation of the oxide plane at the metal interface is determined by the mechanism of transfer of metal atoms from the metal to the oxide or by the kinetically favored interfaces. In general, it is to be expected that given a general metal surface, subject to the restrictions imposed by the growth mechanism, it will rarely be possible for the oxide to be oriented so that the coherency condition is satisfied.[122]

Semicoherent Interfaces

The strain associated with a coherent interface raises the total energy of the system and for sufficiently large atomic misfit or interfacial area, it becomes energetically more favorable to replace the coherent interface with a semicoherent interface in which the disregistry is periodically taken up by misfit dislocations. If a' and a are respectively the lattice parameters of the unstressed oxide and the metal, the misfit between the two lattices (δ) is defined by

$$\delta = \frac{(a' - a)}{a}.$$

In one dimension the lattice misfit can be accommodated without long range strain fields by a set of edge dislocations with a spacing D given by

$$D = \frac{a'}{\delta},$$

or approximately, for small δ,

$$D = \frac{b}{\delta},$$

where $b = \frac{(a' + a)}{2}$ is the Burgers vector of the dislocations. The matching in the interfaces is almost perfect except around the dislocation cores where the structure is highly distorted and the lattice planes are discontinuous. The interfacial energy of a semicoherent interface can be approximately considered as the sum of two parts (a) a chemical contribution, γ_{ch}, as for a fully coherent interface, and (b) a structural term γ_{st}, which is the extra energy due to the misfit dislocations, i.e.

$$\gamma_{(\text{semicoherent})} = \gamma_{ch} + \gamma_{st}.$$

The structural contribution increases rapidly as δ becomes larger and it levels out when $\delta = 0.25$, because the dislocation strain fields begin to overlap and cancel each other. Misfit dislocations may be regarded as glissile slip dislocations in the immediate vicinity of the interface.

As the oxide layer grows and moves away from the original metal/oxide interface, the misfit dislocations will cease to be glissile and become sessile *growth* dislocations.[123] The misfit dislocations may be mobile in the neighborhood of the interface because there is a high flux of defects passing through the interface as a result of the oxidation reaction. This process can make climb a relatively easy process for the misfit dislocations at the metal/oxide interface. In terms of this model, the stresses in the growing oxide will be large in a fairly narrow layer near the metal/oxide interface. This was observed by Dankov and Churaev[124] who studied the distortion of the metal films deposited on mica substrates when oxygen was admitted.

Although oxides are supposed to deform plastically only at very high temperatures, extensive plastic deformation has been observed at temperatures above 0.85 T_m, and signs of considerable plastic deformation have also been frequently observed in oxides formed on metals.[122] This could be due to departures from stoichiometry, but

there is no evidence that nonstoichiometry necessarily increases ductility. Ashbee and Smallman[125] showed that nonstoichiometric rutile TiO_2 was completely brittle below 1000 °C whereas stoichiometric TiO_2 showed a small degree of ductility as low as 600 °C. The rutile formed by oxidizing titanium is considerably more non-stoichiometric than this. Therefore it is not expected to show any plastic deformation below 1000 °C. But it is plastic and at 950 °C the oxide scale exhibits considerable rumpling and other indication of extensive plastic flow. Although the plastic flow is not due to nonstoichiometry, it may be due to the presence of a defect flux produced by the oxidation reaction.[122] However, the defect flux is constant throughout the oxide layer, whereas most of the plastic flow appears to be taking place near to the metal/oxide interface. This may be attributable to the fact that away from the interface the misfit stresses have been relieved. Alternatively the anomalously large plastic flow of the oxide may be due to the very large release of energy at the interface; most oxidation reactions are strongly exothermic. This model suggests that there is a layer of oxide close to the metal surface which is capable of considerable plastic flow. In this layer, dislocations are nucleated as a result of misfit strain. These misfit dislocations can move to a limited extent under the influence of the defect flux and further relax the stress. The oxide remote from the interface contains a number of grown in sessile dislocations and is relatively strain-free.

Incoherent interfaces

When the interatomic distance differs by more than 25 %, i.e. one dislocation every four interplanar spacings, the regions of poor fit around the dislocation cores overlap and the interface cannot be considered as coherent, i.e. it is incoherent. Very little is known about the detailed atomic structure of incoherent interfaces, but they

have many features in common with high-angle grain boundaries. They probably have a disordered atomic structure in that the interface lacks the long-range periodicity of coherent and semicoherent interfaces; although, like high-angle grain boundaries, they may have a step-like structure caused by low index planes protruding into the interface.

4.2 Crystallographic Models of Interphase Boundaries

Whereas structural models of grain boundaries in metals[126]-[129] and ceramic materials[130] are well developed, much less is known about the structure and properties of interphase boundaries. Most of the discussions in this section are based on structural models in metals and the lock-in model, which is the structural model of metal/ionic crystal interfaces.

4.2.1 Dislocation models

Perhaps the earliest attempt to develop a dislocation-type concept of the structure of grain boundaries was the proposal of Tayler[131] describing a boundary as a sequence of step-like wedges joined at common lattice points. Burgers[132] and Bragg[133] developed dislocation models for small-angle grain boundaries. The boundary was considered as a *surface of misfit* which could be viewed as an infinite aligned array of edge dislocations. This model which was initially developed for small-angle boundaries[132],[133] may be formally extended into the large-angle regime, as it is possible to interpret any interface geometrically in terms of a dislocation array.[134] Obviously, all dislocation models of a large-angle grain boundary have a problem in that the dislocation spacings are comparable with dislocation core dimensions, and hence the core structure and core interaction effects may be significant.[135]

4.2.2 Coincidence models

It was first shown by Friedel[136] that for certain misorientations about rational axes there exist superlattices on which a fraction of the lattice points in the two crystals coincide. Consider two interpenetrating lattices (lattice 1 and lattice 2). Assume lattice 1 to be fixed and all the changes, such as translation, rotation, etc, are performed with lattice 2. With the relative orientation of the two lattices given, lattice 2 is translated in such a way that one of its points coincides with a point in lattice 1. That point shall be termed a *lattice coincidence site*. It is possible that there exist an infinite number of those points, due to the periodicity of the two lattices. This is referred to as a coincidence site lattice (CSL) and is independent of the interfacial plane. The ratio of the volumes of coincidence and crystal lattice unit cells is designated Σ. It should be obvious that all rotational symmetry elements yield $\Sigma = 1$.[137] The next highest degree of coincidence in the cubic system, $\Sigma = 3$, occurs for the familiar twinning operation. In the face-centered lattice twinning, there is such coincidence every third (111) plane. When the CSL concept is used in the description of grain boundaries, it is necessary to also consider the orientation of the boundary plane. For grain boundaries inclined to CSL planes a ledge structure is anticipated[138],[139] in order to maximize the area of good matching. The coincidence site lattice grain boundary model has previously been shown to be widely applicable to cubic metals, and more recently to ionic solids.[140]

The coincidence site lattice concept was generalized by Bollman[141] to include coincidences of any equivalent points, lines, or planes. Such coincidences are called O-points, -lines, and -planes, respectively, and are regions of exact matching, or *minimum-strain points*, between two interpenetrating crystal lattices. The O-lattice

theory is completely general and embodies many of the concepts of the theories of twinning, and the coincidence site lattice, each of which may be regarded as a special case.[142] A further aspect of O-points is that they are origins to which the two crystal lattices are related by a particular transformation. The misfit between O-elements is accommodated by dislocations which conserve low-energy structures.

For example, the O-lattice, and consequently the misfit dislocation structure of the Al/γ–Al_2O_3 phase boundary, can be obtained as follows. According to Bollman[141] the translation vectors, $\mathbf{x}_O$, giving the points of good fit, i.e. the O-lattice are given by

$$\mathbf{x}_O = (\mathbf{I} - \mathbf{A}^{-1})^{-1}\,\mathbf{x}$$

where **I** is the identity matrix, **A** is the transformation matrix, and the vectors **x** define the primitive reference lattice. For the two lattices of the aluminum and γ–Al_2O_3 crystals it also can be seen by choosing the aluminum lattice as reference that the appropriate two-dimensional reference matrix, which, for this example, corresponds to a $<001>$ projection of both aluminum and γ–Al_2O_3 crystals, is given by

$$\mathbf{x} = \begin{bmatrix} a/2 & a/2 \\ a/2 & -a/2 \end{bmatrix},$$

where a is the lattice constant of Al. The transformation matrix, **A**, is the product of a rotation matrix and a matrix describing the distortion necessary to transform the unit cell of the reference lattice into the unit cell of the other lattice. For the present $\Sigma = 1 : \Sigma = 1$ Al/γ–Al_2O_3 interface, this distortion is simply a half of the ratio of the lattice parameters, and the rotation is 0°. Hence

$$\mathbf{A} = \alpha \begin{bmatrix} \cos 0^\circ & -\sin 0^\circ \\ \sin 0^\circ & \cos 0^\circ \end{bmatrix}$$

with $\alpha = \dfrac{a'}{2a}$, where a' is the lattice constant of γ–Al_2O_3. This gives

$$\mathbf{I} - \mathbf{A}^{-1} = \begin{bmatrix} 1-\alpha & 0 \\ 0 & 1-\alpha \end{bmatrix}$$

and

$$[\mathbf{I} - \mathbf{A}^{-1}]^{-1} = \begin{bmatrix} 1/(1-\alpha) & 0 \\ 0 & 1/(1-\alpha) \end{bmatrix}.$$

Hence

$$\mathbf{x}_O = \begin{bmatrix} \alpha' & \alpha' \\ \alpha' & -\alpha' \end{bmatrix}$$

with $\alpha' = \frac{a}{2(1-\alpha)} = 21.3a$ for the $\Sigma = 1 : \Sigma = 1$ Al/γ-Al_2O_3 interface. Interface misfit dislocations are expected to run along the boundaries of the Wigner-Seitz cell of the O-lattice, i.e. along <110> directions with a spacing equal to $\sqrt{2} \times 21.3a = 12.2$ nm. One possible interface structural configuration is as follows. The lattice planes have perfect matches at coincidence sites, but lattice planes get gradually more and more out of register, until midway between points of near coincidence a $\frac{a}{2}$<110> edge misfit dislocation is accommodated. Such a dislocation structure is consistent with the displacement shift complete (DSC)[141] lattice calculations for fcc/fcc systems.[143] Thus the interface would consist of coherent, square domains bounded by pure edge dislocations.

4.2.3 Plane Matching Models

Pumphrey[144],[145] suggests that the matching of a set of low index lattice planes across a grain boundary provides for a low energy configuration. Hence, according the plane matching model, a grain boundary will assume the structure necessary to preserve continuity of low index atom planes across its interface.

4.2.4 Lock-In Model

Fecht and Gleiter[146] proposed the lock-in model to describe the atomic structure of interphase boundaries of low energy between noble metals and ionic crystals. According to this model, a low energy configuration is reached when low index planes and close-packed directions of the two phases are parallel. Assuming that the plane of the interphase boundary between a metal and an ionic crystal lies parallel to the low energy (cleavage) plane of the ionic crystal, the *surface* of the ionic crystal may be described in terms of a set of close packed rows of atoms separated by relatively deep *valleys*. The closest packed rows of the atoms at the *surface* of the metal form a *lock-in* configuration with the valleys of the *surface* of the underlying ionic crystal. With increasing lattice mismatch the width of the *row* and the *valleys* becomes gradually incompatible. So the number of low energy *lock-in* configurations decreases.

Fecht *et al.* [147] investigated the energy of interphase boundaries between noble metals (Au, Cu) and various ionic crystals (LiF, NaCl, KCl, MgO, Al_2O_3, mica) by means of the plate/sphere method, and suggested that the coincidence model is not applicable to describe the structure of interphase boundaries of low energy between noble metals and ionic crystals, but the atomic structure of the low energy boundaries observed may be understood in terms of the proposed lock-in model.

4.2.5 Polyhedral Unit Models

The basic idea of the polyhedral unit model is that the structure and properties of a grain boundary may be described in terms of a two-dimensional array of one or several types of atomic configurations (also termed atomic clusters or polyhedral units).[129],[148] Brandon *et al.* [138] proposed that low energy boundaries are obtained if boundaries lie in the most densely packed plane of the coincidence lattice. The low

energy was rationalized in terms of a two-dimensional array of an atomic configuration containing a coincidence atom plus the surrounding atoms. The positions of the atoms in such a structural unit was assumed to deviate little from the positions that they would occupy in the perfect lattice because the strain is small that is associated with the special atomic configuration, resulting in a high density coincidence boundary. On the basis of the computed atomic structure of grain boundaries in fcc metals it was suggested[149] that the structure of a grain boundary may be described by a two-dimensional periodic pattern of characteristic atomic groups which were shown to consist of a central atom surrounded by five, six or seven atoms. These *five-, six-, or seven-coordinated units* were proposed[129] as representing the basic structural elements of a general grain boundary.

CHAPTER 5

HIGH-RESOLUTION TRANSMISSION ELECTRON MICROSCOPY

5.1 Theory of Image Formation

This section below gives a general outline of phase contrast imaging and some concepts useful for the interpretation of high-resolution transmission electron micrographs.

All transmission electron microscopy may be categorized as utilizing amplitude contrast or phase contrast. In amplitude contrast imaging, the image is formed by one beam of electrons, that being either the forward scattered beam or one scattered through a specific angle, normally a Bragg scattering angle in the specimen. Thus, a conventional bright field image is a magnified map of the amplitude variation of the forward scattered electron beam, whereas a dark field image is a magnified map of the amplitude variation of one of the Bragg scattered beams. But, high-resolution transmission electron microscopy requires the use of more than one scattered beam. The phase shifts caused by the specimen and by the wave aberration of the objective lens create phase contrast as an interference effect between the primary and scattered electron waves; this is referred to as phase contrast imaging. Unlike amplitude contrast imaging where contrast in the image arises from local variations of scattering amplitudes across the area from the specimen, phase contrast imaging is capable of resolving single atoms, provided aberrations within the microscope are low enough to recreate the transmitted information of the specimen.

In phase contrast imaging, two or a row of beams produce a fringe pattern whereas three or non-colinear beams produce a lattice image. The desired lattice spac-

ings must be within the resolution limit of the microscope, that is, the lens system must preserve the coherence of the image forming beams. This implies that the imaging conditions must be optimized for the resolution capability, e.g. via specimen, objective lens design and electronic and mechanical stability of the microscope.

The electrons emitted into the vacuum and then accelerated between cathode and anode by the gun interact with the specimen in an electron microscope. Electrons are elastically scattered at the nuclei of the specimen atoms by the Coulomb force and elastic scattering can be considered as an electron-nucleus interaction in which the atomic electron cloud screens the Coulomb potential. Transmission electron microscopy can provide high-resolution because elastic scattering is an interaction process that is highly localized to the region occupied by the screened Coulomb potential of an atomic nucleus, whereas inelastic scattering is more diffuse; it spreads out over about a nanometer.[150] For small-angle scattering, the term elastic scattering is automatically reserved for interactions in which a negligible amount of energy is transferred to the nucleus and electrons are scattered with no appreciable energy loss. Considerable energy can however be transferred from an electron to a nucleus at high electron energies and large scattering angles.

In order to obtain an image which is directly interpretable in terms of the actual atomic arrangement in a crystal, special experimental conditions must be satisfied. First, since the observations in high-resolution electron microscopy are limited to the two-dimensional projected atomic structure, interpretation of an image in terms of the projected atom positions requires that the very thin specimen be oriented precisely along low index poles with planar spacings within the resolution limit of the microscope. Second, the combined influence of aberrations, defocus and aperture limitations

of the objective lens must be such as to turn the information into an image intensity which has some direct relationship with the projected potential of the specimen structure.

A useful approximation in the description of the interaction of the electron beam with the specimen is found in the assumption that there is no absorption and the phase shift is caused only by the specimen, that is, a phase object. An incident wavefunction ψ_0 is modified by the specimen to

$$\psi = \psi_0 e^{-i\sigma t\,\phi_p(x,y)}$$

where σ is the electron interaction parameter, t specimen thickness, and $\phi_p(x,y)$ the projected potential.

A further approximation, known as the weak-phase object approximation, assumes weak scattering within the specimen and therefore, that the phase shift is still $\frac{\pi}{2}$ but amplitude is very small. Under these conditions:

$$\psi \approx \psi_0[1 - i\sigma t\,\phi_p(x,y)].$$

Application of this requires that

$$t \ll \frac{1}{\sigma\phi_p}.$$

Hence, the required thickness decreases with increasing atomic number, though it is less that 100 Å for all materials of interest. The above form of the exit wavefunction has a straightforward physical interpretation. The dominant transmitted wave is approximated by ψ_0 while to this is added a relatively weak scattered wave of amplitude $\sigma t\,\phi_p(x,y)$ and phase $-\frac{\pi}{2}$ relative to the unscattered portion, as it is purely complex. For such thickness and assuming ideal aberration-free imaging, i.e. one that imposes a phase shift of $-\frac{\pi}{2}$ on all scattered beams, the amplitude distribution

$F(u,v)$ in the back-focal plane can be obtained by integration over all of the surface elements of the specimen plane, i.e. the Fourier transform of ψ, and the wave amplitude distribution is obtained by integrating over all elements of area of the focal plane, i.e the inverse Fourier transform of $F(u,v)$. Thus, a linear relationship between image intensity and projected potential is obtained

$$I(x,y) = 1 - 2\sigma t\, \phi_p(x,y).$$

In practice, however, complete reconstruction is not achieved in the back-focal plane due to lens aberrations, an aperture, and microscope instabilities. Spherical aberration reduces the focal length for beams at larger scattering angle. Since the beams and wavefronts are orthogonal, the wavefronts beyond a lens with spherical aberration are more strongly curved in the outer zones of the lens; there is a difference of optical path relative to the spherical wavefronts of an ideal lens. The wave amplitudes are therefore not all in phase at the Gaussian image point. A phase shift by defocusing of the lens has also to be considered; this can be generated either by a displacement of the specimen or by a change of focal length. Allowing for such spherical aberration and a lens defocus Δf , the phase shift relative to the optic axis is

$$\chi = \frac{\pi}{2}(C_s \lambda^3 k^4 - 2\Delta f\, \lambda k^2).$$

where k is the spatial frequency in reciprocal lattice space, C_s is the spherical aberration coefficient of the lens, and the other terms have the usual meaning. The action of this contribution can be represented by a multiplication of the amplitudes at the focal plane by the phase factor $\exp[i\,\chi(k)]$, and in high-resolution electron microscopy these perturbations are represented by a linear contrast transfer function (CTF)[151]-[154] to describe the objective lens action, that is, a plot of $\sin\chi$ versus k, as shown in the top-right corner of Fig. 13, for a JEOL JEM 200CX microscope. Under the weak-phase

object (WPO) approximation, the transmitted beam and the real components of the scattered beams interfere to form the image, i.e. a scattered beam's contribution is proportional to sin χ. For negative χ, the scattered beams interfere destructively with the transmitted beam, producing *black* atom images whereas a positive χ leads to *white* atoms.

For a WPO, the largest number of beams will contribute to the image by maximizing the portion of the CTF where $\sin \chi = \pm 1$ or close to it. Requiring that $|\sin \chi| \geq \frac{1}{e}$ over the maximum range of spatial frequencies leads to the Scherzer defocus value [155]

$$\Delta f_{\text{Scherzer}} = 1.2\,(C_s\,\lambda)^{1/2}.$$

The first zero of sin χ at Scherzer defocus gives the Scherzer resolution limit

$$d_{\text{Scherzer}} = 0.7\ C_s^{1/4}\lambda^{3/4}.$$

This is the highest resolution at which one may hope to directly interpret a high-resolution image in terms of the projected atom positions. It is possible to get information beyond this Scherzer limit, even though some lower angle scattering is excluded, by proper adjustment of the defocus of the objective lens to reach the linear image resolution limit [156] or the information retrieval limit which is set by the chromatic aberration and voltage and current instabilities.[157]

Decreasing the defocus value leads to high order passbands at

$$\Delta f_n = [\frac{1}{2} C_s\,\lambda(8n + 3)]^{1/2}$$

which may be employed to resolve finer detail, $n = 0$ giving the Scherzer passband. It is apparent that the resolution improves with both decreasing C_s and λ.

While working at the microscope, one needs to select the proper defocus to optimize resolution, and uses the minimum contrast condition as a reference point. At

this defocus setting, scattered beams are as close to a $-\frac{\pi}{2}$ total phase shift as possible, minimizing interference with the transmitted beam. This is given by

$$\Delta f_{\text{min}} = -0.44\,(C_s\,\lambda)^{1/2}$$

where $|\sin\chi| \leq 1 - \frac{1}{e}$ over the maximum range of spatial frequencies.

It has been assumed that a) the electron beam is monochromatic and b) the incident wave is planar or spherical (point source-spatial coherence). In reality, the electron emission process gives a beam with an energy width of 1–2 eV for thermionic and 0.2–0.3 eV for field-emission guns,[150] and the electron source has a finite size.

The variations of electron energy δE as well as those of the acceleration voltage and the lens currents δV and δI respectively result in variations Δ of the defocusing. A good approximation to the spread in focus Δ is expressed as

$$\Delta = C_c \left\{ (\frac{\delta V}{V})^2 + 4(\frac{\delta I}{I})^2 + (\frac{\delta E}{E})^2 \right\},$$

where C_c is the chromatic aberration coefficient, $\delta V/V$ and $\delta I/I$ are the high voltage and lens current ripple respectively, and $\delta E/E$ is the fractional energy spread of the electron beam. The influence of the focus spread on the CTF [158] is shown as a Gaussian damping function

$$K_c(k) = \exp\left\{ -\frac{\pi}{2} \left[\frac{\pi \Delta^2 k^2 \lambda}{4} \right]^2 \right\},$$

which depends only on k. The function $K_c(k)$ therefore acts as an envelope function. The envelope functions for a Gaussian spread of focus of half-width 50 Å at the accelerating voltage 200 keV, are shown in the middle-left of Figs. 13 (a) and (b). The envelope function due to spread of focus (or chromatic aberration) slopes gradually to zero, transferring higher frequencies only partially.

If a finite electron-source size and hence a finite illumination aperture is used, many of the electrons in a supposedly parallel beam in fact travel at an oblique angle to the optic axis. This influence on the CTF [157],[159] is generally expressed with a envelope function for a beam divergence:

$$K_s(k) = \exp\left[- \frac{(\pi C_s \lambda^2 k^3 - \pi \Delta f k)^2 \alpha^2}{ln\, 2} \right].$$

Unlike the envelope $K_c(k)$, which depends only on k, $K_s(k)$ depends also on the illumination aperture α and defocus Δf. The envelope functions for a beam divergence semi-angle of 0.3 milliradian and other values characteristic of a JEOL JEM 200CX microscope are shown in the middle-right of Figs. 13 (a) and (b). The divergence envelope function is steeper, and its shape and cutoff frequency change with changes in defocus; at the higher degrees of underfocus the cutoff frequency is higher, allowing more higher frequencies to contribute to the image, but mid-range frequencies are damped. Thus, it is desirable to maximize both the spatial and temporal coherence of the source and minimize microscope instabilities to resolve finer detail.

5.2 Theory of Image Simulation

This section gives the essential background on calculated lattice image simulations required for consideration of subsequent chapters.

The current generation of electron microscopes makes possible the attainment of atomic resolution in the image of crystals.[2] However, the image contrast in the high-resolution electron micrographs varies rapidly with objective lens focus and specimen thickness. Only for very thin specimens, typically less than 50-100 Å for many oxide and silicate minerals, and a few tens of Angstroms for most metals and alloys, and for selective settings of defocus does the image contrast bear a one to one correspondence

to the specimen structure.[160] For specimens thicker than the above limits, there is no simple relationship between the image and the projected specimen structure. To provide proper interpretation of the image it is usually necessary to match experimental images to computer simulated images for a range of defocus values and specimen thickness. In particular, interpretation of images of defects (e.g. interfaces) and complex structures such as found in ceramics generally requires matching of the images with companion computed image simulations for reliable interpretation.

The starting point for image formation is to model the electron microscope as a simple system of electron beam, specimen and lens system (Fig. 9). Generally the initial electron beam is considered to be a parallel beam of plane wave electrons. The microscope lens system is replaced by one spherically-aberrated lens which can be regarded as representing the objective lens. In a real electron microscope, the objective lens has the crucial duty of reassembling the diffracted beams emerging from the specimen into the image, which is merely magnified further by subsequent lenses.

In any simulation three functions representing the electron wave amplitude must be computed at the three positions within the model microscope; at the exit surface of the specimen, $\psi(\mathbf{x})$; at the back-focal plane of the objective lens, $F(\mathbf{k})$; and the image plane of the lens, $\Psi(\mathbf{x})$.

The computation of the exit-surface wave $\psi(\mathbf{x})$, involves mainly the model specimen structure (the only microscope parameter involved is the energy of the electrons in the incident beam). The wave at the back-focal plane, $F(\mathbf{k})$, is obtained via a simple Fourier transform of the exit-surface wave $\psi(\mathbf{x})$. Calculation of the image from the electron wave at the diffraction plane does not involve the specimen, but only microscope parameters, such as objective lens defocus and spherical aberration. Together

with the objective aperture size and position, these modify $F(\mathbf{k})$ before it is transformed, into $\Psi(\mathbf{x})$, the image amplitude.

Current image simulation calculations are usually based on the multislice method[161] in which the amplitude and phase at the exit-surface of a crystalline specimen is found by treating the crystal as consisting of N slices of thickness Δz so that the total thickness $t = N\Delta z$. The crystal potential of each slice is then replaced by the two dimensional projected potential for sufficiently small Δz. The effect of the first slice on the incident wave is calculated; the resulting wavefunction is then propagated through free space to the next slice. This is repeated until the desired thickness is achieved.

First, a calculational unit cell is selected with specification of atomic species and coordinates. The Fourier coefficients of potential (structure factors) at the reciprocal lattice points are calculated by summing over all atoms in the unit cell:

$$V_{\mathbf{k}} = \frac{h^2}{2\pi m_e e V_c} \sum_j e_{f_j} | \mathbf{k} | \exp(-2\pi i \, \mathbf{k} \cdot \mathbf{r}_j)$$

where V_c is the volume of the unit cell, j identifies the atoms in the unit cell, e_f and $\mathbf{r}$ are the electron scattering factors and the positions of the atoms, respectively, $\mathbf{k}$ gives a reciprocal lattice position, $\mathbf{k} \equiv [u, v]$, and the other terms have the usual meaning. The electron scattering factor, which is defined as the Fourier transform of the potential distribution for each atom, can also be computed from experimental X-ray structure factors. Inclusion of all $V_{\mathbf{k}}$ within 4 $\mathring{\text{A}}^{-1}$ of the origin of reciprocal space provides sufficient accuracy for most calculations.[156]

Fourier transformation of the $V_{\mathbf{k}}$ values produces $\phi_p(\mathbf{x})$ the crystal potential of one unit cell projected in the direction of the electron beam. The effect of such a thin

slice of crystal on the electron beam is that of a phase object, and the electron *transmission function* for the slice is

$$q(\mathbf{x}) = \exp[i\,\sigma\phi_p(\mathbf{x})\Delta z]$$

where Δz is the *slice thickness* and σ is the interaction parameter for the electrons of the designated energy.

The exit-surface wave at the desired crystal thickness, $t = m\,\Delta z$, is found from $q(\mathbf{x})$ by iteration. After m slices the electron wave $\psi(\mathbf{x})$ is given by

$${}^{m}f(\mathbf{x}) = [{}^{m-1}f(\mathbf{x}) * {}^{m}p(\mathbf{x})]\,{}^{m}q(\mathbf{x})$$

where ${}^{m}q(\mathbf{x})$ is the transmission function of the m th slice and ${}^{m}p(\mathbf{x})$ is the small-angle approximation to the free space propagator for the distance between the (m-1)th and m th slices (i.e. the familiar Fresnel propagator); * represents the convolution operation.

The diffraction plane wavefield ${}^{m}F(\mathbf{k})$ is obtained from ${}^{m}f(\mathbf{x})$ by Fourier transformation. In fact, the multislice is typically carried out in reciprocal space, leading directly to $F(\mathbf{k})$

$${}^{m}F(\mathbf{k}) = [{}^{m-1}F(\mathbf{k})\,{}^{m}P_{\mathbf{k}}] * {}^{m}Q_{\mathbf{k}}$$

where $P_{\mathbf{k}}$ and $Q_{\mathbf{k}}$ are the Fourier transforms of $p(\mathbf{x})$ and $q(\mathbf{x})$.

In order to compute the image plane intensity of the image-plane wave, one needs to include the effects of objective lens defocus and spherical aberration. These parameters act merely to change the phases of the diffracted electron beams passing through the aperture of the lens. Thus, the modified back-focal plane wavefield becomes;

$$F_m(\mathbf{k}) = F(\mathbf{k})A_{\mathbf{k}}\exp[i\,\chi(\mathbf{k})]$$

where:

$$\chi = \frac{\pi}{2}(C_s \lambda^3 k^4 - 2\Delta f \ \lambda k^2),$$

as shown in the previous section 5.1. The objective aperture function $A_{\mathbf{k}}$ is unity for beams passing through the aperture and zero for those outside.

The convergent character of the incident electron beam and the spread of focus produced by the energy spread in the incident electrons have the effect of smearing the microscope image by making it a composite of high-resolution images. Incident beam convergence produces composite images formed by the summation of the many images, each at a different angle within the incident cone. Spread of focus produces a composite formed from images summed over a range of defocus. These influences can be taken into account by modifying the back-focal plane wavefield.

Whereas an accurate value of the beam convergence α can be measured directly from a diffraction pattern obtained with focussed illumination, the spread of focus Δ for a particular electron microscope must either be estimated by matching an experimental image with ones computed using different values of Δ, or approximated from known values of the chromatic aberration coefficient C_c and high voltage and lens current ripple.

Lastly, the simulated image, i.e. the intensity in the image plane, can be calculated by a Fourier transform of the fully modified back-focal plane wavefield to obtain the amplitude $\Psi(\mathbf{x})$ followed by squaring of the amplitude:

$$I(\mathbf{x}) = \Psi(\mathbf{x}) \cdot \Psi^*(\mathbf{x}).$$

CHAPTER 6

EXPERIMENTAL PROCEDURES

6.1 Specimen Preparation for Transmission Electron Microscopy

The 99.999 % pure polycrystalline and single crystal aluminum were used. The chemicals, sodium hydroxide, concentrated nitric acid, and ethanol were general laboratory grades. The aluminum ingot was cut into coupons of 1.4 mm$\times$3 mm$\times$20 mm. The coupons were cleaned in sodium hydroxide and washed in ethanol, and then sealed in evacuated quartz tubes and annealed at 550 ° C for 5 days.

A single surface preparation was used throughout this study. A suitable sample preparation should 1) avoid mechanical distortion of the surface, 2) produce a smooth surface, 3) avoid surface contamination which can become included in the growing oxide film and modify its defect structure. Although conventional electropolishing of Al fulfills the first two requirements, previous work[12] revealed that residual perchlorate ions from typical electropolishing baths seriously reduced the ionic resistance of subsequently formed alumina films. For this reason the chemical surface preparation described below was used.

For the clean and flat surface preparation, the sample was mechanically polished and chemically etched in sodium hydroxide, dipped into nitric acid and washed in anhydrous methanol. The sample was stored in an atmospheric pressure desiccator for 1 day to allow formation of a uniform room temperature oxide, and then oxidized in 1 atm air at either 500 ° C or 600 ° C for times from 0.5 hr to 4 weeks. All the oxidation treatments were terminated by an iced water quench.

Cross-section TEM specimens have the great attraction that all the important interfaces between aluminum and oxide can be observed directly. Although specimen preparation was not easy, the most successful specimen preparation technique[162],[163] is described below (Fig. 10). Two oxidized samples were bonded face to face with epoxy (5 ton epoxy, Devcon Company) and then squeezed with a clip to minimize the epoxy layer thickness between two samples. After a minimum setting period of 1 day, the bonded samples were sliced into small pieces (2.8 mm$\times$3 mm$\times$2.8 mm) with a diamond saw. The sliced sample was mounted with wax (80 ° C melting point) onto a quartz disc so that the interesting interfaces were perpendicular to the plane of the disc. The sample was polished mechanically on a rotating wheel with 600 grit paper. The final polishing was accomplished with 0.03 μm alumina paste. This polishing procedure was repeated on the other side of the specimen until a final thickness of between 50 and 100 μm was achieved. The sample was separated from the quartz disc by dissolving the wax in a beaker of ethanol. The sample was then dried and glued to a copper grid for support and easy handling.

The rotating specimen stage of the Gatan ion mill, cooled with liquid nitrogen, was used for ion beam milling at 17 ° gun tilt, 5 kV gun voltage and 50 μA specimen current. The final milling was accomplished with at 12 ° gun tilt, 10 μA specimen current. A higher yield of good specimens can be obtained if more mechanically thinning is employed, because this reduces the preferential ion beam milling effect on the epoxy.

6.2 High-Resolution Transmission Electron Microscopy

High-resolution micrographs were obtained under optimum conditions, as defined in CHAPTER 5. The microscope for this study was the JEOL JEM 200CX (high-

resolution pole piece, C_s = 1.2 mm, C_c = 1.4 mm at 200 keV).

Generally, the filament (LaB_6) was operated with a brighter central spot in an undersaturated mode in order to increase beam coherence.[164] The first condenser lens was turned off to enhance brightness and the condenser aperture was inserted for optimum trade-off between brightness and beam coherence. Following careful alignment of the imaging system, the specimen was tilted using a combination of the extinction contours in the bright-field (BF), and Kikuchi lines and the high-order Laue zone (HOLZ) lines to produce the highest symmetry in diffraction pattern corresponding to the chosen zone axis (most cases in a <110> orientation).

The beams corresponding to reciprocal lattice vectors with magnitude greater than the reciprocal space position at the point-to-point resolution limit will contribute only to the background noise in the image. Choosing a suitable objective aperture can exclude these beams, thereby improving image contrast.

The adjustment of objective astigmatism was the most critical step. At lower magnification, astigmatism was corrected by adjusting the Fresnel fringe for even width around a hole or protrusion. At high magnification (400 k× or above), the amorphous region was observed and adjusted to maximize the symmetry of phase contrast while slightly under and overfocusing the objective lens. At the correct stigmator setting, the amorphous region should show fine grain non-directional contrast as the focus is taken above and below the minimum contrast condition. The objective lens current is then adjusted to obtain an image with minimum phase contrast. This establishes the minimum contrast condition (Δf_{min}), where image shift due to spherical aberration has been offset by an objective lens at underfocus from the Gaussian image plane ($\Delta f = 0$) given by $\Delta f_{min} = -0.44\ C_s \lambda^2$. Since this is easily observed and cal-

culated for known C_s and λ, it serves as reference point, from which the objective lens can be defocussed in set increments to reach the optimum focus condition.

The through-focal series of images, starting from an overfocused condition and proceeding incrementally through minimum contrast and continuing to at least the third pass-band, was taken on the desired specimen area. Exposures of 4 sec at 530 k$\times$ magnification were generally used. Amorphous edges were included in the images whenever possible, to obtain information about defocus, astigmatism and specimen drift by optical diffraction (see following) of the developed negative on a laser bench.

Optical diffraction was performed on high-resolution micrographs to determine the CTF from spatial frequencies recorded in the image. A coherent He-Ne laser light source ($\lambda = 6328$ Å) was used to illuminate a high-resolution micrograph negative on an optical bench, and the optical diffraction patterns were recorded on Type 52 Polaroid film, usually at exposures of about 1/125 sec. Optical selected area diffraction patterns were also obtained from high-resolution electron micrographs simply by placing an aperture in the path of the laser. This technique allowed diffraction information to be obtained from areas as small as 20 Å, thereby revealing detail which was obscured during conventional selected area diffraction in the microscope.

6.3 Image Simulations

Simulated high-resolution electron microscope lattice images are calculated on the Lawrence Berkeley Laboratory (LBL) Control Data Corp. 7600 computer using the LBL MSLICE programs developed by R. Kilaas.[165] These programs at LBL are able to compute scattering factors, perform multislicing, simulate the effect of the microscope lenses, plot images as gray level plots, plot projected slice potentials, compute and plot diffraction patterns, plot amplitudes and phases of selected beams as a

function of thickness and plot contrast transfer functions. The image simulation programs employed only in Figs. 41 and 42 are from Arizona State University MULTISLICE programs developed by O'Keefe and Skarnulis,[166] and later modified into the ZOLZPROG series of programs by Spence.[167] In this section the LBL MSLICE programs will be discussed. The LBL MSLICE computer simulation programs for an image consist of three programs, PHSGR, MULTI, DISPL. They are run in succession and each of these programs except PHSGR uses the output of the previous program plus its own input file containing additional operating parameters to calculate the final image. PHSGR calculates the effective potential seen by the electron as it moves through the specimen, MULTI then calculates the electron distribution as a function of specimen thickness after the actual propagation of the electron through the specimen and DISPL calculates the interaction between the electrons and the imaging system of the microscope before synthesizing the final image. Each of these programs, and the values commonly used as input parameters in this study are described briefly below.

6.3.1 PHSGR

PHSGR calculates the effective potential from electron scattering factors which are calculated using relativistic Hatree-Fock atomic wave functions.[168] In principle the potential should include all scattering processes, both elastic and inelastic. However, in practice only elastic scattering is usually included.

The typical parameters as input to PHSGR are the simulation cell dimensions (A, B and C), atom positions, the atomic numbers of species, the number of atoms, the space group symmetry operators, isotropic temperature factors and the projection directions. In this study, all images were simulated with the electron beam incident

along the $<110>_{oxide}$ direction, since all the high-resolution images were taken along this direction. For a perfect crystal, one simply selects some multiple of the crystal unit cell parameters in the x and y directions respectively for A and B as shown in Fig. 19 (a). In effect, the programs calculate an image for a periodic array of the unit cells as shown in Fig. 18, the so-called *periodic extension* method. The use of Fourier transforms requires that the unit cell be smoothly varying at the boundaries. However, since this is impossible for the interface, this causes anomalous image effects near the cell boundary. The simulation unit cells used in the calculations of images of the interface are made of sufficient size so as to isolate the interface from these anomalous image effects. Although there is 2.5 % misfit between the lattice parameters of the γ–Al_2O_3 and those of the aluminum, it is assumed that the lattice parameters of both crystals are the same at the aluminum/oxide interface for the computer image simulation. The input files, including atom positions of Al (atomic number 13, isotropic temperature factor 0.3) and O (atomic number 8, isotropic temperature factor 0.7), are shown in the APPENDIX.

6.3.2 MULTI

The part of the computation, which treats the interaction between the specimen and the electron beam, is mostly based upon a dynamical multislice formulation proposed by Cowley-Moodie.[169] This calculation involves solving the one-electron Schrödinger equation. Beginning with the known electron distribution at the top of the specimen, MULTI calculates the electron wave function at each slice from the wave function at the previous slice, and stacks these outputs to produce the multislice scattered wave from a thick crystal. Output from thicknesses of interest are saved for final input to DISPL. The important values input for MULTI are the

accelerating voltage of the microscope (200 keV for the JEOL JEM 200CX), the phase grating slice thickness, sampling points of beams to be used in the multislice calculation and the the coordinates (h ,k) of the Laue circle center, to distinguish whether the electron beam is tilted with respect to the crystal, or vise-versa. In this image simulation, calculations are performed using 256×256 sampling points and the coordinates (h =0, k =0) of the Laue circle center.

6.3.3 DISPL

DISPL combines the beams from MULTI in a Fourier series to form the electron lattice image, taking into account the effects of the imaging system of the microscope. DISPL plots images as gray level plots to dispose the simulated image intensities using the Varian Plotter at the LBL Computer Center. The important microscope parameters and typical values for the JEOL JEM 200CX that were used as input for DISPL are spherical aberration coefficient (C_s = 1.2 mm), semi-angle of illumination (α = 1.0 mrad), half-width of Gaussian spread of defocus (Δ = 50 Å), objective lens defocus (Δf = +360 to -3000 Å), radius of objective aperture (0.5 Å^{-1}), h ,k coordinates of the optic axis and objective aperture center (0,0).

CHAPTER 7

RESULTS AND DISCUSSION

7.1 Conventional Transmission Electron Microscopy Studies

Results show that there are a number of possible crystallographic orientation relationships between the oxide and the aluminum matrix. However, crystalline γ–Al_2O_3 forms in two major crystallographic relationships with the aluminum matrix: parallel and twinned. The $[1\bar{1}0]_{Al} \mid\mid [1\bar{1}0]_{oxide}$ matrix/oxide selected area diffraction (SAD) pattern obtained by the 10 hr oxidation of aluminum at 500 ° C is shown in the top of Fig. 11, and may be compared directly with the completely-indexed schematic diffraction pattern shown in the bottom of Fig. 11. By comparing these two patterns, it is clear that the {111} oxide reflections are parallel to {111} aluminum matrix reflections and the {220} oxide reflections are also parallel to {220} aluminum matrix reflections with a parallel orientation relationship. The intensely bright spots of the pattern originate from the metal side of the interface and the weaker spots originate from the oxide.

In this orientation, the eight spots immediately surrounding the forward-scattered beam are the first-order $[1\bar{1}0]_{oxide}$ reflections; these {111} reflections represent a lattice spacing of about 4.6 Å. The high-intensity first-order $[1\bar{1}0]_{Al}$ reflections, {111} reflections representing a lattice spacing of about 2.3 Å, are almost coincident with the second-order $[1\bar{1}0]_{oxide}$ reflections with a parallel orientation relationship. Further, note that all the periodicities of the matrix reflections are about twice those of the oxide reflections, however, they are not completely coincident; there is a small misfit between them. Analysis of these diffraction patterns is based on the fact that alumi-

num has a face-centered cubic (fcc) structure with the lattice parameter 4.05 Å and that the oxide is γ-type aluminum oxide. The γ-Al_2O_3 has a defect spinel structure and its lattice parameter (7.90 Å) is very close to twice that of aluminum with a 2.5 % misfit.

If the two diffraction patterns are compared carefully, it is clearly seen that the extra oxide reflections due to {111} twinning in the oxide are located at $\frac{1}{3}$ of the distance from the oxide reflections along the <111> oxide directions. In the fcc systems twinning occurs on {111} planes, and so, the twinning matrix $T^{[170]}$ is

$$T_{111} = \frac{1}{3}\begin{bmatrix} -1 & 2hk & 2hl \\ 2hk & -1 & 2kl \\ 2hl & 2kl & -1 \end{bmatrix}$$

for the reflection {hkl}. For fcc twinning the elements inside the matrix shown are integers. Then, because of the factor $\frac{1}{3}$ outside the matrix, all third-order reciprocal lattice spots for the matrix (oxide) will coincide with allowed reciprocal lattice spots for the twin. In fcc crystals it can be seen that twin spots either coincide with matrix (oxide) spots or are positioned one third along <111> directions. For example, in fcc with twin plane (111)

$$200 \rightarrow \frac{1}{3}(\bar{2}44)_T = \bar{1}11 + \frac{1}{3}(111).$$

The twin spots that do not coincide with matrix (oxide) points are thus displaced from matrix (oxide) points by vectors of $\pm\frac{1}{3}$<111>.

In addition, it is clear that there are streaks from the oxide reflections along the <111> directions. These streaks imply that there are thin planar defects (twins, stacking faults or second phases) on {111} oxide planes. Actually the spots are

streaked because of the fineness of the twin lamellae and the stacking faults in the oxide as shown in later sections. The twinning and stacking faults in the oxide will be discussed in later sections.

The {200}, i.e. $\{hk0\}$, $h+k = 4n+2$ oxide reflections were observed in all of the $[1\bar{1}0]_{oxide}$ SAD patterns in this study, as shown in the electron diffraction pattern in Fig. 11. The $\{hk0\}$, $h+k = 4n+2$ oxide reflections are kinematically forbidden in the $Fd3m$ space group of the spinel structure.[171]-[174] To determine the origin of the forbidden reflections, two possible explanations have to be taken into account, i.e. 1) double diffraction of the electron beams, which is often found in electron diffraction, and 2) a superlattice structure caused by the ordering of the cation interstitial sites in the spinel structure. The strong {200} oxide reflections in this figure are kinematically forbidden but can arise due to double diffraction. For example, diffracted intensity can occur in the (200) position by double diffraction from the (111) and $(\bar{1}\bar{1}1)$ oxide reflection spots, i.e. $(111) + (\bar{1}\bar{1}1) = (002)$.

It is possible to determine whether or not certain forbidden reflections are present due to double diffraction by tilting the crystal about the axis containing the forbidden reflections. If the forbidden spots disappear after the crystal has been tilted to the extent that intensity from the reflections outside of the forbidden row can no longer contribute toward double diffraction, then it may be concluded that the spots are due to double diffraction. This tilting experiment was applied to determine whether or not the {200}, i.e. $\{hk0\}$, $h+k = 4n+2$ oxide reflections were due to double diffraction. The result shows that the {200} spots do not persist as the oxide crystal is tilted to obtain a <100> zone axis orientation. The {200}, {420} reflections in [100] zone axis diffraction patterns cannot occur by double diffraction. Thus it is concluded that these

spots are due to double diffraction.

Figure 12 shows the conventional bright-field images of the aluminum/oxide interfaces obtained by cross-sectional TEM specimen preparation as described previously. As shown by Fig. 12, the 5 hr oxidation treatment at 500 ° C was designed to produce a crystalline oxide beneath the amorphous oxide. At the shorter oxidation time or lower oxidation temperatures, amorphous oxide was always observed but crystalline oxides were rarely observed.

The amorphous oxide layer with the lighter contrast on the top surface grows on the aluminum matrix, whereas the crystalline oxide with the darker contrast nucleates at the aluminum/oxide interface and protrudes into the aluminum matrix. As indicated by the marker in this figure, the amorphous oxide is about 35 Å thick and the crystalline oxide protrudes about 800 Å deep. In this study, the crystalline oxides were tilted to reveal the edges of the oxide in a $<110>_{oxide}$ orientation. In this figure, the crystalline oxide shows a triangular shape and the angle between the crystalline oxide/aluminum interfaces is 70.5 °, which implies that the crystalline oxide/aluminum interface is composed of the {111} planes of the cubic crystal.

The contrast of the crystalline oxide crystal in a random orientation in the microscope was so low compared to the aluminum matrix that the oxide crystal was tilted to get a dark contrast as shown in Fig. 12. This dark contrast of the oxide crystal was obtained by maximizing the scattering contrast difference between the oxide crystal and the aluminum matrix. For example, some oxide crystals on the left side of Fig. 12 (b) show a low contrast compared to the aluminum matrix since these crystal are not oriented to show a high scattering contrast.

As shown in Fig. 12 (b), the 10 hr oxidation treatment at 500 ° C produced a

number of the crystalline oxides which nearly covered the aluminum surface. These crystalline oxides show that the angle between the two crystalline oxide/aluminum interfaces is 70.5°, as indicated in the figure. Note that the crystalline oxides protrude about 1000 Å deep into the aluminum matrix, indicating that the crystalline oxide grows into the aluminum matrix by inward diffusion of oxygen through the overlying amorphous oxide.

By comparing Figs. 12 (a) and (b), it may be concluded that the γ–Al_2O_3 crystallites, which nucleate at the metal/amorphous oxide interface, rapidly achieve a terminal depth and shape, and the nucleation continues until the crystallites impinge on one another on the surface. This conclusion is in agreement with previous studies[5],[7],[12] by conventional replica techniques that the crystal oxides nucleated from the amorphous oxide/metal interface grow to a fixed depth into the underlying metal by inward diffusion of oxygen through the overlying amorphous film. Notice that the oxide crystal shapes are not roughly cylindrical as thought,[12] but they are determined by the combinations of the {111} planes.

As shown by Fig. 12 (c), the 4 week oxidation treatment at 600°C produced about 2000 Å thick crystalline and amorphous oxides. From Fig. 12, it is clearly seen that the amorphous oxide/crystalline oxide interface is smooth whereas the crystalline oxide/aluminum interface is faceted. Thus it may be concluded that the crystalline γ-Al_2O_3 grows with faceted interfaces into the aluminum matrix, whereas the amorphous oxide grows on the top surface.

7.2 High-Resolution Transmission Electron Microscopy of Al and γ-Al_2O_3

7.2.1 Determination of Optimum Defocus Conditions

In order to obtain a high-resolution image which is directly interpretable in terms of the projected potential, special experimental conditions must be satisfied as discussed in section 5.2. In particular, the influence of lens aberrations with beam divergence and microscope instabilities must be taken into account. These factors which introduce perturbations in the phase of the scattered wave in high-resolution transmission electron microscopy (HRTEM) are represented by the contrast transfer function (CTF) of the microscope. Thus interpretation of a HRTEM image in terms of the atomic structure of the specimen requires a detailed knowledge of the CTF and the spatial frequencies of the specimen.

In this study, the CTF for the JEOL JEM 200CX was determined over a wide range of defocus values using the MSLICE Computer program developed by Kilaas.[165] The important microscope parameters used as input for the program were typical values for the JEOL JEM 200CX, i.e. accelerating voltage (V = 200 keV), spherical aberration coefficient (C_s = 1.2 mm), objective lens defocus (Δf = +720 to -2300 Å), half-width of Gaussian spread of defocus (Δ = 50 Å), and semi-angle of illumination (α = 0.3 mrad). Note that a smaller value for α was used in computing these CTF's than for the simulated images which follow; this was done in order to slightly reduce damping of the CTF at the higher spatial frequencies and thereby, observe the behavior of the CTF under the best possible conditions.

The contrast transfer function at objective lens defocus values of -660 and -750 Å are shown in Figs. 13 (a) and (b), respectively. The relations between the spatial frequency and the objective lens defocus value for the phase shift $\chi = n\frac{\lambda}{2}$, where n is

an integer, are shown in the top-left corners of these figures. They also show the original undamped form of the CTF in the top-right corner, graphs of the damping functions due to the the energy spread (Δ) and convergence (α) of the electron beam in the middle, and the damped contrast transfer function in the bottom-right corner of Fig. 13.

The locations of the spatial frequencies of the first-order reflections for both the oxide and aluminum matrix are also indicated by small thin markers for the oxide and small thick markers for the aluminum in these graphs, along the horizontal axes where the CTF = 0. The first thin marker represents the frequency for the {111} oxide reflection at about 0.21 $\mathring{A}^{-1}$, the second thin marker for the {220} oxide reflection at about 0.36 $\mathring{A}^{-1}$, and the third thick marker for the {111} aluminum matrix reflection at about 0.43 $\mathring{A}^{-1}$.

Notice that at Scherzer defocus in Fig. 13 (a) only spatial frequencies out to about 0.40 $\mathring{A}^{-1}$ are transferred with $\sin \chi = -1$ by the objective lens, whereas spatial frequencies greater than this are either truncated as the CTF goes to zero at about 0.42 $\mathring{A}^{-1}$, or are transferred with the opposite phase. Thus, the spatial frequency 0.43 for the {111} aluminum reflection is transferred with $\sin \chi \sim 0.12$ and Scherzer defocus does not represent the optimum objective lens setting for this frequency in the aluminum. However, when $\Delta = -750$ $\mathring{A}$ as shown in Fig. 13 (b), the spatial frequencies for the {111}, {220} reflections of the oxide and the {111} reflection of the aluminum matrix can be transferred with $|\sin \chi| > 0.38$, furthermore with the same negative phase. Thus, this objective lens setting can represent one of the optimum imaging conditions for this specimen. When the specimen acts as a weak-phase object, the high-resolution image will consist of black atoms on a white background, because $\sin\chi$ is

negative at this defocus value. The darkness of the atoms is simply related to the projected specimen potential.

Figure 14 shows the CTF over a range of defocus values starting from +720 Å and continuing through the minimum contrast condition $\Delta f_{\text{min}} = -240$ Å, Scherzer defocus $\Delta f_{\text{Scherzer}} = -660$ Å, the second pass band $\Delta f_{\text{2nd}} = -1300$ Å, the third pass band $\Delta f_{\text{3rd}} = -1690$ Å, and out to the fourth pass band at $\Delta f_{\text{4th}} = -2300$ Å, which are obtained from the defocus calculation equation for the higher order pass bands in section 5.1.

From the graphs in Fig. 14, it can be seen that the spatial frequencies for the {111} oxide and {111} matrix reflections are transferred relatively well at defocus values of about -600, -750, -1450 and -1690 Å, whereas those for the {220} oxide and {111} matrix reflections are transferred relatively well at defocus values of about -600, -750, -1000, -1200, -1300 and -2300 Å. However, note that at a defocus value of -600 Å the spatial frequencies of the oxide reflections are transferred by the objective lens with the opposite phase to those of the {111} matrix reflections.

7.2.2 Experimental High-Resolution Image of Al

Figure 15 shows an experimental high-resolution electron microscopy image of pure aluminum in a <110> orientation. All the atomic columns are clearly visible in the micrograph and the spacing of the {200} plane is indicated by the marker. The brightness of atomic columns slowly increases from the left to the right side of the micrograph with the thickness change of the specimen. Furthermore, there are many patches with slightly dark contrast, where the brightness of some atoms is completely dark even in this perfect aluminum structure. This contrast change might be due to local thickness variations caused by the ion-milling or because there is an overlayer on

the surface due to amorphous oxide[175] or specimen contamination.

7.2.3 Experimental High-Resolution Image of γ-Al_2O_3

Figure 16 shows a low-magnification view of experimental high-resolution electron microscopy images of γ–Al_2O_3, in the sample which was oxidized for 2 weeks at 600 ° C. The edge of the specimen is off to the top of the micrograph, i.e. the sample thickness is decreasing from the bottom to the top in the micrograph. The image character of the oxide is shown in greater detail in the enlargements in Figs. 17 (a)-(d) corresponding to the images from the thick area to the thin area in Fig. 16. From these enlargements, it is readily apparent that there are significant changes in the contrast due to the specimen thickness changes although all the micrographs in this figure were taken at the same defocus setting. The sensitive contrast change with specimen thickness is due to the fact that relatively many beams of the oxide in reciprocal space contribute to the image forming process compared with those of aluminum, and the local contrast change may arise from local thickness variations in the specimen, defects in the oxide, or an overlayer on the surface due to amorphous oxide or specimen contamination.

7.2.4 Image Calculation for γ-Al_2O_3 Structure

The main purpose of this section is to examine simulated HRTEM images of the γ–Al_2O_3 crystal structure in order to know how variations of specimen thickness and objective lens defocus value affect the appearance of these images. This information will then indicate if HRTEM images can be used to estimate the specimen thickness and defocus value, by comparison of simulated images and experimental images.

The actual atom positions used for image simulations are shown in Fig. 18, where

it is assumed that the aluminum atoms are distributed at random in the octahedral and the tetrahedral sites. This calculational unit cell contains 3×3 unit cells of Fig. 19 (a).

Figure 19 (b) shows the projected potential for the calculational unit cell in Fig. 18. This projected potential shows that the atom positions which contain two aluminum atoms along the projected direction have a much larger projected potential than those which contain one aluminum atom, and that the projected potentials of two oxygen atoms are slightly larger than those of one aluminum atom in the calculational unit cell. This is because the projected potentials of atoms increase with scattering factor and the density of the atoms. The high scattering factor of Al atoms as compared to O atoms leads to the different sizes of the projected potential. There are small mismatches of the projected potentials at the unit cell boundaries due to the incomplete printing of the computer printer. However, this fact does not affect the present image simulations because all the actual calculations were done for the perfect projected potentials.

A series of calculated images from the projected potential shown in Fig. 19, as a function of both objective lens defocus and specimen thickness up to 250 Å, is shown in Fig. 20, where the atom positions of the unit cell are also shown superimposed in the upper-left corners of simulated images at each defocus value.

The simulated images show relatively good contrast over a wide range of defocus values, because 31 beams including the {111}, {200} and {220} reflections from the oxide specimen contribute to the image formation in the objective aperture, although the CTF's do not always transfer well all the spatial frequencies. Only small changes in objective lens defocus result in relatively large changes in contrast because many

spatial frequencies which effect the image formation are affected by the variations of the CTF with lens defocus values. In addition, there is a similar contrast change in the appearance of the images with thickness.

Thus, these image simulations indicate that it is possible to estimate objective lens defocus value and specimen thickness for experimental images by comparing experimental and simulated images. Note that, whereas it is possible to determine the objective lens defocus from a HRTEM negative to the accuracy needed for correct image interpretation by using an optical bench, it is extremely difficult to measure the specimen thickness in the very thin areas where HRTEM images are most interpretable.

Figure 21 shows an enlarged experimental HRTEM image of γ–Al_2O_3 crystal from Fig. 16. All of the high-resolution lattice images were taken with a $<110>_{oxide}$ electron beam direction in this study. The bright spots in this image are arrayed in a rectangular pattern. Comparison of this image contrast with a series of simulated images in Fig. 20 shows that good agreement is obtained for a specimen thickness of 250 Å and at an objective lens defocus setting of –660 Å. This fact is clearly illustrated by the inset calculated HRTEM image of a γ–Al_2O_3 crystal, obtained under imaging conditions of –660 Å defocus and 250 Å thickness, as shown in the bottom-right corner of this image. There is excellent agreement between these two images, further substantiating the validity of the model in Fig. 18, i.e. the aluminum atoms are disordered in the octahedral sites and the tetrahedral sites in the spinel oxide.

7.3 Nucleation of Crystalline Oxide at Al/Amorphous Oxide Interface

7.3.1 Al/Amorphous Oxide Interface

Aluminum always shows an amorphous oxide layer on its surface from room temperature to its melting temperature. Since the high temperature crystalline oxide is nucleated at the aluminum/amorphous oxide interface, it is important to determine the effect of the pre-existing amorphous oxide layer on the nucleation of the crystalline oxide.

Figure 22 shows a high-resolution electron microscopy image of the aluminum/amorphous oxide interface in a sample which was oxidized for 5 hr at 500 ° C. The amorphous oxide gives rise to the mottled contrast characteristics of all amorphous materials.[176] This micrograph was taken in a <110> orientation. Three major crystallographic planes, {111} and {110}, are superimposed on the aluminum matrix and the spacing of the {111} planes is indicated by the marker in the bottom-right corner of this figure. Comparing these planes with the macroscopic interface shows that the aluminum/amorphous interface is close to a {110} plane. It is easily seen that the interface is sharply defined but is not smooth on the atomic scale. Furthermore, the roughness arises from the presence of facets with heights of several to ten {111} aluminum interplanar spacings as indicated by the superimposed arrows.

This {111} faceting may be related to the surface energy of aluminum. These {111} surfaces will be most favorable for the aluminum surface since surfaces parallel to {111} planes are of lowest energy for aluminum as shown in Table 4.

Figure 23 shows a high-resolution electron microscopy image of the aluminum/amorphous oxide interface, again taken in a <110> orientation, produced by a 5 hr oxidation treatment at 500 ° C. Two {111} crystallographic planes are

superimposed on the aluminum matrix and the spacing of the {111} planes is indicated by the marker in the bottom-right corner of this figure. Comparing these planes with the macroscopic interface shows that the aluminum/amorphous interface is parallel to {111} planes. It is easily seen that the interface is not sharply defined, but a little diffuse, which is different from the previous interface in Fig. 22. Furthermore, this interface is rough with heights of 50 Å, and the roughness arises from the protrusion of the aluminum lattice into the amorphous oxide. This roughness of the interface is consistent with Jackson's theory[120] that most metals have $L_f/T_m \simeq R$ and are therefore predicted to have rough interfaces.

From the micrographs in Figs. 22 and 23, it is possible to conclude that the aluminum/amorphous oxide interface structure is dependent on the surface orientation of aluminum: this anisotropy may be related to the anisotropic nucleation density of the crystalline oxide at this interface.

7.3.2 Nucleation of Crystalline Oxide

Figure 24 shows a low magnification lattice image of the aluminum/amorphous oxide interface, again taken in a <110> orientation, where the crystalline oxides are nucleated from the 0.5 hr oxidation of aluminum at 500 °C. The amorphous oxide is about 70 Å thick. The fringes located in the oxide extend from aluminum along the arrow direction in this figure. There are four crystalline oxide nuclei at the aluminum/amorphous oxide interface as indicated by arrows in the figure. The oxide nuclei reside upon the interface in hemispherical cap shapes with their long dimension running along the aluminum/amorphous oxide interface. The thickest region in the oxide nuclei is 25 Å thick. The aluminum/crystalline oxide interface is smooth whereas the amorphous/crystalline oxide interface is relatively rough in this figure.

Figure 25 shows an enlargement of the oxide nucleus at the center of Fig. 24. Sighting along the arrow directions shows that the oxide nucleus with two perpendicular fringes can be easily distinguished from the aluminum matrix. The aluminum/crystalline oxide interface is macroscopically flat whereas the fringes in the oxide nucleus protrude into the amorphous oxide, indicating that the crystalline oxide nucleates by structural rearrangement within the amorphous oxide into the crystalline phase at the aluminum/amorphous oxide interface. That is, an embryo of the new crystalline oxide phase exists within the amorphous oxide layer. This effectively means that, for nucleation of the crystalline phase, the composition of the oxide is attained in the amorphous oxide, and all that has to be done is to rearrange atoms into the structure of the crystalline phase. Three important crystallographic planes of the aluminum are superimposed in the bottom-left corner of this figure. Comparing these planes with the aluminum/crystalline oxide interface shows that the interfacial plane of the aluminum/crystalline oxide interface is macroscopically a {311} plane of the aluminum and microscopically faceted with the low index planes. Using the 2.33 Å spacing of the {111} aluminum planes as an internal magnification standard, it was found that the oxide lattice fringe spacing is 1.98 Å, which corresponds to the {400} spacing of the γ-Al_2O_3. By sighting along the (111) aluminum planes, it is concluded that these planes are continuous as they cross the aluminum/crystalline oxide interface and become the {400} oxide planes with a 4.5° anticlockwise rotation and that the the aluminum/crystalline oxide interface is largely coherent. Again by sighting along the $(11\bar{1})$ aluminum planes, it is concluded that these planes are also continuous as they cross the interface and become the {400} oxide planes with a 15° clockwise rotation. Notice that the oxide at the nucleation stage in this figure is not faceted whereas the oxide at the growth stages as shown in later sections shows {111} faceting.

A further analysis of the aluminum/oxide nuclei interface shown in Fig. 25 was performed by optical microdiffraction with the electron micrograph negative on the laser optical bench. The results are given in Fig. 26. In this figure, the $[1\bar{1}0]$ fcc aluminum optical diffraction pattern is superimposed on a [001] spinel oxide pattern which has four-fold rotational symmetry. That is, the $[1\bar{1}0]$ aluminum direction is parallel to the [001] oxide direction. The high-resolution image in Fig. 25 can be compared directly with the corresponding completely-indexed optical diffraction pattern. By comparing these two, it is clear that the spacings and rotational angles in the fringes of the oxide nucleus with respect to the aluminum described above are correct and the fringes in the oxide nucleus correspond to the (400) and (040) oxide planes. In the optical diffraction pattern, the laser detected {220} oxide periodicities as indicated by the arrow heads, indicating that the nucleus must be the oxide phase, not the fcc aluminum since the {110} aluminum periodicities, which are almost identical with the {220} oxide periodicities, are forbidden in the fcc structure.

The image of the oxide nucleus in Fig. 25 shows {400} periodicities but does not show {200} periodicities, and thus the optical diffraction pattern does not show the {200} reflections as shown in Fig. 26, since the {200}, i.e. $\{hk\,0\}$, $h+k = 4n+2$ oxide reflections are kinematically forbidden in the $Fd\,3m$ space group of the spinel structure and these forbidden reflections cannot arise due to double diffraction in a [100] orientation as discussed in section 7.1. From these facts, it is concluded that the nucleus already transformed to the spinel γ–Al_2O_3 phase.

Figure 27 shows an enlargement of the region between the first and the second nuclei from the left side in Fig. 24. The two oxide nuclei are not separated, but connected by a 10 Å thick neck arrowed in the center of this figure. Note that the left

nucleus has the same orientation as the right one with respect to the aluminum matrix.

Figure 28 shows an enlargement of the third nucleus from the left side in Fig. 24. The oxide nucleus at the center in Fig. 28 isolated from the neighboring nuclei is 18 Å thick and 100 Å wide. At the right end of the interface, the image reveals a 10 Å thick nucleus. The aluminum/crystalline oxide interface is macroscopically flat whereas the oxide nuclei protrude into the amorphous oxide, again indicating that the crystalline oxide heterogeneously nucleates by structural rearrangement of the amorphous oxide at the aluminum/amorphous oxide interface. Again observe that the oxide at the nucleation stage in this figure is not faceted, implying that atom rearrangement is occurring at the interface. Otherwise, the nucleus might be faceted with the low energy interface since the interfacial energy contribution to the free energy change for nucleation is relatively large for a small nucleus. Again three important crystallographic aluminum planes are superimposed in the bottom-left corner of this figure. Comparing these planes with the aluminum/amorphous oxide interface shows that the interfacial plane of the aluminum/amorphous oxide interface is macroscopically a {311} plane of the aluminum and microscopically faceted with the low index planes. The aluminum/crystalline oxide is also macroscopically a {311} aluminum plane and microscopically faceted with the low index planes just as described in Fig. 25. By sighting along the (111) aluminum planes, it is possible to conclude that these planes are continuous as they cross the aluminum/crystalline oxide interface and become the (400) oxide planes with a 4.5° anticlockwise rotation as indicated by the solid line in the figure and that the aluminum/crystalline oxide interface is largely coherent. Sighting along the $(11\bar{1})$ aluminum planes shows that these planes become the (040) oxide planes with a 15° clockwise rotation. It is concluded that all the oxide nuclei in Fig.

24 have the same orientation with respect to the aluminum matrix even though they nucleate at different sites. This is probably due to the fact that this nucleus orientation is favorable on this aluminum surface and experimental conditions.

Notice that the [001] direction of all the oxide nuclei in Fig. 24 is parallel to the $[1\bar{1}0]$ aluminum direction and the (400) oxide plane has a 4.5 ° misorientation with the (111) matrix plane as also shown in the optical diffractogram in Fig. 26. This orientation relationship is consistent with the nucleation mechanism proposed by Gerdes and Young.[177] They have performed a comprehensive review of the literature for oriented overgrowths in face-centered cubic systems. They showed that the importance of a nucleation mechanism is based on alignment of close-packed (CP) directions. Depending on the temperature and crystalline character of the substrate, their mechanism results in either 1) alignment of close-packed directions in the deposit with corresponding directions in the substrate or 2) maximization of the close-packed directions in the deposit plane parallel to the interface. The oxide nucleus orientation observed above in Fig. 24 corresponds to the first case whereas a parallel or a twin orientation relationship corresponds to the second case.

The possibility that the effect of electron-induced radiation damage in the amorphous oxide might lead to an effective crystallization of amorphous oxide and nucleate this crystalline oxide is excluded, since all of these crystalline oxide nuclei are nucleated at the aluminum/amorphous oxide interface and all four oxide nuclei have the same orientation relationship with the matrix; whereas crystalline oxide[178],[179] formed from radiation damage is nucleated from the center of the exposed area and shows the sporadic and random orientation of the crystal patches. Furthermore, in this study, crystallization of the amorphous oxide due to the electron-induced radia-

tion damage has not been observed in the microscope.

Figure 29 shows a low magnification high-resolution image of the nucleated crystalline oxide at the interface, taken in a <110> aluminum and oxide orientation, produced by 1 hr oxidation at 500 °C. The amorphous oxide is about 70 Å thick whereas the crystalline oxide is about 110–190 Å thick, as indicated by the 10 nm marker. The amorphous oxide/crystalline oxide interface is smooth whereas the aluminum/crystalline interface shows some roughness with heights of up to 80 Å, indicating that the crystalline oxide grows from the aluminum/amorphous interface into the aluminum matrix even though the crystalline oxide nucleates by rearranging atoms within the amorphous oxide at the aluminum/amorphous oxide interface as described above. The dark contrast in the aluminum shows vacancy loops lying along the {111} planes. The dark fringes at the aluminum/oxide interface indicate that there is overlapping matrix at the oxide edges due to the fact that the oxide edge is not in an exact <110> orientation through the thickness of the foil. In this figure, sighting along the {111} planes shows that these planes are continuous as they cross the interface and become the {111} aluminum planes, with a parallel orientation relationship; $[1\bar{1}0]_{Al} \,||\, [1\bar{1}0]_{oxide}$, $(111)_{Al} \,||\, (111)_{oxide}$.

7.3.3 Amorphous/Crystalline Oxide Interface

Generally, the amorphous/crystalline oxide interface is not edge-on in a <110> orientation due to the fact that the smooth macroscopic amorphous oxide/crystalline oxide interface is parallel to the original surface of the aluminum. In order to gain more information about the amorphous/crystalline oxide interface, attempts were made to find the interface in a thin region, thereby increasing the possibility for the interface to lie along an exact <110> orientation through the thickness of the foil.

Figure 30 shows a high-resolution image of one such amorphous/crystalline oxide interface, produced by the 0.5 hr oxidation treatment at 600 ° C. Two {111} planes of the oxide, projected in a <110> orientation, are superimposed on the image of the crystalline oxide. By sighting along the (111) planes parallel to the face of the oxide, it is concluded that the amorphous oxide/crystalline oxide interfacial plane is a {111} plane of the crystalline oxide. This flat {111} interface is in agreement with Jackson's theory[120] that oxides (high values of L_f/T_m) generally have flat close-packed interfaces.

7.4 Al/Oxide Interface with Parallel Orientation Relationship

7.4.1 High-Resolution Transmission Electron Microscopy Images

Figure 31 shows a low magnification lattice image of the aluminum/oxide interface in a $[1\bar{1}0]_{Al} \,||\, [1\bar{1}0]_{oxide}$ orientation, produced by 0.5 hr oxidation at 600 ° C. The objective lens defocus value was determined by an optical diffraction pattern from the amorphous edge of the sample in the bottom-right corner in the micrograph, that is, the sample thickness is decreasing from the upper-left corner to the lower-right corner in the micrograph. Notice that the crystalline oxide, about 900 Å thick, contains a number of faults and twins, and there are relatively small areas of perfect crystalline oxide between these faults.

For this image, an objective aperture of radius of 1.0 $Å^{-1}$, which has a diameter that is greater than the resolution limit of the JEOL JEM 200CX, was used to eliminate higher-order spatial frequencies, as shown in the corresponding electron diffraction pattern in Fig. 32. There are streaks from the oxide reflections along the <111> directions due to the twin lamellae and stacking faults in Fig. 31, and there

are extra spots due to the twinning in the oxide and double diffraction.

In Fig. 33, the crystallographic character of the interface is shown in greater detail in an enlargement of the interface located in the lower center of Fig. 31. This image clearly reveals the atomic structure of the interface. The {111} crystallographic planes and the {111} spacing in the aluminum matrix are indicated in the bottom-left and bottom-right corners of this figure, respectively. By sighting along the (111) matrix plane and comparing this plane with the oxide face in Fig. 33, it is concluded that the broad face of the oxide is a {111} plane of the oxide and the aluminum.

This oxide shape is much clearer in another enlargement of this interface in Fig. 34, which was taken with a different objective lens defocus setting. From this figure, it is readily apparent that, by sighting the $(11\bar{1})$ matrix plane, another face of the oxide is also a {111} plane of the oxide and the aluminum. It also shows a 65 Å high ledge which grows parallel to a {111} plane of the oxide.

Another important feature apparent from the micrographs in Figs. 33 and 34 is that the {111} oxide planes are continuous as they cross the broad face of the oxide and the edge of the growth ledge into the oxide and become the {111} matrix planes.

These crystallographic aspects are confirmed by the high-resolution images in the subsequent micrographs, such as Fig. 35, which were taken with different objective lens defocus values. From these figures, it was found that the interface is highly crystallographic and coherent with a parallel orientation relationship: $(111)_{Al} \,||\, (111)_{oxide}$, $[1\bar{1}0]_{Al} \,||\, [1\bar{1}0]_{oxide}$. In addition, the habit planes of the crystalline oxide are the {111} octahedral planes of the oxide and the oxide grows parallel to these planes, by a ledge mechanism. These growth characteristics lead to the oxide shapes, which are determined by the combinations of the {111} oxide faces.

7.4.2 Construction of Atomic Models and Image Simulations

Although the crystallographic aspects of the previous lattice images have enabled a variety of factors to be deduced about the oxidation process, it is impossible to determine the exact atomic structure of the aluminum/oxide interface from the images because the interfacial structure is complex and the important atom spacings in the oxide are beyond the resolution limit of the modern high-resolution transmission electron microscope. Hence, an effort was made to resolve atomic detail at the interfaces. However, in order to be able to interpret atomic detail, atomic models of the interfaces were first constructed, and a number of simulated images were calculated from these models.

All the atom models in this study are the projected atom positions which are seen when the structure is viewed in a $<110>_{oxide}$ orientation. In this model, the oxygen atoms are represented by large circles. The aluminum atoms at the octahedral or tetrahedral sites are represented by small single or triple circles, respectively, and aluminum atoms in the metal are represented by double circles. Numbers in the circles show the relative heights of atoms in multiples of $\frac{a}{8}[1\bar{1}0]_{oxide}$, or $\frac{a}{4}[1\bar{1}0]_{Al}$.

One question which arose during the initial stages of this study was which sublattice of the oxide, the aluminum sublattice or the oxygen sublattice, is coincident with the lattice of the aluminum matrix across the interface, in constructing the atomic model of the aluminum/oxide {111} interface with a parallel orientation relationship. This question is important with regard to this study because this would allow the interface model to be directly correlated with the atomic mechanisms of aluminum oxidation.

A proposed atomic model of the aluminum/oxide {111} interface with a parallel orientation relationship is shown in Fig. 36. The oxide crystal in the top and the aluminum crystal in the bottom compose an atomic model of a coherent (111) interface. The choice of the atom positions at the interface was not totally arbitrary since the white dots in the oxide in experimental HRTEM images such as Figs. 33 and 34 are coincident with those in the aluminum matrix, which suggests that a sublattice of the oxide structure may be coincident with the lattice of the aluminum matrix.

One major assumption made in constructing this model in Fig. 36, was that the aluminum sublattice of the oxide could preserve the aluminum lattice of the aluminum metal. That is, this interface in Fig. 36 is also referred to as the $\Sigma = 1 : \Sigma = 1$ aluminum/oxide interface, using the terminology of the coincidence site lattice theory,[142] as discussed in section 4.2.2. Thus, the aluminum sublattice planes of the oxide are completely continuous as they cross the interface and become the aluminum lattice planes of the aluminum.

Since the cation layers between the {111} oxygen layers are found alternatively to be kagome layers and mixed layers, as discussed in section 3.2.2, it is possible to choose which cation layer starts the stacking from the interface. Thus, another assumption included in the model was that the cation stacking of the {111} planes in the oxide starts with a kagome layer rather than with a mixed layer from the interface.

However, both of these assumptions can be verified by comparing experimental HRTEM images of the oxide and the aluminum/oxide interface, which are interpretable in terms of both types and positions of atomic species, with calculated images of these structures under comparable specimen and microscope conditions. Many image

simulations were performed in order to accomplish this and the results of these simulations are discussed in the following section.

Furthermore, all the calculational atom models of the interfaces in this study assume that the aluminum ions in the spinel oxide are disordered, that there are no lattice parameter changes associated with the oxidation reaction, and that no relaxations have occurred around the interfaces. These simplifications do not destroy the integrity of the model, and will not affect the simulations for the present analyses, although there is a 2.5 % misfit between the lattice parameters of the oxide and the aluminum.

The projected potential obtained from the model is shown in Fig. 37 (b), which contains 3 unit cells of the atom model of Fig. 36 in the x-axis. In this study, all the projected potentials and the simulated images of all the interfaces also contain 3 unit cells of the corresponding atom models in the x-axis. Notice from this projected potential that the atom positions with two aluminum atoms along the projected direction have a much larger projected potential than those with only one aluminum atom along the projected direction; the projected potential of two oxygen atoms is still slightly larger than that of one aluminum atom. This is because the projected potentials of atoms increase with the scattering power of the atoms. The high scattering factor of Al atoms as compared to O atoms leads to the different sizes of the projected potential. The higher concentration of the atoms causes greater electron scattering.

Figure 38 shows a through-focus series of computed images for a variety of crystal thicknesses from 50 Å to 300 Å, based on the model described above. The actual atomic positions from the atomic model are shown in the top-left corner of this figure, where each frame of the simulated image contains 3 calculational unit cells in the x-

axis. The contrast from the oxide in these images is usually the same as that in the previous simulations except that in the image of thicker crystals, such as on the right side of Fig. 38, the uneven matching of the projected potential at the interface creates the anomalous image effect in the vicinity of the interface with increasing specimen thickness. There is a similar progression in the appearance of this boundary effect with the objective lens defocus values. However, this effect is not important in images of thinner crystals.

Note, in the thin crystals, the oxide which contains Al and O can be readily distinguished from the aluminum matrix in the lower part of the image. From these images for crystal thickness less than 50 Å, the brightness of the atoms in the matrix corresponds directly with the projected potential at the defocus values of –980, –1080, –1440, –1460 and –1580 Å, whereas the darkness of the atoms in the matrix corresponds directly with the projected potential at the defocus values of –750, –800, –1190, –1290 and –1690 Å. The atomic positions of the aluminum are not visible even for crystal thickness less than 50 Å, at defocus values of +360, –50, –10, –50 and -700 Å, where the spatial frequency for the {111} aluminum reflection is not transferred well by the objective lens (see the CTF's in Fig. 14). In addition, it is observed that for thicknesses greater than about 100 Å, the image contrast does not correspond directly with the projected potential and, furthermore, shows a contrast reversal in some images. Also the aluminum matrix displays a strong double periodicity along the <200> direction at defocus values of -1080, -1290 and -1690 Å. This is because a crystal which has a thickness which is enough to produce a strong Bragg scattered waves cannot be treated as a weak-phase object, but, in this case, the interference among the diffracted waves must be take into account.

As illustrated by Fig. 6, there is another possible way for the cation stacking of the {111} planes in the oxide from the interface starts with a mixed layer rather than with a kagome layer as shown in Fig. 36. This second atomic model of the aluminum/oxide {111} interface with a parallel orientation relationship was constructed on the left and the projected potential for this model is shown on the right in Fig. 39. Notice again that the aluminum sublattice of the oxide can preserve the aluminum lattice of the aluminum metal as proposed for the model in Fig. 39. Thus, the aluminum sublattice planes of the oxide are completely continuous as they cross the interface and become the aluminum lattice planes of the aluminum. Image simulations were done for this model to determine whether the cation stacking of the {111} oxide planes starts with a mixed layer or a kagome layer from the interface. Figure 40 is a series of calculated images which show how the image contrast at the interface changes as a function of specimen thickness at defocus values of –730, –1100 and –1300 Å.

There is one more possible atomic model for the aluminum/oxide {111} interface with a parallel orientation relationship as shown on the left of Fig. 41, which was based on the *lock-in* model.[146],[147] A very important feature from this model in Fig. 41 is that, assuming that the plane of the interphase boundary between a metal and an oxide crystal lies parallel to the low energy {111} plane of the oxide crystal, the *surface* of the oxide crystal is described in terms of a set of close packed rows of oxygen atoms separated by relatively deep *valleys*, and the closest packed rows of the atoms at the *surface* of the aluminum matrix form a *lock-in* configuration with the *valleys* of the *surface* of the overlying oxide crystal. Note that the size of the oxygen ion ($r = 1.40$ Å) is very similar to that of the aluminum atom ($r = 1.42$ Å) in the bulk phases.[85] In this model the oxygen sublattice of the oxide, instead of the

aluminum sublattice as proposed for the model in Fig. 36, can preserve the aluminum lattice of the aluminum metal. Thus, the oxygen sublattice planes of the oxide are completely continuous as they cross the interface and become the aluminum lattice planes of the aluminum.

This additional series of simulated images of the aluminum/oxide interface with a parallel orientation relationship as a function of specimen thickness up to 280 Å and defocus value is shown in Fig. 42, which was obtained from the projected potential of Fig. 41, using the Arizona State University MULTISLICE programs. Again that the projected potential and each simulated image contain 3 unit cells of the atomic model on the left of Fig. 41 in the x-axis.

7.4.3 Comparison of Experimental HRTEM Images with Simulated Images

An enlargement in Fig. 43 shows an experimental image of the aluminum/oxide interface in the sample which was oxidized for 0.5 hr at 600 ° C. The edge of the foil is located at the right, as evidenced by the amorphous layer which is visible in Fig. 31. Comparison of the image contrast in Fig. 43 with the simulated images in Fig. 38 shows that good agreement is obtained for a sample thickness of 100 Å at defocus value of –750 Å. This is clearly illustrated by the inset simulated image of the interface at –730 Å defocus and 100 Å thickness, which is shown on the right-middle of Fig. 43. Notice the excellent agreement between the calculated and experimental images in this figure. That is, the bulk aluminum and oxide in the experimental image show good agreement with the simulated image, and the relation between the stacking in the oxide and matrix at the interface agrees with the model interface proposed in Fig. 36. Thus, because all of the conditions needed for correct interpretation of an

experimental image are satisfied for this micrograph, it is possible to conclude that the model for the interface shown in Fig. 36 is correct.

By comparing the experimental image in Fig. 43 with the simulated image of the interface at –730 Å defocus and 100 Å thickness in Fig. 40, it is easily shown that they do not show good agreement just at the interface, although they show good agreement in the bulk aluminum and oxide. Furthermore, by comparing the experimental image in Fig. 43 with the simulated images in Figs. 38 and 41, it is possible to confirm that the atom model in Fig. 36 is correct. Thus, it is possible to determine that the cation stacking sequence in the oxide starts with a kagome layer from the interface as shown in Fig. 36 rather than with a mixed layer as shown in Fig. 39.

The simulated images in Fig. 42 were included for comparison with the experimental HRTEM images such as Figs. 33 and 34 and the simulated images in Fig. 38. In Fig. 42 the bright dots in the oxide are not coincident with those in the aluminum matrix. As shown by comparing these simulated images with the experimental HRTEM images such as Figs. 33, 34 and 35, there is no good agreement between the experimental and simulated images. Thus, it is concluded that the experimental HRTEM images show good agreement with the atomic model shown by Fig. 36 rather than with the atomic model shown by Fig. 41, suggesting that the aluminum sublattice of the oxide instead of the oxygen sublattice can coincide with the aluminum lattice of the aluminum metal, and further that the proposed atomic model in Fig. 36 is correct.

7.4.4 Atomic Mechanisms of Oxidation

Now that the atomic structure and chemistry of the oxide and the aluminum/oxide {111} interface with a parallel orientation relationship have been determined at the atomic level, it is possible to further establish the relationship between the structural and compositional components of the transformation, thus enabling the atomic mechanisms of aluminum oxidation to be described at the single-atom level.

One important feature apparent from the micrographs in Figs. 33, 34 and 35 is that the interface is coherent and the {111} planes are continuous as they cross the growth ledge into the oxide. Furthermore, the edge of the growth ledge is often indistinct, whereas the terrace is generally sharply defined and atomically flat. This implies that atomic attachment for the oxide growth occurs at the edges. Furthermore, it may be possible that the growth of the oxide occurs by the movement of kinks in the ledge rather than by overall forward propagation of the growth ledge, and that the ledge is not parallel to <110>. It must be remembered that once an oxygen atom crosses the interface into the aluminum, it is highly unlikely that it will jump back into the oxide due to the favorable bonding situation and reduction in free energy that it experiences in the aluminum. Thus, advancement of the aluminum/oxide interface can occur by atomic attachment at kinks, that is, by diffusion of O atoms across kinks in the ledges and this step is the limiting reaction in the growth process if the reaction is controlled by the interface. The advancement of the growth ledges parallel to the {111} oxide planes maintains the {111} habit plane of the oxide: the atomic mechanisms of oxide growth leading to this habit plane will be discussed in greater detail later in section 7.8.2.

The calculated and experimental HRTEM images of the interface previously analyzed in section 7.4.3 show that the correct model for the aluminum/oxide interface is illustrated by Fig. 36 rather than by Figs. 39 and 41. This conclusion leads to a proposed transformation mechanism of aluminum to the oxide structure with a parallel orientation relationship as illustrated by Fig. 44.

Figure 44 (a) shows a unit cell of the aluminum, whereas (d) shows a corresponding unit cell of the oxide, in the coincidence site cell for the $\Sigma = 1 : \Sigma = 1$ aluminum/oxide interface in Fig. 36. Notice that there is coincidence of aluminum atom sites of the aluminum and oxide. However, this figure does not mean that the oxide growth occurs step by step by nucleation and growth of this unit cell, but that the oxide grows by diffusion of atoms across the interface, which accompanies the compositional and structural changes.

In order for the oxide to grow from the interface, two things must happen: 1) there must be a structural change by shuffling of aluminum atoms which allows the oxide to have the required atomic arrangement, 2) there must be a corresponding compositional change by diffusion of aluminum and oxygen atoms, which allows the pure aluminum to become the stoichiometric Al_2O_3 composition. Note that in this case the compositional and structural aspects of the oxidation transformation do not necessarily occur independently. That is, the compositional change due to the diffusion may be accomplished with the structural change.

The structural change occurs by diffusion of aluminum for one quarter of Al sites to the tetrahedral site of the oxide, which allows the aluminum atoms to have the required atomic arrangement for the oxide structure. The lattice correspondence in Fig. 44 does not relate primitive unit cells, hence the atoms inside the cell have to

undergo rearrangements (shuffle). The shuffles indicated in Fig. 44 (c) are necessary to obtain the final spinel arrangement shown in Fig. 44 (d).

The major compositional change occurs by absorbing vacancies for one third of Al sites and diffusion of oxygen into the octahedral sites of the aluminum, which allows the pure aluminum to become the stoichiometric Al_2O_3 which contains two thirds of the pure Al sites, with reference to the unit cell of the $\Sigma = 1 : \Sigma = 1$ aluminum/oxide coincidence site lattice. That is, the unit cell of spinel γ–Al_2O_3, volume 493.04 $\mathring{A}^3$, contains $21\frac{1}{3}$ Al atoms, whereas $2\times2\times2$ unit cells of aluminum, volume 527.52 $\mathring{A}^3$, consist of 32 Al atoms. This means that in order for a cell of γ–Al_2O_3 to form, there must be $10\frac{2}{3}$ vacancies in that volume of the matrix crystal from which it will be formed, which will transform to octahedral or tetrahedral interstices of the new oxide phase. At the 600 ° C oxidation temperature used in this study, there should be an abundance of vacancies available for those aluminum sites.

Quenching experiments on pure aluminum[97],[98] have shown that the concentration of vacancies is 10^{-4} after quenching from 550 ° C. This concentration is abundant for the absorption reaction when it is in dynamic equilibrium at high temperatures from the various vacancy sources, e.g. dislocations, grain boundaries, interphase boundaries and surfaces.

The vacancy absorption mechanism in this proposed mechanism is analogous to the vacancy absorption mechanism in the aging mechanism in alloy Al-Mg-Si.[67] Decomposition of supersaturated solid solution Al-Mg-Si of quasibinary composition results in precipitation of a stable β phase (Mg_2Si). It has a cubic lattice of type CaF_2 (space group $Fm\,3m$) with parameter $a = 6.39$ $\mathring{A}$. The orientation relations with the

matrix are $[001]_\beta \,||\, [100]_{Al}$; $[\bar{1}10]_\beta \,||\, [001]_{Al}$. The unit cell of phase Mg_2Si, volume 260.9 $\mathring{A}^3$, contains 12 atoms, whereas four unit cells of aluminum, volume 263.76 $\mathring{A}^3$, consist of 16 atoms. This means that in order for a defect-free cell of β phase to form, there must be four vacancies in that volume of the matrix crystal from which it will be formed, which will transform to octahedral interstices of the new phase. This agrees with the conclusion of Thomas[99] that there is rigid binding of vacancies with precipitates and agrees with the results of Panseri and Federighi[180] and Miraille *et al.*. [181] Thomas[99] has shown that the concentration of vacancies in this Al-Mg-Si alloy is $\sim 3x10^{-6}$ after quenching from 550 ° C whereas the concentration of the quenched-in vacancies in pure aluminum is 10^{-4} and that of binary aluminum alloys[99] actually increases with alloying (e.g. in dilute Al-Cu alloys concentrations of 10^{-3} were found[99]). Thus, it was concluded that the major fraction of vacancies in Al-Mg-Si alloy are condensed into the precipitate.[99] When the alloy has composition Al-1.4 wt.% Mg_2Si and the usual quenching methods are used, a deficit of quenching vacancies is created so that some octahedral interstices of the precipitate phase remain unfilled by aluminum atoms, that is, the metastable phase contains defects, i.e. interstitial atoms in the initial stages of its existence.

There should be a small volume contraction due to the ionization process of the aluminum and oxygen atoms for the oxide structure, which allows the lattice parameter of the aluminum structure to become that of the spinel oxide with a 2.5 % contraction along all directions, as shown by Figs. 44 (b) and (c). This factor needs to be taken into account in order to accurately describe the atomistics of the growth process. According to this transformation mechanism, the oxide experiences a slight contraction in all directions during growth. Note that the shape change associated with the shear component of the transformation can be accommodated by the use of several

variants of the lattice correspondence. However, any volume change which is part of the transformation cannot be accommodated in this way. The accommodation of excess volume can only be accomplished either elastically, or by a nonconservative process[182],[183] without the constraint imposed by the conservation of lattice sites. The misfit between the lattice parameters of the aluminum and the oxide can be fully accommodated with misfit dislocations, that is, one $\frac{a}{3}<111>$ dislocation for every 42 {111} matrix planes. Furthermore, these Frank dislocation loops should possess an interstitial character and reside within the oxide, requiring the addition of *interstitial* atoms for the oxide growth, if the contraction is to be accommodated in the manner suggested by Dahmen *et al.* .[184]

One important feature of this proposed mechanism is that there is a small volume contraction (7 %) rather than a volume expansion (49 %) as thought[18] due to the so-called Pilling Bedworth ratio, that is, the ratio of the volume per metal in the oxide to the volume per metal atom in the metal. Pilling and Bedworth[46] suggested that the stresses in an oxide on a metal could be determined from the Pilling and Bedworth ratio.

7.5 Al/Oxide Interface with Twin Orientation Relationship

7.5.1 High-Resolution Transmission Electron Microscopy Images

Most of the $<110> \,||\, <110>$ aluminum/oxide SAD patterns contain twin spots which were briefly noted during the previous analyses. It was first found that the oxide has a twin orientation relationship with the aluminum matrix. The twinning in the oxide was clearly identified by comparing the high-resolution image such as Fig. 31, which contains a number of twins in the oxide, with the twinning reflections of the

oxide in the electron diffraction patterns such as Figs. 11 and 32. Actually, previous investigators[5],[20] reported the SAD patterns of the aluminum and oxide, which contain the twin reflections, but they did not notice that there is a twinning in the oxide.

Figure 45 shows a high resolution image of the aluminum/oxide interface with a twin orientation relationship: $(11\bar{1})_{Al} \,||\, (111)_{oxide}$, $[1\bar{1}0]_{Al} \,||\, [1\bar{1}0]_{oxide}$, which was produced the 0.5 hr oxidation at 600 °C. This image, taken in a <110> orientation, clearly reveals the atomic structure of the interface. The {111} aluminum spacing and two {111} crystallographic planes in the oxide are indicated by the markers in the bottom-right and top-right corners of this figure, respectively. Notice that there is a 71 Å high growth ledge, as indicated on the left of this figure.

Again, by sighting along the (111) oxide planes parallel to the oxide face, it is possible to conclude that the interfacial plane is a common {111} plane of the oxide and the aluminum, and these {111} planes are completely continuous as they cross the edge of the ledge, which also grows parallel to these planes, and become the {111} planes of the aluminum, just as for the ledge on the oxide face in section 7.4.1.

The other {111} planes of the oxide and the aluminum which are not parallel to the interfacial plane are indicated by the dashed lines in the middle of this figure. By a 70 ° 32′ rotation of the oxide images about <110> axis, or by a mirror reflection with respect to a (111) interfacial plane, the {111} planes of the oxide are macroscopically coincident with those of the matrix. Thus, it is possible to conclude that there is a {111} twinning relationship between the oxide and the aluminum, and this interfacial plane is largely coherent, as was observed for the previous oxide in section 7.4.1. Note that, in face-centered cubic systems, {111} twinning can be described as a mirror reflection with respect to a (111) plane, or a 70 ° 32′ rotation about <110> axis.

However, it is difficult to determine the exact atomic arrangement at the edge of the growth ledge, which is due to the fact that there may be some overlapping matrix at the growth edge. The presence of this overlapping matrix is due to the fact that the oxide edge is not in an exact <110> orientation through the thickness of the foil, causing an overlap of the matrix at the edge.

Sometimes the interface between aluminum and its oxide is not completely planar, as evidenced in Fig. 46, where the oxide was produced by the 0.5 hr oxidation treatment at 600 °C. In this figure, by sighting along the (111) planes parallel to the oxide face, it is possible to conclude that a ledge, which is three {111} aluminum planes thick, is present at the interface and the terraces of the ledge are the {111} planes of the oxide. Whereas the movement of such a ledge obviously does not contribute to the macroscopic growth rate of the oxide as significantly as does the larger growth ledge, it indicates that the crystalline oxide can grow parallel to the {111} planes of the oxide, by the movement of such a ledge.

Thus, it was found that, for the interface with a twin orientation relationship, the habit plane of the crystalline oxide is a common {111} octahedral plane of the oxide and the aluminum, and the oxide grows parallel to these planes by the movement of the growth ledge as for the interface with a parallel orientation relationship in section 7.4.1.

7.5.2 Construction of Atomic Models and Image Simulations

It is difficult to determine the exact atomic structure of these interfaces from images in Figs. 45 and 46, due to the complexity of the interfacial structure and the change in contrast which occurs at the interfaces. This contrast change may have resulted from a thickness change in the specimen, due to the preferential etching at the interface which occurs during the ion-milling for the specimen preparation. By combining the structural information from these images with electron diffraction information, a model for the aluminum/oxide interface with a twin orientation relationship is constructed as shown in Fig. 47.

Examination of the model in Fig. 47, which was projected in a $<110>$ orientation, shows that the $\{111\}$ planes of the oxide in the top are parallel to the $\{111\}$ planes of the matrix in the bottom. In addition, the $\{111\}$ interface between the oxide and matrix with a mirror reflection symmetry is indicated by the dashed lines in the middle of the model. By comparing the atomic positions of the aluminum and the oxide, it is possible to find that there is a mirror symmetry between them.

One major assumption made in constructing this model in Fig. 47, is that the aluminum sublattice of the oxide can preserve the aluminum lattice of the aluminum metal with a $\{111\}$ mirror symmetry. This interface in Fig. 47 is also referred to as the $\Sigma = 3 : \Sigma = 3$ aluminum/oxide interface, using the terminology of the coincidence site lattice theory, as discussed in section 4.2.2. Another assumption included in the model is that the cation stacking of the $\{111\}$ planes in the oxide starts with the mixed layer from the interface. In addition, this model assumes that there are no lattice parameter changes associated with the oxidation reaction and that no relaxations have occurred around the interface.

The projected potential for this interface, which contains 3 unit cells of the atomic model of Fig. 47 in the x-axis, is shown in Fig. 48. Figure 49 shows a series of computed images of the aluminum/oxide interface with a twin orientation relationship as a function of specimen thickness at objective lens defocus values of –400, –800 and –980 Å, based on the projected potential in Fig. 48.

There is another possible way to model the interface, in which the cation stacking of the {111} planes in the oxide from the interface starts with a kagome layer rather than with a mixed layer as shown in Fig. 47. This atomic model of the aluminum/oxide interface with a twin orientation relationship was constructed on the left of Fig. 50, which is the same as that in Fig. 47 except that the cation stacking in the oxide starts with a kagome layer from the interface in Fig. 50. The projected potential for this model is shown on the right of Fig. 50.

Figure 51 shows a series of simulated images of this additional aluminum/oxide interface as a function of specimen thickness at objective lens defocus values of –400, –800 and –980 Å, based on the projected potential shown in Fig. 50. Notice that the contrast from the oxide and matrix in these images is usually the same as that in the previous simulations in Fig. 49 except that there is a contrast difference from the interfaces.

Figure 52 shows an experimental HRTEM image of the aluminum/oxide interface in the sample which was oxidized for 0.5 hr at 600 ° C. Comparison of the contrast and periodicities of bright spots at the interface in this image with the simulated images in Figs. 49 and 51 shows that good agreement is obtained for a specimen thickness of about 100 Å at –980 Å defocus from Fig. 49 rather than from Fig. 51. This fact is clearly illustrated by the inset simulated image of the interface at –980 Å defocus and

for 100 Å thickness, as shown in Fig. 52. Thus, it is possible to conclude that the model for the interface shown by the atomic positions in Fig. 47 is correct, indicating that the aluminum sublattice of the oxide can preserve the aluminum lattice of the aluminum metal with a {111} mirror symmetry.

7.5.3 Atomic Mechanisms of Oxidation

Now that the structure of the aluminum/oxide {111} interface with a twin orientation relationship has been determined at the atomic level, it is possible to describe the atomic mechanism of aluminum oxidation at the single-atom level by combining the information available from high-resolution microscopy and image simulations.

Figure 53 shows a proposed transformation mechanism of aluminum to the oxide with a twin orientation relationship. Figure 53 (a) shows a unit cell of the aluminum in the coincidence site cell for the $\Sigma = 3 : \Sigma = 3$ aluminum/oxide interface, in Fig. 47 in section 7.5.2, whereas (d) shows a corresponding unit cell of the oxide. There is coincidence of aluminum atom sites of the aluminum and the oxide every third (111) plane. However, this figure does not mean that the oxide growth occurs step by step by nucleation and growth of this unit cell, but that the oxide grows by diffusion of atoms across the interface, which accompanies the compositional and structural changes, that is, by migrating of the interface.

For the oxide to grow from the interface, two things must happen: 1) there must be a structural change from the fcc aluminum lattice to the spinel oxide structure with a twin orientation, 2) there must be a corresponding compositional change, which allows the pure aluminum to become the stoichiometric Al_2O_3. Also in this case the compositional and structural aspects of the oxidation transformation do not necessarily occur independently. That is, the compositional change due to the diffusion of

the aluminum and oxygen atoms may be accomplished with the structural change.

The major structural change occurs 1) by the $\frac{a}{6}[11\bar{2}]$ twinning shear[185] of the aluminum atoms, as indicated by arrows in Fig. 53 (a), which allow the oxide to have a twin orientation relationship with the aluminum matrix, and 2) by the shuffles indicated in Fig. 53 (c), which are necessary to obtain the final spinel oxide arrangement in (d). The important step in the shuffle is the jump of aluminum atoms by diffusion from one quarter of Al sites to the tetrahedral site in the oxide, which allows the aluminum ions to have the required atomic arrangement for the oxide structure.

The twinning shear of the aluminum atoms for the structural change to the twin orientation is described below.

1) The twinning shear can be accomplished by a coupled shearing movement,[186] which shows that the motion of intermediate planes between coincidence planes can consist of various pairs of equal and opposite translations, for example of (111) planes in $[11\bar{2}]$ direction, the familiar twinning shear, as indicated by arrows in Fig. 53 (a) and in the schematics in Fig. 54 (a). Since the translations form a system of shears of alternating sign between coincidence planes, twinning could take place by such a mechanism over an extended region without extensive shear; in fact, in this case any atom moves but the distance $\frac{a}{\sqrt{6}}$ in the $[11\bar{2}]$ direction.

This effect can be easily visualized by considering Fig. 54, which shows the coupled shearing movement used to accomplish the twinning transformation as shown in (a). If each block in Fig. 54 represents each (111) plane, examination shows that if the second block is translated to the right by $\frac{a}{6}[11\bar{2}]$, the third block is translated to the left by by $-\frac{a}{6}[11\bar{2}]$, and the fourth block is not translated, an overall shape change

does not occur with a three-plane repeating pattern.

2) The twinning shear can also be accomplished by the *rotational movement*[186] about coincidence sites, which shows that the motion of intermediate planes between coincidence planes can consist of various pairs of two different translations of the three $\frac{a}{6}<112>$ in a (111) plane, as shown in Fig. 54 (b). This mechanism is also highly favorable from the reason described above.

3) The twinning shear can be accomplished by the incorporation of equal numbers of all three different types of Shockley partial dislocations on every {111} plane. This situation is highly favored from a strain energy viewpoint, since the strain fields of the three variants of Shockley partial dislocations would tend to cancel one another and eliminate long-range strains parallel to the habit plane of the oxide. This effect can be easily visualized by considering Fig. 54 (c), which shows that when all three variants of Shockley partials on the {111} planes are used to accomplish the twinning transformation, the partial dislocations may be stacked vertically at the oxide edge. There is a negligible strain energy associated with these configurations at the edge since an overall shape change does not occur. Examination shows that if the second block is translated to the right by $\frac{a}{6}[11\bar{2}]$, the third block is translated to the left by $\frac{a}{6}[\bar{2}11]$, and the fourth block is similarly translated to the left by $\frac{a}{6}[1\bar{2}1]$, it results in the same twinning shear as the coupled shearing movement.

4) The twinning shear can be accomplished by the passage of the same $\frac{a}{6}[11\bar{2}]$ Shockley partial dislocations along every {111} plane of the aluminum, as shown in Fig. 54 (d). This situation is not favored from a strain energy viewpoint, and an overall shape change occurs.

The three-plane repeating pattern is not certain at the edge of the growth ledge in Fig. 45, due to the fact that the oxide edge is not in an exact <110> orientation through the thickness of the foil, causing an overlap of the matrix at the edge. However, if the edge lies along the exact <110> orientation through the thickness of the foil, it may be possible to identify the three-plane repeating pattern, demonstrating that all three types of Shockley partial dislocations are participating in the transformation and growth of this oxide with a twin orientation. This three-plane repeating pattern will be particularly interesting because it appears to relate directly to the structural transformation from the matrix to the twinned oxide.

The major compositional change occurs by absorbing vacancies for one third of Al sites and diffusion of oxygen into the octahedral sites of the aluminum, which allows the pure aluminum to become the stoichiometric Al_2O_3 containing two thirds of the pure Al sites, with reference to the unit cell of the $\Sigma = 3$ coincidence site lattice.

That is, the unit cell of spinel γ–Al_2O_3 in Fig. 53 (d), volume 369.78 $\mathring{A}^3$, contains 16 Al atoms, whereas the unit cell of aluminum Fig. 53 (a), volume 395.62 $\mathring{A}^3$, consists of 24 Al atoms. This means that in order for a cell of γ–Al_2O_3 to form, there must be 8 vacancies in that volume of the matrix crystal from which it will be formed, which will transform to octahedral or tetrahedral interstices of the new oxide phase. At the 600 ° C oxidation temperature used in this study, there should be an abundance of vacancies available for those aluminum sites. Quenching experiments on pure aluminum[97],[98] have shown that the concentration of vacancies is 10^{-4}. This vacancy concentration is abundant for the absorption reaction when it is in dynamic equilibrium at high temperatures. This vacancy absorption mechanism can be confirmed by the same conclusion as described in section 7.4.4.

Finally, there should be a small volume contraction due to the ionization process of the aluminum and oxygen atoms, which allows the lattice parameter of the aluminum structure to become that of the spinel oxide with a 2.5 % contraction along all directions, as shown by Figs. 53 (b) and (c). Unlike the glissile Shockley partial dislocations which are stacked at the edge, elastic misfit at the aluminum/oxide interface boundary due to the slight contraction, occuring in all directions of the oxide during transformation, can be accommodated by the generation of misfit dislocations, that is such $\frac{1}{3}<111>$ dislocations loops around the oxide periphery, with Burgers vectors normal to the faces.

7.6 A Twin Boundary in the Oxide

7.6.1 High-Resolution Transmission Electron Microscopy Image

The crystalline oxide does not always maintain a perfect structure. For example, the lattice image in Fig. 31 shows that the crystalline oxide contains a number of faults and twins, and there are relatively small areas of perfect crystalline oxide between these faults. A twin boundary in the oxide can be also readily deduced from the combinations of the oxides with a parallel and a twin orientation relationship.

Figure 55 shows an enlargement of the oxide image, which is off the top-right corner of a low magnification lattice image of Fig. 31, which contains many oxide crystals with parallel or twin orientation relationships. Comparing this enlargement with Fig. 31 shows that the top and bottom oxide crystals in Fig. 55 have a parallel orientation relationship, whereas the middle oxide crystal has a twin orientation relationship with the matrix. The middle oxide crystal is about 30 Å thick with 6 {111} planes as indicated by the 4.6 Å marker which represents a {111} spacing of the oxide.

By sighting along the (111) oxide planes parallel to the oxide boundary, it is easily seen that there are two boundaries, which are the common {111} planes of two oxide crystals. The other {111} planes of each oxide which are not parallel to the boundary are indicated by the dashed lines in the middle of Fig. 55. By a $70^\circ 32'$ rotation of the upper oxide images about <110> axis, or by a mirror reflection with respect to a (111) interfacial plane, the {111} planes of the upper oxide are macroscopically coincident with those of the lower oxide.

Thus, it is possible to conclude that there is {111} twinning between the oxide crystals, which can be described macroscopically as a mirror reflection or microscopically as a glide plane with respect to a (111) interfacial plane. Using the terminology of the coincidence site lattice theory, such a boundary is referred to macroscopically as a $\Sigma = 3$, {111} boundary.

7.6.2 Construction of Atomic Model and Image Simulations

The main objective of this section is to examine simulated HRTEM images of a twin boundary in order to determine the atomic model of this boundary. A possible atomic model for a (111) twin boundary in the oxide is shown in Fig. 56. Two oxide crystals in the top and bottom in Fig. 56 form a coherent (111) twin boundary as indicated by the dashed lines in the middle of this figure. The choice of the atom positions at the boundary was not totally arbitrary since the positions of the white dots in experimental HRTEM images of Fig. 55 suggest that there is a glide symmetry rather than the mirror reflection symmetry, that is, there may be a glide symmetry for a sublattice between two crystals.

One major assumption made in constructing this model in Fig. 56 is that there is a mirror reflection with respect to the (111) boundary, indicated by the dashed lines,

for the oxygen sublattice, whereas there is a glide symmetry for the aluminum sublattice between two crystals. In addition, all oxygen ions have four aluminum ion neighbors and there are no aluminum ions very close to one another in polyhedra with one face common, in order to obey Pauling's rule.[85] Notice that this atomic model in Fig. 56 is also described as a twin boundary with a stacking fault of type III[107],[108] as discussed in section 3.2.4. Hornstra[107] predicted that this boundary with a stacking fault of type III will be most favorable energetically in the spinel oxide.

The projected potential, which contains 3 unit cells of the atomic model of Fig. 56 in the x-axis, is shown in Fig. 57. Figure 58 is a series of simulated images of a twin boundary showing the image contrast changes as a function of specimen thickness and objective lens defocus. The actual atomic positions are superimposed in the top-left corner of this figure.

There is one additional variant of this atomic model as shown in Fig. 59, which is obtained from the atomic model in Fig. 56 by operating the mirror reflection with respect to the (111) boundary indicated by the dashed lines in Fig. 56, or by rotating by 180° about $[11\bar{2}]$ axis such that that the top and bottom of the model are inverted. The projected potential is shown in Fig. 60. This additional series of simulated images of a twin boundary in the oxide as a function of specimen thickness is shown in Fig. 61, for objective lens defocus values of –500 and –850 Å. Again, the atomic positions are superimposed in the top-left corner of this figure.

Note that if any of the images in Fig. 58 are rotated by 180° such that the tops and bottoms of the images are inverted, these new images are not the same as those in Fig. 61. Thus, the exact structure of the boundary cannot be determined by the examination of its simulated image alone in Fig. 58. However, it can be uniquely determined

if the experimental image in Fig. 55 is compared with the simulated images in Figs. 58 and 61.

Comparison of the contrast and periodicities of bright spots at the boundary and in both crystals in the experimental image in Fig. 55 with the simulated images in Fig. 58 shows that good agreement is obtained for a specimen thickness of about 200 Å at –850 Å defocus from Fig. 58. However, good agreement cannot be obtained from Fig. 61 by comparing the periodicities of bright spots of the experimental image in Fig. 55 with those of the simulated images in Fig. 61. This fact is clearly illustrated by the inset simulated image of the boundary, at –850 Å defocus and 200 Å thickness from Fig. 58, as shown superimposed on the middle-right of the image in Fig. 62. Notice the matching of the spot periodicities in both crystals between the experimental and simulated images. Thus, it is possible to conclude that the correct model for a twin boundary in the oxide is illustrated by Fig. 56 rather than by Fig. 59. Furthermore, this defect shown in Fig. 56 is a twin boundary with a stacking fault of type III.[107],[108] However, this conclusion does not exclude the possibility that there might be a twin boundary with a stacking fault of other types.

7.6.3 Atomic Mechanism for Twin Boundary Formation in Oxide

Figure 63 shows the proposed mechanism for twin boundary formation in the oxide. Figure 63 (a) shows the aluminum crystal, whereas Fig. 63 (d) shows the oxide crystal containing a twin boundary with a stacking fault of type III, projected in a $<110>$ orientation, as indicated in the accompanying legends at the bottoms of these figures. The twin plane is indicated by the dashed lines in the middle of these figures.

The lower half represents the aluminum transformation to oxide with a parallel orientation relationship. The major chemical change occurs by absorbing vacancies for one third of Al sites and diffusion of oxygen into the octahedral sites of the aluminum, whereas the structural change occurs by a small volume contraction due to the ionization process of the aluminum and oxygen atoms and by shuffling one quarter of Al sites to the tetrahedral site, with reference to the unit cell of the $\Sigma = 1$ coincidence site lattice, just as described in section 7.4.4.

The upper half represents the aluminum transformation to oxide with a twin orientation relationship. The major structural change occurs by the $\frac{a}{6}[11\bar{2}]$ twinning shear of the aluminum atoms, indicated by arrows in Fig. 63 (a), by a small volume contraction, and by shuffling one quarter of Al sites to the tetrahedral site to have the required atomic arrangement for the oxide structure with a twin orientation, whereas the major chemical change occurs by absorbing vacancies for one third of Al sites, and diffusion of oxygen into the octahedral sites of the aluminum, with reference to the unit cell of the $\Sigma = 3$ coincidence site lattice, as described previously in section 7.5.3. Thus, this results in a twin boundary with a stacking fault of type III in the oxide.

7.7 Multiple Twinning in the Oxide

7.7.1 High-Resolution TEM Images of Parallel Multiple Twinning

With increasing oxidation time, the oxide grows by increasing the number of the grains. At the late stages of oxidation, all of the polycrystalline oxide islands are composed of twin related grains. Figure 64 shows a high-resolution lattice image of γ–Al_2O_3 with a parallel multiple twinning, produced by the 4 week oxidation treatment of aluminum at 600 ° C. This image was taken in a <110> oxide orientation.

Each oxide crystal is indicated by the dashed lines, in the middle of this figure, which represent a {111} plane of each oxide. The boundary plane is a common {111} plane of the oxides. In this image, a first twinning from the top layer produced the 7 {111} planes thick oxide layer with a twin orientation. A second twinning on an octahedral plane parallel to the first restored the original orientation and produce a parallel-sided twin band. This subsequent growth twinning on an octahedral plane of the same set, that is, parallel to the existent twin plane leads to successive parallel twin bands in the whole oxide as shown in Fig. 64.

As indicated by the marker, which represents a {111} spacing of the oxide, the oxide plates are about 4 to 45 {111} oxide planes thick, indicating that thickening of the oxide occurs by the passage of the growth ledge, with such thicknesses, along the broad {111} oxide faces as shown in sections 7.4.4 and 7.5.1.

Figure 65 shows a high-resolution image of γ–Al_2O_3 containing tips of twin bands, obtained from the oxidation of aluminum for 2 weeks at 600 ° C. There are two twin bands on the left side of the crystal as indicated by the dashed {111} planes whereas there is no twin band on the right side. This indicates that, on the left side, a first twinning produced the 4 {111} planes thick twin band, a second twinning on an

octahedral plane parallel to the first restored the original orientation, a third twinning produced the twin band again and a fourth twinning restored the original orientation, whereas, on the right side, there was no twinning. There is a stacking fault on the {111} plane as indicated by the arrow.

Figure 66 shows an enlargement of the middle of Fig. 31. In this figure, there are many stacking faults in the oxide, showing that the twinning or faulting on the {111} planes can occur with one or several {111} plane thickness during the oxide growth process.

7.7.2 High-Resolution TEM Images of Nonparallel Multiple Twinning

However, the twin plane is not always parallel only to an octahedral plane as shown in Fig. 67. This figure shows a low magnification lattice image of an oxide with a nonparallel multiple twinning,[187]-[192] produced by the 4 week oxidation at 600 ° C. As indicated by the marker in the top-left corner, the oxide is about 1000 Å thick, whereas the aluminum matrix without revealing the lattice fringes is shown in the bottom-right corner of this figure.

The size of a twin is increased with the depth from the surface, i.e. with the decrease of the growth rate, since the oxide growth rate depends on the the protective oxide thickness. This fact suggests that the formation of twinned nuclei is promoted when driving force for the oxidation is high. Furthermore, the growth twin formation might be due to a growth accident[190] since a twinning accident will be increased with the growth rate. Notice that this polycrystalline oxide is composed entirely of multiply-twinned crystals.

The presence of twinned oxides in this area can be verified by taking a dark-field image using a twin oxide reflection if the density of spots in reciprocal space is low.

However, the interfacial areas contain two phases. In addition, the oxide phase occasionally exhibited three or more variants of twinning. Therefore, in the worst case, four or more complicated diffraction patterns overlapped and make spot selection for dark-field imaging extremely difficult. Furthermore, the size of the individual twins are so small in this area that there is no convenient examination by conventional transmission electron microscopy methods, even when the dark field imaging technique is used. Thus, high-resolution electron microscopy reveals much more information about the multiple twinning in the oxide.

An enlargement of the left region of Fig. 67 as shown in greater detail on the left of Fig. 68 clearly shows that there are extensive twin relationships with more than two oxide orientations. The schematic diagram on the right of Fig. 68 shows the regions which correspond to the oxide grains in the high-resolution image on the left of Fig. 68. In the image the prominent lattice fringes are seen as (111) and $(11\bar{1})$ intersecting at 70.5°. The orientations of the regions designated with letters on the right of Fig. 68 were determined by comparing the angles of the {111} fringes in the high-resolution images with the values calculated in octahedral multiple twinning[191] in face-centered cubic crystals.

A face-centered cubic structure crystal, I, twins and the resultant individual, II, twins again (nonparallel) and the resultant individual, III, twins again to generate a third crystal, IV. First-order[191] twinning between I and II in the fcc structure can be interpreted geometrically as a rotation about [110] of 70°32′. Further, second-order twinning between I and III, and third-order twinning between I and IV can be considered as rotations about [110] of 38°57′ and 31°35′, respectively.[193]

The thick and thin lines in each grain in Fig. 68 represent the {111} and (001)

planes of each oxide grain, which are projected in a $[1\bar{1}0]$ oxide orientation, as indicated in the accompanying legend in the bottom-left corner of this diagram. It is evident that the rotations generating II_b and III_b from II_a, and IV_a from III_b, can all be taken to be $70^\circ 32'$ each about the common pole [110]. Thus, it becomes evident that the [110] direction is the zone axis to the five (111) planes. It clearly shows that the twinning plane is a {111} plane in this figure. All crystals are connected by the first-order {111} octahedral twins, and thus no twin can grow unless one face coincides with an adjacent crystal.

All orientations found could be ascribed to multiple twinning, as if the orientations in this figure originated in the oxide growth from a single nucleus. The orientation relationships may be represented:

$$III_b \text{——} II_a \text{——} III_a \text{——} IV_a$$

with boundary contacts between the second-order twins $II_b\, III_b$, and $II_a\, IV_a$, as well as the remaining first-order twins. Of the four possible first order twins of II_a, two were present in this image and designated by III with subscripts. One second order twin of II_a is designated by IV with subscript. Four crystals, designated by III with subscripts are first order twins of II_a and II_a is a second order twin of II_b. The second-order twin join, which is termed the boundary between individuals related by two nonparallel stages of twinning,[193] is not clear in this image, but it is generally straight close to a {221} plane, i.e. one of the mirror planes of two crystals. The region of high-order twin, IV, is small compared to those of II or III, probably, because its orientation with respect to the matrix orientation or the growth direction was not favorable for growth.

As shown in the electron diffraction pattern in Fig. 70, a $70^\circ 32'$ rotation of the electron diffraction pattern of III_b about $<110>$ axis, generates II_a, and a further

$70^\circ 32'$ rotation of II_a about <110> axis, generates III_a. Also, notice that a {111} reflection from a crystal is coincident with that from the neighboring crystals, indicating that the {111} planes are the twin planes. These facts further confirm the twinning relations of the oxide as shown in the high-resolution images.

An enlargement of the right region of Fig. 67 as shown on the top of Fig. 69 shows that the oxide has the {111} multiple twinning just as for the oxide in Fig. 68. The orientations of the crystals designated with letters are also shown in the schematic diagram on the bottom of Fig. 69. The orientation relationships may be represented:

$$III_b \text{——} II_a \text{——} III_a .$$

Figure 71 shows a high-resolution lattice image of a similar oxide with a multiple twinning, produced by the 2 week oxidation at 600° C, taken in a <110> oxide orientation. The amorphous oxide on the top surface, off to the top side of the micrograph, is ion-milled away during specimen preparation and the specimen around the bottom region in this figure is so thick for high-resolution imaging that the image does not reveal the fringes around the aluminum/oxide interface, that is, the sample thickness is increasing from the top to the bottom in the micrograph. However, it clearly shows that there is the multiple twinning in the oxide. The oxide is about 600 Å thick, as indicated by the marker which represents a {111} oxide spacing on the right of this figure. The orientations of the crystals which were determined by measuring the angles of the {111} fringes in the high-resolution images, are designated with letters on each crystal as shown in Fig. 71. It is evident that the rotations generating II_b and III_b from II_a, and IV_a from III_b, can all be taken to be $70^\circ 32'$ each about the common pole [110]. Thus, the orientation relationships may be represented:

III_b ——II_a ——III_a ——IV_a .

It clearly shows that there is {111} multiple twinning in the oxide in this figure. All the twinned crystals are connected by the first-order {111} octahedral twins, and thus no twin can grow unless one face coincides with an adjacent crystal, just as for the oxide in the previous figures. This further indicates that the growing oxide nucleated new grains by twinning at the {111} faces of the oxide, as if the orientations in this figure originated in the oxide growth from a single nucleus.

When the two second-order twins intersect, as shown as III_a and III_b on the left side of Fig. 71, the new twin, II_a , is nucleated beneath the second-order twin join, i.e. the boundary between the nonparallel second-order twins, instead of continuing the growth of the second-order twin join. The nucleated crystal is the first-order twin of the two neighboring intersecting grains, thus, this leads to two coherent {111} boundaries rather than one higher energy boundary between the second-order twins in the oxide to minimize the boundary energy.

An additional example is shown on the right side of this figure. When the two third-order twins intersect, as III_b and IV_a , two new twins, II_a and III_a , are nucleated beneath the third-order twin join with growing the oxide. One new grain II_a is the first-order twin of III_b and another new grain, III_a , is the first-order twin of IV_a , respectively. Thus, the two third-order twins, III_b and IV_a , are connected by the three first-order {111} boundaries as shown in this figure. That is, during the oxide growth, three coherent {111} twin boundaries are formed instead of the third-order twin join, i.e. the boundary between individuals is related by two nonparallel third-order twinning.

These indicate that there is a strong driving force for nucleation of new first-

order twin at the higher-order twin intersection, in order to form the coherent {111} twin boundary instead of the high-order twin join to minimize the boundary energy.

Note that first-order {111} twinning has associated with it a specific coincidence superlattice, which differs from those accompanying second- and third-order twinning, this leads to the lowest boundary energy with a sharp cusp in the surface energy γ-plot. With fourth- and higher-order twinning of a face-centered structure, there are no lattice points common to both individuals and therefore no coincidence site superlattice exists.

Since most boundaries in the oxide are {111} coherent twin boundaries, the twin boundaries at least in this oxide cannot act as a path of easy diffusion as thought,[194],[195] except that the oxide layer is very thin at the initial stages of oxidation. Cathcart *et al.* [195] proposed that the twin boundaries in the mosaic spread of twinning in NiO[195] and copper oxide[194] act as paths of easy diffusion to relate the oxidation rate anisotropy to the twin density.

For the images in Figs. 68, 69 and 71, notice that two {111} planes of all the orientations in the twinned oxide have a common [110] zone axis, whereas the orientations, the {111} planes of which are not edge-on in this <110> orientation, are not observed.

The results clearly show that all the grains in the oxide share their {111} planes with neighboring grains, indicating that the growing oxide nucleates new grains by twinning at the {111} faces of the oxide. Furthermore, the morphologies of the oxide are determined by the different combinations of the twin related grains.

7.7.3 Atomic Mechanism for Multiple Twinning in Oxide

Figure 72 shows a proposed multiple twinning model in the oxide. Each tetrahedron represents the Thompson tetrahedron corresponding to each spinel oxide orientation. Thus, the faces of the tetrahedron represent the {111} octahedral planes of the fcc spinel oxide and the edges represent the lattice translation of the oxide, $\frac{1}{2}<110>$. A face-centered cubic structure crystal, I, twins and the resultant individual, II, twins again (nonparallel) and the resultant individual, III, twins again to generate a third crystal, IV. Note that the next twinned crystals are obtained by the successive rotation about a $<110>$ axis of $70^\circ 32'$, with sharing of their {111} octahedral planes with the neighboring crystals. Also, there are four possible first-order twins, which share the four {111} planes of each tetrahedron. However, of the four possible first order-twin variants of each tetrahedron, only one variant, II, III and IV is shown in Fig. 72. The various combinations of these Thompson tetrahedra including all variants would produce a multiple twinning in the oxide.

However, among these many possible orientations, only four orientations, II_a, III_a, III_b and IV_a, are observed in a high-resolution image from Figs. 68, 69 and 71, since two {111} planes of only these four orientations in the twinned oxide are edge-on in a $<110>$ orientation, whereas those of the other variants are inclined to the electron beam, in Fig. 72.

Figure 73 shows a proposed atomic mechanism for new grain nucleation by multiple twinning, projected in a $<110>$ orientation. A close-packed layer of atoms can be added to the octahedral planes of a face-centered cubic spinel oxide in two possible positions, the right position continues the original orientation, the wrong one forms the first layer of a twin. Oxygen ions have attached in a position that continues the

correct stacking order of the {111} planes of the spinel oxide in Fig. 73 (a). The Thompson tetrahedra, which correspond to the oxide crystals, are shown in the bottom-right corners of these figures. But in Fig. 73 (b), oxygen ions have attached in a *twin* position that begins a twinning with a stacking fault of type III.

These wrong positions are identical as far as the distance to nearest neighbors is concerned, although the distance to second nearest neighbors is slightly changed. Similar stacking mistakes on the {100} and {110} planes require first nearest neighbor mistakes and are thus unlikely to occur. One concludes from this as well as from numerous other observations that the energy associated with such a twin interface is small, and thus that it would not be difficult to form.

Thus, if during the oxide growth a few oxygen atoms were to fall into the wrong set of positions, the first layer of a twin would be formed, and if conditions were favorable to its growth the twinned orientation would propagate itself to give a twin of detectable width. A second error in positioning on an octahedral plane parallel to the first would restore the original orientation and produce a parallel-sided twin band. Another second error in positioning on an octahedral plane nonparallel to the first would create an additional orientation and produce a multiple twinning in the oxide. This mechanism indicates that twins can form whenever the oxide grows, and that the number and width of twins formed would be controlled solely by the frequency of accidents.

It is reasonable to conclude that the high-order twins are the result of progressive octahedral twinning through several generations in the oxide growth. The nucleus for a twinned orientation could have its origin in a *stacking fault* on the close-packed octahedral plane. Thus, all the grains in the oxide share their {111} planes with neigh-

boring grains and the growing oxide nucleates new grains by twinning at the {111} faces of the oxide.

However, twins with the orientation most favorable to the growth direction (maximum chemical potential gradient of the oxygen atoms), or favorable to the boundary energy minimization in the oxide as shown in section 7.7.2 will grow relatively fast and be dominant in the further growth. The extensive twinning is probably promoted during oxidation by the constraint imposed by the volume decrease, and to an irregular growth front.

The proposed mechanism is consistent with the observation and the conclusion of Tabata and Ishii.[196] They observed many parallel or nonparallel twins in the spinel oxide grown from the melt, and concluded that the mechanism of the twin formation is due to the introduction of stacking disorder between the oxygen close-packed layers.

7.8 Al/Oxide Interface which is not a {111} Al Plane

7.8.1 High-Resolution Transmission Electron Microscopy Images

The aluminum/oxide interface is no longer a {111} aluminum plane, when either the original oxide nucleus does not have a parallel or a twin orientation, or the oxide crystal grows with nonparallel multiple twinning even if the original nucleus has a parallel or a twin orientation relationship.

Figure 74 shows a low magnification high-resolution image of the aluminum/oxide interface, produced by the 2 week oxidation at 600 °C. As indicated by the marker in this figure, the oxide in the middle is about 450 Å thick. In this image, taken in a <110> oxide orientation, the oxide reveals the two dimensional lattice image, whereas the aluminum matrix reveals only the one dimensional {111}

fringes, indicating that there is a misorientation between the two crystals.

The fringes along the 4 o'clock direction around the aluminum/oxide interface are identified as the Moiré fringes by calculating the spacing and the angle of these lines using the well-known Moiré formula:[176]

$$d = \frac{d_1 d_2}{\sqrt{d_1^2 + d_2^2 - 2d_1 d_2 \cos\theta}}$$

where d_1 and d_2 are the spacings of the lattice planes misoriented by θ at the interface. The angle (ρ) between the structural Moiré lines and the trace of lattice 1 is given by:

$$\sin\rho = \frac{d_1 \sin\theta}{\sqrt{d_1^2 + d_2^2 - 2d_1 d_2 \cos\theta}}.$$

This is due to the fact that there are some overlapping oxides around the interface, which leads to light/dark Moiré fringes through the thickness of the aluminum matrix. The presence of this overlapping oxide is due to the fact that the growing oxide exists through the thickness of the foil, causing an overlap of the oxide around the interface.

The region covered with the Moiré fringes is much broader at the edge of the 450 Å thick growth ledge on the right side of Fig. 74 than around the atomically flat {111} oxide interfacial plane, implying that the main growth of this oxide occurs by the movement of this large growth ledge, further by atomic attachment at the edge of this ledge.

The structural character of a growth ledge and twins of Fig. 74 is shown in greater detail in the enlargement in Fig. 75. Two important {111} crystallographic planes in the oxide are superimposed on the oxide in the top-right corner. The twinning in the oxide is indicated by superimposing the white dashed lines on the left side

of the oxide in this figure. By sighting along the $(11\bar{1})$ oxide planes parallel to the oxide face in this figure, it is possible to conclude that the aluminum/oxide interface is comprised of a {111} octahedral plane of the oxide and a random plane of the aluminum.

Furthermore, a 39 Å thick growth ledge grows parallel to the {111} planes of the oxide, indicating that the thickening of the oxide occurs by the movement of such a growth ledge. Notice that there are four {111} twin boundaries in the oxide, and the aluminum/oxide interface on the right side in the figure coincides with a twin boundary in the oxide, indicating that the growing oxide nucleates a new growth ledge by twinning, confirming the proposed mechanism of the nucleation of the new grain by twinning in section 7.7.3. The edge of this growth ledge does not show the atomic detail due to the complexity of the atomic structure of the growing edge and the overlapping matrix.

Figure 76 shows an additional example of the high-resolution image with the growth ledges, obtained from the same oxidation treatment as that of Fig. 74. One 70 Å thick growth ledge grows parallel to the {111} oxide planes from the right side and another 20 Å thick ledge grows parallel to the same planes from the left side in this figure.

In Fig. 77, the structural character of the edge of a large growth ledge is shown in greater detail in the enlargement of the ledge on the right side of Fig. 74. Several important crystallographic planes, {111} and {002}, in the oxide are superimposed on the oxide in the middle of this figure. The angle between {111} planes of the oxide and the aluminum, as indicated by 63°, shows the misorientation between the oxide and the aluminum. There are several regions of hexagonal contrast bounded by the low

index {111} and {002} planes around the tip of the oxide as indicated by the curved arrow.

Figure 78 shows an enlargement of the bottom-right corner of Fig. 31. Three low index planes are superimposed on the oxide image in the bottom-left corner of this figure. Comparing these planes with the oxide/vacuum interface shows that the crystalline oxide surface, is faceted with {111} and {002} faces of the oxide at the near atomic level. There are some hexagonal shapes in the oxide image, which are also bounded by {111} and {002} faces with 20 to 40 Å width. This is due to the fact that the oxide is preferentially etched on these {111}, {002} planes during the ion-milling for the specimen preparation, indicating that the surface energy of these surfaces is relatively low compared with the other high index planes in this oxide.

The aluminum/oxide interfaces in Figs. 79 and 80 clearly show the structural character of the atomically flat {111} habit planes of the oxide, indicating that atomic attachment is not occurring at this atomically flat interface. The 20 {111} oxide planes are matched by the 37 {111} aluminum planes, indicated by arrows in the aluminum and the oxide, and the images indicate that there is no strain field associated with the interface.

Figure 81 shows a high-resolution image of the aluminum/oxide interface, obtained from the oxidation for 2 weeks at 600 ° C. A 550 Å wide edge is not faceted with {111} oxide planes and there are the Moiré fringes in the broad region around this edge, indicating that the main growth process is occurring around this edge. Comparing the superimposed {111} oxide planes on the oxide image with the oxide faces shows that the oxide faces are the {111} oxide planes except at the growth front, implying that this oxide in the figure starts to form the {111} facets with the growth.

Although the heights and structures of the growth ledges have enabled a variety factors to be deduced about the growth process, the images do not show atomic detail at the edges of the growth ledges. Hence, an effort was made to obtain better images which might resolve atomic detail at the growth ledges. In order to gain more information about the atomic structure of the edges of the growth ledge, additional attempts were made to find an oxide whose edge was in a very thin region near the the edge of the specimen, thereby increasing the possibility for the growth edge to lie along an exact <110> oxide orientation through the thickness of the foil.

Figure 82 shows a high-resolution image of one such oxide with the aluminum, oxidized for 2 weeks at 600° C, taken in a <110> oxide orientation. Two important {111} crystallographic planes in the oxide are superimposed on the oxide of this figure. The oxide edge lies along a near {110} oxide plane on a macroscopic level, but it is faceted along {111} oxide planes down to the near atomic level on a microscopic level. The interface is resolved into {111} facets with one to ten {111} oxide plane width. Most of these microscopic ledges are one {111} oxide plane thick. Such microscopic ledges are not revealed by the previous ledges. This faceting at the near atomic level at the edge demonstrates that the oxide is highly crystallographic on both macroscopic and microscopic levels and therefore, there is an extreme tendency for all aluminum/oxide interfaces to lie along the {111} octahedral planes of the oxide even on a very fine scale, presumably due to the kinetic contribution to the atomic mechanism of aluminum oxidation as follows in the next section.

7.8.2 Atomic Mechanism of Oxide Growth Leading to {111} Facets

Results of all the previous high-resolution electron microscopy images in this study show that the habit planes of the crystalline oxide are always the {111} octahedral planes of the oxide and the oxide grows parallel to these planes, by a ledge mechanism.

One question that arises at this point is why the habit planes of the crystalline oxide are always the {111} octahedral planes of the oxide. The proposed atomic mechanisms in sections 7.4.4 and 7.5.3 explain well the transformation of aluminum to the oxide structures, but these mechanisms do not forecast the position of the interface between the aluminum and the oxide.

Interfacial energy effects appear to be exerting a rather large influence in determining the overall shape of the oxide. That is, there is a tendency for all the interfaces of the precipitate in the matrix to lie along the low-energy close-packed planes, presumably because this minimizes both the chemical and structural contributions to the interfacial energy, as discussed in the section 4.1.3. The surface energy values of aluminum[20] and spinel oxides[197] are shown in Tables 4 and 5. These tables show that surfaces parallel to {111} planes are of lowest energy for $MgAl_2O_4$ spinel as well as some spinel ferrites with large differences, and these surfaces are also of lowest energy for aluminum. This surface energy contribution to the boundary energy will be favorable for the Al/oxide interface to lie along the {111} octahedral planes.

But one cannot discuss oxide/metal interfaces on the assumption that the forming oxide may freely choose its lowest energy plane. To some extent, the interface orientation of the growing oxide is determined by the mechanism of transfer of oxygen atoms from the oxide to the metal or by the kinetically favored interfaces.[122] In gen-

eral, it is to be expected that the interface orientation is subject to the restrictions imposed by the growth mechanism. Thus, the growth mechanism based on the kinetic considerations will be discussed in the following paragraphs.

The results of all the previous high-resolution electron microscopy studies can thus be summarized at this point as showing that the edges of the ledges are often indistinct and inclined from a <110> oxide orientation, and thus the growth of both the faces and edges of the oxide does not occur by the attachment of individual atoms randomly on the broad {111} oxide face as illustrated in Fig. 83 (a), but instead by the attachment of atoms at edge of the growth ledge as illustrated in Fig. 83 (b).

Assuming that the oxygen atoms must attach to the oxide by completing the coordination of the aluminum atom, this leads to the prediction that the habit planes of the crystalline oxide should be the {111} octahedral planes of the oxide. For the aluminum/oxide to advance during oxidation, single oxygen atoms or small groups of oxygen atoms cross the interface so as to add to the oxide face and then to be considered part of the oxide.

The exact growth mechanism will depend on the orientation of the crystallographic face involved. The atomic arrangement on {100}, {110} and {111} faces for the spinel oxide structure, projected in a <110> orientation, is shown in Fig. 84. Solid and dashed lines represent a <110> projection of the {111} planes and the <110> edges of oxygen octahedra or tetrahedra, respectively. The nucleated octahedra and tetrahedra are indicated by thick lines in this figure. For the sake of simplicity, the atoms in the aluminum matrix are not shown in this figure.

The atomic structure on the smooth faces of these three orientations is very different with respect to addition of new oxygen atoms to the oxide. The requirement

that adding oxygen atoms must complete the coordination of the aluminum atom for a successful nucleation of oxygen polyhedra, poses no problem on the {100} or {110} faces. For {100} faces, a single oxygen atom for the aluminum atom in the octahedral sites or simultaneous jumps of two oxygen atoms for the aluminum atom in the tetrahedral sites, can add to a {100} face to satisfy the coordination. For {110} faces, nucleation of a new polyhedra requires simultaneous jumps of two oxygen atoms for the aluminum atoms in the octahedral sites or a single atom jump for that in the tetrahedral sites.

However, on {111} faces, nucleation of a new polyhedra is more difficult since it requires simultaneous jumps of three oxygen atoms in Fig. 84 (c). Thus, it is extremely difficult to grow normal to a {111} oxide plane. Further growth can take place more easily by expanding on the established nucleus rather than by producing new nuclei. On {100}, {110} and {111} faces the nuclei may expand by a single jump of one oxygen atom or simultaneous jumps of two oxygen atoms. This process limits how fast growth of the oxide can occur along a crystallographic plane if the overall oxidation process is controlled by the interface reaction. Rapid growth parallel to the {111} faces leads to the {111} habit planes of the oxide.

On the {111} surface, further growth for the next mixed layer, which contains the octahedral and tetrahedral sites, is not difficult since a single jump of oxygen atom for nucleation of a tetrahedron can complete the coordination of the aluminum atom in the tetrahedral sites. Since the {111} cation layers consist of two types of layer, namely, a mixed layer and a kagome layer alternatively, this leads to the ledge with the two oxygen layers corresponding to a {111} oxide layer. This prediction is in agreement with the fact that most of the microscopic ledges in Fig. 82 are one {111}

oxide plane thick.

When the nucleus has attached in a position that begins the twinning, the twin is nucleated at the interface as described in section 7.7.3. No first nearest neighbor mistakes have been made by the twin cluster and hence, the excess energy of this defect is small. Similar stacking mistakes on the {100} and {110} faces require first nearest neighbor mistakes and are thus unlikely to occur. In this study, twins are only observed on the {111} faces.

Figure 85 shows the face of the spinel oxide with the growth ledges, projected in a <110> orientation. The growth ledges always show corners, as shown in this figure, where a single jump of a oxygen atom or simultaneous jumps of two oxygen atoms can complete the coordination of the aluminum ion. This growth process is easier to compare with that normal to the {111} faces of the oxide. Thus, the oxide grows easily by the movement of the growth ledges, as observed by previous high-resolution images in this study.

From this point, this proposed atomic mechanism is analogous to the standard terrace-ledge-kink mechanism of growth which was originally proposed for the growth of close-packed interfaces of a solid into a vapor or liquid,[198] as illustrated in Fig. 83. Furthermore, this proposed mechanism appears to be valid for describing the growth of the spinel oxide from melted oxide. Tabata and Ishii[196] have shown that all the spinel $MgAl_2O_4$ crystal grown from the melt had octahedral habit with {111} planes.

CHAPTER 8

SUMMARY OF RESULTS

A transmission electron microscopy study of the aluminum/oxide interface was carried out at high-resolution in order to perform highly detailed analyses of the crystallographic aspects required for nucleation and growth of the aluminum oxide, so that the mechanisms of nucleation and growth could be modelled on an atomic level. In conjunction with computer simulation comparisons, the images reveal directly the atomic structure of the oxide, the base metal, and all internal interfaces. The following results have been obtained:

1. In the early stages of oxidation, crystalline γ–Al_2O_3 forms in two major crystallographic relationships with the aluminum matrix: (a) parallel and (b) twinned. In addition, the crystalline γ–Al_2O_3 grows with faceted interfaces into the aluminum matrix from the aluminum/amorphous oxide interface.

2. The aluminum/amorphous oxide interface structure is dependent on the surface orientation of aluminum. This interface is faceted on a macroscopic {110} aluminum surface, whereas it is diffuse on a {111} aluminum surface.

3. The hemispherical crystalline oxide nuclei, less than 25 Å thick, protrude into the amorphous oxide from the macroscopically flat aluminum/crystalline oxide interface, indicating that the crystalline oxide nucleates by the structural rearrangement of atoms within the amorphous oxide into the structure of the crystalline phase at the aluminum/amorphous oxide interface.

4. The parallel orientation interface is a coherent {111} plane of the aluminum and the oxide. Comparison between experimental high-resolution electron microscopy

images and simulated images leads to a complete model of the interface. From this model, a complete model for this transformation has been proposed as follows. Aluminum transforms to the oxide structure by shuffling one quarter of the Al sites, by absorbing vacancies for one third of the Al sites, and by diffusion of oxygen into the octahedral sites of the aluminum, with reference to the $\Sigma = 1$ coincidence site lattice.

5. The twin orientation interface is a coherent {111} plane of the aluminum and the oxide. A complete model for this transformation has also been proposed as follows. Aluminum transforms to the oxide structure by a twinning shear, followed by shuffling one quarter of the Al sites, by absorbing vacancies for one third of the Al sites, and by diffusion of oxygen into the octahedral sites of the aluminum, with reference to the $\Sigma = 3$ coincidence site lattice.

6. Comparison between experimental and simulated high-resolution images of a twin boundary in the oxide shows that it is a macroscopic $\Sigma = 3$ twin boundary with a stacking fault of type III. A complete model for this twin boundary formation has also been proposed.

7. In the later stages of oxidation, the crystalline oxide itself is characterized by parallel or nonparallel multiple internal twins which comprise the polycrystalline nature of the oxide. A complete model for this multiple twin formation has been proposed.

8. When the aluminum/oxide interface is neither a parallel nor a twin orientation, the aluminum/oxide interface comprises a {111} plane of the oxide and a random plane of the aluminum. A complete model for this transformation has also been proposed as follows. Assuming that the oxygen atoms must attach to the oxide

by completing the coordination of the aluminum atom, this leads to the prediction that the habit planes of the crystalline oxide should be the {111} octahedral planes of the oxide.

CHAPTER 9

CONCLUSIONS

1. Crystalline γ–Al_2O_3 nucleates by the structural rearrangement of the atoms within the amorphous oxide into the structure of the crystalline phase at the aluminum/amorphous oxide interface.

2. The crystalline γ–Al_2O_3 grows parallel to the {111} octahedral planes of the oxide, often by a ledge mechanism.

3. The growing oxide nucleates new grains by twinning.

4. For the parallel orientation interface, aluminum transforms to the oxide structure by shuffling one quarter of the Al sites, by absorbing vacancies for one third of the Al sites, and by diffusion of oxygen, with reference to the $\Sigma = 1$ coincidence site lattice.

5. For the twin orientation interface, aluminum transforms to the oxide structure by a twinning shear, followed by shuffling one quarter of the Al sites, by absorbing vacancies for one third of the Al sites, and by diffusion of oxygen, with reference to the $\Sigma = 3$ coincidence site lattice.

6. For the random orientation interface, based on the assumption that the oxygen atoms must attach to the oxide by completing the coordination of the aluminum atom, the {111} habit growth of the oxide can be predicted.

ACKNOWLEDGEMENTS

This thesis would not have been possible without the help and support of a number of people to whom I owe gratitude.

First, I would like to express my appreciation to my research advisor, Professor Ronald Gronsky for his encouragement, support and outstanding advice throughout this research for three years. I would also like to thank to Professor Alan W. Searcy for his kind helps and time, serving on my committees and inspecting the thesis, and to Professor J. Stringer for his support and suggestions he offered since Professor Whittle's death. In addition, I thank Professor Hans-Rudolf Wenk for his critical review of this thesis.

Many thanks to all of my associates, Roar, Jamie, Eduardo, Jim, Mike and Roseann in the Gronsky group for their friendship and useful discussions. Especially, I take pleasure in acknowledging Roar Kilaas for access to his MSLICE and CTF programs, and for showing me how to run these programs. I also thank Dr. M.A. O'Keefe for access to the A.S.U. programs and Jim Howe for showing me how to run these.

My appreciation goes to the supporting staffs at the National Center for Electron Microscopy and the Materials and Molecular Research Division of the LBL for their assistance. In particular, thanks goes to D. Ackland for his help on the JEOL JEM 200CX and for keeping the microscope in good condition. I would also like to thank all the people at the LBL Photo Lab for providing many micrographs. Thanks to all of the wonderful and generous people who have enriched my experiences at Berkeley.

Finally, I am deeply in debt to my parents and all the other members in the family for their tremendous support and love throughout my entire educational career. Especially, I want to thank my wife Namsoon for her love and support, and my

daughter Hye-Kyung and my son Jin-Kyu for their indulgence during the many hours spent away from them.

This research was supported by the Director, Office of Energy Research, Office of Basic Energy Sciences, Materials Science Division of the U.S. Department of Energy under Contract No. DE-AC03-76SF00098.

APPENDIX

CALCULATIONAL UNIT CELL ATOM POSITIONS

The atom species and the atomic numbers of species are listed in the first and second columns. In the next three columns, atom coordinates are given in terms of the A, B and C dimensions of the calculational cell. The origin of the cell is at the lower left corner.

γ-Al_2O_3 Model

A = 7.900 B = 5.590 C = 5.590 Å

28 Atoms

Al	13	.25000000	.00000000	.00	Al	13	.75000000	.00000000	.50
Al	13	.50000000	.25000000	.25	Al	13	.50000000	.25000000	.75
Al	13	.25000000	.50000000	.00	Al	13	.75000000	.50000000	.50
Al	13	.00000000	.75000000	.25	Al	13	.00000000	.75000000	.75
Al	13	.12500000	.25000000	.50	Al	13	.87500000	.25000000	.00
Al	13	.37500000	.75000000	.50	Al	13	.62500000	.75000000	.50
O	8	.00000000	.00000000	.00	O	8	.00000000	.00000000	.50
O	8	.50000000	.00000000	.00	O	8	.50000000	.00000000	.50
O	8	.25000000	.25000000	.25	O	8	.25000000	.25000000	.75
O	8	.75000000	.25000000	.25	O	8	.75000000	.25000000	.75
O	8	.00000000	.50000000	.00	O	8	.00000000	.50000000	.50
O	8	.50000000	.50000000	.00	O	8	.50000000	.50000000	.50
O	8	.25000000	.75000000	.25	O	8	.25000000	.75000000	.75
O	8	.75000000	.75000000	.25	O	8	.75000000	.75000000	.75

Al/Oxide Interface Model with Parallel Orientation

Starting with a Kagome Layer

A =9.6754845 B = 27.366403 C = 5.5861436 Å

146 Atoms

O	8	.00000000	.00000000	.00
O	8	.25000000	.00000000	.25
O	8	.50000000	.00000000	.00
O	8	.75000000	.00000000	.25
O	8	.00000000	.25000000	.00
O	8	.25000000	.25000000	.25
O	8	.50000000	.25000000	.00
O	8	.75000000	.25000000	.25
O	8	.16666667	.08333333	.00
O	8	.41666667	.08333333	.25
O	8	.66666667	.08333333	.00
O	8	.91666667	.08333333	.25
O	8	.16666667	.33333333	.00
O	8	.41666667	.33333333	.25
O	8	.66666667	.33333333	.00
O	8	.91666667	.33333333	.25
O	8	.08333333	.16666667	.25
O	8	.33333333	.16666667	.00
O	8	.58333333	.16666667	.25
O	8	.83333333	.16666667	.00
O	8	.08333333	.41666667	.25
O	8	.33333333	.41666667	.00
O	8	.58333333	.41666667	.25
O	8	.83333333	.41666667	.00
O	8	.00000000	.50000000	.00
O	8	.25000000	.50000000	.25
O	8	.50000000	.50000000	.00
O	8	.75000000	.50000000	.25
Al	13	.08333333	.04166667	.25
Al	13	.33333333	.04166667	.50
Al	13	.58333333	.04166667	.75
Al	13	.33333333	.10416667	.00
Al	13	.00000000	.12500000	.00
Al	13	.16666667	.14583333	.50
Al	13	.16666667	.20833333	.00
Al	13	.41666667	.20833333	.75
Al	13	.91666667	.20833333	.25
Al	13	.16666667	.27083333	.50
Al	13	.33333333	.29166667	.00
Al	13	.00000000	.31250000	.00
Al	13	.00000000	.37500000	.50
Al	13	.25000000	.37500000	.75
Al	13	.75000000	.37500000	.25
Al	13	.00000000	.43750000	.00
Al	13	.16666667	.45833333	.50
Al	13	.33333333	.47916667	.00
Al	13	.08333333	.54166667	.25
Al	13	.33333333	.54166667	.50

O	8	.00000000	.00000000	.50
O	8	.25000000	.00000000	.75
O	8	.50000000	.00000000	.50
O	8	.75000000	.00000000	.75
O	8	.00000000	.25000000	.50
O	8	.25000000	.25000000	.75
O	8	.50000000	.25000000	.50
O	8	.75000000	.25000000	.75
O	8	.16666667	.08333333	.50
O	8	.41666667	.08333333	.75
O	8	.66666667	.08333333	.50
O	8	.91666667	.08333333	.75
O	8	.16666667	.33333333	.50
O	8	.41666667	.33333333	.75
O	8	.66666667	.33333333	.50
O	8	.91666667	.33333333	.75
O	8	.08333333	.16666667	.75
O	8	.33333333	.16666667	.50
O	8	.58333333	.16666667	.75
O	8	.83333333	.16666667	.50
O	8	.08333333	.41666667	.75
O	8	.33333333	.41666667	.50
O	8	.58333333	.41666667	.75
O	8	.83333333	.41666667	.50
O	8	.00000000	.50000000	.50
O	8	.25000000	.50000000	.75
O	8	.50000000	.50000000	.50
O	8	.75000000	.50000000	.75
Al	13	.08333333	.04166667	.75
Al	13	.58333333	.04166667	.25
Al	13	.83333333	.04166667	.00
Al	13	.83333333	.10416667	.50
Al	13	.50000000	.12500000	.50
Al	13	.66666667	.14583333	.00
Al	13	.41666667	.20833333	.25
Al	13	.66666667	.20833333	.50
Al	13	.91666667	.20833333	.75
Al	13	.66666667	.27083333	.00
Al	13	.83333333	.29166667	.50
Al	13	.50000000	.31250000	.50
Al	13	.25000000	.37500000	.25
Al	13	.50000000	.37500000	.00
Al	13	.75000000	.37500000	.75
Al	13	.50000000	.43750000	.50
Al	13	.66666667	.45833333	.00
Al	13	.83333333	.47916667	.50
Al	13	.08333333	.54166667	.75
Al	13	.58333333	.54166667	.25

Al	13	.58333333	.54166667	.75
O	8	.16666667	.58333333	.00
O	8	.41666667	.58333333	.25
O	8	.66666667	.58333333	.00
O	8	.91666667	.58333333	.25
Al	13	.00000000	.62500000	.00
Al	13	.25000000	.62500000	.25
Al	13	.50000000	.62500000	.00
Al	13	.75000000	.62500000	.25
Al	13	.16666667	.70833333	.00
Al	13	.41666667	.70833333	.25
Al	13	.66666667	.70833333	.00
Al	13	.91666667	.70833333	.25
Al	13	.08333333	.79166667	.25
Al	13	.33333333	.79166667	.00
Al	13	.58333333	.79166667	.25
Al	13	.83333333	.79166667	.00
Al	13	.00000000	.87500000	.00
Al	13	.25000000	.87500000	.25
Al	13	.50000000	.87500000	.00
Al	13	.75000000	.87500000	.25
Al	13	.16666667	.95833333	.00
Al	13	.41666667	.95833333	.25
Al	13	.66666667	.95833333	.00
Al	13	.91666667	.95833333	.25

Al	13	.83333333	.54166667	.00
O	8	.16666667	.58333333	.50
O	8	.41666667	.58333333	.75
O	8	.66666667	.58333333	.50
O	8	.91666667	.58333333	.75
Al	13	.00000000	.62500000	.50
Al	13	.25000000	.62500000	.75
Al	13	.50000000	.62500000	.50
Al	13	.75000000	.62500000	.75
Al	13	.16666667	.70833333	.50
Al	13	.41666667	.70833333	.75
Al	13	.66666667	.70833333	.50
Al	13	.91666667	.70833333	.75
Al	13	.08333333	.79166667	.75
Al	13	.33333333	.79166667	.50
Al	13	.58333333	.79166667	.75
Al	13	.83333333	.79166667	.50
Al	13	.00000000	.87500000	.50
Al	13	.25000000	.87500000	.75
Al	13	.50000000	.87500000	.50
Al	13	.75000000	.87500000	.75
Al	13	.16666667	.95833333	.50
Al	13	.41666667	.95833333	.75
Al	13	.66666667	.95833333	.50
Al	13	.91666667	.95833333	.75

Al/Oxide Interface Model with Parallel Orientation

Starting with a Mixed Layer

A = 9.6754845 B = 27.366403 C = 5.5861436 Å

140 Atoms

O	8	.00000000	.00000000	.00
O	8	.25000000	.00000000	.25
O	8	.50000000	.00000000	.00
O	8	.75000000	.00000000	.25
O	8	.00000000	.25000000	.00
O	8	.25000000	.25000000	.25
O	8	.50000000	.25000000	.00
O	8	.75000000	.25000000	.25
O	8	.16666667	.08333333	.00
O	8	.41666667	.08333333	.25
O	8	.66666667	.08333333	.00
O	8	.91666667	.08333333	.25

O	8	.00000000	.00000000	.50
O	8	.25000000	.00000000	.75
O	8	.50000000	.00000000	.50
O	8	.75000000	.00000000	.75
O	8	.00000000	.25000000	.50
O	8	.25000000	.25000000	.75
O	8	.50000000	.25000000	.50
O	8	.75000000	.25000000	.75
O	8	.16666667	.08333333	.50
O	8	.41666667	.08333333	.75
O	8	.66666667	.08333333	.50
O	8	.91666667	.08333333	.75

O	8	.16666667	.33333333	.00
O	8	.41666667	.33333333	.25
O	8	.66666667	.33333333	.00
O	8	.91666667	.33333333	.25
O	8	.08333333	.16666667	.25
O	8	.33333333	.16666667	.00
O	8	.58333333	.16666667	.25
O	8	.83333333	.16666667	.00
O	8	.08333333	.41666667	.25
O	8	.33333333	.41666667	.00
O	8	.58333333	.41666667	.25
O	8	.83333333	.41666667	.00
O	8	.00000000	.50000000	.00
O	8	.25000000	.50000000	.25
O	8	.50000000	.50000000	.00
O	8	.75000000	.50000000	.25
Al	13	.08333333	.04166667	.25
Al	13	.33333333	.04166667	.50
Al	13	.58333333	.04166667	.75
Al	13	.33333333	.10416667	.00
Al	13	.00000000	.12500000	.00
Al	13	.16666667	.14583333	.50
Al	13	.16666667	.20833333	.00
Al	13	.41666667	.20833333	.75
Al	13	.91666667	.20833333	.25
Al	13	.16666667	.27083333	.50
Al	13	.33333333	.29166667	.00
Al	13	.00000000	.31250000	.00
Al	13	.00000000	.37500000	.50
Al	13	.25000000	.37500000	.75
Al	13	.75000000	.37500000	.25
Al	13	.00000000	.43750000	.00
Al	13	.16666667	.45833333	.50
Al	13	.33333333	.47916667	.00
Al	13	.08333333	.54166667	.25
Al	13	.33333333	.54166667	.00
Al	13	.58333333	.54166667	.25
Al	13	.83333333	.54166667	.00
Al	13	.00000000	.62500000	.00
Al	13	.25000000	.62500000	.25
Al	13	.50000000	.62500000	.00
Al	13	.75000000	.62500000	.25
Al	13	.16666667	.70833333	.00
Al	13	.41666667	.70833333	.25
Al	13	.66666667	.70833333	.00
Al	13	.91666667	.70833333	.25
Al	13	.08333333	.79166667	.25
Al	13	.33333333	.79166667	.00

O	8	.16666667	.33333333	.50
O	8	.41666667	.33333333	.75
O	8	.66666667	.33333333	.50
O	8	.91666667	.33333333	.75
O	8	.08333333	.16666667	.75
O	8	.33333333	.16666667	.50
O	8	.58333333	.16666667	.75
O	8	.83333333	.16666667	.50
O	8	.08333333	.41666667	.75
O	8	.33333333	.41666667	.50
O	8	.58333333	.41666667	.75
O	8	.83333333	.41666667	.50
O	8	.00000000	.50000000	.50
O	8	.25000000	.50000000	.75
O	8	.50000000	.50000000	.50
O	8	.75000000	.50000000	.75
Al	13	.08333333	.04166667	.75
Al	13	.58333333	.04166667	.25
Al	13	.83333333	.04166667	.00
Al	13	.83333333	.10416667	.50
Al	13	.50000000	.12500000	.50
Al	13	.66666667	.14583333	.00
Al	13	.41666667	.20833333	.25
Al	13	.66666667	.20833333	.50
Al	13	.91666667	.20833333	.75
Al	13	.66666667	.27083333	.00
Al	13	.83333333	.29166667	.50
Al	13	.50000000	.31250000	.50
Al	13	.25000000	.37500000	.25
Al	13	.50000000	.37500000	.00
Al	13	.75000000	.37500000	.75
Al	13	.50000000	.43750000	.50
Al	13	.66666667	.45833333	.00
Al	13	.83333333	.47916667	.50
Al	13	.08333333	.54166667	.75
Al	13	.33333333	.54166667	.50
Al	13	.58333333	.54166667	.75
Al	13	.83333333	.54166667	.50
Al	13	.00000000	.62500000	.50
Al	13	.25000000	.62500000	.75
Al	13	.50000000	.62500000	.50
Al	13	.75000000	.62500000	.75
Al	13	.16666667	.70833333	.50
Al	13	.41666667	.70833333	.75
Al	13	.66666667	.70833333	.50
Al	13	.91666667	.70833333	.75
Al	13	.08333333	.79166667	.75
Al	13	.33333333	.79166667	.50

Al	13	.58333333	.79166667	.25
Al	13	.83333333	.79166667	.00
Al	13	.00000000	.87500000	.00
Al	13	.25000000	.87500000	.25
Al	13	.50000000	.87500000	.00
Al	13	.75000000	.87500000	.25
Al	13	.16666667	.95833333	.00
Al	13	.41666667	.95833333	.25
Al	13	.66666667	.95833333	.00
Al	13	.91666667	.95833333	.25

Al	13	.58333333	.79166667	.75
Al	13	.83333333	.79166667	.50
Al	13	.00000000	.87500000	.50
Al	13	.25000000	.87500000	.75
Al	13	.50000000	.87500000	.50
Al	13	.75000000	.87500000	.75
Al	13	.16666667	.95833333	.50
Al	13	.41666667	.95833333	.75
Al	13	.66666667	.95833333	.50
Al	13	.91666667	.95833333	.75

Al/Oxide Interface Model with Parallel Orientation

Based on Lock-In Model

A = 9.675484 B = 27.366403 C = 5.586144 Å

132 Atoms

O	8	.0000000	.0000000	.00
O	8	.2500000	.0000000	.75
O	8	.7500000	.0000000	.75
O	8	.2500000	.2500000	.75
O	8	.7500000	.2500000	.75
O	8	.4166667	.0833333	.75
O	8	.9166667	.0833333	.75
O	8	.4166667	.3333333	.75
O	8	.9166667	.3333333	.75
O	8	.3333333	.1666667	.50
O	8	.5000000	.0000000	.00
O	8	.0000000	.2500000	.00
O	8	.5000000	.2500000	.00
O	8	.1666667	.0833333	.00
O	8	.6666667	.0833333	.00
O	8	.1666667	.3333333	.00
O	8	.6666667	.3333333	.00
O	8	.0833333	.1666667	.25
O	8	.5833333	.1666667	.25
O	8	.8333333	.1666667	.50
O	8	.0833333	.4166667	.75
O	8	.0833333	.4166667	.25
O	8	.5833333	.4166667	.25
O	8	.8333333	.4166667	.00
Al	13	.0833333	.0416667	.25
Al	13	.5833333	.0416667	.25
Al	13	.3333333	.0416667	.50

O	8	.0000000	.0000000	.50
O	8	.5000000	.0000000	.50
O	8	.0000000	.2500000	.50
O	8	.5000000	.2500000	.50
O	8	.1666667	.0833333	.50
O	8	.6666667	.0833333	.50
O	8	.1666667	.3333333	.50
O	8	.6666667	.3333333	.50
O	8	.0833333	.1666667	.75
O	8	.2500000	.0000000	.25
O	8	.7500000	.0000000	.25
O	8	.2500000	.2500000	.25
O	8	.7500000	.2500000	.25
O	8	.4166667	.0833333	.25
O	8	.9166667	.0833333	.25
O	8	.4166667	.3333333	.25
O	8	.9166667	.3333333	.25
O	8	.3333333	.1666667	.00
O	8	.5833333	.1666667	.75
O	8	.8333333	.1666667	.00
O	8	.3333333	.4166667	.50
O	8	.3333333	.4166667	.00
O	8	.5833333	.4166667	.75
O	8	.8333333	.4166667	.50
Al	13	.0833333	.0416667	.75
Al	13	.5833333	.0416667	.75
Al	13	.8333333	.0416667	.00

Al	13	.3333333	.1041667	.00
Al	13	.0000000	.1250000	.00
Al	13	.1666667	.1458333	.50
Al	13	.1666667	.2083333	.00
Al	13	.4166667	.2083333	.75
Al	13	.9166667	.2083333	.25
Al	13	.1666667	.2708333	.50
Al	13	.3333333	.2916667	.00
Al	13	.0000000	.3125000	.00
Al	13	.0000000	.3750000	.50
Al	13	.2500000	.3750000	.75
Al	13	.7500000	.3750000	.25
Al	13	.0000000	.4375000	.00
Al	13	.1666667	.4583333	.50
Al	13	.3333333	.4791667	.00
O	8	.0000000	.5000000	.00
O	8	.2500000	.5000000	.75
O	8	.7500000	.5000000	.75
Al	13	.2500000	.7500000	.75
Al	13	.7500000	.7500000	.75
Al	13	.4166667	.5833333	.75
Al	13	.9166667	.5833333	.75
Al	13	.4166667	.8333333	.75
Al	13	.9166667	.8333333	.75
Al	13	.3333333	.6666667	.50
Al	13	.8333333	.6666667	.25
Al	13	.3333333	.9166667	.50
Al	13	.8333333	.9166667	.50
O	8	.5000000	.5000000	.00
Al	13	.0000000	.7500000	.00
Al	13	.5000000	.7500000	.00
Al	13	.1666667	.5833333	.00
Al	13	.6666667	.5833333	.00
Al	13	.1666667	.8333333	.00
Al	13	.6666667	.8333333	.00
Al	13	.0833333	.6666667	.25
Al	13	.5833333	.6666667	.25
Al	13	.0833333	.9166667	.25
Al	13	.5833333	.9166667	.25
Al	13	.8333333	.1041667	.50
Al	13	.5000000	.1250000	.50
Al	13	.6666667	.1458333	.00
Al	13	.4166667	.2083333	.25
Al	13	.6666667	.2083333	.50
Al	13	.9166667	.2083333	.75
Al	13	.6666667	.2708333	.00
Al	13	.8333333	.2916667	.50
Al	13	.5000000	.3125000	.50
Al	13	.2500000	.3750000	.25
Al	13	.5000000	.3750000	.00
Al	13	.7500000	.3750000	.75
Al	13	.5000000	.4375000	.50
Al	13	.6666667	.4583333	.00
Al	13	.8333333	.4791667	.50
O	8	.0000000	.5000000	.50
O	8	.5000000	.5000000	.50
Al	13	.0000000	.7500000	.50
Al	13	.5000000	.7500000	.50
Al	13	.1666667	.5833333	.50
Al	13	.6666667	.5833333	.50
Al	13	.1666667	.8333333	.50
Al	13	.6666667	.8333333	.50
Al	13	.0833333	.6666667	.75
Al	13	.5833333	.6666667	.75
Al	13	.0833333	.9166667	.75
Al	13	.5833333	.9166667	.75
O	8	.2500000	.5000000	.25
O	8	.7500000	.5000000	.25
Al	13	.2500000	.7500000	.25
Al	13	.7500000	.7500000	.25
Al	13	.4166667	.5833333	.25
Al	13	.9166667	.5833333	.25
Al	13	.4166667	.8333333	.25
Al	13	.9166667	.8333333	.25
Al	13	.3333333	.6666667	.00
Al	13	.8333333	.6666667	.00
Al	13	.3333333	.9166667	.00
Al	13	.8333333	.9166667	.00

Al/Oxide Interface Model with Twin Orientation

Starting with a Mixed Layer

A = 9.6754845 B = 27.366403 C = 5.5861436 Å

140 Atoms

O	8	.00000000	.00000000	.00	O	8	.00000000	.00000000	.50
O	8	.25000000	.00000000	.25	O	8	.25000000	.00000000	.25
O	8	.50000000	.00000000	.00	O	8	.50000000	.00000000	.50
O	8	.75000000	.00000000	.25	O	8	.75000000	.00000000	.75
O	8	.00000000	.75000000	.00	O	8	.00000000	.75000000	.50
O	8	.25000000	.75000000	.25	O	8	.25000000	.75000000	.75
O	8	.50000000	.75000000	.00	O	8	.50000000	.75000000	.50
O	8	.75000000	.75000000	.25	O	8	.75000000	.75000000	.75
O	8	.16666667	.91666667	.00	O	8	.16666667	.91666667	.50
O	8	.41666667	.91666667	.25	O	8	.41666667	.91666667	.75
O	8	.66666667	.91666667	.00	O	8	.66666667	.91666667	.50
O	8	.91666667	.91666667	.25	O	8	.91666667	.91666667	.75
O	8	.16666667	.66666667	.00	O	8	.16666667	.66666667	.50
O	8	.41666667	.66666667	.25	O	8	.41666667	.66666667	.75
O	8	.66666667	.66666667	.00	O	8	.66666667	.66666667	.50
O	8	.91666667	.66666667	.25	O	8	.91666667	.66666667	.75
O	8	.08333333	.83333333	.25	O	8	.08333333	.83333333	.75
O	8	.33333333	.83333333	.00	O	8	.33333333	.83333333	.50
O	8	.58333333	.83333333	.25	O	8	.58333333	.83333333	.75
O	8	.83333333	.83333333	.00	O	8	.83333333	.83333333	.50
O	8	.08333333	.58333333	.25	O	8	.08333333	.58333333	.75
O	8	.33333333	.58333333	.00	O	8	.33333333	.58333333	.50
O	8	.58333333	.58333333	.25	O	8	.58333333	.58333333	.75
O	8	.83333333	.58333333	.00	O	8	.83333333	.58333333	.50
O	8	.25000000	.50000000	.25	O	8	.25000000	.50000000	.75
O	8	.50000000	.50000000	.00	O	8	.50000000	.50000000	.50
O	8	.75000000	.50000000	.25	O	8	.75000000	.50000000	.75
Al	13	.08333333	.95833333	.25	Al	13	.08333333	.95833333	.75
Al	13	.33333333	.95833333	.50	Al	13	.58333333	.95833333	.25
Al	13	.58333333	.95833333	.75	Al	13	.83333333	.95833333	.00
Al	13	.33333333	.89583333	.00	Al	13	.83333333	.89583333	.50
Al	13	.00000000	.87500000	.00	Al	13	.50000000	.87500000	.50
Al	13	.16666667	.85416667	.50	Al	13	.66666667	.85416667	.00
Al	13	.16666667	.79166667	.00	Al	13	.41666667	.79166667	.25
Al	13	.41666667	.79166667	.75	Al	13	.66666667	.79166667	.50
Al	13	.91666667	.79166667	.25	Al	13	.91666667	.79166667	.75
Al	13	.16666667	.72916667	.50	Al	13	.66666667	.72916667	.00
Al	13	.33333333	.70833333	.00	Al	13	.83333333	.70833333	.50
Al	13	.00000000	.68750000	.00	Al	13	.50000000	.68750000	.50
Al	13	.00000000	.62500000	.50	Al	13	.25000000	.62500000	.25
Al	13	.25000000	.62500000	.75	Al	13	.50000000	.62500000	.00
Al	13	.75000000	.62500000	.25	Al	13	.75000000	.62500000	.75
Al	13	.00000000	.56250000	.00	Al	13	.50000000	.56250000	.50
Al	13	.16666667	.54166667	.50	Al	13	.66666667	.54166667	.00
Al	13	.33333333	.52083333	.00	Al	13	.83333333	.52083333	.50
Al	13	.08333333	.04166667	.25	Al	13	.08333333	.04166667	.75

Al	13	.33333333	.04166667	.50
Al	13	.58333333	.04166667	.75
Al	13	.33333333	.04166667	.00
Al	13	.00000000	.12500000	.00
Al	13	.00000000	.12500000	.50
Al	13	.25000000	.12500000	.75
Al	13	.75000000	.12500000	.25
Al	13	.16666667	.20833333	.00
Al	13	.41666667	.20833333	.75
Al	13	.91666667	.20833333	.25
Al	13	.16666667	.20833333	.50
Al	13	.33333333	.29166667	.00
Al	13	.08333333	.29166667	.25
Al	13	.33333333	.29166667	.50
Al	13	.58333333	.29166667	.75
Al	13	.00000000	.37500000	.50
Al	13	.25000000	.37500000	.75
Al	13	.75000000	.37500000	.25
Al	13	.00000000	.37500000	.00
Al	13	.16666667	.45833333	.50
Al	13	.16666667	.45833333	.00
Al	13	.41666667	.45833333	.75
Al	13	.91666667	.45833333	.25
Al	13	.58333333	.04166667	.25
Al	13	.83333333	.04166667	.00
Al	13	.83333333	.04166667	.50
Al	13	.50000000	.12500000	.50
Al	13	.25000000	.12500000	.25
Al	13	.50000000	.12500000	.00
Al	13	.75000000	.12500000	.75
Al	13	.41666667	.20833333	.25
Al	13	.66666667	.20833333	.50
Al	13	.91666667	.20833333	.75
Al	13	.66666667	.20833333	.00
Al	13	.83333333	.29166667	.50
Al	13	.08333333	.29166667	.75
Al	13	.58333333	.29166667	.25
Al	13	.83333333	.29166667	.00
Al	13	.25000000	.37500000	.25
Al	13	.50000000	.37500000	.00
Al	13	.75000000	.37500000	.75
Al	13	.50000000	.37500000	.50
Al	13	.66666667	.45833333	.00
Al	13	.41666667	.45833333	.25
Al	13	.66666667	.45833333	.50
Al	13	.91666667	.45833333	.75

Al/Oxide Interface Model with Twin Orientation

Starting with a Kagome Layer

A = 9.6754845 B = 27.366403 C = 5.5861436 Å

140 Atoms

O	8	.00000000	.00000000	.00
O	8	.25000000	.00000000	.25
O	8	.50000000	.00000000	.00
O	8	.75000000	.00000000	.25
O	8	.00000000	.50000000	.00
O	8	.25000000	.50000000	.25
O	8	.50000000	.50000000	.00
O	8	.75000000	.50000000	.25
Al	13	.08333333	.04166667	.25
Al	13	.33333333	.04166667	.50
Al	13	.58333333	.04166667	.75
Al	13	.33333333	.04166667	.00
Al	13	.00000000	.12500000	.00
Al	13	.00000000	.12500000	.50
O	8	.00000000	.00000000	.50
O	8	.25000000	.00000000	.25
O	8	.50000000	.00000000	.50
O	8	.75000000	.00000000	.75
O	8	.00000000	.50000000	.50
O	8	.25000000	.50000000	.75
O	8	.50000000	.50000000	.50
O	8	.75000000	.50000000	.75
Al	13	.08333333	.04166667	.75
Al	13	.58333333	.04166667	.25
Al	13	.83333333	.04166667	.00
Al	13	.83333333	.04166667	.50
Al	13	.50000000	.12500000	.50
Al	13	.25000000	.12500000	.25

Al	13	.25000000	.12500000	.75
Al	13	.75000000	.12500000	.25
Al	13	.16666667	.20833333	.00
Al	13	.41666667	.20833333	.75
Al	13	.91666667	.20833333	.25
Al	13	.16666667	.20833333	.50
Al	13	.33333333	.29166667	.00
Al	13	.08333333	.29166667	.25
Al	13	.33333333	.29166667	.50
Al	13	.58333333	.29166667	.75
Al	13	.00000000	.75000000	.50
Al	13	.25000000	.75000000	.75
Al	13	.75000000	.75000000	.25
Al	13	.00000000	.75000000	.00
Al	13	.16666667	.45833333	.50
Al	13	.16666667	.45833333	.00
Al	13	.41666667	.45833333	.75
Al	13	.91666667	.45833333	.25
O	8	.00000000	.75000000	.00
O	8	.25000000	.75000000	.25
O	8	.50000000	.75000000	.00
O	8	.75000000	.75000000	.25
O	8	.08333333	.58333333	.25
O	8	.33333333	.58333333	.00
O	8	.58333333	.58333333	.25
O	8	.83333333	.58333333	.00
O	8	.16666667	.66666667	.00
O	8	.41666667	.66666667	.25
O	8	.66666667	.66666667	.00
O	8	.91666667	.66666667	.25
O	8	.08333333	.83333333	.25
O	8	.33333333	.83333333	.00
O	8	.58333333	.83333333	.25
O	8	.83333333	.83333333	.00
O	8	.16666667	.91666667	.00
O	8	.41666667	.91666667	.25
O	8	.66666667	.91666667	.00
O	8	.91666667	.91666667	.25
Al	13	.16666667	.54166667	.00
Al	13	.41666667	.54166667	.75
Al	13	.91666667	.54166667	.25
Al	13	.16666667	.60416667	.50
Al	13	.00000000	.62500000	.00
Al	13	.33333333	.64583333	.00
Al	13	.08333333	.70833333	.25
Al	13	.33333333	.70833333	.50
Al	13	.58333333	.70833333	.75
Al	13	.33333333	.77083333	.00

Al	13	.50000000	.12500000	.00
Al	13	.75000000	.12500000	.75
Al	13	.41666667	.20833333	.25
Al	13	.66666667	.20833333	.50
Al	13	.91666667	.20833333	.75
Al	13	.66666667	.20833333	.00
Al	13	.83333333	.29166667	.50
Al	13	.08333333	.29166667	.75
Al	13	.58333333	.29166667	.25
Al	13	.83333333	.29166667	.00
Al	13	.25000000	.75000000	.25
Al	13	.50000000	.75000000	.00
Al	13	.75000000	.75000000	.75
Al	13	.50000000	.75000000	.50
Al	13	.66666667	.45833333	.00
Al	13	.41666667	.45833333	.25
Al	13	.66666667	.45833333	.50
Al	13	.91666667	.45833333	.75
O	8	.00000000	.75000000	.50
O	8	.25000000	.75000000	.75
O	8	.50000000	.75000000	.50
O	8	.75000000	.75000000	.75
O	8	.08333333	.58333333	.75
O	8	.33333333	.58333333	.50
O	8	.58333333	.58333333	.75
O	8	.83333333	.58333333	.50
O	8	.16666667	.66666667	.50
O	8	.41666667	.66666667	.75
O	8	.66666667	.66666667	.50
O	8	.91666667	.66666667	.75
O	8	.08333333	.83333333	.75
O	8	.33333333	.83333333	.50
O	8	.58333333	.83333333	.75
O	8	.83333333	.83333333	.50
O	8	.16666667	.91666667	.00
O	8	.41666667	.91666667	.75
O	8	.66666667	.91666667	.50
O	8	.91666667	.91666667	.75
Al	13	.41666667	.54166667	.25
Al	13	.66666667	.54166667	.50
Al	13	.91666667	.54166667	.75
Al	13	.66666667	.60416667	.00
Al	13	.50000000	.62500000	.50
Al	13	.83333333	.64583333	.50
Al	13	.08333333	.70833333	.75
Al	13	.58333333	.70833333	.25
Al	13	.83333333	.70833333	.00
Al	13	.83333333	.77083333	.50

Al	13	.16666667	.79166667	.50
Al	13	.00000000	.81250000	.00
Al	13	.00000000	.87500000	.50
Al	13	.25000000	.87500000	.75
Al	13	.75000000	.87500000	.25
Al	13	.00000000	.93750000	.00
Al	13	.33333333	.95833333	.00
Al	13	.16666667	.97916667	.50
Al	13	.66666667	.79166667	.00
Al	13	.50000000	.81250000	.50
Al	13	.25000000	.87500000	.25
Al	13	.50000000	.87500000	.00
Al	13	.75000000	.87500000	.75
Al	13	.50000000	.93750000	.50
Al	13	.83333333	.95833333	.50
Al	13	.66666667	.97916667	.00

A Twin Boundary Model in the Oxide

A = 9.6754845 B = 27.366403 C = 5.5861436 Å

168 Atoms

O	8	.00000000	.00000000	.00
O	8	.25000000	.00000000	.25
O	8	.50000000	.00000000	.00
O	8	.75000000	.00000000	.25
O	8	.00000000	.75000000	.00
O	8	.25000000	.75000000	.25
O	8	.50000000	.75000000	.00
O	8	.75000000	.75000000	.25
O	8	.16666667	.91666667	.00
O	8	.41666667	.91666667	.25
O	8	.66666667	.91666667	.00
O	8	.91666667	.91666667	.25
O	8	.16666667	.66666667	.00
O	8	.41666667	.66666667	.25
O	8	.66666667	.66666667	.00
O	8	.91666667	.66666667	.25
O	8	.08333333	.83333333	.25
O	8	.33333333	.83333333	.00
O	8	.58333333	.83333333	.25
O	8	.83333333	.83333333	.00
O	8	.08333333	.58333333	.25
O	8	.33333333	.58333333	.00
O	8	.58333333	.58333333	.25
O	8	.83333333	.58333333	.00
O	8	.00000000	.50000000	.00
O	8	.25000000	.50000000	.25
O	8	.50000000	.50000000	.00
O	8	.75000000	.50000000	.25
Al	13	.08333333	.95833333	.25
Al	13	.33333333	.95833333	.50
O	8	.00000000	.00000000	.50
O	8	.25000000	.00000000	.25
O	8	.50000000	.00000000	.50
O	8	.75000000	.00000000	.75
O	8	.00000000	.75000000	.50
O	8	.25000000	.75000000	.75
O	8	.50000000	.75000000	.50
O	8	.75000000	.75000000	.75
O	8	.16666667	.91666667	.50
O	8	.41666667	.91666667	.75
O	8	.66666667	.91666667	.50
O	8	.91666667	.91666667	.75
O	8	.16666667	.66666667	.50
O	8	.41666667	.66666667	.75
O	8	.66666667	.66666667	.50
O	8	.91666667	.66666667	.75
O	8	.08333333	.83333333	.75
O	8	.33333333	.83333333	.50
O	8	.58333333	.83333333	.75
O	8	.83333333	.83333333	.50
O	8	.08333333	.58333333	.75
O	8	.33333333	.58333333	.50
O	8	.58333333	.58333333	.75
O	8	.83333333	.58333333	.50
O	8	.00000000	.50000000	.50
O	8	.25000000	.50000000	.75
O	8	.50000000	.50000000	.50
O	8	.75000000	.50000000	.75
Al	13	.08333333	.95833333	.75
Al	13	.58333333	.95833333	.25

Al	13	.58333333	.95833333	.75
Al	13	.33333333	.89583333	.00
Al	13	.00000000	.87500000	.00
Al	13	.16666667	.85416667	.50
Al	13	.16666667	.79166667	.00
Al	13	.41666667	.79166667	.75
Al	13	.91666667	.79166667	.25
Al	13	.16666667	.72916667	.50
Al	13	.33333333	.70833333	.00
Al	13	.00000000	.68750000	.00
Al	13	.00000000	.62500000	.50
Al	13	.25000000	.62500000	.75
Al	13	.75000000	.62500000	.25
Al	13	.00000000	.56250000	.00
Al	13	.16666667	.54166667	.50
Al	13	.33333333	.52083333	.00
O	8	.00000000	.25000000	.00
O	8	.25000000	.25000000	.25
O	8	.50000000	.25000000	.00
O	8	.75000000	.25000000	.25
O	8	.08333333	.41666667	.25
O	8	.33333333	.41666667	.00
O	8	.58333333	.41666667	.25
O	8	.83333333	.41666667	.00
O	8	.16666667	.33333333	.00
O	8	.41666667	.33333333	.25
O	8	.66666667	.33333333	.00
O	8	.91666667	.33333333	.25
O	8	.08333333	.16666667	.25
O	8	.33333333	.16666667	.00
O	8	.58333333	.16666667	.25
O	8	.83333333	.16666667	.00
O	8	.16666667	.08333333	.00
O	8	.41666667	.08333333	.25
O	8	.66666667	.08333333	.00
O	8	.91666667	.08333333	.25
Al	13	.16666667	.45833333	.00
Al	13	.41666667	.45833333	.75
Al	13	.91666667	.45833333	.25
Al	13	.16666667	.39583333	.50
Al	13	.00000000	.37500000	.00
Al	13	.33333333	.35416667	.00
Al	13	.08333333	.29166667	.25
Al	13	.33333333	.29166667	.50
Al	13	.58333333	.29166667	.75
Al	13	.33333333	.22916667	.00
Al	13	.16666667	.20833333	.50
Al	13	.00000000	.18750000	.00

Al	13	.83333333	.95833333	.00
Al	13	.83333333	.89583333	.50
Al	13	.50000000	.87500000	.50
Al	13	.66666667	.85416667	.00
Al	13	.41666667	.79166667	.25
Al	13	.66666667	.79166667	.50
Al	13	.91666667	.79166667	.75
Al	13	.66666667	.72916667	.00
Al	13	.83333333	.70833333	.50
Al	13	.50000000	.68750000	.50
Al	13	.25000000	.62500000	.25
Al	13	.50000000	.62500000	.00
Al	13	.75000000	.62500000	.75
Al	13	.50000000	.56250000	.50
Al	13	.66666667	.54166667	.00
Al	13	.83333333	.52083333	.50
O	8	.00000000	.25000000	.50
O	8	.25000000	.25000000	.75
O	8	.50000000	.25000000	.50
O	8	.75000000	.25000000	.75
O	8	.08333333	.41666667	.75
O	8	.33333333	.41666667	.50
O	8	.58333333	.41666667	.75
O	8	.83333333	.41666667	.50
O	8	.16666667	.33333333	.50
O	8	.41666667	.33333333	.75
O	8	.66666667	.33333333	.50
O	8	.91666667	.33333333	.75
O	8	.08333333	.16666667	.75
O	8	.33333333	.16666667	.50
O	8	.58333333	.16666667	.75
O	8	.83333333	.16666667	.50
O	8	.16666667	.08333333	.00
O	8	.41666667	.08333333	.75
O	8	.66666667	.08333333	.50
O	8	.91666667	.08333333	.75
Al	13	.41666667	.45833333	.25
Al	13	.66666667	.45833333	.50
Al	13	.91666667	.45833333	.75
Al	13	.66666667	.39583333	.00
Al	13	.50000000	.37500000	.50
Al	13	.83333333	.35416667	.50
Al	13	.08333333	.29166667	.75
Al	13	.58333333	.29166667	.25
Al	13	.83333333	.29166667	.00
Al	13	.83333333	.22916667	.50
Al	13	.66666667	.20833333	.00
Al	13	.50000000	.18750000	.50

Al	13	.00000000	.12500000	.50	Al	13	.25000000	.12500000	.25
Al	13	.25000000	.12500000	.75	Al	13	.50000000	.12500000	.00
Al	13	.75000000	.12500000	.25	Al	13	.75000000	.12500000	.75
Al	13	.00000000	.06250000	.00	Al	13	.50000000	.06250000	.50
Al	13	.33333333	.04166667	.00	Al	13	.83333333	.04166667	.50
Al	13	.16666667	.02083333	.50	Al	13	.66666667	.02083333	.00

Additional Twin Boundary Model in the Oxide

A = 9.6754845 B = 27.366403 C = 5.5861436 Å

168 Atoms

O	8	.00000000	.00000000	.00	O	8	.00000000	.00000000	.50
O	8	.25000000	.00000000	.25	O	8	.25000000	.00000000	.25
O	8	.50000000	.00000000	.00	O	8	.50000000	.00000000	.50
O	8	.75000000	.00000000	.25	O	8	.75000000	.00000000	.75
O	8	.00000000	.25000000	.00	O	8	.00000000	.25000000	.50
O	8	.25000000	.25000000	.25	O	8	.25000000	.25000000	.75
O	8	.50000000	.25000000	.00	O	8	.50000000	.25000000	.50
O	8	.75000000	.25000000	.25	O	8	.75000000	.25000000	.75
O	8	.16666667	.08333333	.00	O	8	.16666667	.08333333	.50
O	8	.41666667	.08333333	.25	O	8	.41666667	.08333333	.75
O	8	.66666667	.08333333	.00	O	8	.66666667	.08333333	.50
O	8	.91666667	.08333333	.25	O	8	.91666667	.08333333	.75
O	8	.16666667	.33333333	.00	O	8	.16666667	.33333333	.50
O	8	.41666667	.33333333	.25	O	8	.41666667	.33333333	.75
O	8	.66666667	.33333333	.00	O	8	.66666667	.33333333	.50
O	8	.91666667	.33333333	.25	O	8	.91666667	.33333333	.75
O	8	.08333333	.16666667	.25	O	8	.08333333	.16666667	.75
O	8	.33333333	.16666667	.00	O	8	.33333333	.16666667	.50
O	8	.58333333	.16666667	.25	O	8	.58333333	.16666667	.75
O	8	.83333333	.16666667	.00	O	8	.83333333	.16666667	.50
O	8	.08333333	.41666667	.25	O	8	.08333333	.41666667	.75
O	8	.33333333	.41666667	.00	O	8	.33333333	.41666667	.50
O	8	.58333333	.41666667	.25	O	8	.58333333	.41666667	.75
O	8	.83333333	.41666667	.00	O	8	.83333333	.41666667	.50
O	8	.00000000	.50000000	.00	O	8	.00000000	.50000000	.50
O	8	.25000000	.50000000	.25	O	8	.25000000	.50000000	.75
O	8	.50000000	.50000000	.00	O	8	.50000000	.50000000	.50
O	8	.75000000	.50000000	.25	O	8	.75000000	.50000000	.75
Al	13	.08333333	.04166667	.25	Al	13	.08333333	.04166667	.75
Al	13	.33333333	.04166667	.50	Al	13	.58333333	.04166667	.25
Al	13	.58333333	.04166667	.75	Al	13	.83333333	.04166667	.00
Al	13	.33333333	.10416667	.00	Al	13	.83333333	.10416667	.50
Al	13	.00000000	.12500000	.00	Al	13	.50000000	.12500000	.50

Al	13	.16666667	.14583333	.50
Al	13	.16666667	.20833333	.00
Al	13	.41666667	.20833333	.75
Al	13	.91666667	.20833333	.25
Al	13	.16666667	.27083333	.50
Al	13	.33333333	.29166667	.00
Al	13	.00000000	.31250000	.00
Al	13	.00000000	.37500000	.50
Al	13	.25000000	.37500000	.75
Al	13	.75000000	.37500000	.25
Al	13	.00000000	.43750000	.00
Al	13	.16666667	.45833333	.50
Al	13	.33333333	.47916667	.00
O	8	.00000000	.75000000	.00
O	8	.25000000	.75000000	.25
O	8	.50000000	.75000000	.00
O	8	.75000000	.75000000	.25
O	8	.08333333	.58333333	.25
O	8	.33333333	.58333333	.00
O	8	.58333333	.58333333	.25
O	8	.83333333	.58333333	.00
O	8	.16666667	.66666667	.00
O	8	.41666667	.66666667	.25
O	8	.66666667	.66666667	.00
O	8	.91666667	.66666667	.25
O	8	.08333333	.83333333	.25
O	8	.33333333	.83333333	.00
O	8	.58333333	.83333333	.25
O	8	.83333333	.83333333	.00
O	8	.16666667	.91666667	.00
O	8	.41666667	.91666667	.25
O	8	.66666667	.91666667	.00
O	8	.91666667	.91666667	.25
Al	13	.16666667	.54166667	.00
Al	13	.41666667	.54166667	.75
Al	13	.91666667	.54166667	.25
Al	13	.16666667	.60416667	.50
Al	13	.00000000	.62500000	.00
Al	13	.33333333	.64583333	.00
Al	13	.08333333	.70833333	.25
Al	13	.33333333	.70833333	.50
Al	13	.58333333	.70833333	.75
Al	13	.33333333	.77083333	.00
Al	13	.16666667	.79166667	.50
Al	13	.00000000	.81250000	.00
Al	13	.00000000	.87500000	.50
Al	13	.25000000	.87500000	.75
Al	13	.75000000	.87500000	.25

Al	13	.66666667	.14583333	.00
Al	13	.41666667	.20833333	.25
Al	13	.66666667	.20833333	.50
Al	13	.91666667	.20833333	.75
Al	13	.66666667	.27083333	.00
Al	13	.83333333	.29166667	.50
Al	13	.50000000	.31250000	.50
Al	13	.25000000	.37500000	.25
Al	13	.50000000	.37500000	.00
Al	13	.75000000	.37500000	.75
Al	13	.50000000	.43750000	.50
Al	13	.66666667	.45833333	.00
Al	13	.83333333	.47916667	.50
O	8	.00000000	.75000000	.50
O	8	.25000000	.75000000	.75
O	8	.50000000	.75000000	.50
O	8	.75000000	.75000000	.75
O	8	.08333333	.58333333	.75
O	8	.33333333	.58333333	.50
O	8	.58333333	.58333333	.75
O	8	.83333333	.58333333	.50
O	8	.16666667	.66666667	.50
O	8	.41666667	.66666667	.75
O	8	.66666667	.66666667	.50
O	8	.91666667	.66666667	.75
O	8	.08333333	.83333333	.75
O	8	.33333333	.83333333	.50
O	8	.58333333	.83333333	.75
O	8	.83333333	.83333333	.50
O	8	.16666667	.91666667	.00
O	8	.41666667	.91666667	.75
O	8	.66666667	.91666667	.50
O	8	.91666667	.91666667	.75
Al	13	.41666667	.54166667	.25
Al	13	.66666667	.54166667	.50
Al	13	.91666667	.54166667	.75
Al	13	.66666667	.60416667	.00
Al	13	.50000000	.62500000	.50
Al	13	.83333333	.64583333	.50
Al	13	.08333333	.70833333	.75
Al	13	.58333333	.70833333	.25
Al	13	.83333333	.70833333	.00
Al	13	.83333333	.77083333	.50
Al	13	.66666667	.79166667	.00
Al	13	.50000000	.81250000	.50
Al	13	.25000000	.87500000	.25
Al	13	.50000000	.87500000	.00
Al	13	.75000000	.87500000	.75

Al	13	.00000000	.93750000	.00
Al	13	.33333333	.95833333	.00
Al	13	.16666667	.97916667	.50
Al	13	.50000000	.93750000	.50
Al	13	.83333333	.95833333	.50
Al	13	.66666667	.97916667	.00

REFERENCES

1. L.W. Hobbs and T.E. Mitchell, in *High Temperature Corrosion,* ed. by R.A. Rapp, NACE, Houston, 76 (1983).
2. R. Gronsky, in *38th Ann. Proc. Electron Microscopy Soc. Amer.,* ed. by G.W. Baily, San Francisco Press, San Francisco, CA, 2 (1980).
3 M.S. Hunter and P. Fowle, *J. Electrochem. Soc.,* **103**, 482 (1956).
4. K. Thomas and M.W. Roberts, *J. Appl. Phys.,* **32**, 70 (1961).
5. P.E. Doherty and R.S. Davis, *J. Appl. Phys.,* **34**, 619 (1963).
6. M.J. Dignam, *J. Electrochem. Soc.,* **109**, 184 (1962).
7. J.J. Randall, Jr. and W.J. Bernard, *J. Appl. Phys.,* **35**, 1317 (1964).
8. R.S. Goodrich, Jr. and G.S. Ansell, *Trans. Met. Soc. AIME,* **230**, 1372 (1964).
9. M.A. Heine and P.R. Sperry, *J. Electrochem. Soc.,* **112**, 359 (1965).
10. R. Natesh and G.S. Ansell, *Acta Met.,* **14**, 1735 (1966).
11. E. Suito, M. Shiojiri and H. Morigawa, *Japan. J. Appl. Phys.,* **5**, 1197 (1966).
12. A.F. Beck, M.A. Heine, E.J. Caule and M.J. Pryor, *Corros. Sci.,* **7**, 1 (1967).
13. H.A. Francis, *J. Appl. Phys.,* **38**, 715 (1967).
14. R.K. Hart and J.K. Maurin, *Surf. Sci.,* **20**, 285 (1970).
15. A.J. Brock, *J. Electrochem. Soc.,* **117**, 549 (1970).
16. A.J. Brock and M.A. Heine, *J. Electrochem. Soc.,* **119**, 1124 (1972).
17. C.A. Grove, G. Judd and G.S. Ansell, *J. Materials Sci.,* **7**, 393 (1972).
18. A.J. Brock and M.J. Pryor, *Corros. Sci.,* **13**, 199(1973).

19. G.M. Scamans and E.P. Butler, *Metall. Trans. A*, **6A**, 2055 (1975).

20. P.S. Corkish, Ph.D. Thesis, University of Liverpool (1976).

21. A. Csanady, A. Barna and P.B. Barna, *Oxid. Met.*, **13**, 245 (1979).

22. K. Shinohara, H. Kyogoku, T. Seo and K. Kumoda, *Memoirs of the Ehime University, Sec. III,* **9**, 157 (1981).

23. K. Shinohara, H. Kyogoku, K. Kumoda and T. Seo, *Memoirs of the Ehime University, Sec. III,* **9**, 165 (1980).

24. A. Csanady and J. Kurthy, *J. Materials Sci.*, **16**, 2919 (1981).

25 A.J. Brock, G.R. Irani and M.J. Pryor, *Oxid. Met.*, **15**, 77 (1981).

26 K. Wefers, *Aluminum*, **57**, 722 (1981).

27. J.Y. Lee, in *43rd Ann. Proc. Electron Microscopy Soc. Amer.*, ed. by G.W. Baily, San Francisco Press, San Francisco, CA, 268 (1985).

28. G.C. Weatherly, *Acta Met.*, **19**, 181 (1971).

29. V.L.K. Lou, T.E. Mitchell and A.H. Heuer, *J. Am. Ceram. Soc.*, **68**, 49 (1985).

30. A.W. Searcy, in *Chemical and Mechanical Properties of Inorganic Materials,* ed. by A.W. Searcy, D.V. Ragone and U. Colombo, Wiley-Interscience, New York, 15 (1970).

31. D.R. Stall and H. Prophet, *JANAF Thermochemical Tables,* Second Edition, NSRDS-NBS 37, National Bureau of Standards (1971).

32. G.L. Hunt and I.M. Ritche, *Oxid. Met.*, **2**, 361 (1971).

33. M.H. Deville, *De l'Aluminium*, Mallet-Bachelier, Paris (1859).

34. J.W. Richards, *Aluminium*, 2nd Edition, Sampson, Low, Marston, Searle and Rivington Ltd. (1890).

35. W.H.J. Vernon, *Trans. Faraday Soc.*, **23**, 152 (1927).

36. R.K. Hart, *Proc. Roy. Soc.*, **A236**, 68 (1956).

37. D.D. Eley and P.R. Wilkinson, *Proc. Roy. Soc.*, **A254**, 327 (1960).

38. N.F. Mott, *Trans. Faraday Soc.*, **39**, 472 (1940).

39. N.F. Mott, *Trans. Faraday Soc.*, **35**, 1175 (1939).

40. M.A.H. Lanyon and B.M. Trapnell, *Proc. Roy. Soc.*, **227**, 387 (1954-55).

41. D.D. Eley and P.R. Wilkinson, *Structure and Properties of Thin Films*, ed. by C.A. Neugebauer, J.B. Newkirk and D.A. Vermilyea, John Wiley & Sons, New York, 508 (1959).

42. E.E. Huber, Jr. and C.T. Kirk, Jr., *Surf. Sci.*, **5**, 447 (1966).

43. C.T. Kirk, Jr. and E.E. Huber, Jr., *Surf. Sci.*, **9**, 217 (1968).

44. A. Bianconi, R.Z. Bachrach, S.B.M. Hagstrom and S.A. Flodstrom, *Phys. Rev.* **19**, 2837 (1979).

45. D. Norman, S. Brennan, R. Jaeger and J. Stohr, *Surf. Sci.*, **105**, L297 (1981).

46. N.B. Pilling and R.W. Bedworth, *J. Inst. Metals*, **29**, 529 (1923).

47. W.W. Smeltzer, *J. Electrochem. Soc.*, **103**, 209 (1956).

48. E.A. Gulbransen and W.S. Wysong, *J. Phys. Colloid. Chem.*, **57**, 1087 (1947).

49. D.W. Alymore, S.J. Gregg and W.B. Jepson, *J. Inst. Metals*, **88**, 205 (1959-1960).

50. C.N. Cochran and W.C. Sleepy, *J. Electrochem. Soc.*, **108**, 322 (1961).

51. M.J. Dignam and W.R. Fawcett, *J. Electrochem. Soc.*, **133**, 663 (1966).

52. N. Cabrera and N.F. Mott, *Rep. Prog. Physics*, **12**, 163 (1949).

53. M.J. Dignam, W.R. Fawcett and H. Bohni, *J. Electrochem. Soc.*, **113**, 656 (1966).

54. H. Raether, *Acad. Sci., Paris,* **227**, 1247 (1948).

55. R.O. Steiner, Ph.D. Thesis, University of London (1953).

56. E.J.W. Verwey, *J. Chem. Phys.,* **3**, 592 (1935).

57. E.J.W. Verwey, *Z. Kristallogr.,* **91**, 65 (1935).

58. G.D. Preston and L.L. Bircumshaw, *Phil. Mag.,* **22**, 654 (1936).

59. E. Belwe, *Z. Phys.,* **100**, 192 (1936).

60. H.G.F. Wilsdorf, *Nature, Lond.,* **168**, 600 (1951).

61. R.A. Harrington and H.R. Nelson, *Trans. AIME,* **137**, 62 (1940).

62. L. de Brouckère, *J. Inst. Metals,* **71**, 131 (1945).

63. G. Hass, *Optik,* **1**, 134 (1946).

64. J.M. Cowley, *Acta Cryst.,* **6**, 53 (1953).

65. D. Tucker, E.A. Kenik and J. Hren, in *41th Ann. Proc. Electron Microscopy Soc. Amer.,* ed. by G.W. Baily, San Francisco Press, San Francisco, CA, 76 (1983).

66. L. Brewer, in *Electronic Structure and Alloy Chemistry of Transitions Elements,* ed. by P.A. Beck, Interscience Pub., New York, 132 (1963).

67. T.V. Shchegoleva, *Phy. Met. Metall.,* **55**, 59 (1983).

68. Y.A. Bagaryatskiy, *Phy. Met. Metall.,* **1**, 316 (1955).

69. H.A. Wriedt, *Bull. Alloy Phase Diagrams,* **6**, 548 (1985).

70. H. Yanagida and F.A. Kröger, *J. Am. Ceram. Soc.,* **51**, 700 (1968).

71. K.G. Lynn, *Appl. Phys. Lett.,* **44**, 1330 (1980).

72. M. Van Lancker, *Metallurgy of Aluminum Alloys,* John Wiley & Sons, New York, 1 (1967).

73. M.W. Chase, Jr., J.L. Curnett, R.A. McDonaldo and A.N. Syverud, *JANAF Thermochemical Tables, 1978 Supplement,* J. Phys. Chem. Ref. Data, **7**, 793 (1978).

74. K.J. Morrissey, K.K. Czanderna, R.P. Merrill and C.B. Carter, *Ultramicroscopy,* **18**, 379 (1985).

75. B.C. Lippens and J.H. Boer, *Acta Cryst.,* **17**, 1312 (1964).

76. H. Dexpert, J.F. Larue, I. Mutin, B. Moraweck, Y. Bertaud and A. Renouprez, *J. Met.,* **37**, 17 (1985).

77. S.J. Wilson, *J. Solid State Chem.,* **30**, 247 (1979).

78. A.L. Dragoo and J.J. Diamond, *J. Am. Ceram. Soc.,* **50**, 568 (1967).

79. G.W. Morey, *Bull. Am. Ceram. Soc.,* **13**, 79 (1934).

80. J.M. Cowley, *Acta Cryst.,* **6**, 846 (1953).

81. L.P. Fehlner and N.F. Mott, *Oxid. Met.,* **2**, 59 (1970).

82. M.J. Pryor, *Oxid. Met.,* **3**, 523 (1971).

83. S.M. El-Mashri, A.J. Forty, L.A. Freeman and D.J. Smith, *Inst. Phys. Conf. Ser. No. 61,* Institute of Physics, Cambridge, 395 (1981).

84. G.I. Galkin, V.V. Chernyshev and N.E. Markova, *Zashchita Metallov.,* **6**, 209 (1970).

85. L. Pauling, *The Nature of Chemical Bond,* Cornell Univ. Press, Ithaca, New York (1960).

86. S.J. Wilson, *Proc. Brit. Ceram. Soc.,* **69**, 85 (1970).

87. H. Saalfeld, *Clay Min. Bull.,* **3**, 249 (1958).

88. A.J. Leonard, F. Van Cauwelaert and J.J. Fripiat, *J. Phys. Chem.,* **71**, 695 (1967).

89. M. Hansen and K. Anderko, *Constitution of Binary Alloys,* McGraw-Hill, New York (1958).

90. G. Yamaguchi, *Bull. Chem. Soc. Japan,* **43**, 1478 (1970).

91. K.J.D. Mackenzie, *J. Br. Ceram. Soc.,* **5**, 183 (1968).

92. M. Hoch and H.L. Johnston, *J. Am. Chem. Soc.,* **76**, 2560 (1954).

93. S. Yamaguchi, *J. Appl. Phys.,* **45**, 3207 (1974).

94. J.G.A. Rhodin, *Trans. Faraday Soc.,* **14**, 134 (1919).

95. N.E. Filonenko, I.V. Lavrov, O.V. Andreeva and R.L. Pevzner, *Dokl. Akad. Nauk SSSR,* **115**, 583 (1957).

96. V.E. Shevtsov, *Izv. Akad. Nauk SSSR, Met.,* **1**, 60 (1981).

97. P.B. Hirth, J. Silcox, R.E. Smallman and K.H. Westmacott, *Phil. Mag.,* **3**, 897 (1958).

98. F.J. Bradshaw and S. Pearson, *Phil. Mag.,* **2**, 570 (1957).

99. G. Thomas, *J. Inst. Metals,* **90**, 57 (1961-62).

100. M. Kiritani, *J. Phys. Soc. Japan,* **19**, 618 (1964).

101. G. Saada, *Acta Met.,* **10**, 551 (1962).

102. G. Das and J. Washburn, *Appl. Phys. Lett.,* **5**, 151 (1964).

103. J. Washburn, in *An Atomistic Approach to the Nature and Properties of Materials,* ed. by J.A. Pask, John Wiley & Sons, New York, 119 (1967).

104. S. Iida, *J. Phys. Soc. Japan,* **12**, 222 (1957).

105. K.C. Radford and C.W.A. Newey, *Proc. Brit. Ceram. Soc.,* No. 9, 131 (1967).

106. G. Welsch, L. Hwang, A.H. Heuer and T.E. Mitchell, *Phil. Mag.,* **29**, 1371 (1974).

107. J. Hornstra, *J. Phys. Chem. Solids,* **15**, 311 (1960).

108. J. Hornstra, *Proc. 4th Intern. Symposium on Reactivity of Solids,* Elsevier, Amsterdam, 563 (1961).

109. M.L. Kronberg, *Acta Met.,* **5**, 507 (1957).

110. P. Veyssière, J. Rabier and J. Grilhè, *Phys. Stat. Sol. (A),* **31**, 605 (1975).

111. J. Rabier, P. Veyssière and J. Grilhè, *J. Physique Colloq.,* **C9**, 373 (1973).

112. J. Hornstra, *Materials Science Research,* Vol. 1, Plenum Press, New York, 88 (1962).

113. N. Doukhan and B. Escaig, *J. Physique,* **35**, L-181 (1974).

114. P.B. Braun, *Philips Res. Rep.,* **12**, 491 (1957).

115. H. Tabata, H. Okuda and E. Ishii, *Japan. J. Appl. Phys.,* **12**, 7 (1973).

116. O. Van der Biest and G. Thomas, *Phys. Stat. Sol. (A),* **24**, 65 (1974).

117. M.H. Lewis, *Phil. Mag.,* **14**, 1003 (1966).

118. M.H. Lewis, *Phil. Mag.,* **14**, 605 (1968).

119. A. Grün, *Neues Jahrbuch für* Mineralogie, 99 (1918).

120. K.A. Jackson, *Liquid Metals and Solidification,* American Society for Metals, Cleveland, Ohio, 174 (1958).

121. R.D. Gretz, *Vapor Deposition,* ed. by C.F. Powell *et al.* , John Wiley, New York, 149 (1966).

122. J. Stringer, *Met. Reviews,* **11**, 113 (1966).

123. J. Stringer, *Corros. Sci.,* **10**, 513 (1970).

124. P.D. Dankov and P.V. Churaev, *Doklady Akad. Nauk S.S.S.R.,* **73**, 1221 (1950).

125. K.H.G. Ashbee and R.E. Smallman, *Proc. Roy. Soc.,* **A274**, 195 (1963).

126. G.A. Chadwick and D.A. Smith (eds.), *Grain Boundary Structure and Properties,* Academic Press, New York (1976).

127. R.W. Balluffi (ed.), *Materials Science Semin. on Grain Boundary Structure and Kinetics,* Milwaukee, WI, September 15-16, 1979, American Society for Metals, Metals Park, OH (1980).

128. H. Gleiter, *Mat. Sci. Eng.,* **52**, 91 (1952).

129. H. Gleiter, *Korngrenzen in Metalliischen Werkstoffen,* Gebüder Bornträger, Berlin, 18 (1977).

130. M. Rühle, *J. Phys. Coll. C6,* **43**, 115 (1982).

131. G.I. Tayler, *Proc. R. Soc. London, Ser. A,* **145**, 388 (1934).

132. J.M. Burgers, *Proc. Phys. Soc., London,* **52**, 23 (1940).

133. W.L. Bragg, *Proc. Phys. Soc., London,* **52**, 54 (1940).

134. W.T. Read and W. Shockley, *Phys. Rev.,* **78**, 275 (1950).

135. J.C.M. Li, *J. Appl. Phys.,* **32**, 525 (1961).

136. G. Friedel, *Lecons de Cristallographie,* Berger Levrault, Paris (1926).

137. S. Ranganathan, *Acta Cryst.,* **21**, 197 (1966).

138. D.G. Brandon, B. Ralph, S. Ranganathan and M.S. Wald, *Acta Met.,* **12**, 813 (1964).

139. G.H. Bishop and B. Chalmers, *Scr. Met.,* **2**, 133 (1968).

140. C.P. Sun and R.W. Balluffi, *Phil. Mag.*, **32**, 4962 (1982).

141. W. Bollman, *Crystal Defects and Crystalline Interfaces*, Springer, New York (1970).

142. D.A. Smith and R.C. Pond, *Int. Met. Rev.*, **205**, 61 (1976).

143. B. Pieraggi, in *Character of Grain Boundaries, Adv. in Ceramics*, ed. by M.F. Yan and A.H. Heuer, Vol. 6, 117 (1983).

144. P.H. Pumphrey, *Scr. Met.*, **6**, 107 (1972).

145. P.H. Pumphrey, *Scr. Met.*, **7**, 893 (1973).

146. H.J. Fecht and H. Gleiter, *Acta Met.*, **33**, 557 (1985).

147. H.J. Fecht, W. Lojkowski and H. Gleiter, *J. Physique Colloq.*, **C4**, 107 (1985).

148. M.F. Ashby, F. Spaepen and S. Williams, *Acta Met.*, **26**, 1647 (1978).

149. M. Weins, B. Chalmers, H. Gleiter and M.F. Ashby, *Scr. Met.*, **42**, 601 (1969).

150. L. Reimer, *Transmission Electron Microscopy*, Springer-Verlag, New York (1984).

151. K.J. Hanszen, in *Image Processing and Computer-Aided Design in Electron Optics*, ed. by P.W. Hawkes, Academic, London, 16 (1973).

152. K.J. Hanszen, *Z. Angew. Phys.*, **27**, 125 (1969).

153. K.J. Hanszen, in *Advances in Optical and Electron Microscopy*, Vol. 4, ed. by R. Barer and V.E. Cosslett, Academic, London, 1 (1971).

154. P.W. Hawkes, in *Advances in Optical and Electron Microscopy*, Vol. 7, ed. by R. Barer and V.E. Cosslett, Academic, London, 101 (1971).

155. O. Scherzer, *J. Appl. Phys.*, **20**, 20 (1949).

156. M.A. O'Keefe, in *Electron Optical Systems*, SEM Inc., AMF O'Hare (Chicago), 209 (1985).

157. J. Frank, *Optik,* **38**, 519 (1973).

158. K.J. Hanszen and L. Trepte, *Optik,* **32**, 519 (1971).

159. R.H. Wade and J. Frank, *Optik,* **48**, 81 (1977).

160. J.C.H. Spence, *Experimental High-Resolution Electron Microscopy,* Clarendon Press, Oxford, 86 (1981).

161. P. Goodman and A.F. Moodie, *Acta Cryst.;* **A30**, 280 (1974).

162. J.C. Bravman and R. Sinclair, *J. Electron Microscopy Technique,* **1**, 53 (1984).

163. M. Tinker and P.A. Labun, *Oxid. Met.,* **18**, 27 (1982).

164. R. Gronsky, in *Treatise on Materials Science and Technology: Experimental Techniques, 19B,* Academic Press, New York, 325 (1983).

165. R. Kilaas, Ph.D. Thesis, University of California, Berkeley, LBL-19058 (1985).

166. M.A. O'Keefe, P.R. Buseck and S. Iijima, *Nature,* **274** (5669), 322 (1978).

167. J.C.H. Spence, *Notes Accompanying the A.S.U. Multislice Programs* (1980).

168. P.A. Doyle and P.S. Turner, *Acta Cryst.,* **A24**, 390 (1968).

169. J.M. Cowley and A.F. Moodie, *Acta Cryst.,* **10**, 609 (1957).

170. O. Johari and G. Thomas, *Stereographic Projection and Applications,* Wiley-Interscience, New York (1969).

171. A.H. Heuer and T.E. Mitchell, *J. Phys. C: Solid State Phys.,* **8**, L541 (1975).

172. L. Hwang, A.H. Heuer and T.E. Mitchell, *Phil. Mag. A,* **28**, 241 (1973).

173. W.S. Hulscher and G.H. Jonker, *J. Am. Ceram. Soc.,* **55**, 632 (1972).

174. D.S. Walters and G.P. Wirtz, *J. Am. Ceram. Soc.,* **55**, 59 (1972).

175. R. Kilaas and R. Gronsky, *Ultramicroscopy,* **16**, 193 (1981).

176. P.B. Hirth, A. Howie, R.B. Nicholson, D.B. Pashley and M.J. Whelan, *Electron Microscopy of Thin Crystals,* Butterworths, London (1965).

177. R.J. Gerdes and R.A. Young, *Orientation Relations in Simple Thin Film-Substrate Combinations,* Georgia Inst. of Tech., Atlanta, Engineering Experiment Station, (1967).

178. R.S. Timsit, W.G. Waddington, C.J. Humphrey and J.L. Hutchison, *Ultramicroscopy,* **18**, 387 (1985).

179. R.S. Timsit, W.G. Waddington, C.J. Humphrey and J.L. Hutchison, *Appl. Phys. Lett.,* **46**, 830 (1985).

180. C. Panseri and T. Federighi, *J. Inst. Metals,* **94**, 99 (1966).

181. J.P. Miraille, C. Bricht, G. Frade and G. Wyon, *Scr. Met.,* **6**, 891 (1972).

182. U. Dahmen and K.H. Westmacott, *Phys. Stat. Sol. (A),* **80**, 249 (1983).

183. W.T. Read, *Dislocations in Crystals,* McGraw-Hill, New York, 196 (1953).

184. U. Dahmen, A.R. Pelton, M.J. Witcomb and K.H. Westmacott, in *Proceedings of an International Conferences on Solid-Solid Phase Transformations,* The Met. Soc. AIME, Warrendale, PA, 477 (1982).

185. S. Mahajan and D.F. Williams, *Int. Met. Reviews,* **18**, 43 (1973).

186. W.C. Ellis and R.G. Treuting, *Trans. AIME; Journal of Metals,* **191**, 53 (1951).

187. M.S. Abrahams, J.L. Hutchison and G.R. Booker, *Phys. Stat. Sol.,* **63**, K3 (1981).

188. A. Howie and L.D. Marks, *Phil. Mag. A,* **49**, 95 (1984).

189. S. Ino and S. Ogawa, *J. Phys. Soc. Japan,* **22**, 1365 (1967).

190. J.E. Burke, *Trans. AIME; Journal of Metals,* **188**, 1324 (1950).

191. W.C. Ellis and R.G. Treuting, *Trans. AIME; Journal of Metals,* **191**, 1070 (1951).

192. W.C. Ellis, *Trans. AIME; Journal of Metals,* **188**, 886 (1950).

193. J.A. Kohn, *Am. Mineral.,* **43**, 263 (1958).

194. J.V. Cathcart and G.F. Petersen, *J. Electrochem. Soc.,* **115**, 595 (1968).

195. J.V. Cathcart, G.F. Petersen and C.J. Sparks, *J. Electrochem. Soc.,* **116**, 664 (1969).

196. H. Tabata and E. Ishii, *Japan. J. Appl. Phys.,* **12**, 7 (1973).

197. R.K. Mishra and G. Thomas, *J. Appl. Phys.,* **48**, 4576 (1977).

198. J.P. Hirth and G.M. Pound, *Prog. Metal Phys.,* **11**, 1 (1963).

199. H.W. King, *Bull. Alloy Phase Diagrams,* **2**, 401 (1981).

200. W.B. Pearson, *A Handbook of Lattice Spacings and Structures of Metals and Alloys,* Pergamon Press, Oxford, 261 (1958).

201. Landolt-Börnstein Tables, New Series, Group III, *Structure Data of Element and Intermetallic Compounds,* Vol. 6, Springer-Verlag, New York (1971).

202. ASTM card No. 10-425.

203. K.H. Westmacott, R.E. Smallman and P.S. Dobson, *Metal Science J.,* **2**, 177 (1968).

204. R.S. Nelson, D.J. Mazey and R.S. Barnes, *Phil. Mag.,* **11**, 91 (1965).

205. P.A. Thackery and R.S. Nelson, *Phil. Mag.,* **19**, 169 (1968).

TABLES

Table 1. Structural properties of the Al-O phases (25 ° C, 0.1 MPa).

Phase	Space group	Prototype	Lattice parameters, nm			Comment	Ref.
			a	*b*	*c*		
Al	$Fm\,3m$	Cu	0.40496	...	...	...	[199]
α-Al_2O_3	$R\,\bar{3}c$	α-Al_2O_3	0.51272	...	...	α=55.28 °	[200]
			0.47589	...	1.2991	...	[200]
γ-Al_2O_3	$Fd\,3m$	$MgAl_2O_4$	0.7911	...	...	...	[201]
			0.790	...	...	...	[202]
			0.7859	...	...	...	[200]
δ-Al_2O_3	...	δ-Al_2O_3	0.796	...	1.170	...	[201]
			0.795	...	0.779	...	[200]
θ-Al_2O_3	$C\,2/m$	β-Ga_2O_3	1.183	0.292	0.564	β=104 °	[201]
			1.124	0.572	1.174	β=103.33 °	[200]
κ-Al_2O_3	...	...	0.971	...	1.786	...	[200]
χ-Al_2O_3	$P\,6_3/mcm$ or	...	0.556	...	1.344	...	[200]
	$P\,6/mmm$ or	...	...	...	...	...	[200]
	$P\,6_3/mmc$	...	...	...	...	...	[200]

Table 2. Fugacities of O_2 in equilibrium with α-Al_2O_3 and solid Al.[73]

Temperature, °C	O_2 fugacity, Pa
25	1.6×10^{-180}
226.8	1.7×10^{-101}
660.5	2.5×10^{-47}

Table 3. The spinel structure in extended abc-notation.

z'	Occupied position	Kind of ion
10	$b_{1,2,3,4}$	Oxygen ion
9	c_1	Cation in the tetrahedral interstice
8	a_1	Cation in the octahedral interstice
7	b_1	Cation in the tetrahedral interstice
6	$c_{1,2,3,4}$	Oxygen ion
5	–	–
4	$b_{2,3,4}$	Cation in the octahedral interstice
3	–	–
2	$a_{1,2,3,4}$	Oxygen ion
1	b_1	Cation in the tetrahedral interstice
0	c_1	Cation in the octahedral interstice
–1	a_1	Cation in the tetrahedral interstice
–2	$b_{1,2,3,4}$	Oxygen ion

Table 4. Surface energy for aluminum.

Surface energy	Orientation dependence of γ to γ_{111}			Temperature	Reference
erg/cm^2	{111}	{110}	{100}		
$\gamma = 1140$	...	...	...	175 ° C	[203]
...	1	1.05	1.03	550 ° C	[204]
...	1	...	1.11	400 ° C	[205]

Table 5. Values of surface energies for spinel oxide.[197]

Material	{111} Surface (erg/cm^2)	{110} Surface (erg/cm^2)	{100} Surface (erg/cm^2)
$LiFe_5O_8$	222	2122	1331
$NiFe_2O_4$	207	1837	1161
Fe_3O_4	223	2164	1451
$MgAl_2O_4$	298	2702	1446

FIGURE CAPTIONS

Fig. 1. Al-N-O phase stability diagram at 600 ° C showing the range of the solid Al, Al_2O_3 and AlN phase fields. The full circle in the upper-right corner indicates the location of the partial pressures of O_2 and N_2 in air.

Fig. 2. Schematic illustration showing defect and electron flows associated with oxidation of aluminum to form the crystalline γ–Al_2O_3. $V_{\ddot{O}}$ represents the doubly charged vacancy on oxygen site and $M_M^{\times}$ represents the atom at the normal site.

Fig. 3. Partial aluminum-oxygen equilibrium phase diagram showing the range of the aluminum and the α–Al_2O_3 phase fields (after [69]).

Fig. 4. Crystal structures and lattice parameters of the face-centered cubic Al and the spinel oxide, γ–Al_2O_3 at room temperature.

Fig. 5. The Thompson tetrahedron, which aids interpretation of dislocation reactions in the face-centered cubic crystal.

Fig. 6. Spinel structure in $[1\bar{1}0]$ projection. The oxygen atoms are represented by large circles, and the aluminum atoms at the octahedral or tetrahedral sites are represented by small single or triple circles, respectively. Numbers in the circles show the relative heights of atoms in multiples of $\frac{a}{8}[1\bar{1}0]_{\text{oxide}}$. Ions are drawn in thick lines when the height is an even number and in thin lines when the height is an odd number. The {111} stacking sequence is shown on the right side.

Fig. 7. Projection of two consecutive {111} layers of the ideal normal spinel structure. The large open circles represent oxygen ions. The small closed circles

represent cations.

Fig. 8. Atom model of a twin boundary with a stacking fault of type I. The twin plane is indicated by the dashed lines.

Fig. 9. A pictorial guide for the discussion of the various steps in the calculation of a HRTEM image (after [156]).

Fig. 10. Preparation of aluminum/oxide cross-section transmission electron microscopy specimens.

Fig. 11. Experimental aluminum/oxide selected-area diffraction pattern in a $[1\bar{1}0]_{Al}$ || $[1\bar{1}0]_{oxide}$ orientation and corresponding indexed diffraction pattern showing the positions of the aluminum and oxide spots. Note the additional oxide reflections at $\frac{1}{3}$ positions along the $<111>$ directions and $\{002\}$ oxide reflections.

Fig. 12. Bright-field TEM images of the aluminum/oxide interfaces showing the growth of the oxide, produced by (a) the 5 hr oxidation treatment of aluminum at 500 ° C, (b) the 10 hr oxidation at 500 ° C, and (c) the 4 week oxidation at 600 ° C.

Fig. 13. (a) Contrast transfer function at –660 Å the initial undamped form and the damping functions due to both the energy spread (Δ) and divergence (α) of the electron beam, and (b) the same for –750 Å defocus.

Fig. 14. (a)–(d) Contrast transfer function for the JEOL JEM 200CX microscope over a range of objective lens defocus values, where accelerating voltage $V = 200$ keV, spherical aberration coefficient $C_s = 1.2$ mm, half-width of Gaussian spread of defocus $\Delta = 50$ Å, semi-angle of illumination $\alpha = 0.3$ mrad, and

$\Delta f_{\text{Scherzer}} = -660$ Å.

Fig. 15. High-resolution transmission electron microscopy image of $[1\bar{1}0]$ aluminum showing the brightness change of the atoms.

Fig. 16. High-resolution transmission electron microscopy image of $[1\bar{1}0]$ γ–Al_2O_3 which was oxidized for 2 weeks at 600 ° C.

Fig. 17. (a)–(d) Enlargements from γ–Al_2O_3 in Fig. 16.

Fig. 18. Calculational unit cell for computer image simulations of the crystalline oxide assuming that the aluminum ions are disordered in the octahedral sites and the tetrahedral sites. The accompanying legends show the lattice point at the height h = 1 and h = 3 in the bottom-left corner, and the atom positions in the bottom-right corner, respectively.

Fig. 19. (a) Unit cell used for a 3×3 periodic array of the unit cells in Fig. 18. (b) Projected potential for the atomic model in Fig. 18. The atom positions are superimposed on the figure in the top-left corner. The potential contains 3×3 unit cells of the unit cell (a).

Fig. 20. (a)–(d) A series of simulated high-resolution transmission electron microscopy images of the γ–Al_2O_3 atomic model in Fig. 18 shown as a function of objective lens defocus, from 100 to –3000 Å, and specimen thickness, from 50 to 250 Å. The atom position are superimposed in the top-left corner at each defocus setting.

Fig. 21. Experimental and simulated HRTEM images of γ–Al_2O_3 in a <110> oxide orientation. Note the matching between the experimental image and the inset superimposed simulated image of the oxide at –660 Å defocus and 250 Å thickness from Fig. 20.

Fig. 22. Experimental HRTEM image of the aluminum/amorphous oxide interface in a <110> aluminum orientation. The superimposed arrows indicate the {111} micro-facets at the interface.

Fig. 23. Experimental HRTEM image of the aluminum/amorphous oxide interface in a <110> aluminum orientation showing the roughness on the macroscopic {111} aluminum face.

Fig. 24. Low magnification HRTEM image of an aluminum/amorphous oxide interface in a <110> aluminum orientation showing the nucleation of the crystalline oxide at the aluminum/amorphous oxide interface.

Fig. 25. Enlargement of an oxide nucleus at the interface in Fig. 24 showing the details of the oxide and the interfaces.

Fig. 26. Optical diffraction pattern corresponding to Fig. 25 showing the orientation relationship and {220} oxide reflections as indicated by the arrow heads.

Fig. 27. High-resolution image of the crystalline oxide nuclei at the aluminum/amorphous oxide interface showing the connection of two nuclei.

Fig. 28. High-resolution electron microscopy image of the crystalline oxide nucleus at the aluminum/amorphous oxide interface showing the details of the structure of the oxide nucleus and interfaces.

Fig. 29. Low magnification lattice image showing the amorphous/crystalline oxide and the aluminum/crystalline oxide interface with a parallel orientation relationship: $(111)_{Al} \,||\, (111)_{oxide}$, $[1\bar{1}0]_{Al} \,||\, [1\bar{1}0]_{oxide}$, produced by 1 hr oxidation at 500 ° C.

Fig. 30. Experimental HRTEM image of an amorphous/crystalline oxide interface in a <110> oxide orientation showing the {111} interfacial plane of the

crystalline oxide.

Fig. 31. Low magnification lattice image of the aluminum/oxide interface with a parallel orientation relationship: $(111)_{Al} \,||\, (111)_{oxide}$, $[1\bar{1}0]_{Al} \,||\, [1\bar{1}0]_{oxide}$, produced by 0.5 hr oxidation at 600° C. There are many stacking faults and twins in the oxide.

Fig. 32. Selected area diffraction pattern corresponding to Fig. 31.

Fig. 33. Enlargement of the aluminum/oxide interface in Fig. 31 showing that the interfacial planes are coherent {111} oxide planes with a parallel orientation relationship: $(111)_{Al} \,||\, (111)_{oxide}$, $[1\bar{1}0]_{Al} \,||\, [1\bar{1}0]_{oxide}$.

Fig. 34. Experimental HRTEM image of the interface in Fig. 33 with a slightly different defocus setting showing more clearly the interfacial planes.

Fig. 35. (a)-(c) A through-focus series of HRTEM of the interface in Fig. 33. Note the contrast change in the oxide and at the interface with the objective lens defocus.

Fig. 36. Proposed atomic model of the aluminum/oxide (111) interface with a parallel orientation relationship projected in a $[1\bar{1}0]$ orientation showing that the aluminum sublattice of the oxide can preserve the aluminum lattice of the aluminum metal and the cation stacking of the {111} planes in the oxide starts with a kagome layer. In this model, the oxygen atoms are represented by large circles. The aluminum atoms at the octahedral or tetrahedral sites are represented by small single or triple circles, respectively, and aluminum atoms in the metal are represented by double circles. Numbers in the circles show the relative heights of atoms in multiples of $\frac{a}{8}[1\bar{1}0]_{oxide}$, or $\frac{a}{4}[1\bar{1}0]_{Al}$.

Fig. 37. (a) Same as Fig. 36, and (b) projected potential for the interface containing 3 unit cells of (a) in the x-axis.

Fig. 38. (a) and (b) A series of simulated high-resolution transmission electron microscopy images of the proposed aluminum/oxide interface model with a parallel orientation relationship in Fig. 37 shown as a function of objective lens defocus, from 360 to –1850 Å, and specimen thickness, from 50 to 300 Å.

Fig. 39. Additional atomic model of the aluminum/oxide (111) interface with a parallel orientation, projected in a $[1\bar{1}0]$ orientation, showing that the aluminum sublattice of the oxide can preserve the aluminum lattice of the aluminum metal and the cation stacking of the {111} planes in the oxide starts with a mixed layer and projected potential for the interface containing 3 unit cells of atomic model on the left in the x-axis.

Fig. 40. Simulated HRTEM images for the aluminum/oxide interface in Fig. 39, where the cation stacking starts with a mixed layer to be compared with Fig. 38.

Fig. 41. Atomic model of the aluminum/oxide (111) interface based on the *lock-in* model showing that the oxygen sublattice of the oxide can preserve the aluminum lattice of the aluminum metal, and projected potential for the interface containing 3 unit cells of atomic model on the left in the x-axis.

Fig. 42. Simulated high-resolution transmission electron microscopy images of the aluminum/oxide interface model in Fig. 41 shown as a function of objective lens defocus and specimen thickness.

Fig. 43. Experimental and simulated HRTEM images of the aluminum/oxide (111) interface with a parallel orientation relationship. Note the match between the experimental image and the inset superimposed simulated image of the oxide

at –730 Å defocus and 100 Å thickness from Fig. 38.

Fig. 44. Proposed transformation mechanism of aluminum to the oxide structure with a parallel orientation relationship projected in a $[1\bar{1}0]$ orientation. (a) Unit cell of the aluminum, and (d) a corresponding unit cell of the oxide, in the coincidence site cell for the $\Sigma = 1 : \Sigma = 1$ aluminum/oxide interface. In this model, aluminum atoms in the metal are represented by double circles, the oxygen atoms by large circles, and the aluminum atoms at the octahedral or tetrahedral sites by small single or triple circles, respectively. Numbers in the circles show the relative heights of atoms in multiples of $\frac{a}{8}[1\bar{1}0]_{oxide}$, or $\frac{a}{4}[1\bar{1}0]_{Al}$.

Fig. 45. High-resolution image of the aluminum/oxide interface with a twin orientation relationship: $(11\bar{1})_{Al} \,||\, (111)_{oxide}$, $[1\bar{1}0]_{Al} \,||\, [1\bar{1}0]_{oxide}$, produced by 0.5 hr oxidation at 600 ° C.

Fig. 46. High-resolution image of the aluminum/oxide interface with a twin orientation relationship showing a ledge which is three {111} aluminum planes thick.

Fig. 47. Proposed atomic model of the aluminum/oxide (111) interface with a twin orientation relationship projected in a $[1\bar{1}0]$ orientation showing that the aluminum sublattice of the oxide can preserve the aluminum lattice of the aluminum metal with a twin relationship and the cation stacking of the {111} planes in the oxide starts with a mixed layer. In this model, the oxygen atoms are represented by large circles. The aluminum atoms at the octahedral or tetrahedral sites are represented by small single or triple circles, respectively, and aluminum atoms in the metal are represented by double circles. Numbers

in the circles show the relative heights of atoms in multiples of $\frac{a}{8}[1\bar{1}0]_{\text{oxide}}$, or $\frac{a}{4}[1\bar{1}0]_{\text{Al}}$.

Fig. 48. Projected potential for the interface containing 3 unit cells of Fig. 47 in the x-axis.

Fig. 49. Series of simulated high-resolution transmission electron microscopy images of the proposed aluminum/oxide interface model with a twin orientation relationship in Fig. 45 shown as a function of objective lens defocus, –400, –800 and –980 Å, and specimen thickness from 50 to 300 Å.

Fig. 50. Proposed atomic model of the aluminum/oxide (111) interface with a twin orientation relationship projected in a $[1\bar{1}0]$ orientation showing that the cation stacking of the {111} planes in the oxide starts with a kagome layer, and projected potential for the interface containing 3 unit cells of atomic model on the left in the x-axis.

Fig. 51. Series of simulated high-resolution transmission electron microscopy images of the proposed aluminum/oxide interface model with a twin orientation relationship in Fig. 50 shown as a function of objective lens defocus and specimen thickness to be compared with Fig. 49.

Fig. 52. Experimental and simulated HRTEM images of the aluminum/oxide (111) interface with a twin orientation relationship. Note the match between the experimental image and the inset superimposed simulated image of the oxide at –980 Å defocus and 100 Å thickness from Fig. 49.

Fig. 53. Proposed transformation mechanism of aluminum to the oxide structure with a twin orientation relationship projected in a $[1\bar{1}0]$ orientation. (a) Unit cell of

the aluminum, and (d) unit cell of the spinel oxide, in the coincidence site cell for the $\Sigma = 3 : \Sigma = 3$ aluminum/oxide interface. In this model, aluminum atoms in the metal are represented by double circles, the oxygen atoms by large circles, and the aluminum atoms at the octahedral or tetrahedral sites by small single or triple circles, respectively. Numbers in the circles show the relative heights of atoms in multiples of $\frac{a}{8}[1\bar{1}0]_{\text{oxide}}$, or $\frac{a}{4}[1\bar{1}0]_{\text{Al}}$.

Fig. 54. Illustration of four different ways of transforming face-centered cubic (111) planes into twinned planes: (a) using a coupled shearing movement, (b) using the rotational movement, (c) using equal numbers of all three types of Shockley partial dislocations, and (d) using the same Shockley partial dislocation. Each block represents one (111) plane.

Fig. 55. Experimental HRTEM image of twin boundaries in the oxide showing {111} twins as indicated by the dashed lines.

Fig. 56. Atomic model of a twin boundary with a stacking fault of type III projected along <110> direction. The twinning plane is indicated by the dashed lines in the middle. The oxygen atoms are represented by large circles, and the aluminum atoms at the octahedral or tetrahedral sites are represented by small single or triple circles, respectively. Numbers in the circles show the relative heights of atoms in multiples of $\frac{a}{8}[1\bar{1}0]_{\text{oxide}}$. Ions are drawn in thick lines when the height is an even number and in thin lines when the height is an odd number.

Fig. 57. Projected potential for the interface containing 3 unit cells of Fig. 56 in the x-axis.

Fig. 58. Series of simulated HRTEM images for a twin boundary with a stacking fault of type III as a function of objective lens defocus and specimen thickness. The atom positions are superimposed in the top-left corner.

Fig. 59. Additional atomic model of a twin boundary with a stacking fault of type III obtained by the (111) mirror reflection of model, Fig. 56. Explanation as in Fig. 56. The twinning plane is indicated by the dashed lines in the middle.

Fig. 60. Projected potential for the interface containing 3 unit cells of model, Fig. 59, in the x-axis.

Fig. 61. Simulated HRTEM images for a twin boundary in Fig. 59 over a range of crystal thicknesses for objective lens defocus of –500 and –850 Å. The atom positions are superimposed in the top-left corner.

Fig. 62. Experimental and simulated HRTEM images of a twin boundary with a stacking fault of type III. There is matching in their periodicities between the experimental image and the inset superimposed simulated image of the oxide at –850 Å defocus and 200 Å thickness from Fig. 58.

Fig. 63. Proposed mechanism for twin boundary formation in the oxide showing that the lower half represents the aluminum transformation to oxide with a parallel orientation relationship and the upper half represents the aluminum transformation to oxide with a twin orientation relationship, which results in a twin boundary with a stacking fault of type III in the oxide. Explanation as in Figs. 44 and 53.

Fig. 64. Experimental HRTEM image of Al_2O_3 in a <110> orientation showing the parallel multiple twinning as indicated by the dashed {111} planes.

Fig. 65. Experimental HRTEM image of Al_2O_3 in a <110> orientation containing tips of two twin bands.

Fig. 66. Enlargement of the middle of Fig. 31 showing a number of stacking faults in the oxide.

Fig. 67. Low magnification lattice image of the oxide in a <110> oxide orientation showing the nonparallel multiple twinning.

Fig. 68. Enlargement of the left region of Fig. 67 and schematic diagram showing the multiple twinning in the oxide. The superimposed legend shows some important crystallographic planes in the oxide.

Fig. 69. Enlargement of the right region of Fig. 67 and schematic diagram showing the multiple twinning in the oxide.

Fig. 70. Electron diffraction pattern showing the twins in the oxide.

Fig. 71. Experimental HRTEM image of an aluminum/oxide interface in a <110> oxide orientation showing the multiple twinning in the oxide.

Fig. 72. Proposed multiple twinning model showing four Thompson tetrahedra indicated by I, II, III and IV.

Fig. 73. Proposed mechanism for new grain nucleation by twinning, where the oxygen atoms are represented by large circles, and the aluminum atoms at the octahedral or tetrahedral sites are represented by small single or triple circles, respectively. Numbers in the circles show the relative heights of atoms in multiples of $\frac{a}{8}[1\bar{1}0]_{\text{oxide}}$. Solid lines and dashed lines represent projection of the {111} planes and the <110> edges of octahedra or tetrahedra. (a) Growth of the oxide with the correct stacking order, and (b) growth of the oxide with a

stacking fault that begins a twinning.

Fig. 74. Low magnification lattice image of the aluminum/oxide interface which is not a {111} aluminum plane, in a <110> oxide orientation, showing the several growth ledges.

Fig. 75. Enlargement of the aluminum/oxide interface in Fig. 74 showing the {111} oxide interfacial plane and the multiple twinning in the oxide.

Fig. 76. Experimental high-resolution image of the aluminum/oxide interface showing two ledges growing from the right and left side, respectively.

Fig. 77. Enlargement of the edge of the large growth ledge in Fig. 74 showing the Moiré fringes.

Fig. 78. Enlargement of the crystalline oxide/vacuum interface in Fig. 31 showing that the oxide surface is bounded by {002} and {111} planes.

Fig. 79. Experimental high-resolution image of the aluminum/oxide interface showing that the interfacial plane is an atomically flat {111} oxide plane.

Fig. 80. Additional experimental high-resolution image of the aluminum/oxide interface showing that the interfacial plane is an atomically flat {111} oxide plane.

Fig. 81. Experimental high-resolution images of the aluminum/oxide interface, taken in a <110> oxide orientation, showing a large growth edge.

Fig. 82. Experimental high-resolution image of the edge of the growth ledge in a <110> oxide orientation showing the {111} facets at the atomic level. Two {111} oxide planes are superimposed on the oxide image.

Fig. 83. Atomically smooth aluminum/oxide interfaces with atoms represented by cubes, showing by analogy with a solid/liquid interface that: (a) addition of a

single atoms onto a flat {111} surface, and (b) addition to a ledge or a kink.

Fig. 84. Proposed mechanism of oxide growth leading to the {111} facets. Models are projected in a $[1\bar{1}0]$ orientation, where the oxygen atoms are represented by large circles, and the aluminum atoms at the octahedral or tetrahedral sites are represented by small single or triple circles, respectively. Numbers in the circles show the relative heights of atoms in multiples of $\frac{a}{8}[1\bar{1}0]_{\text{oxide}}$. Solid lines and dashed lines represent projection of the {111} planes and the <110> edges of octahedra or tetrahedra. (a) (001) oxide face, (b) (110) oxide face and (c) (111) oxide face.

Fig. 85. Proposed ledge mechanism of oxide growth. Explanation as in Fig. 84.

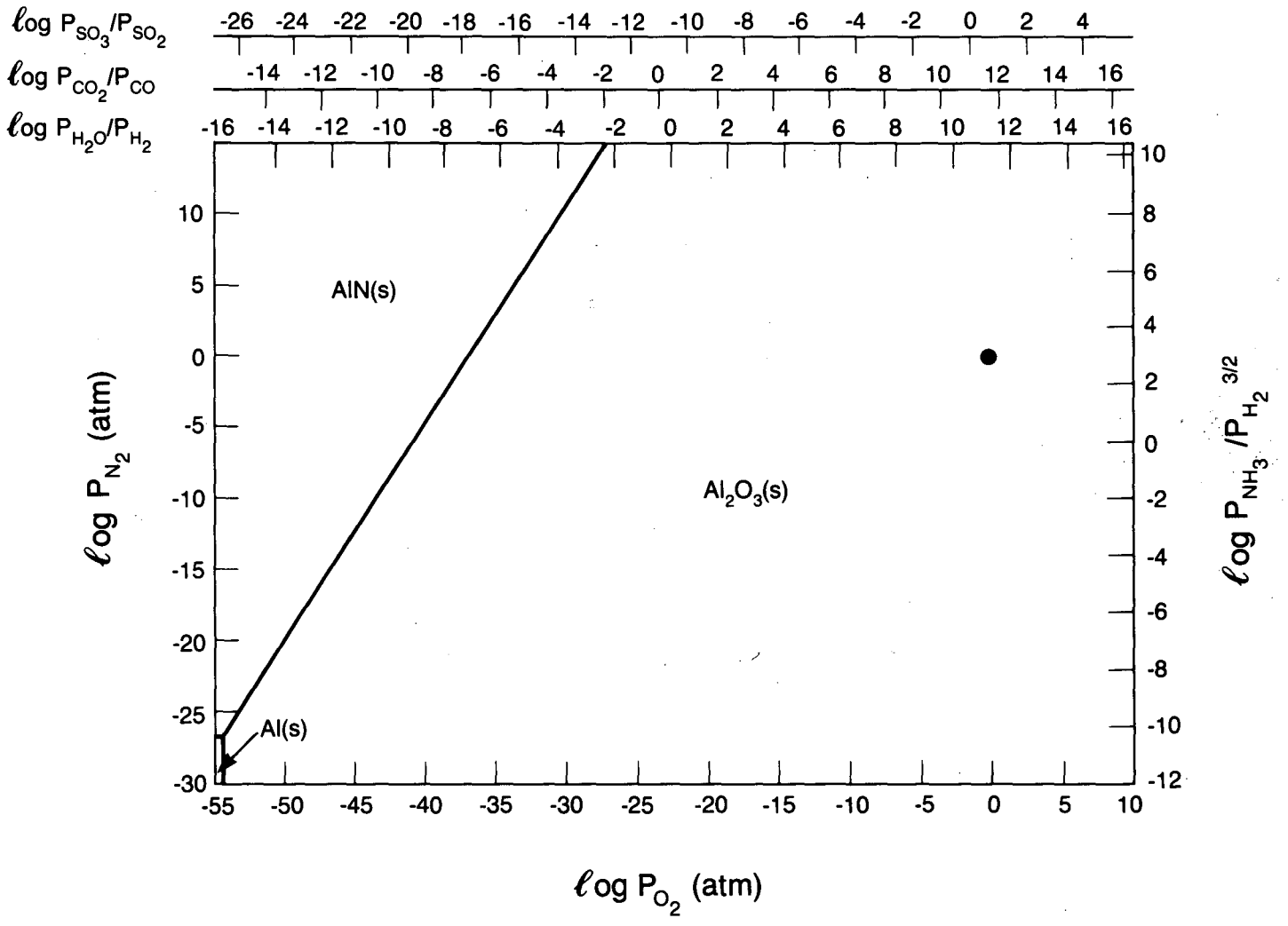

Al-N-O Phase Stability Diagram at 600°C

Fig. 1

XBL 853-8013

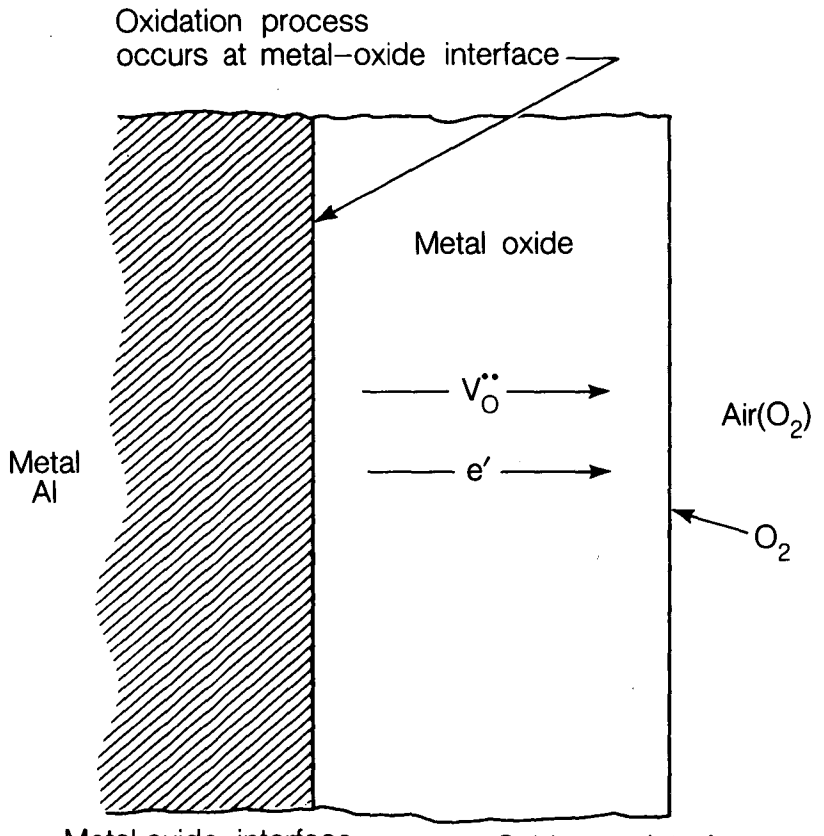

$$2Al_{(metal)} \rightarrow 2Al^{x}_{Al(oxide)} + 3V_O^{\bullet\bullet} + 6e' \qquad 3V_O^{\bullet\bullet} + 6e' + 3/2\ O_2 \rightarrow 3O^{x}_{O(oxide)}$$

Net reaction:

$$2Al + 3/2\ O_2 \rightarrow Al_2O_3$$

XBL 853-1585

Fig. 2

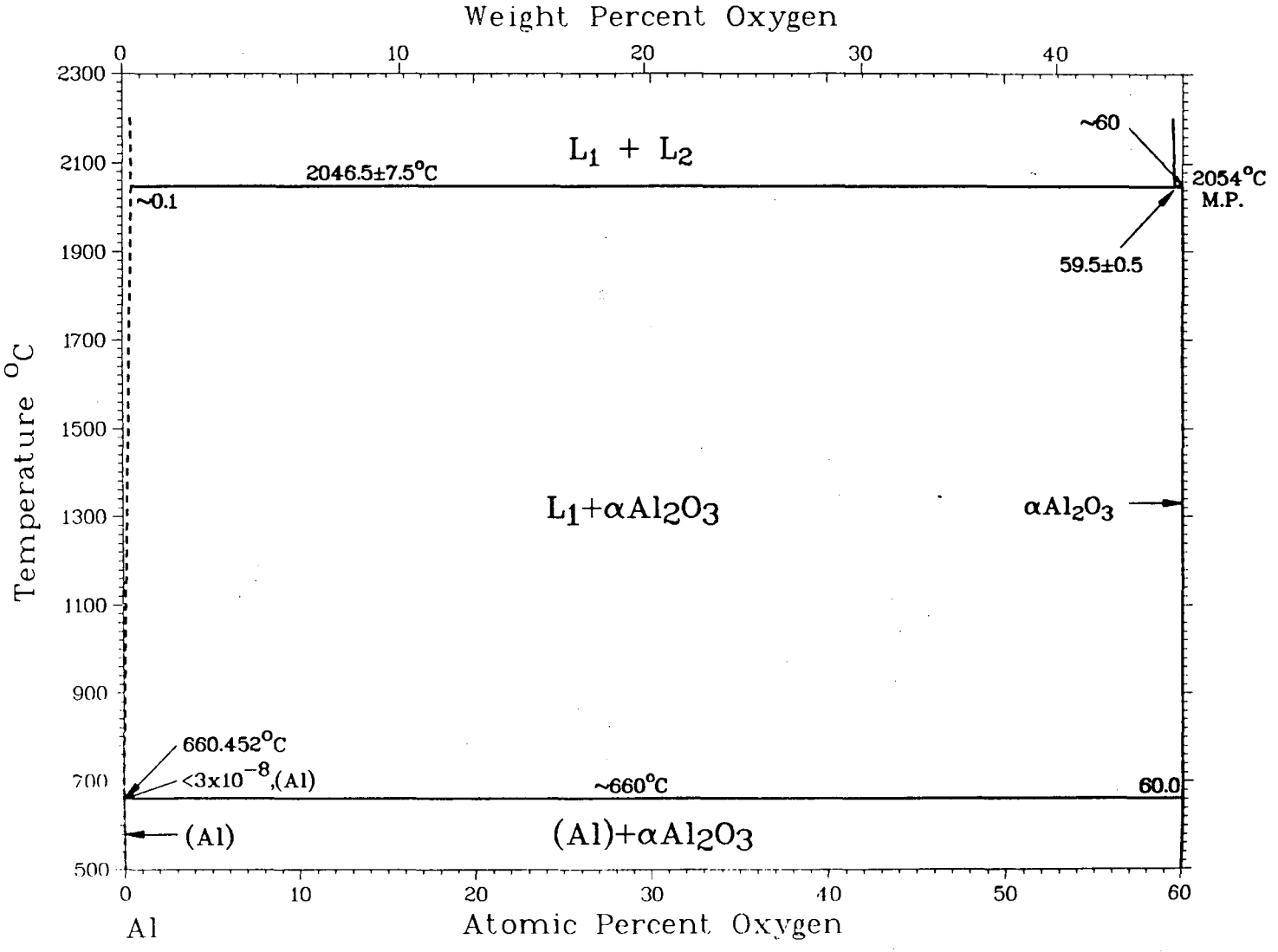

Fig. 3

XBL 862-496

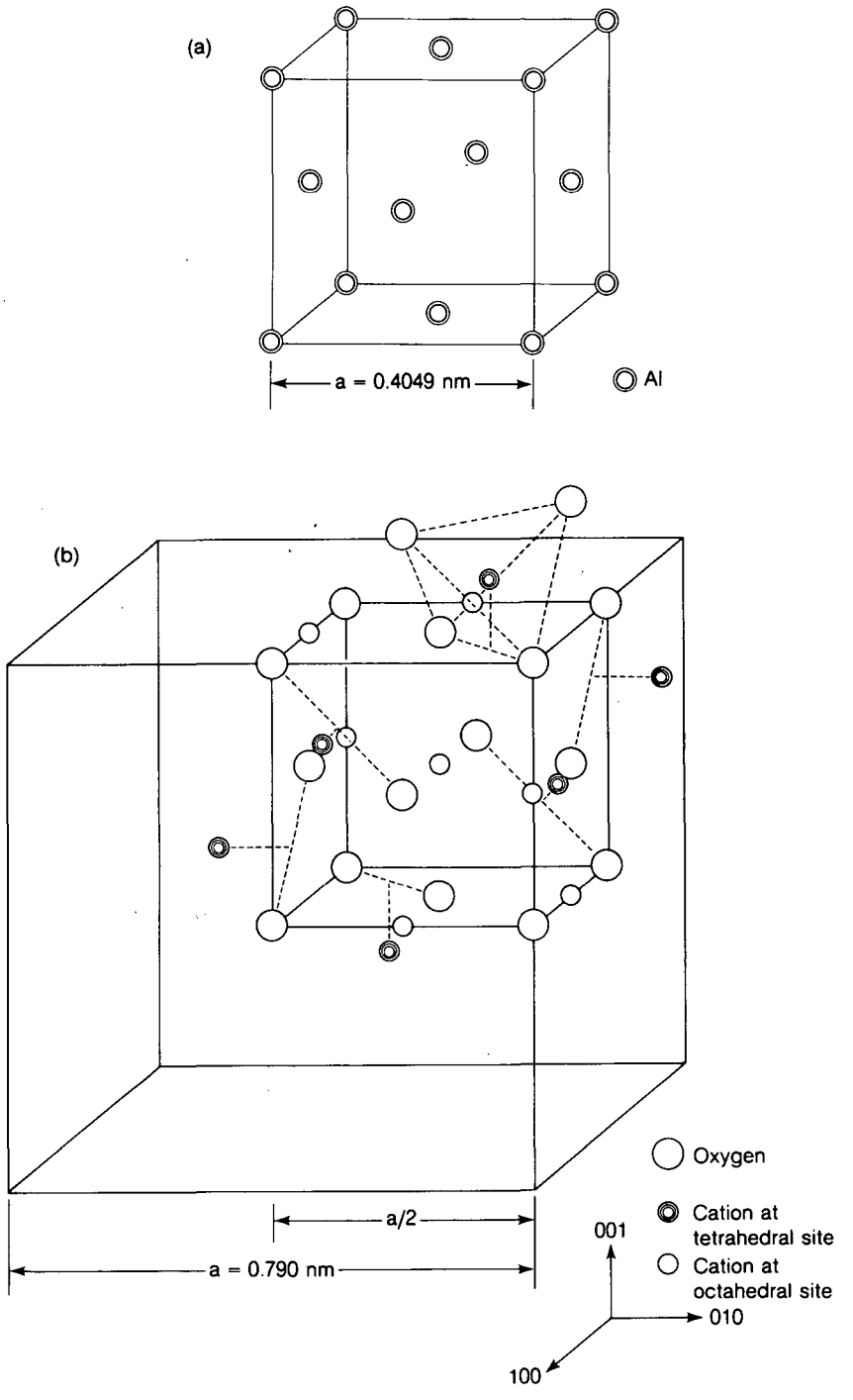
(a)
a = 0.4049 nm
Al
(b)
a/2
a = 0.790 nm
Oxygen
Cation at tetrahedral site
Cation at octahedral site
001
010
100
XBL 853-1584

Fig. 4

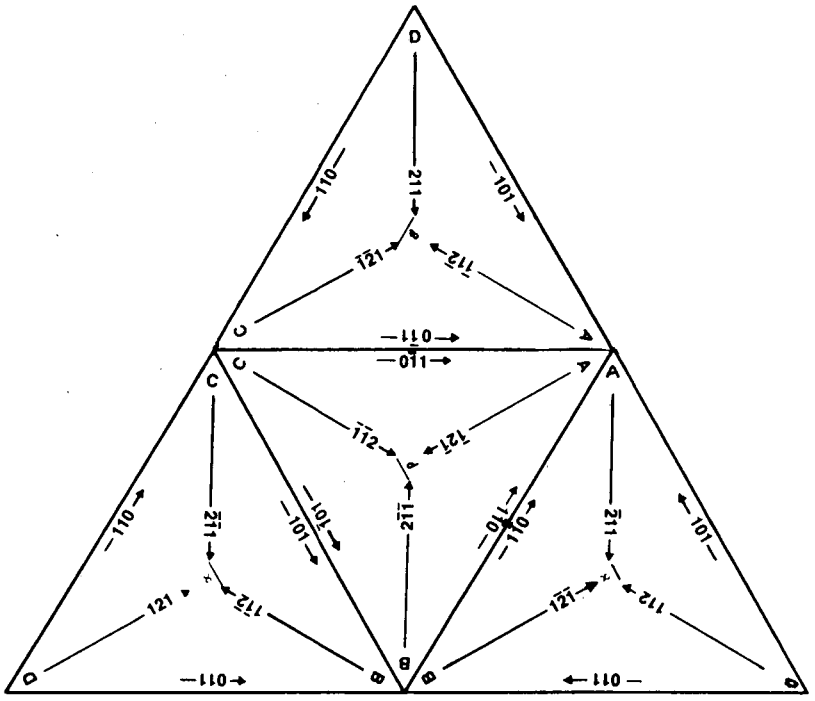

Thompson Tetrahedron

XBL 855-2560

Fig. 5

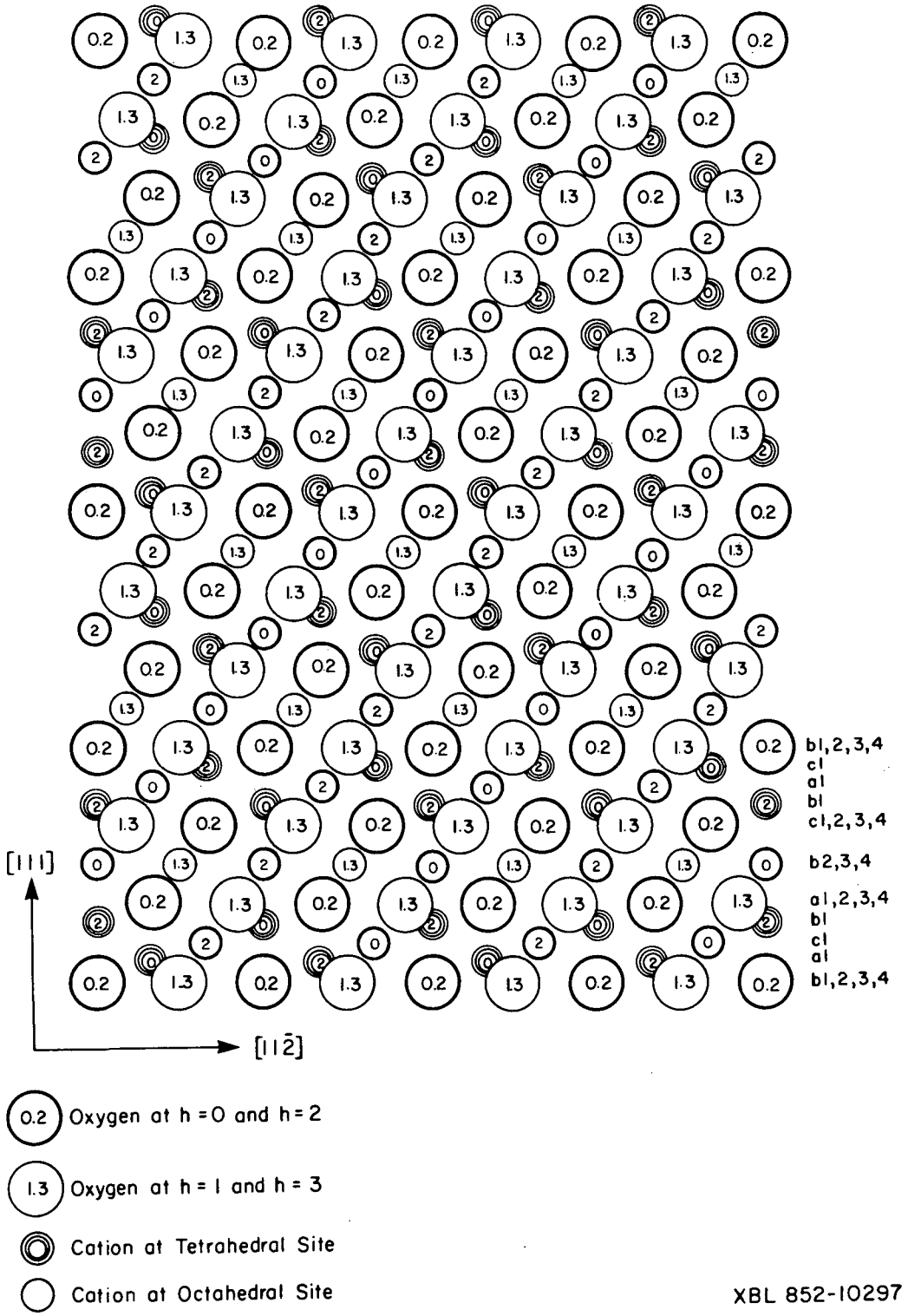
0.2
1.3
0
2
b1,2,3,4
c1
a1
b1
c1,2,3,4
b2,3,4
a1,2,3,4
b1
c1
a1
b1,2,3,4
[111]
[11$\bar{2}$]
Oxygen at h = 0 and h = 2
Oxygen at h = 1 and h = 3
Cation at Tetrahedral Site
Cation at Octahedral Site
XBL 852-10297

Fig. 6

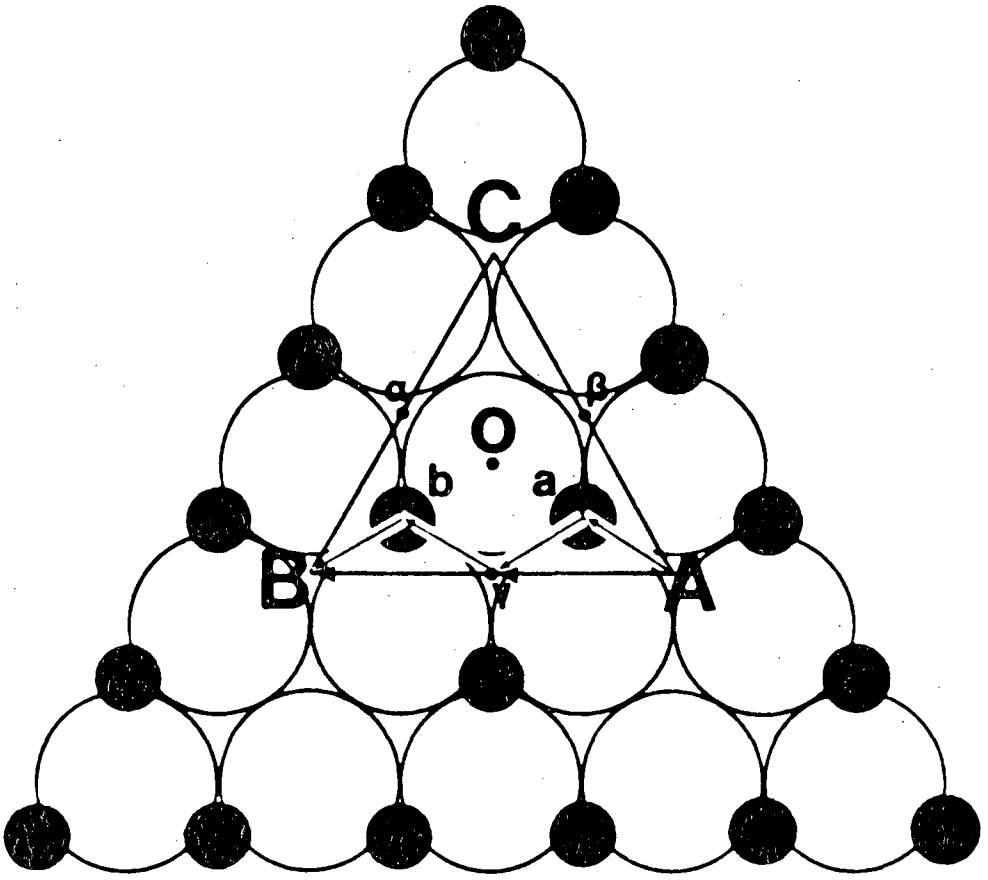

XBL 864-1547

Fig. 7

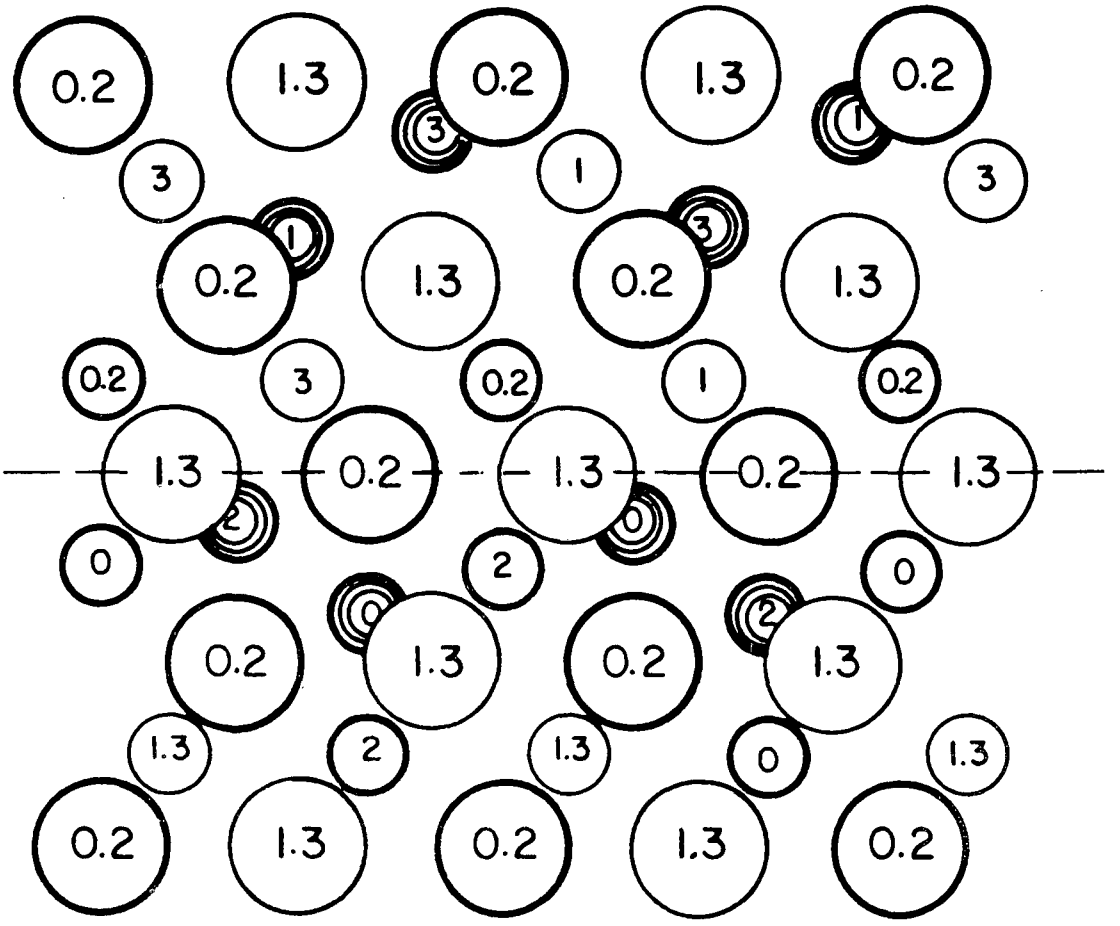

XBL 852-10307

Fig. 8

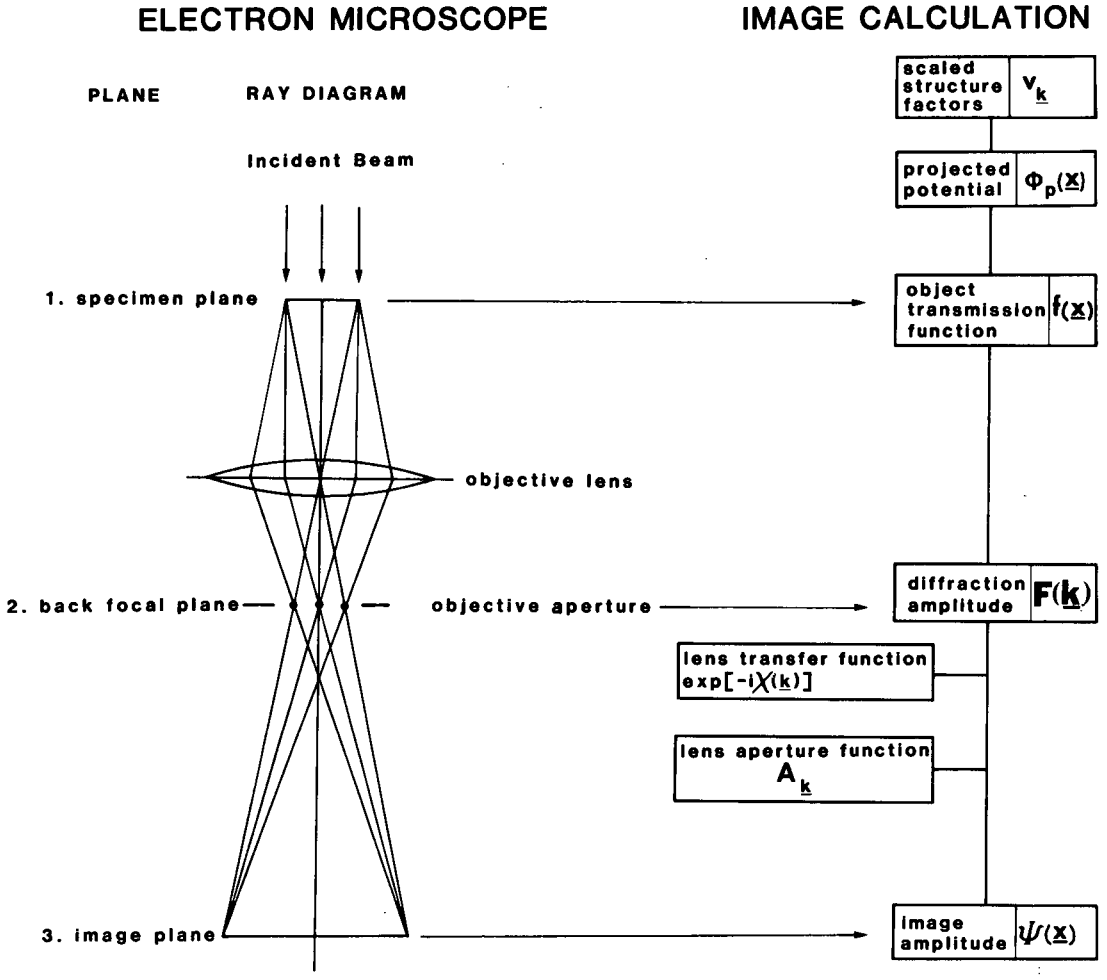

XBL 848-3399A

Fig. 9

1. 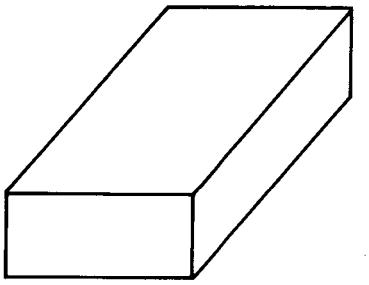

Etch and clean Al

2. 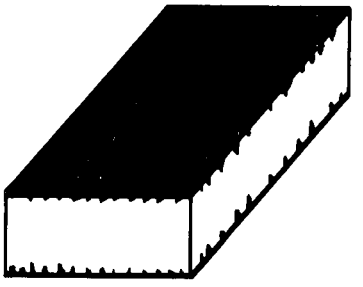

Oxidation

3. 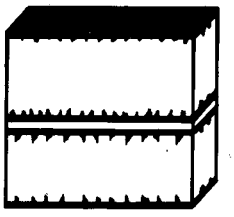

Epoxy and slice

4. 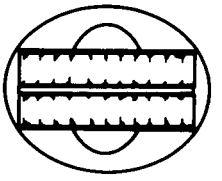

Mechanically thin and mount

5. 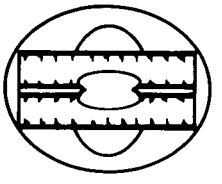

Ion mill

XBL 852-7050

Fig. 10

Diffraction pattern of Al and oxide with parallel orientation relationship

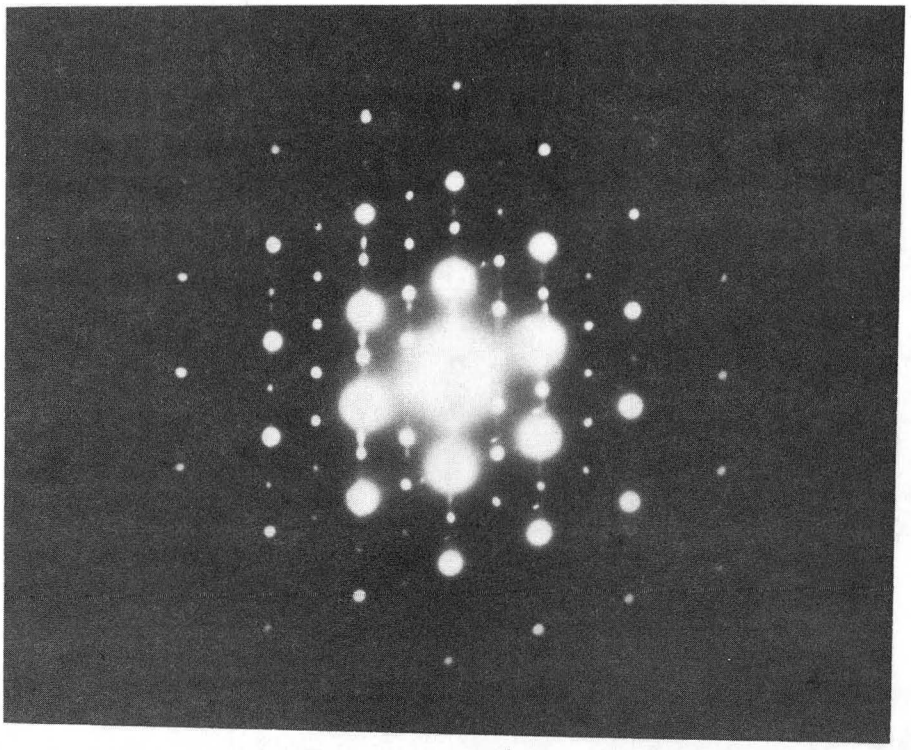

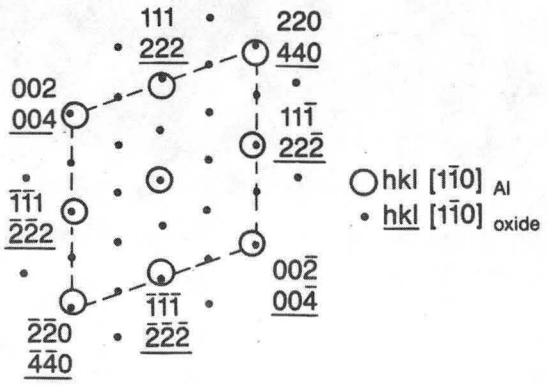

XBB 852-1622A

Fig. 11

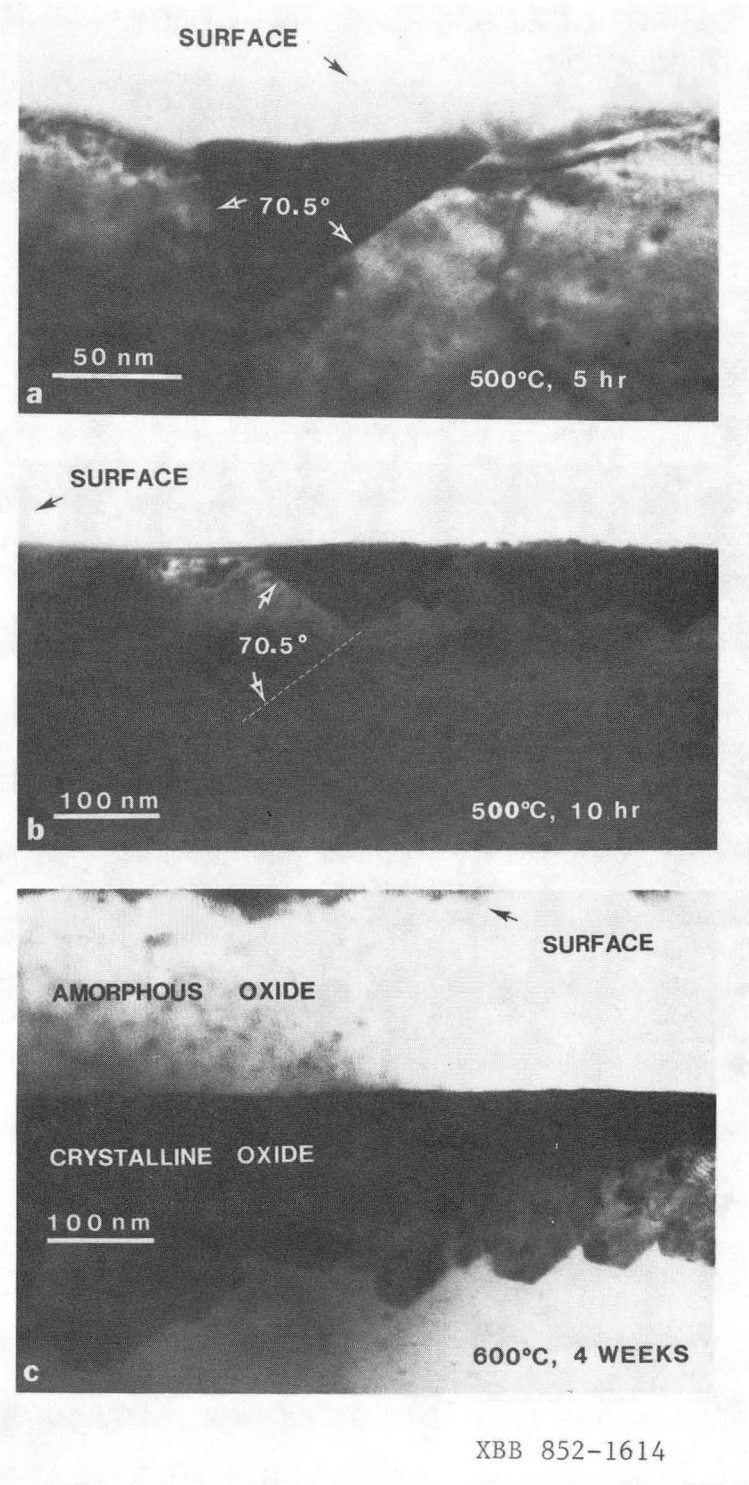

XBB 852-1614

Fig. 12

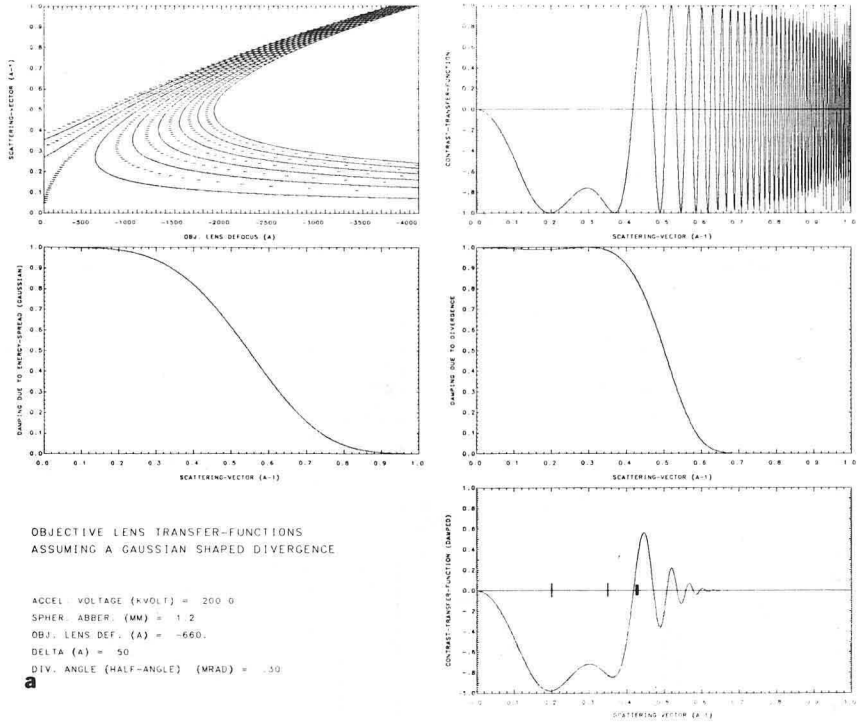
OBJECTIVE LENS TRANSFER-FUNCTIONS
ASSUMING A GAUSSIAN SHAPED DIVERGENCE
ACCEL. VOLTAGE (KVOLT) = 200.0
SPHER. ABBER. (MM) = 1.2
OBJ. LENS DEF. (A) = -660.
DELTA (A) = 50
DIV. ANGLE (HALF-ANGLE) (MRAD) = .50
a
b
XBL 858-3615

Fig. 13

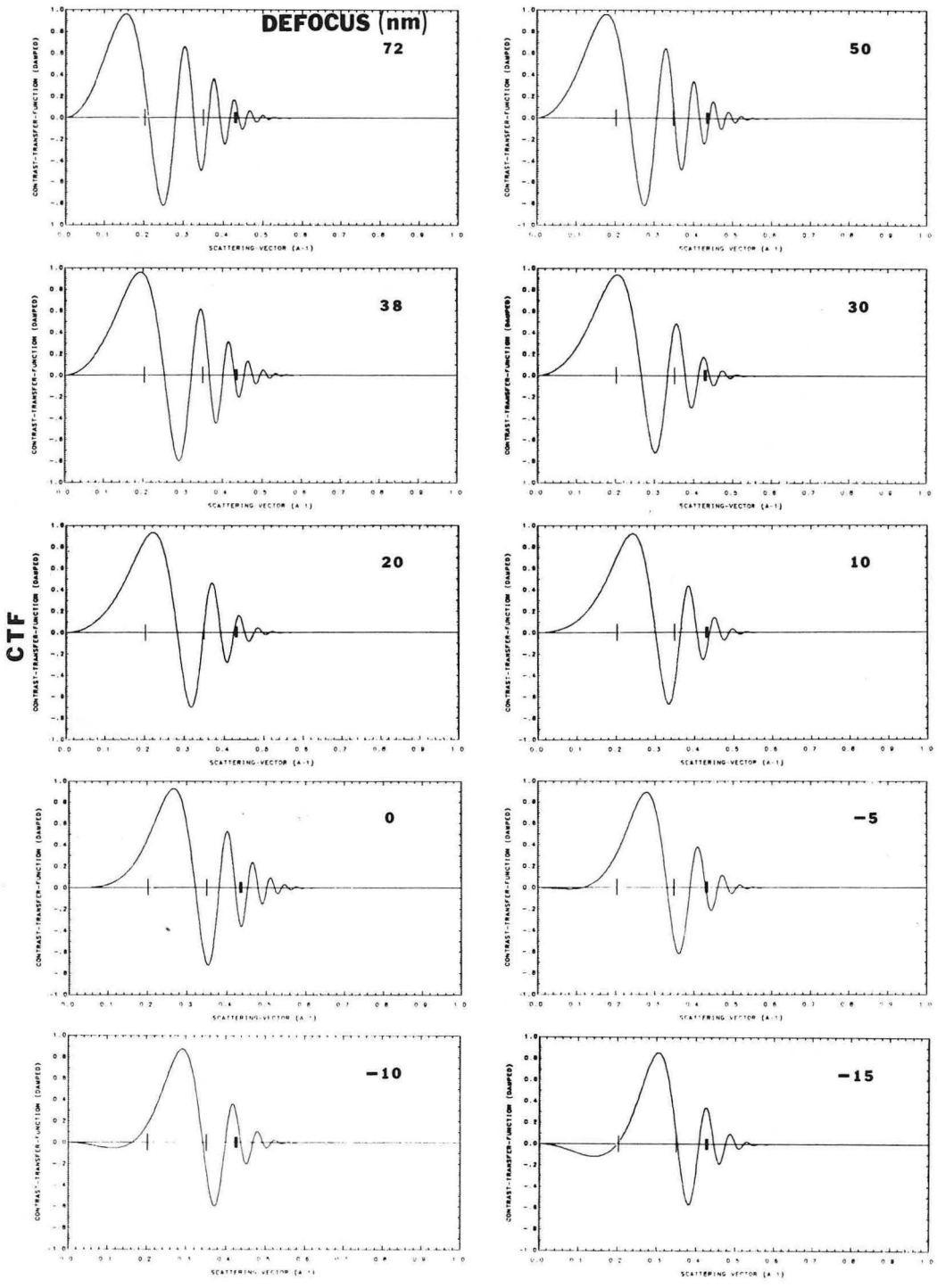

XBL 858-3593

Fig. 14 (a)

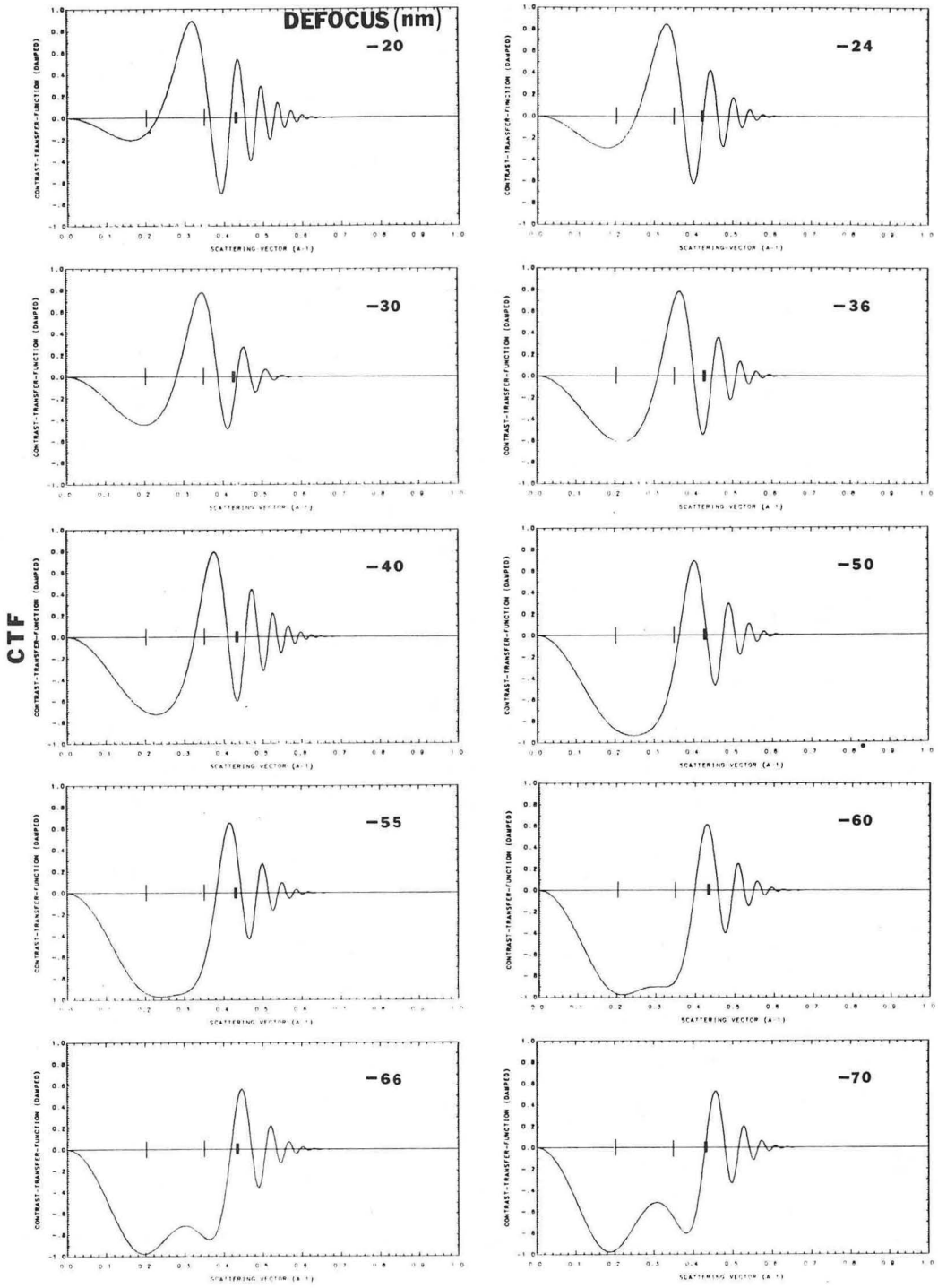

XBL 858-3594

Fig. 14 (b)

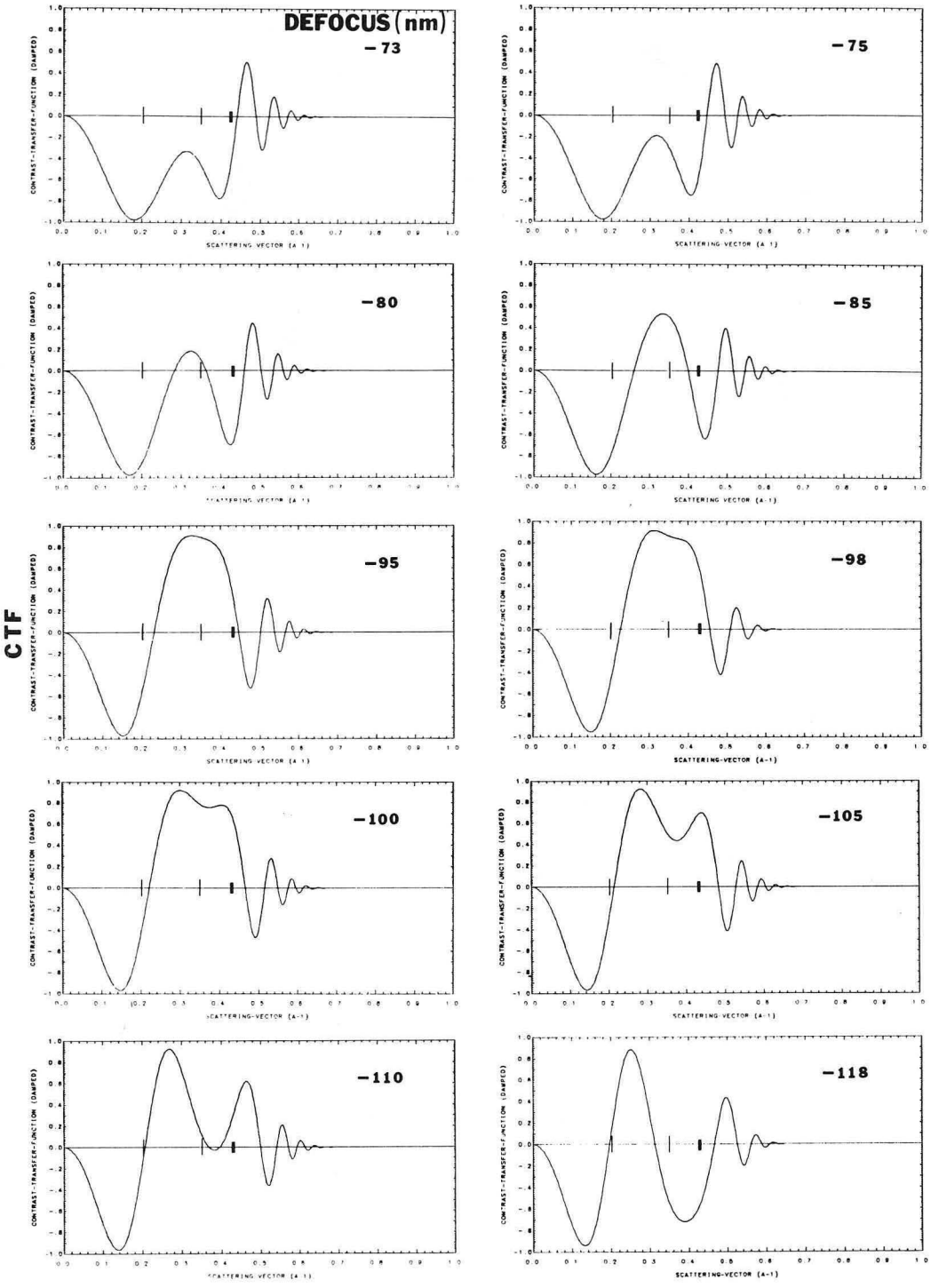

XBL 858-3596

Fig. 14 (c)

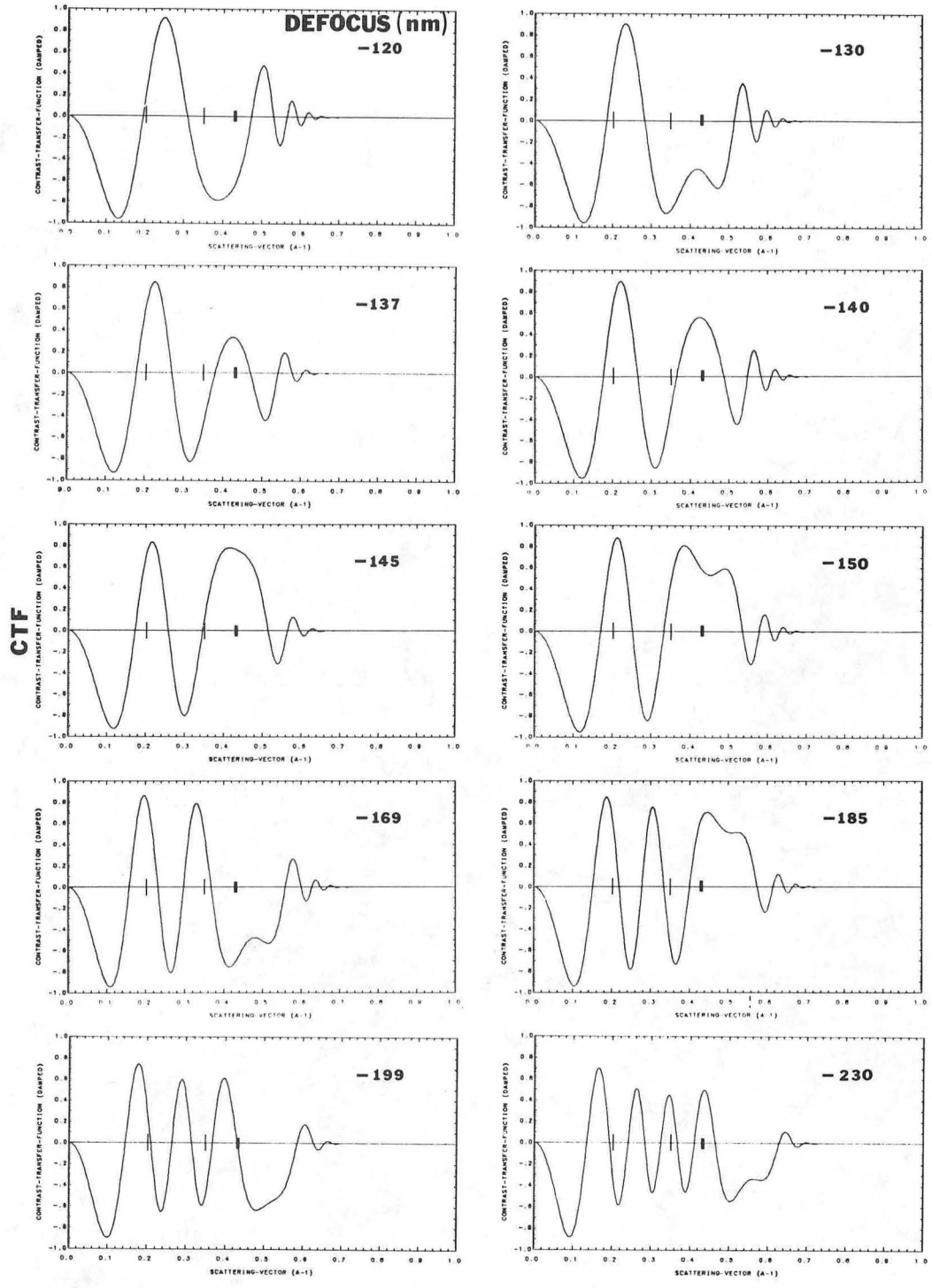

XBL 858-3595

Fig. 14 (d)

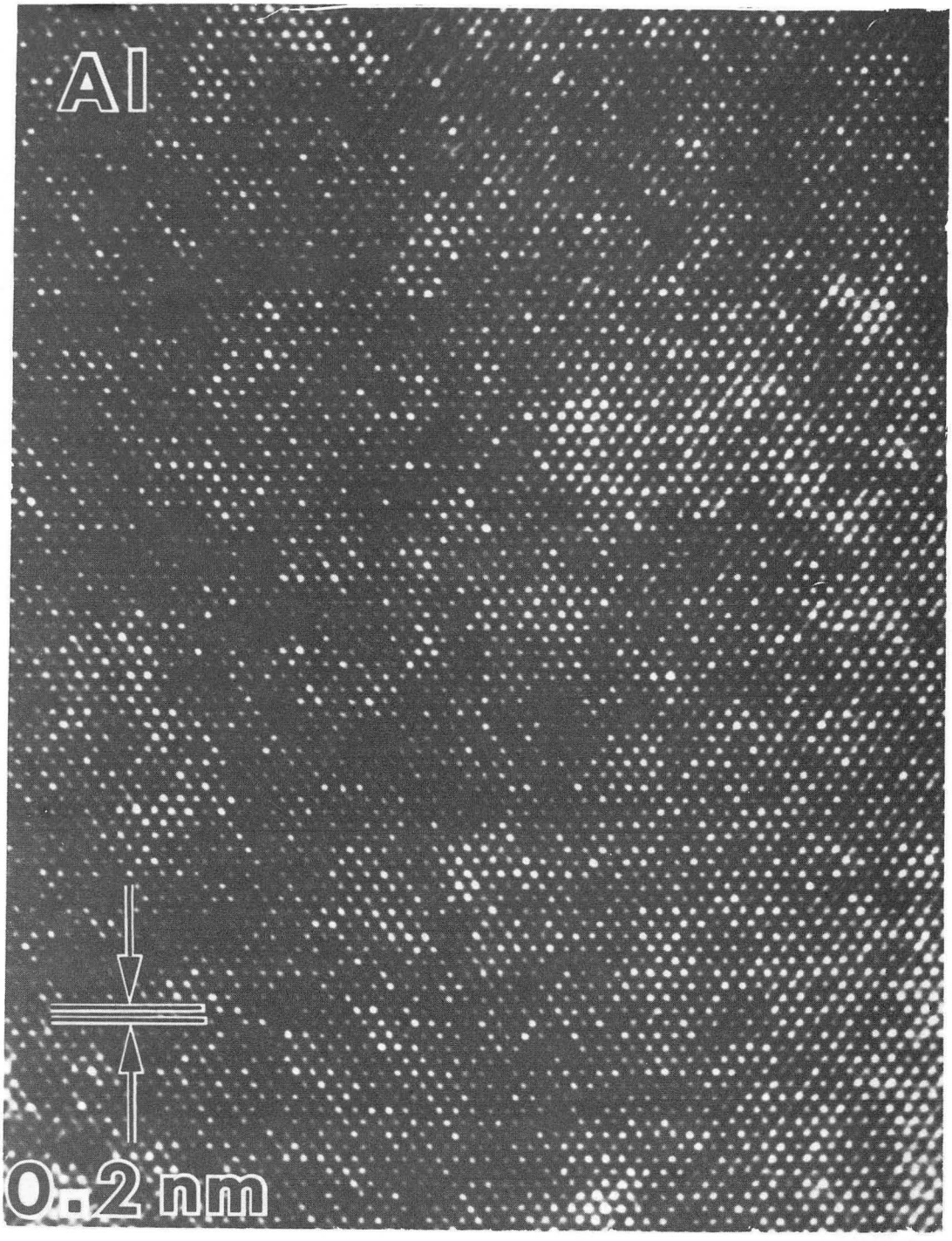

XBB 863-1682

Fig. 15

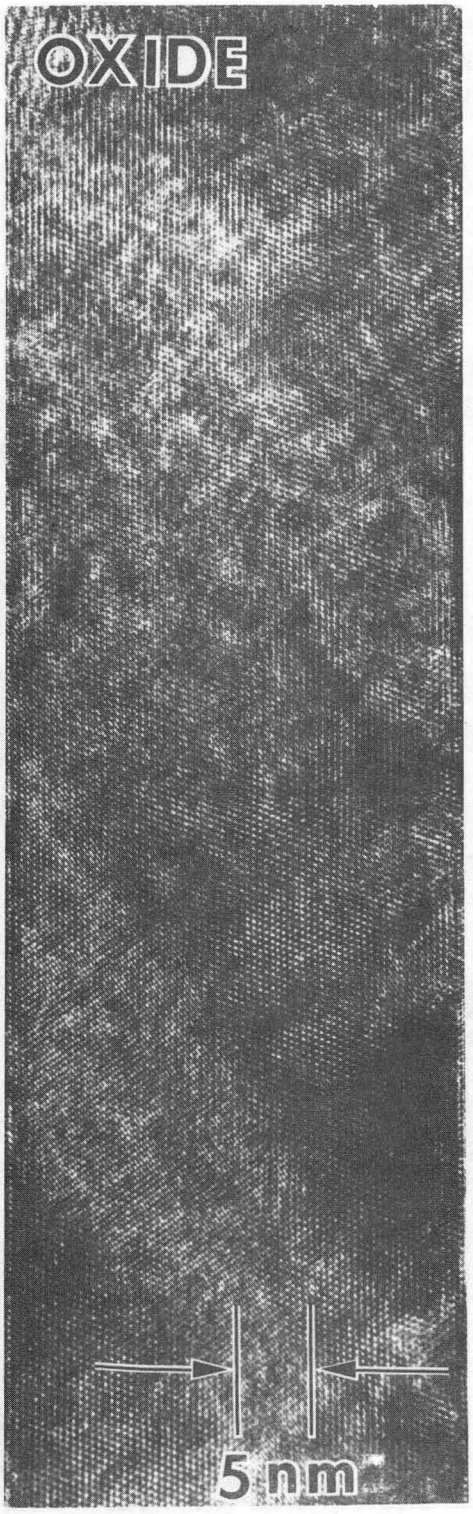

XBB 864-3061

Fig. 16

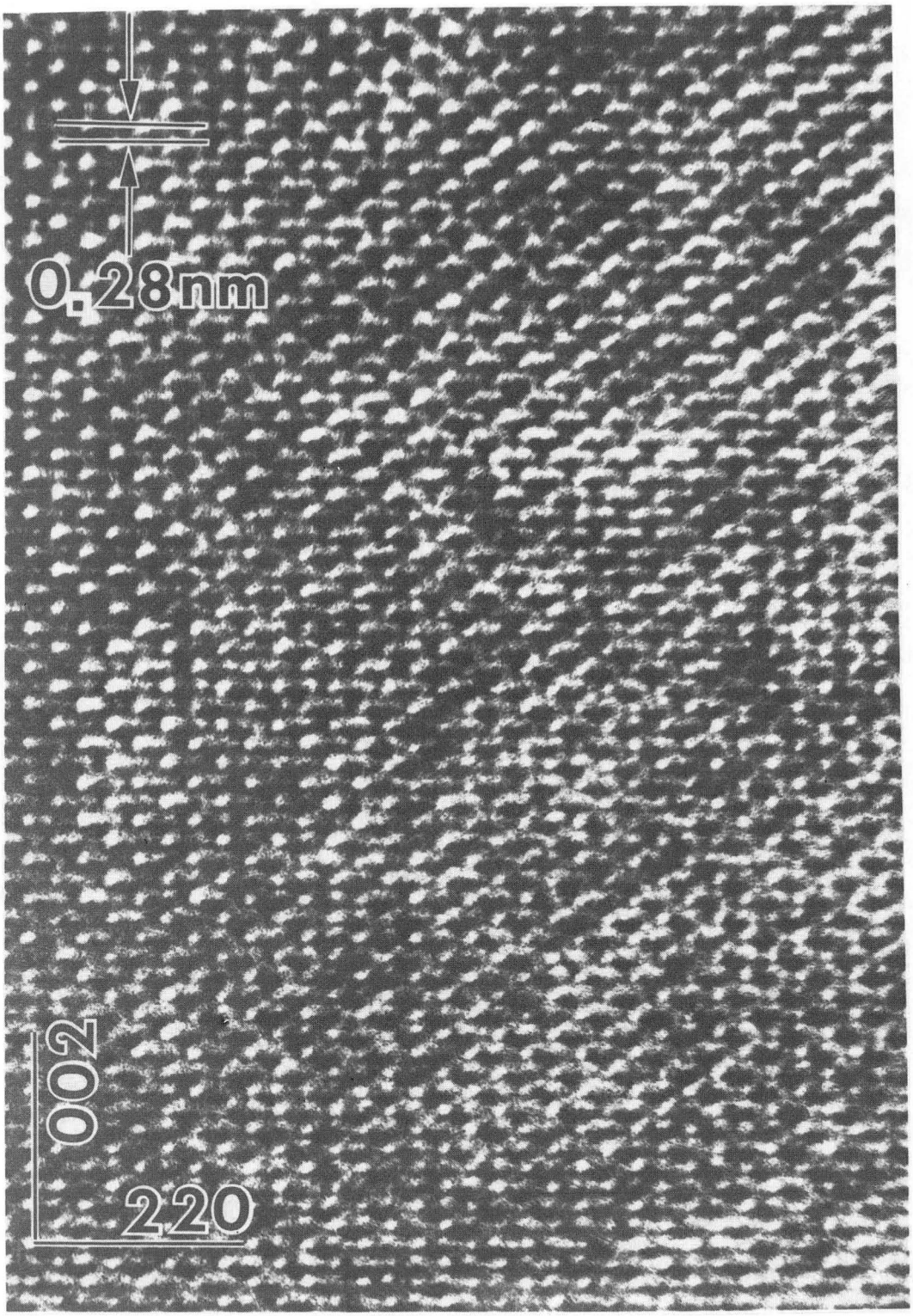

XBB 864-3062

Fig. 17 (a)

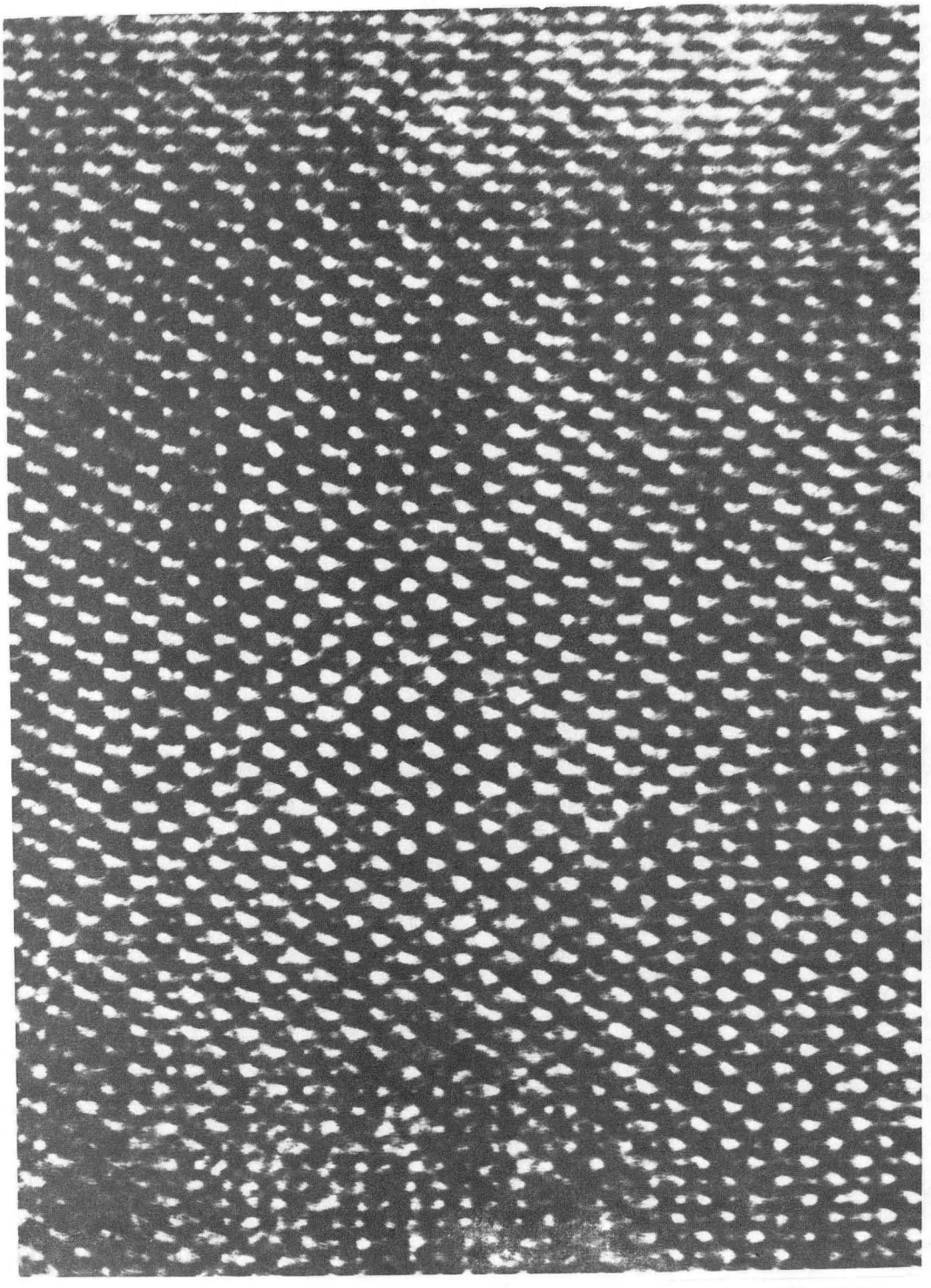

XBB 864-3063

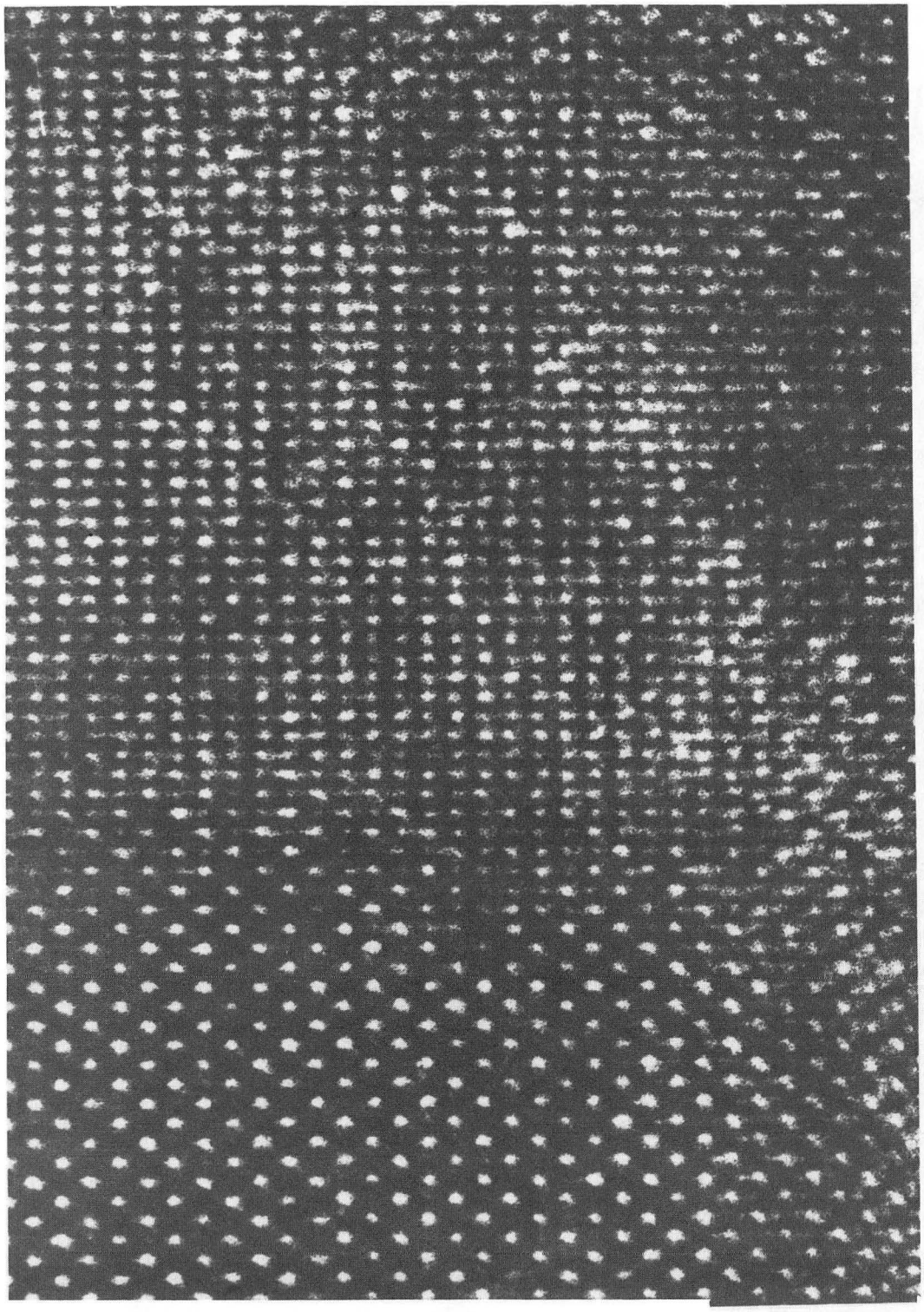

XBB 864-3066

Fig. 17 (c)

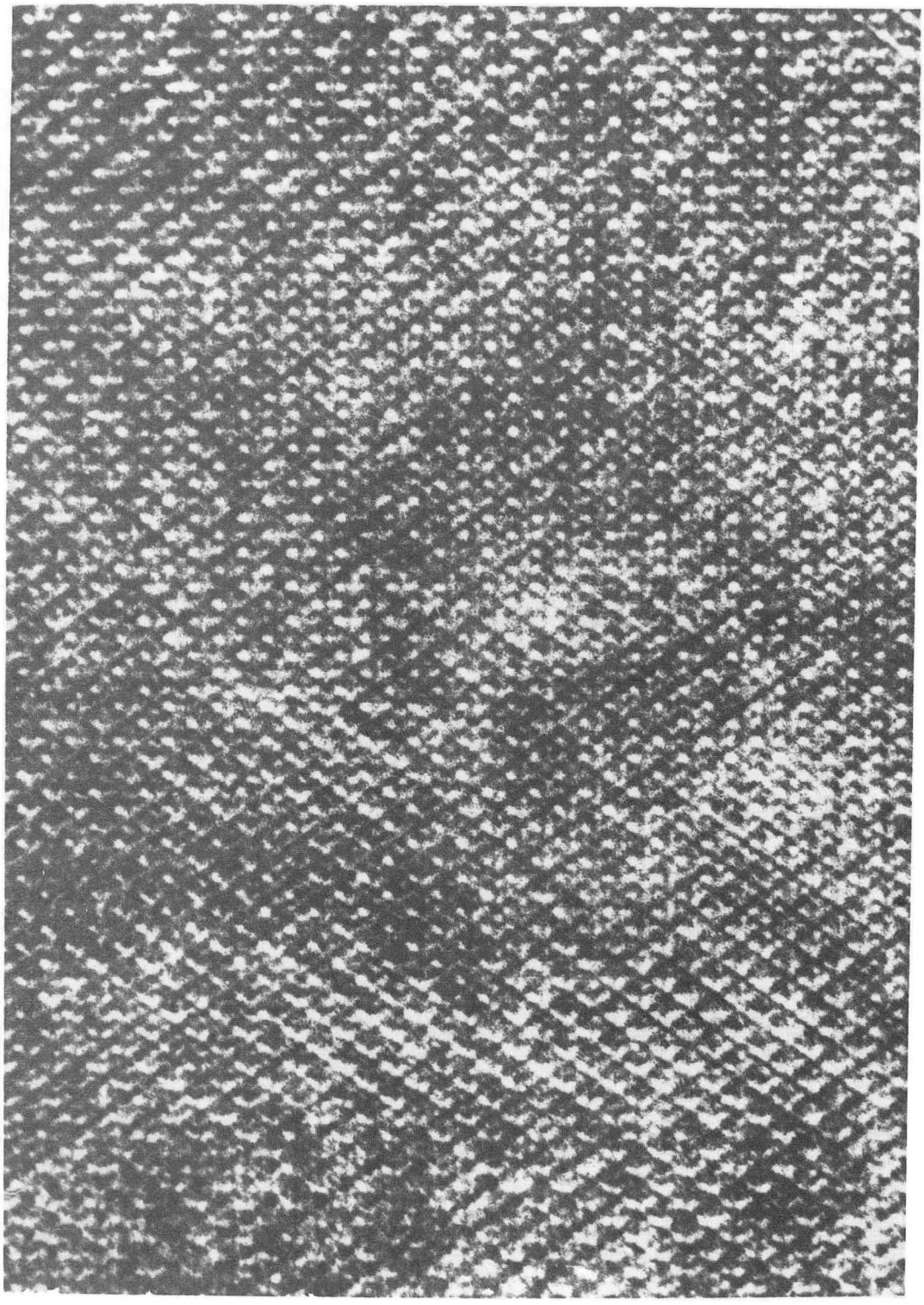

XBB 864-3065

Fig. 17 (d)

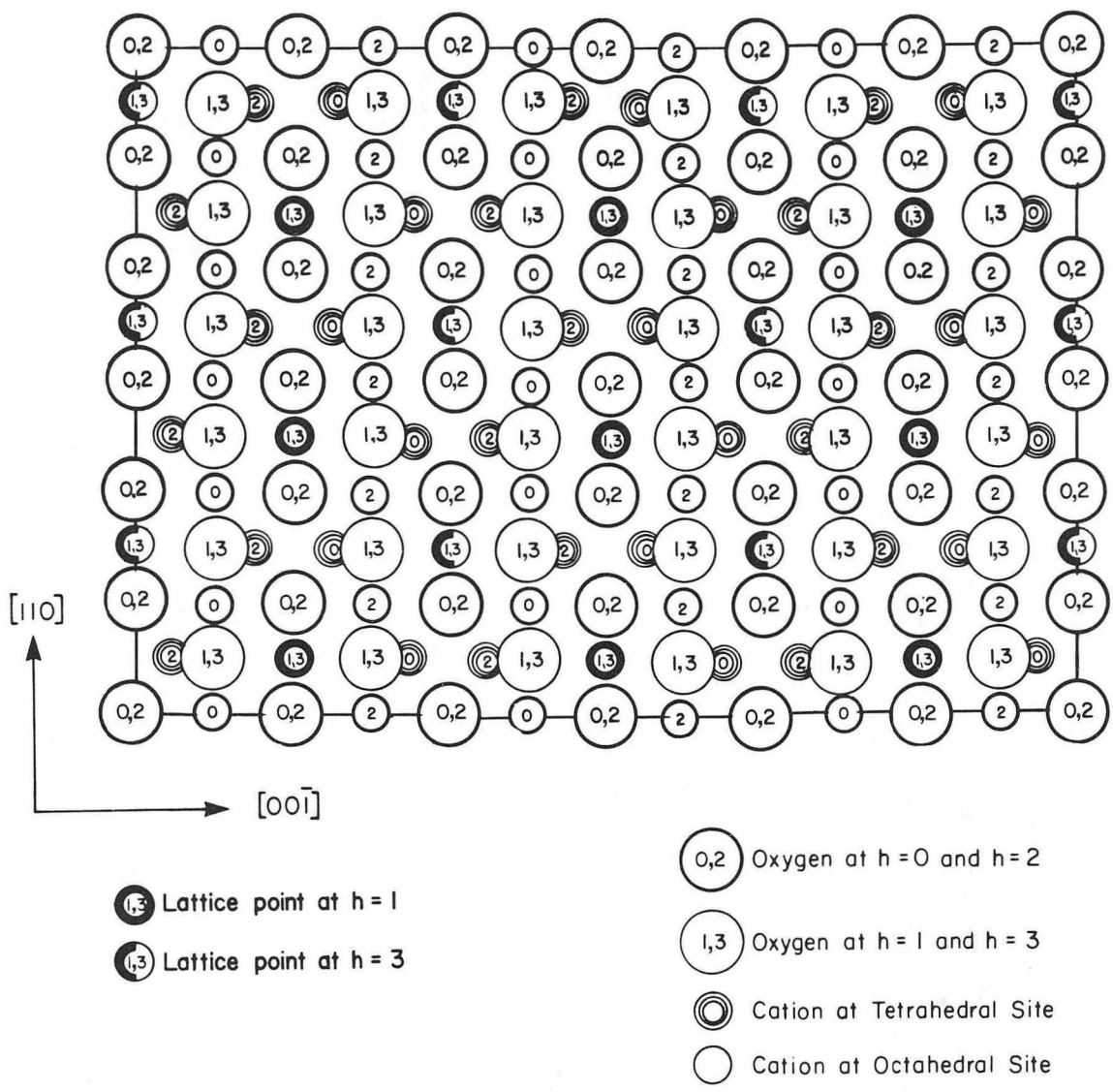
Oxide calculational unit cell for image simulations
[110]
[00$\bar{1}$]
Lattice point at h = 1
Lattice point at h = 3
0,2 Oxygen at h = 0 and h = 2
1,3 Oxygen at h = 1 and h = 3
Cation at Tetrahedral Site
Cation at Octahedral Site
XBL 8510-11714

Fig. 18

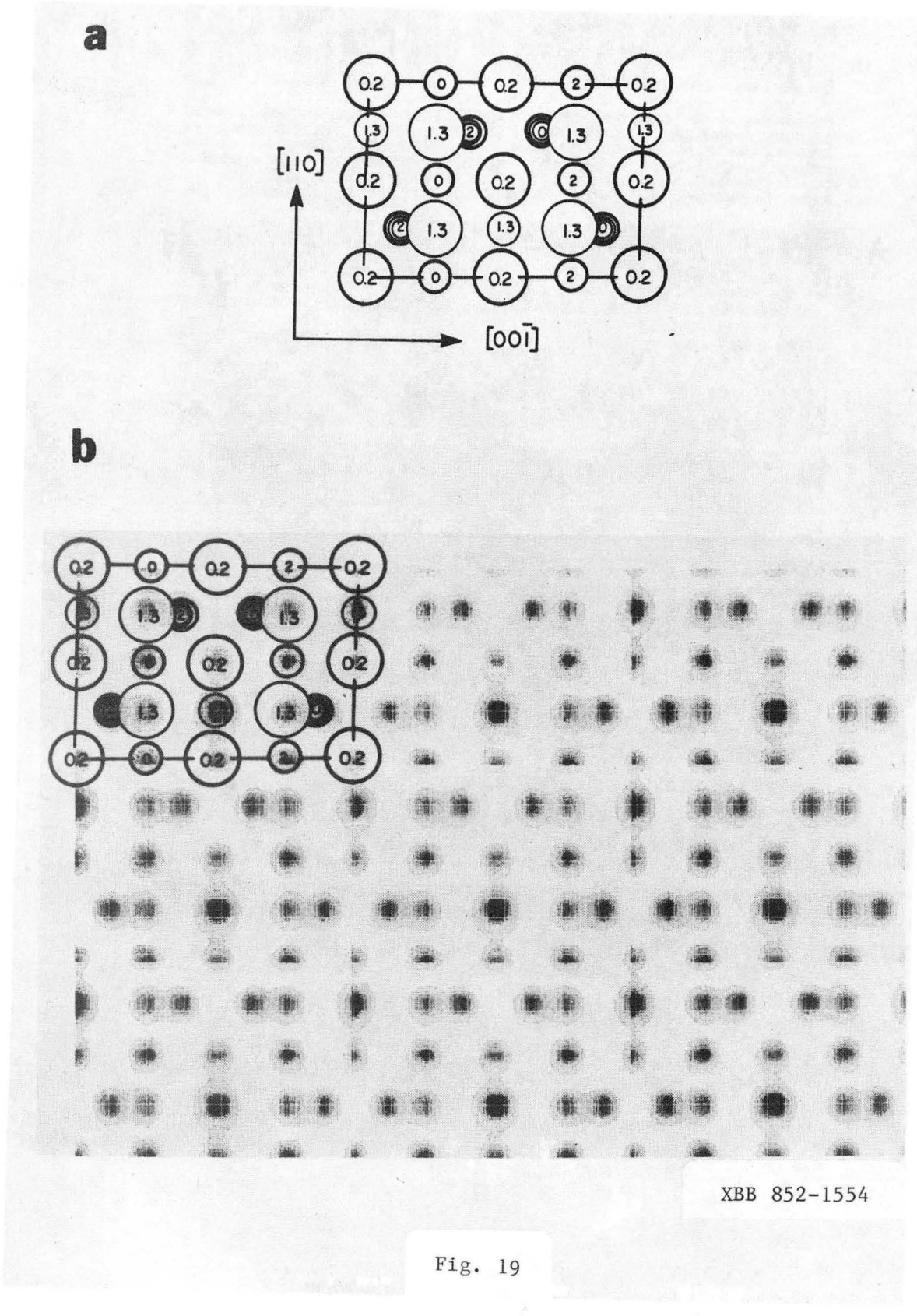

XBB 852-1554

Fig. 19

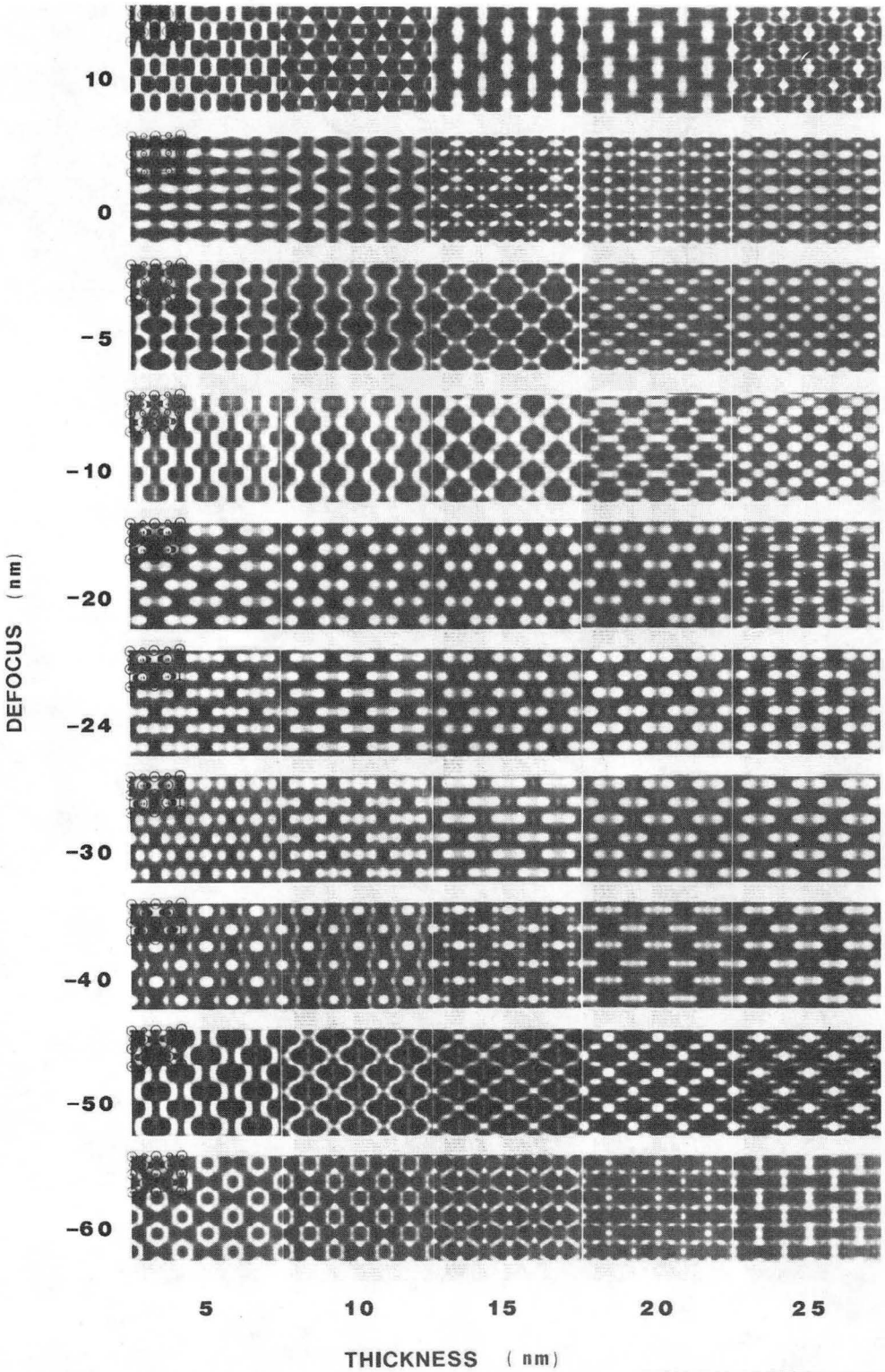

XBB 857-5423

Fig. 20 (a)

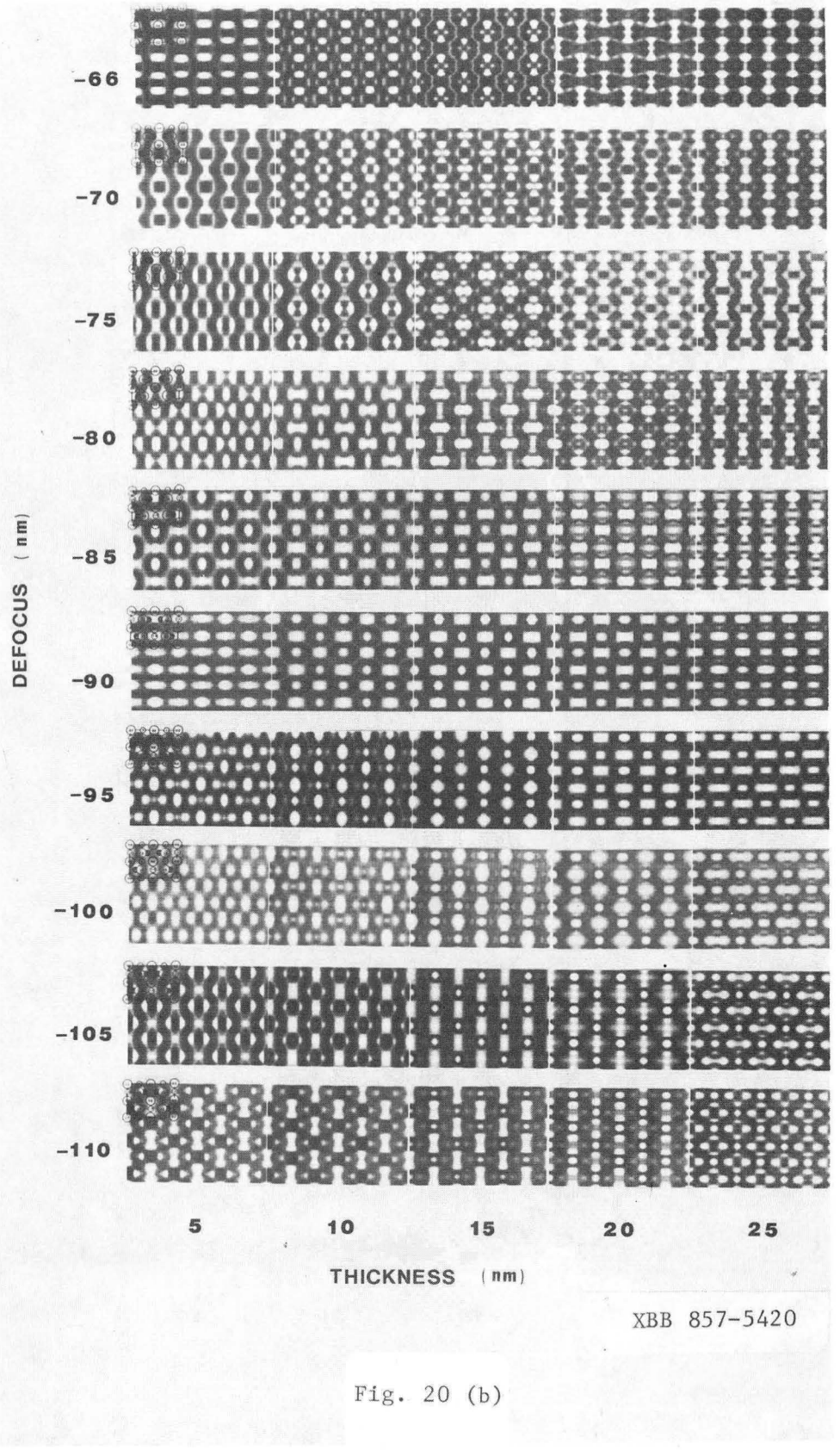
-66
-70
-75
-80
-85
-90
-95
-100
-105
-110
DEFOCUS (nm)
5
10
15
20
25
THICKNESS (nm)
XBB 857-5420

Fig. 20 (b)

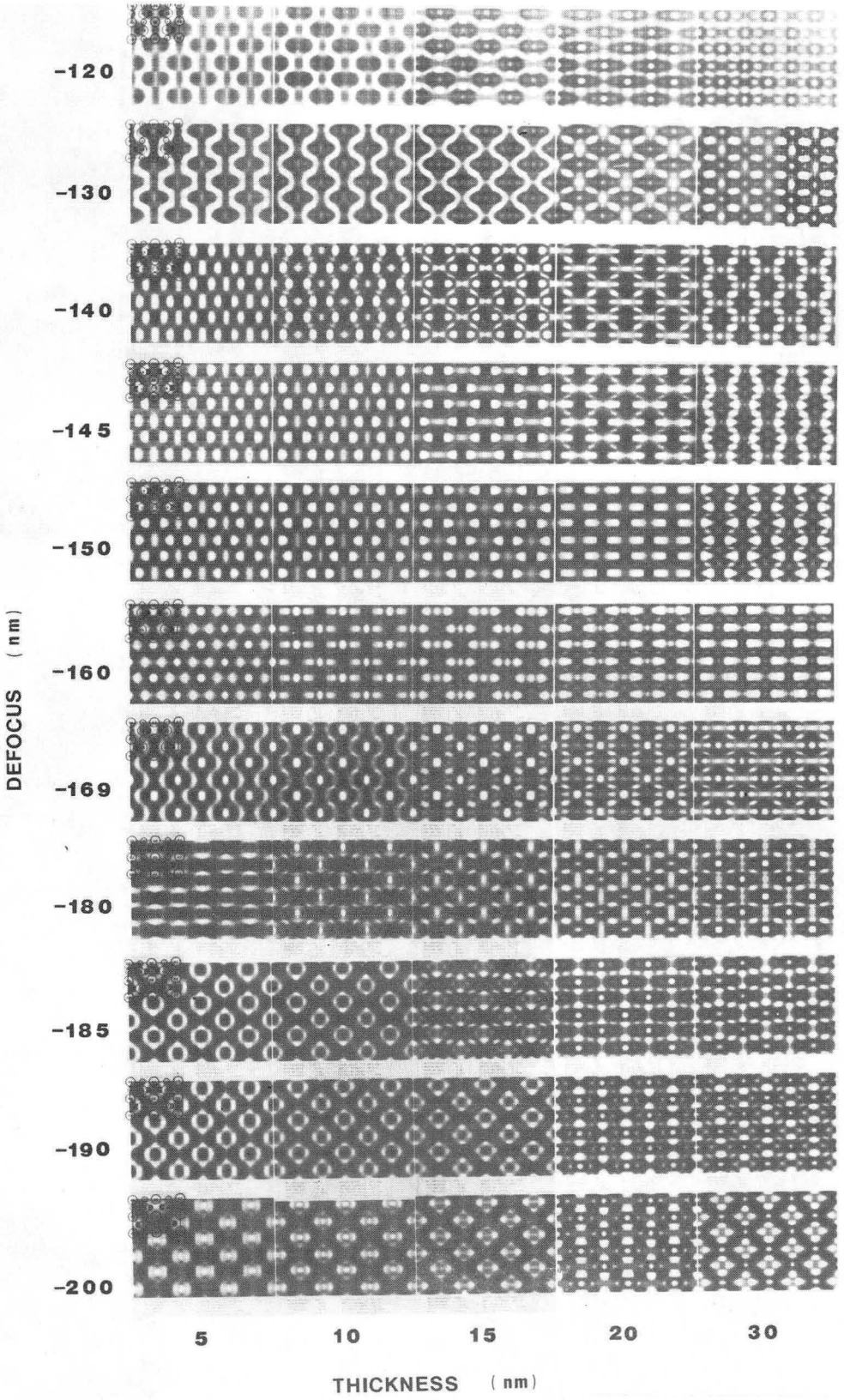

XBB 857-5421

Fig. 20 (c)

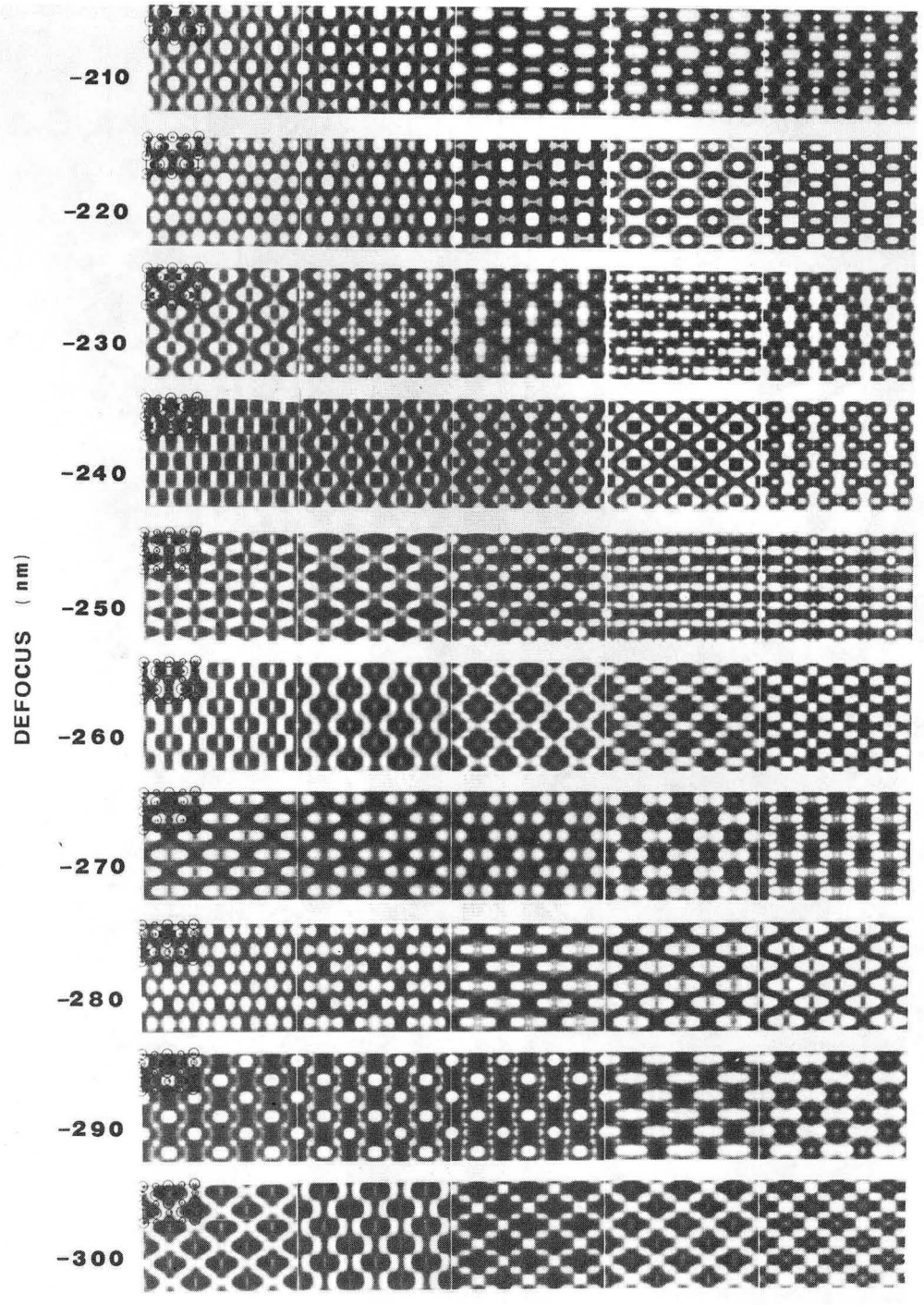

XBB 857-5422

Fig. 20 (d)

Experimental and simulated images of oxide

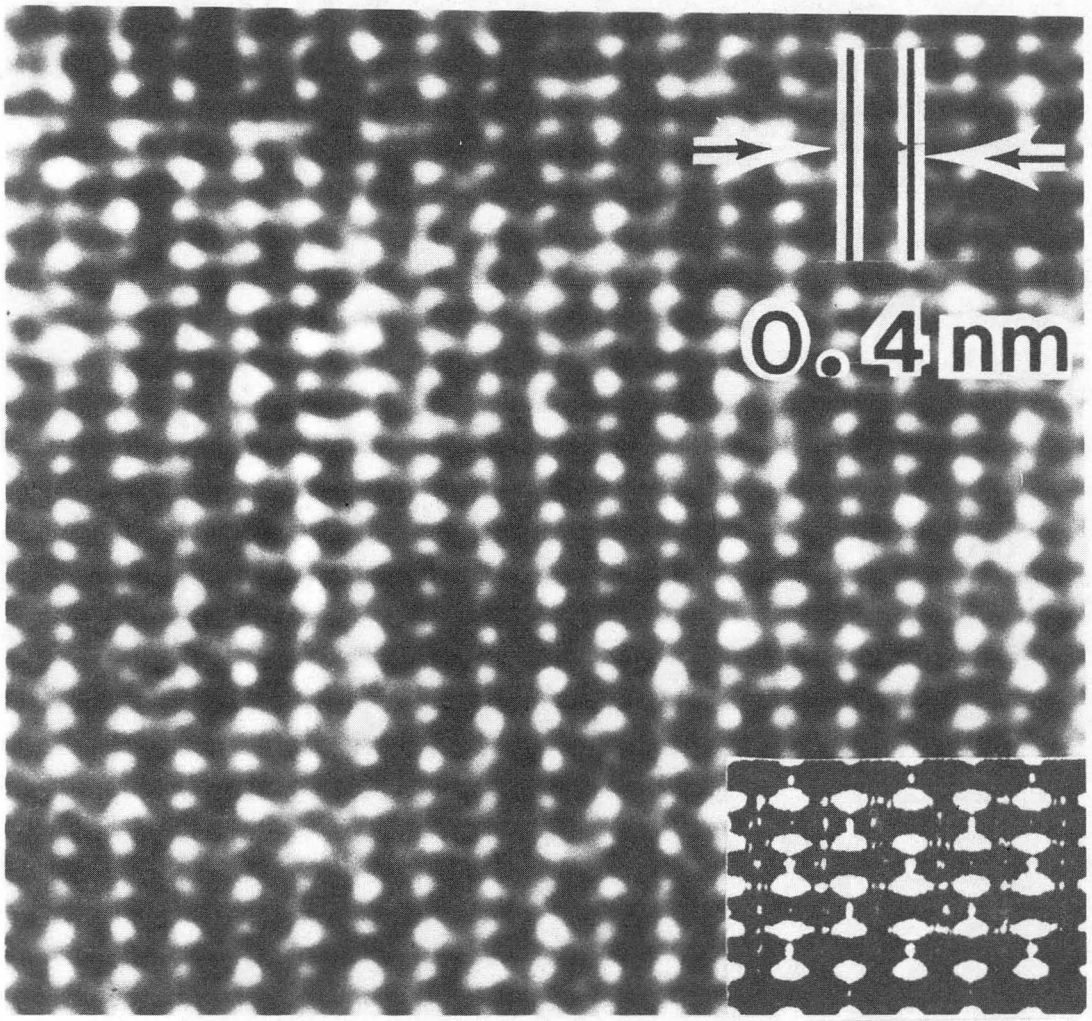

XBB 852-1551A

Fig. 21

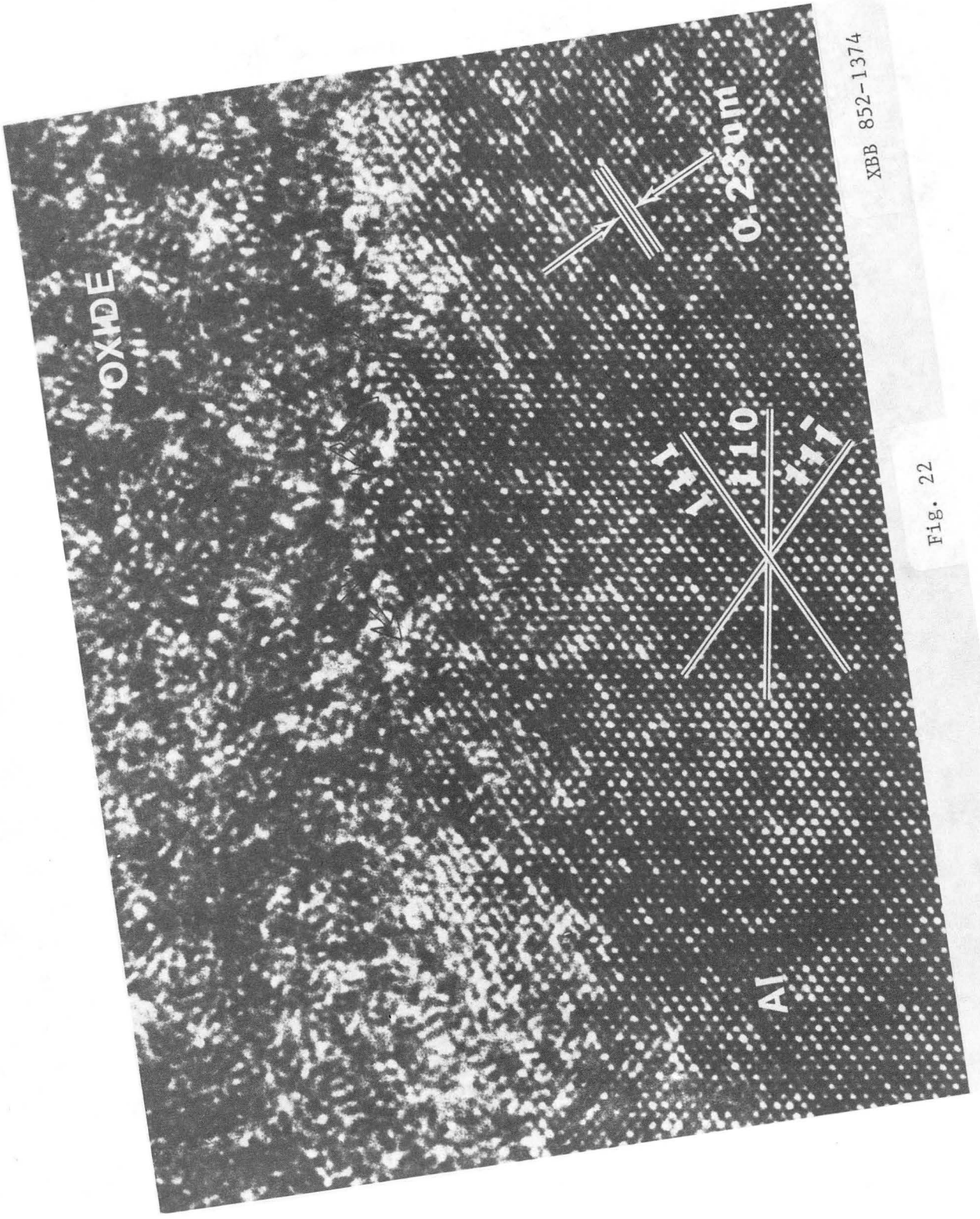

XBB 852-1374

Fig. 22

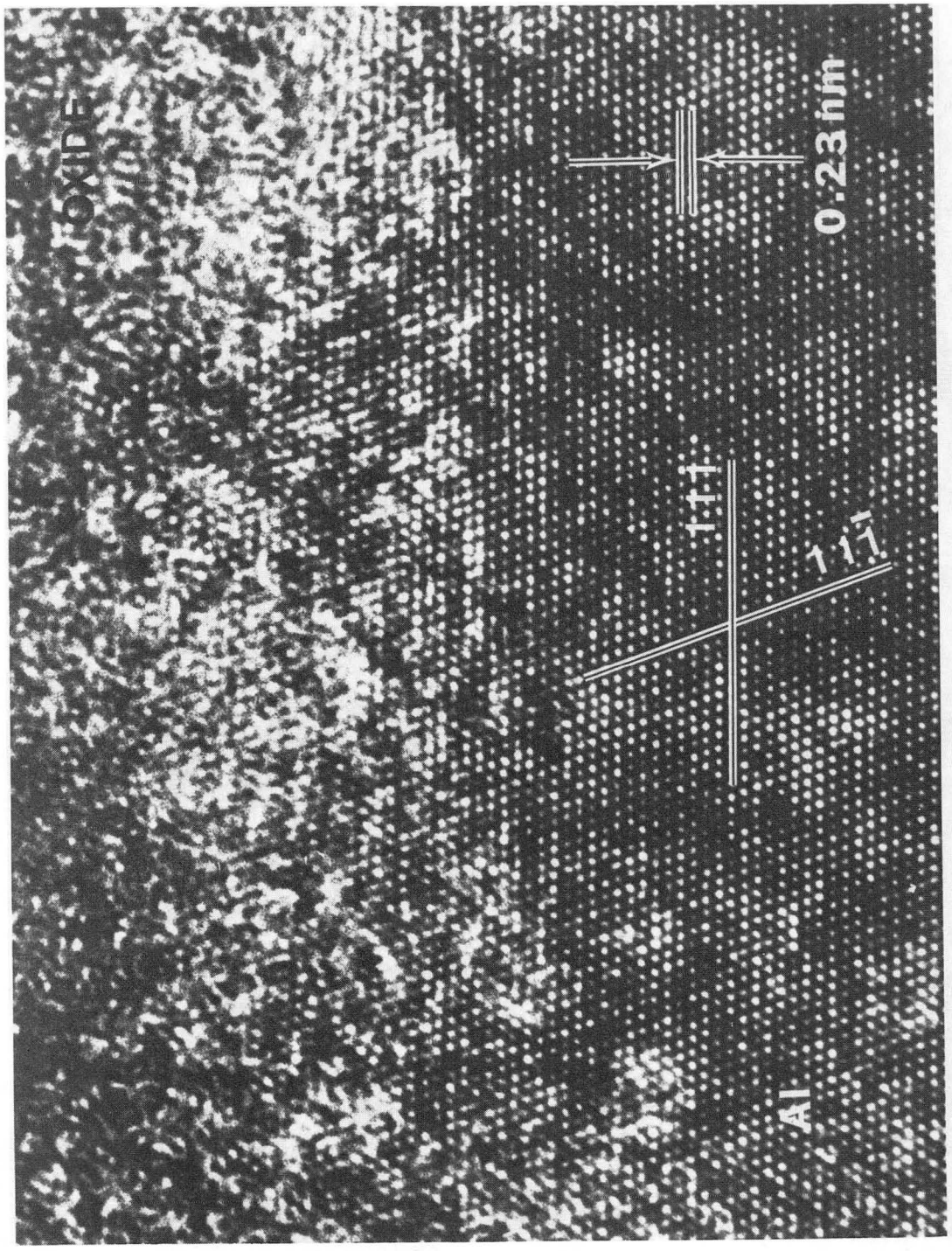

Fig. 23

XBB 852-1375

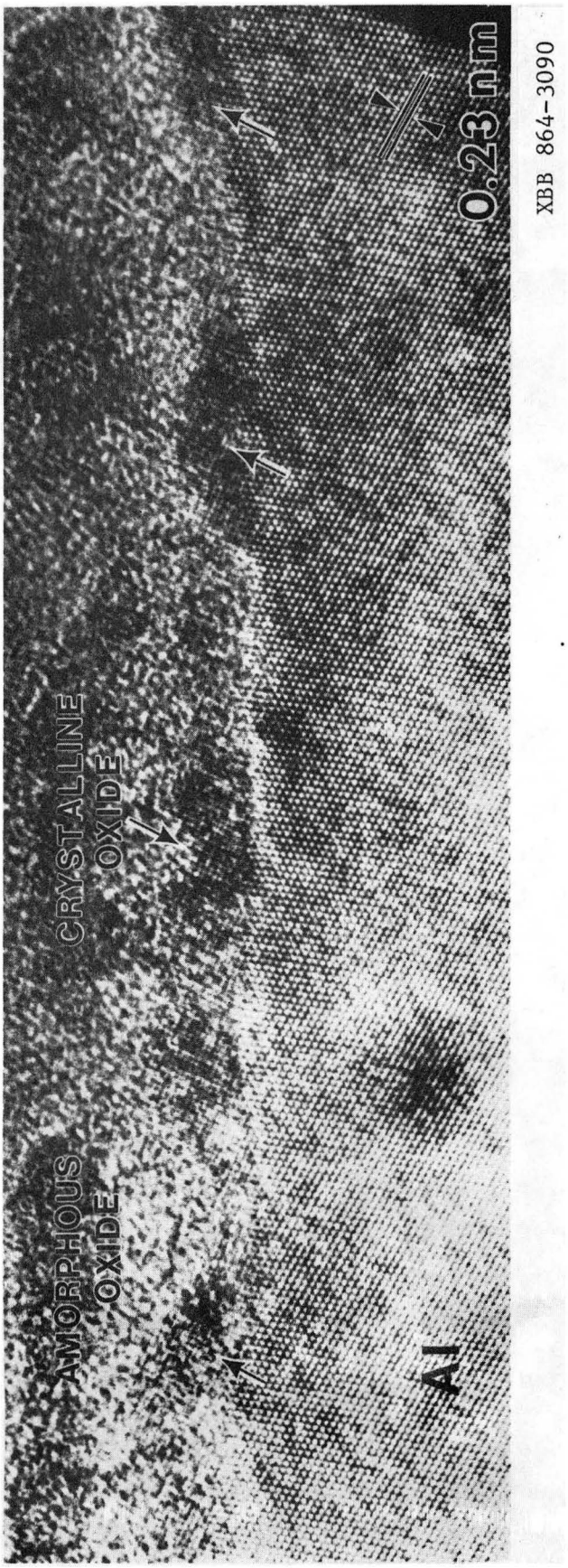

Fig. 24

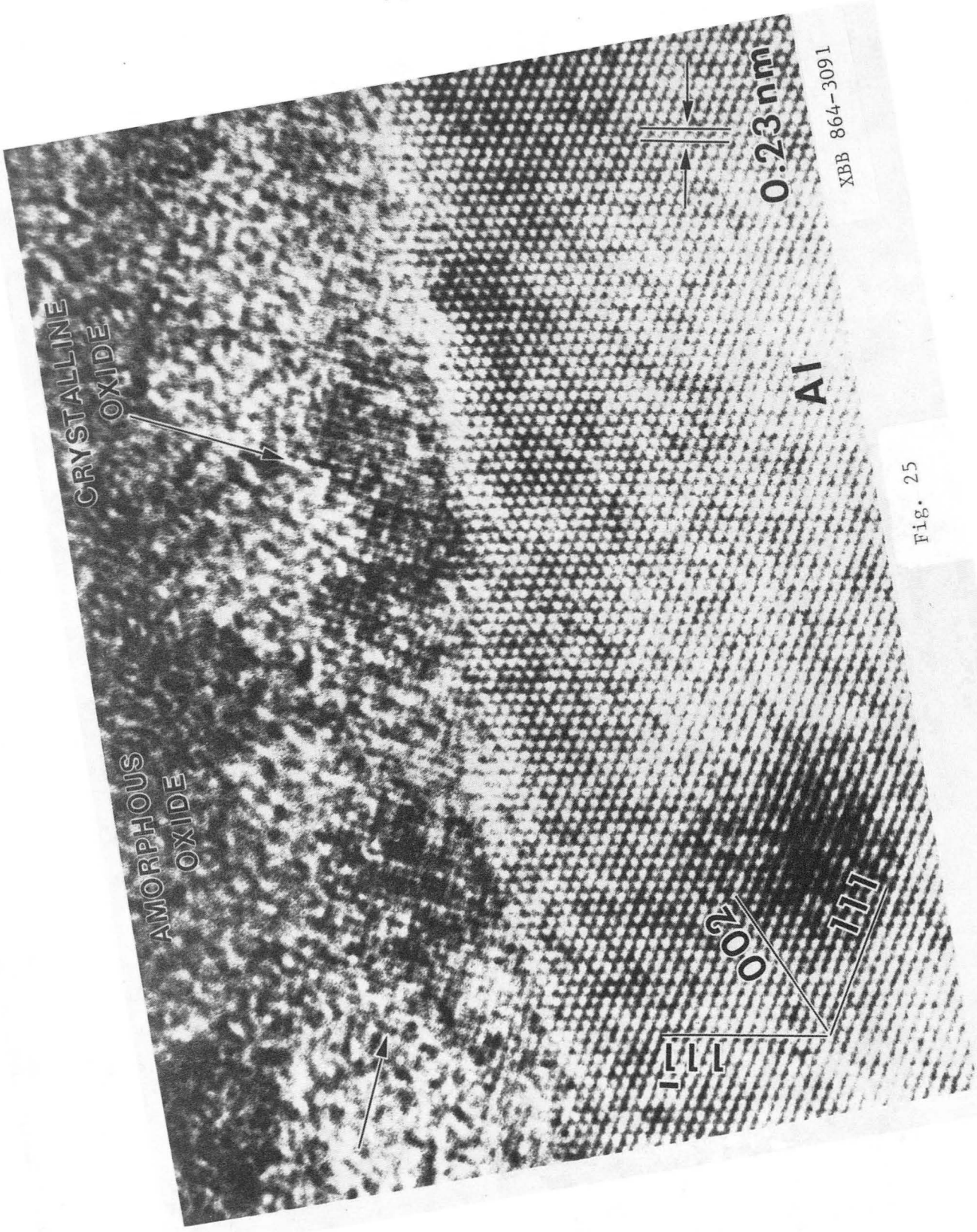

XBB 864-3091

Fig. 25

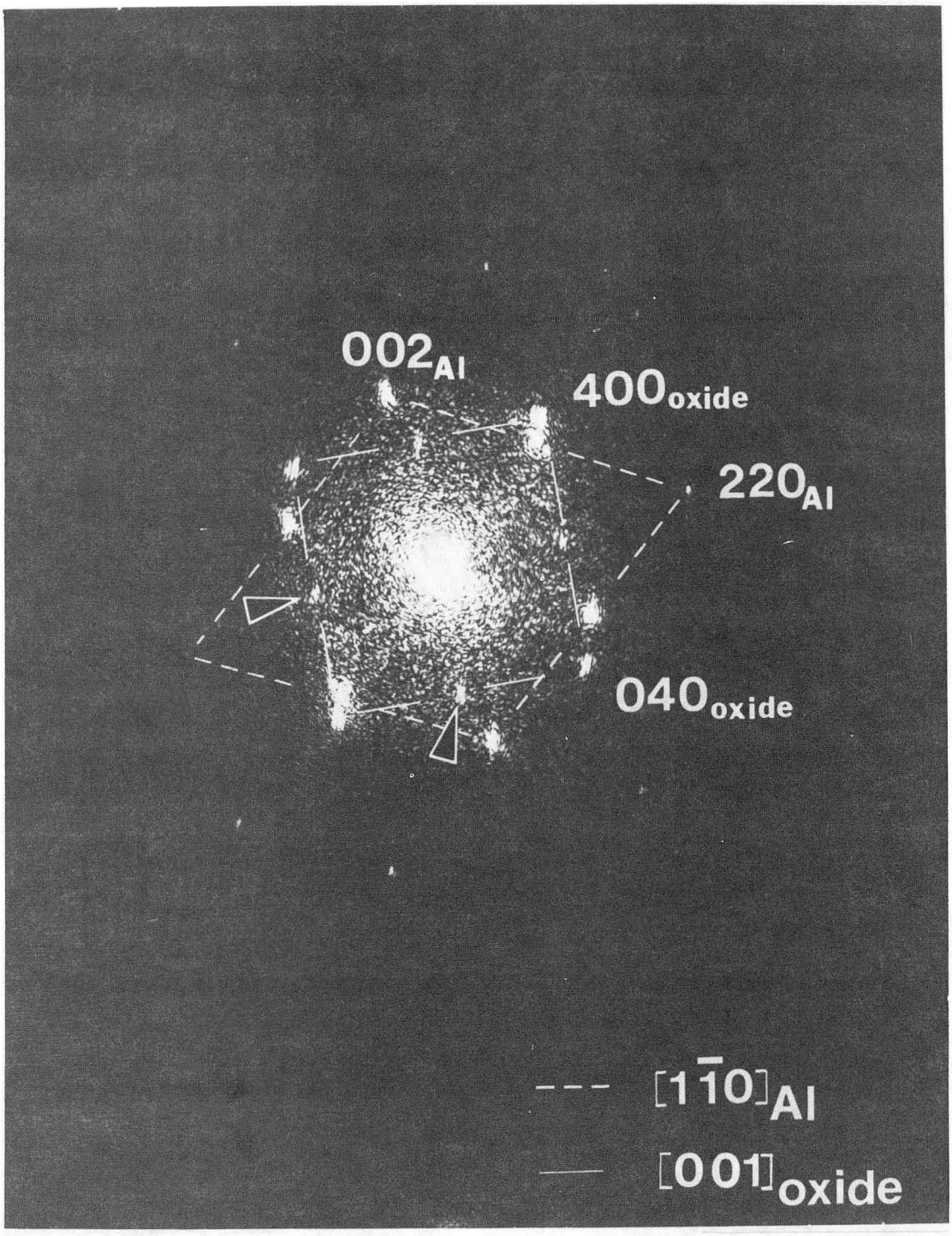

XBB 864-3101

Fig. 26

XBB 864-3087

Fig. 27

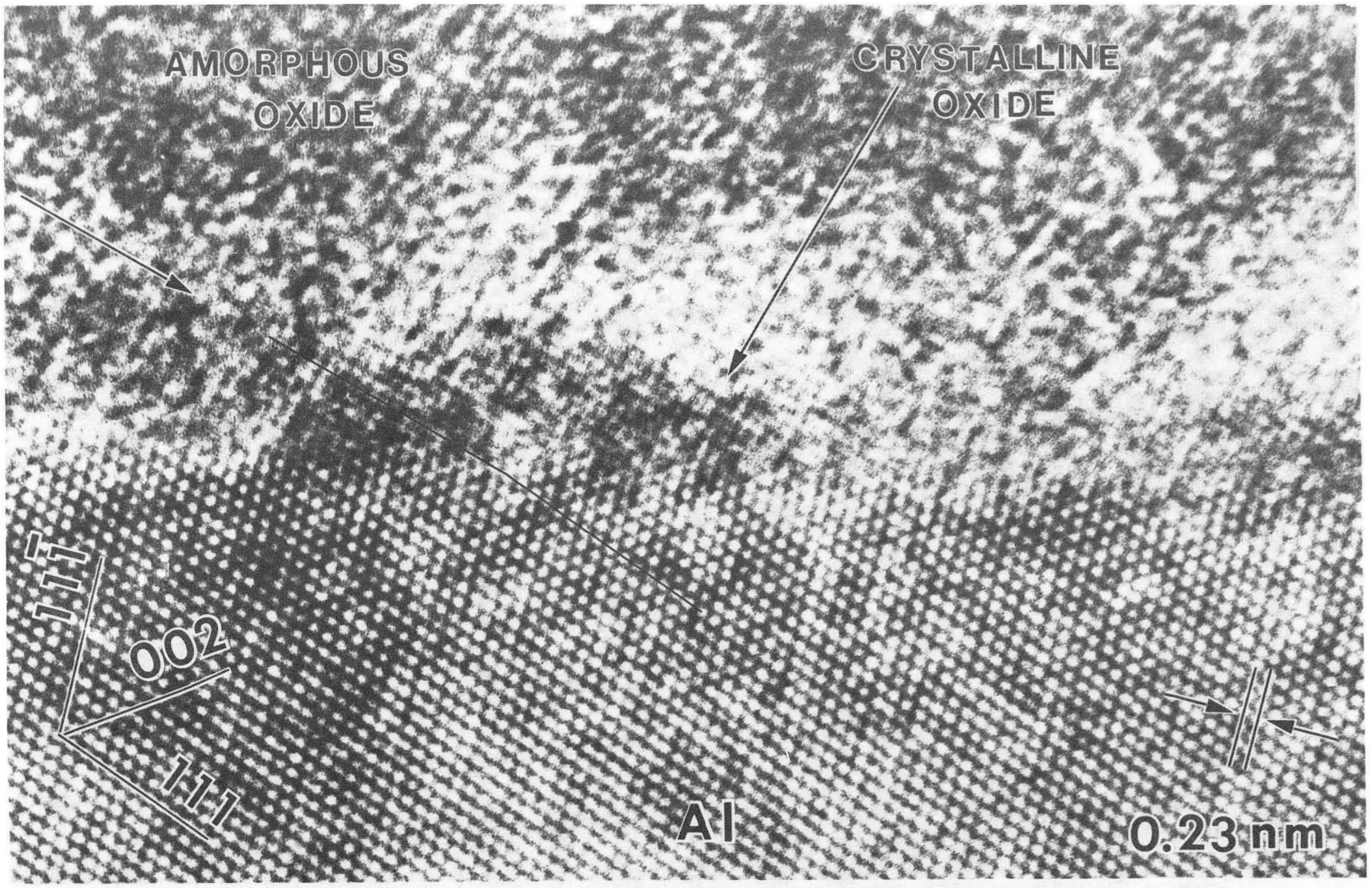

Fig. 28

XBB 864-3086

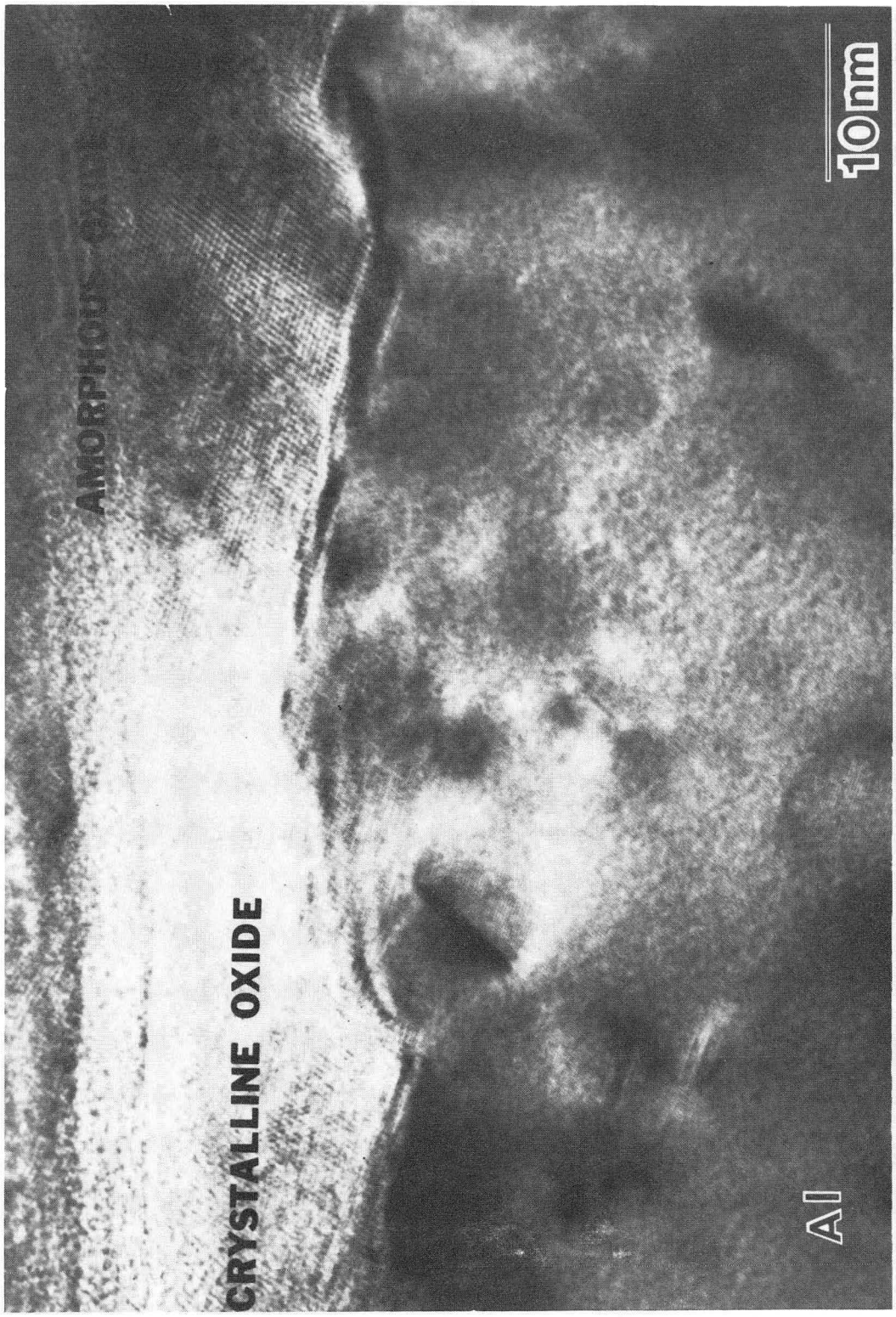

Fig. 29

XBB 863-1683

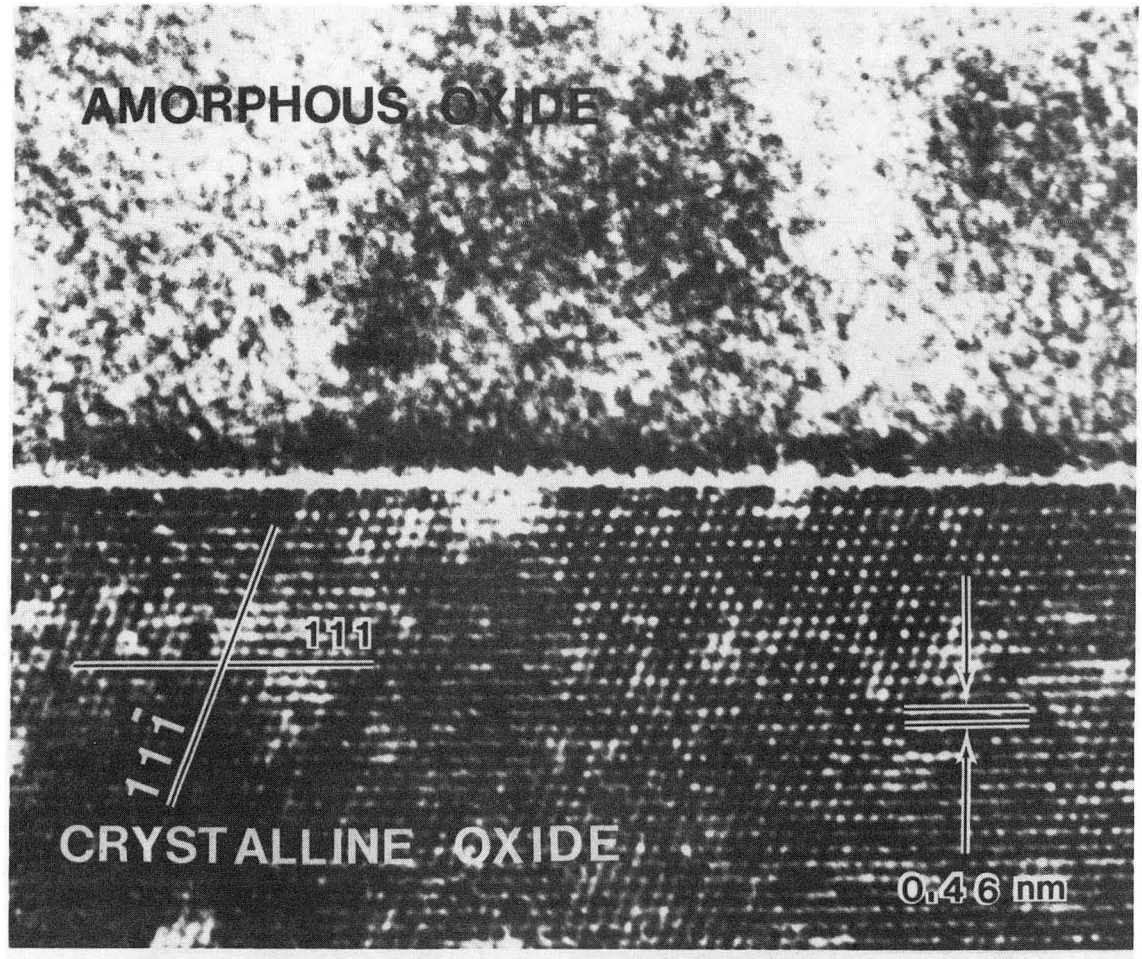

XBB 852-1376

Fig. 30

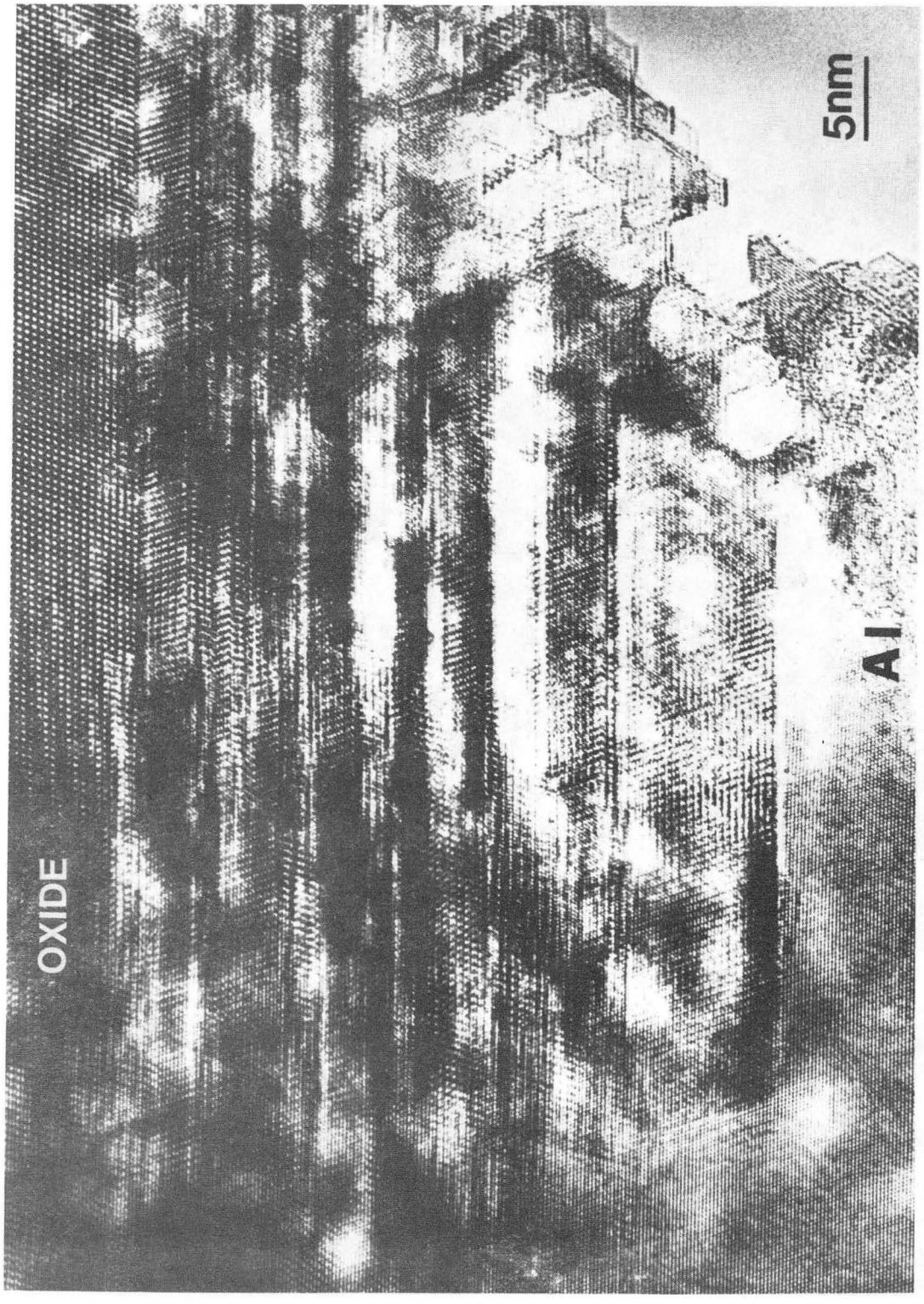

Fig. 31

XBB 864-3092

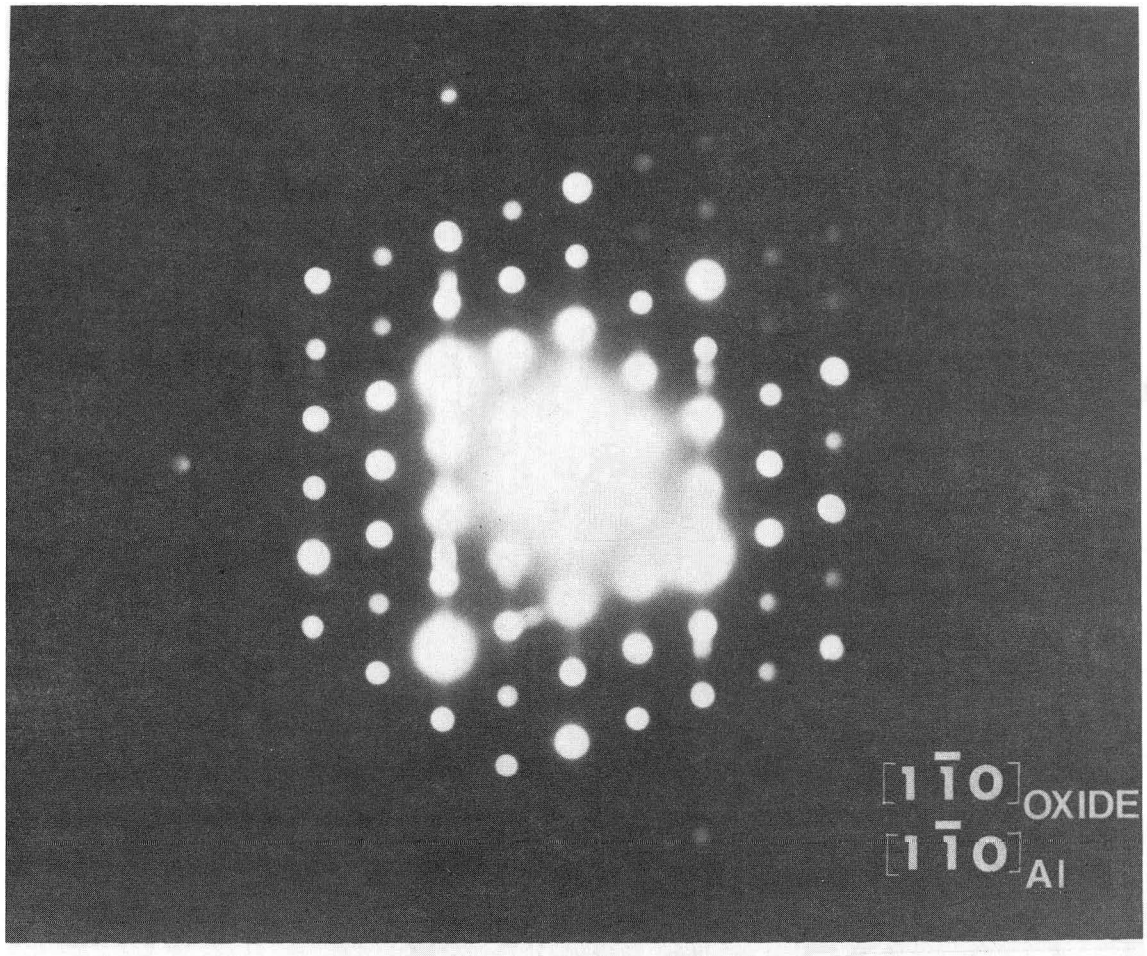

XBB 852-1698

Fig. 32

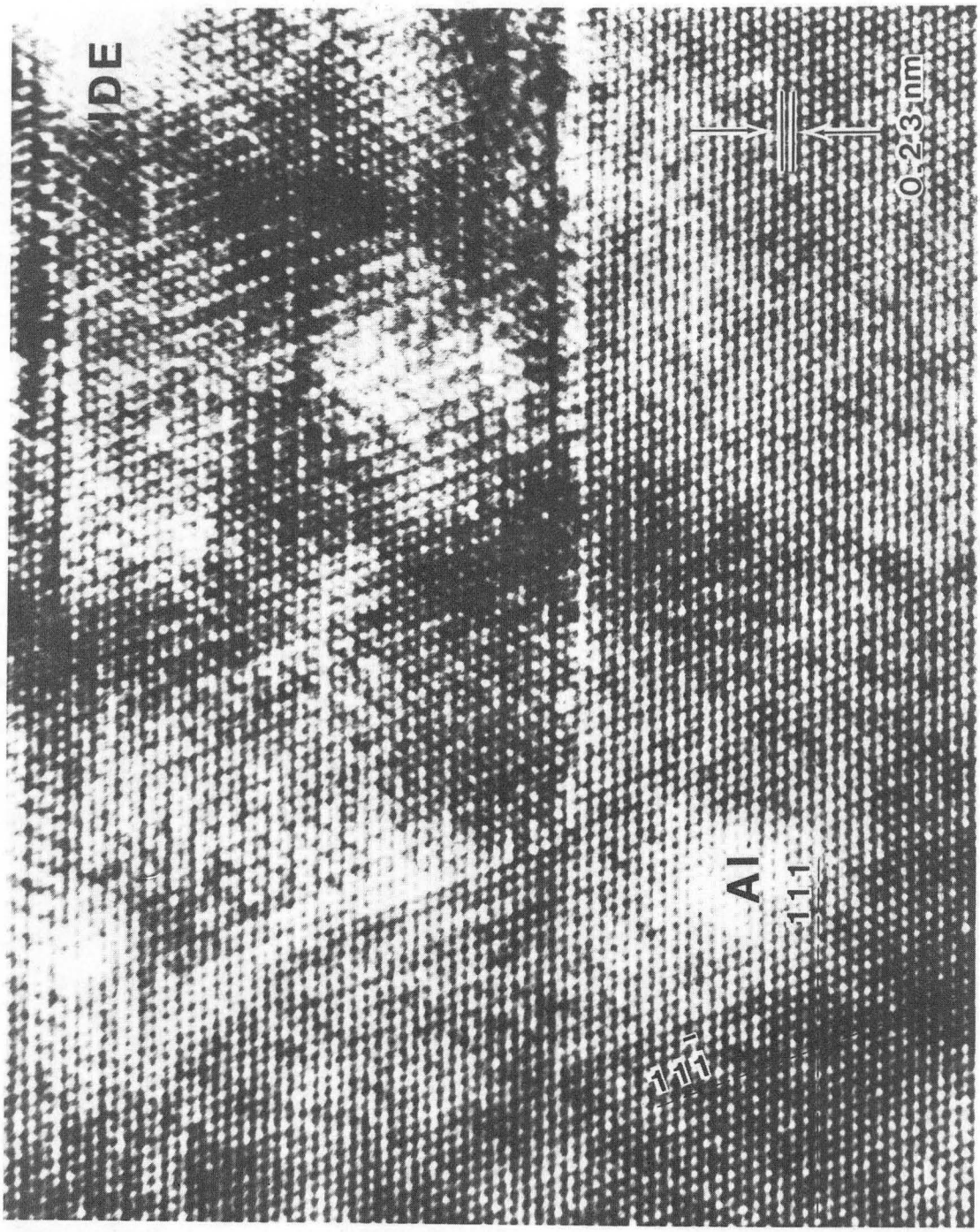

Fig. 33

XBB 857-5305

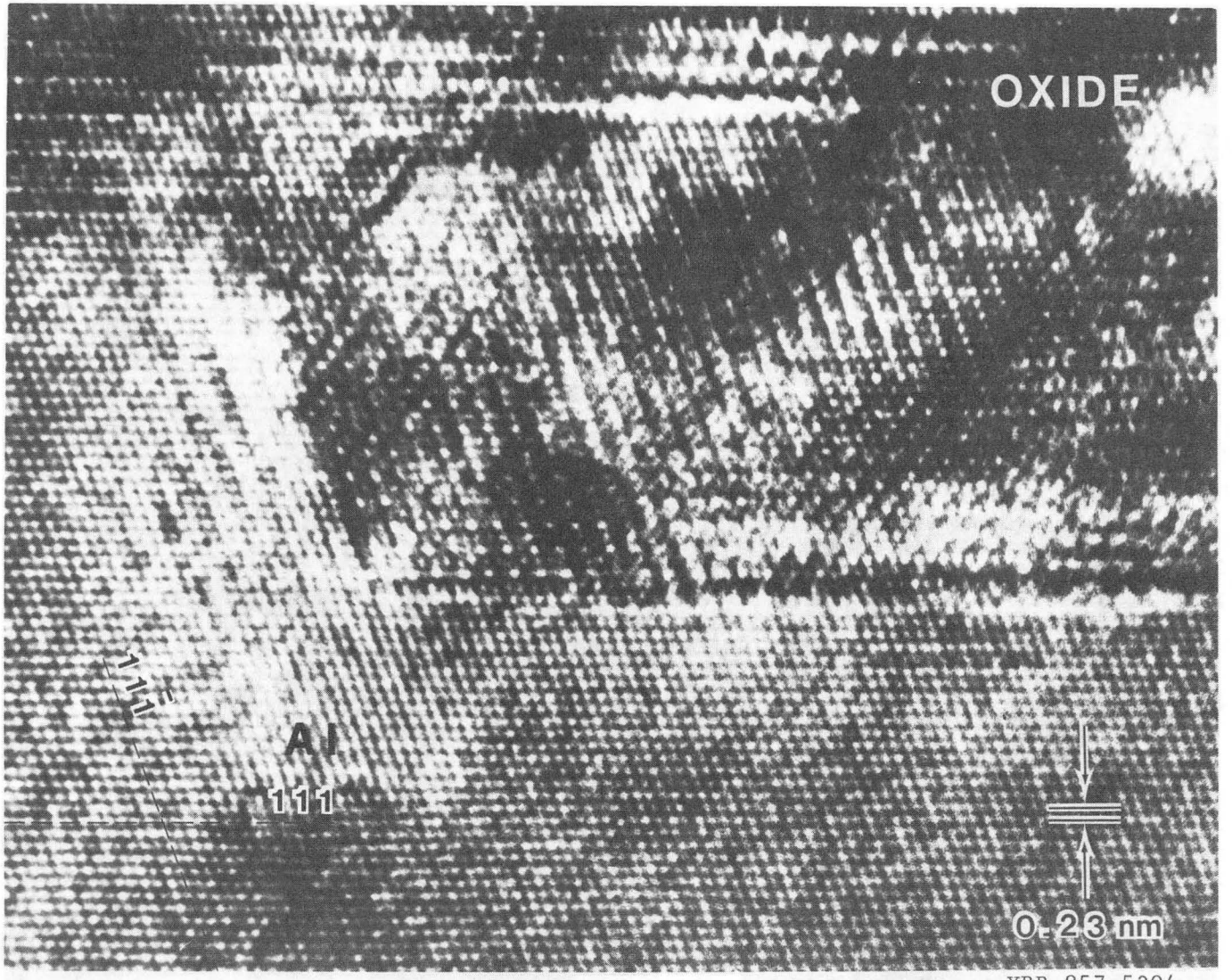

Fig. 34

XBB 857-5304

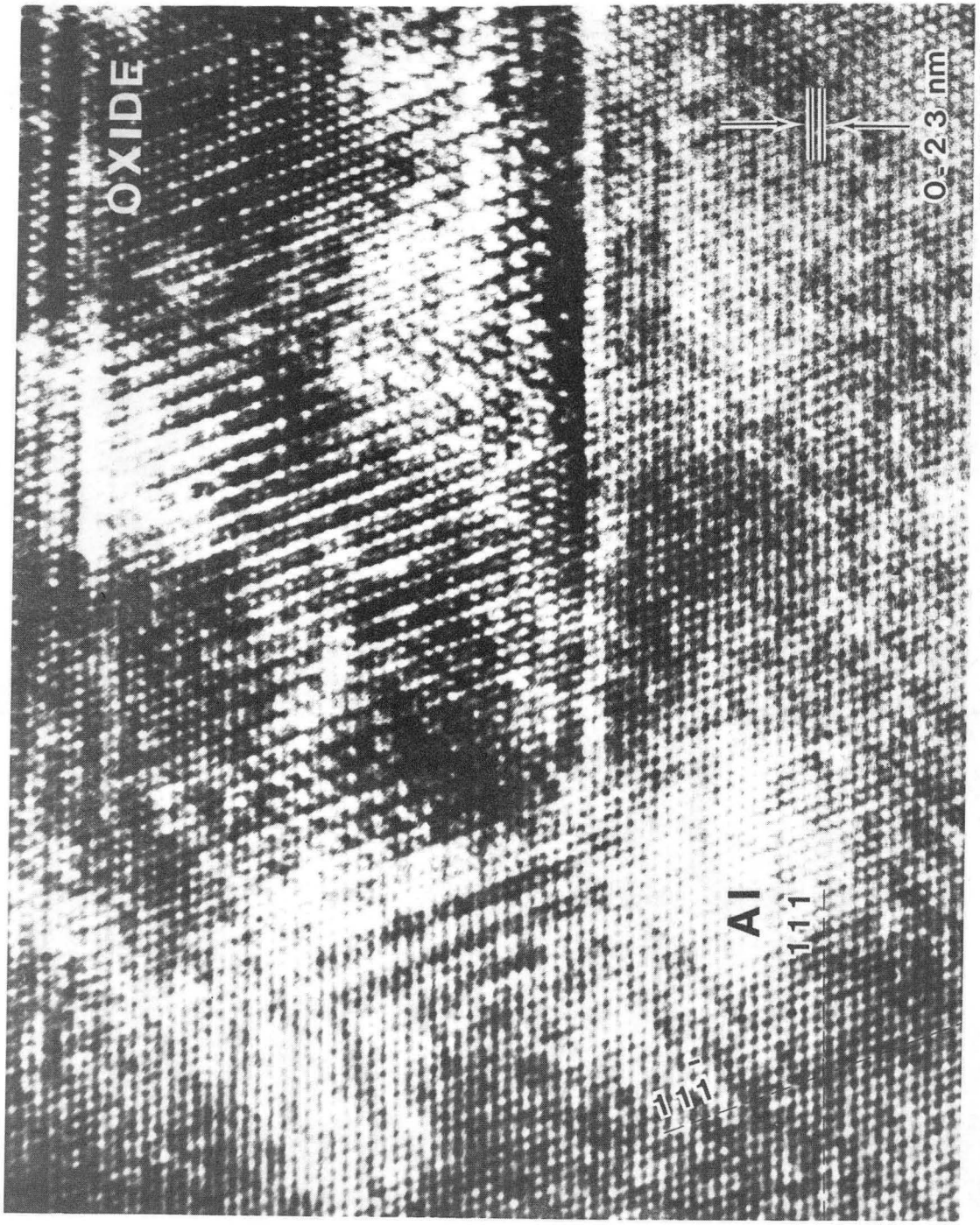

Fig. 35 (a)

XBB 857-5303

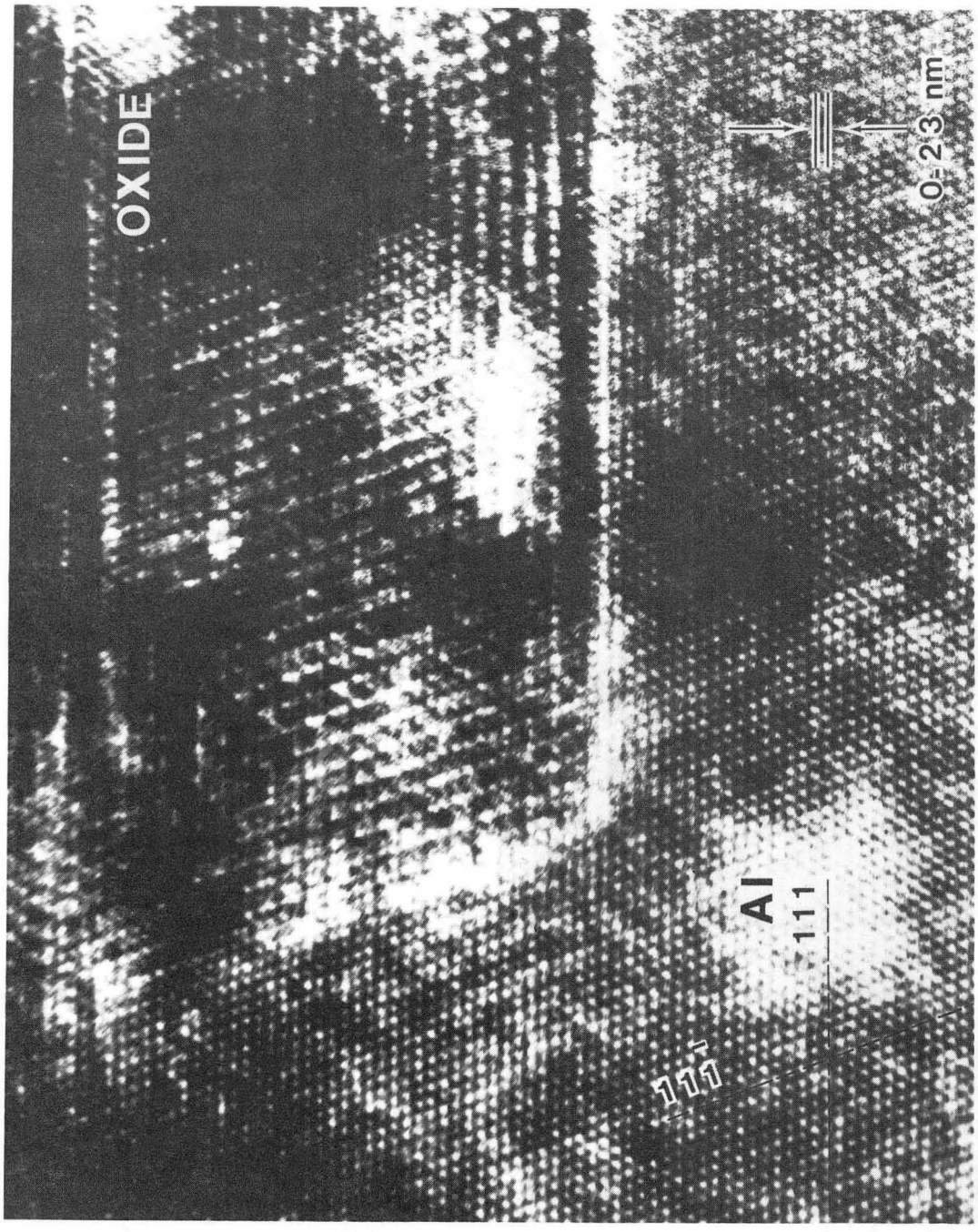

Fig. 35 (b)

XBB 857-5302

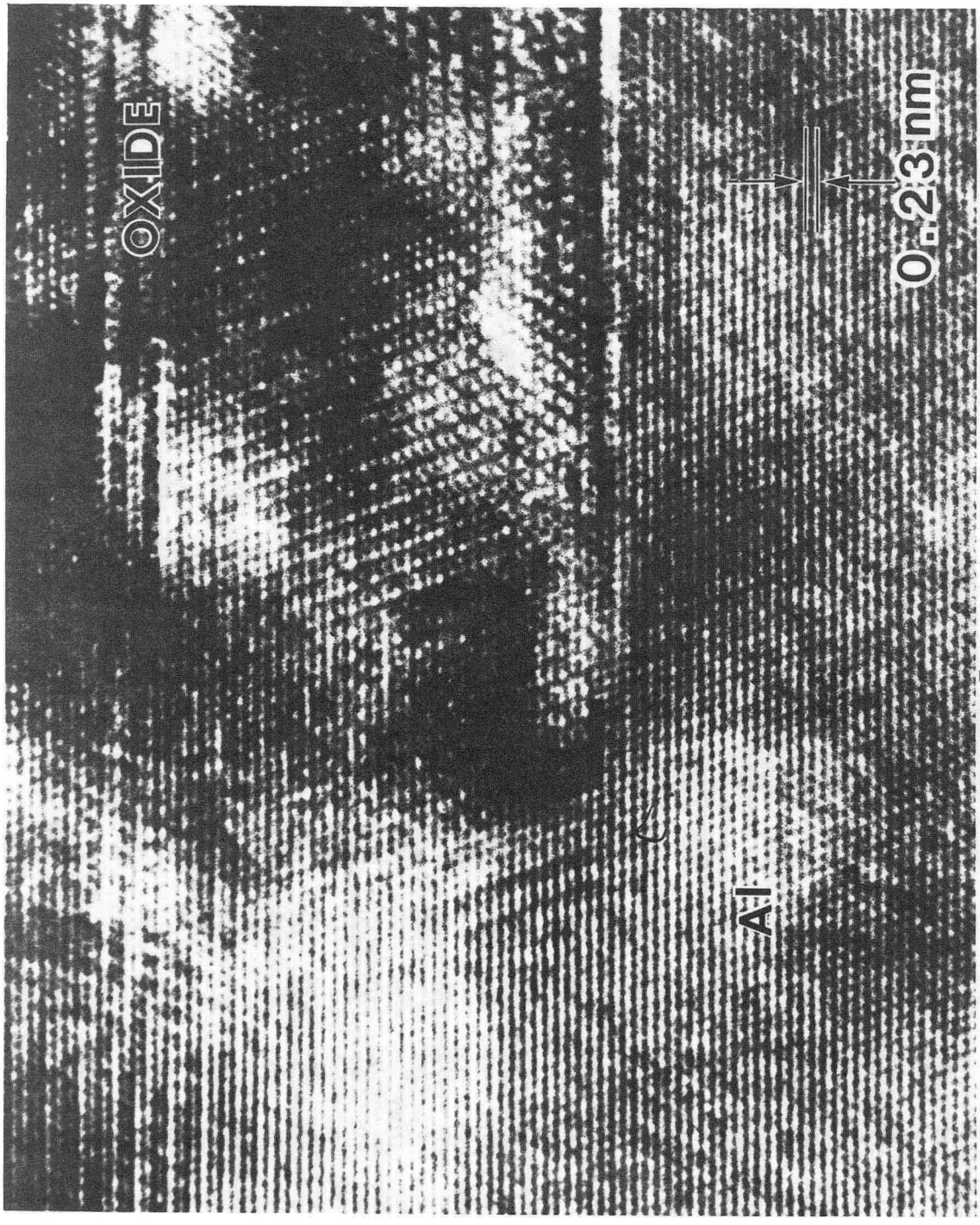

Fig. 35 (c)

XBB 863-1645

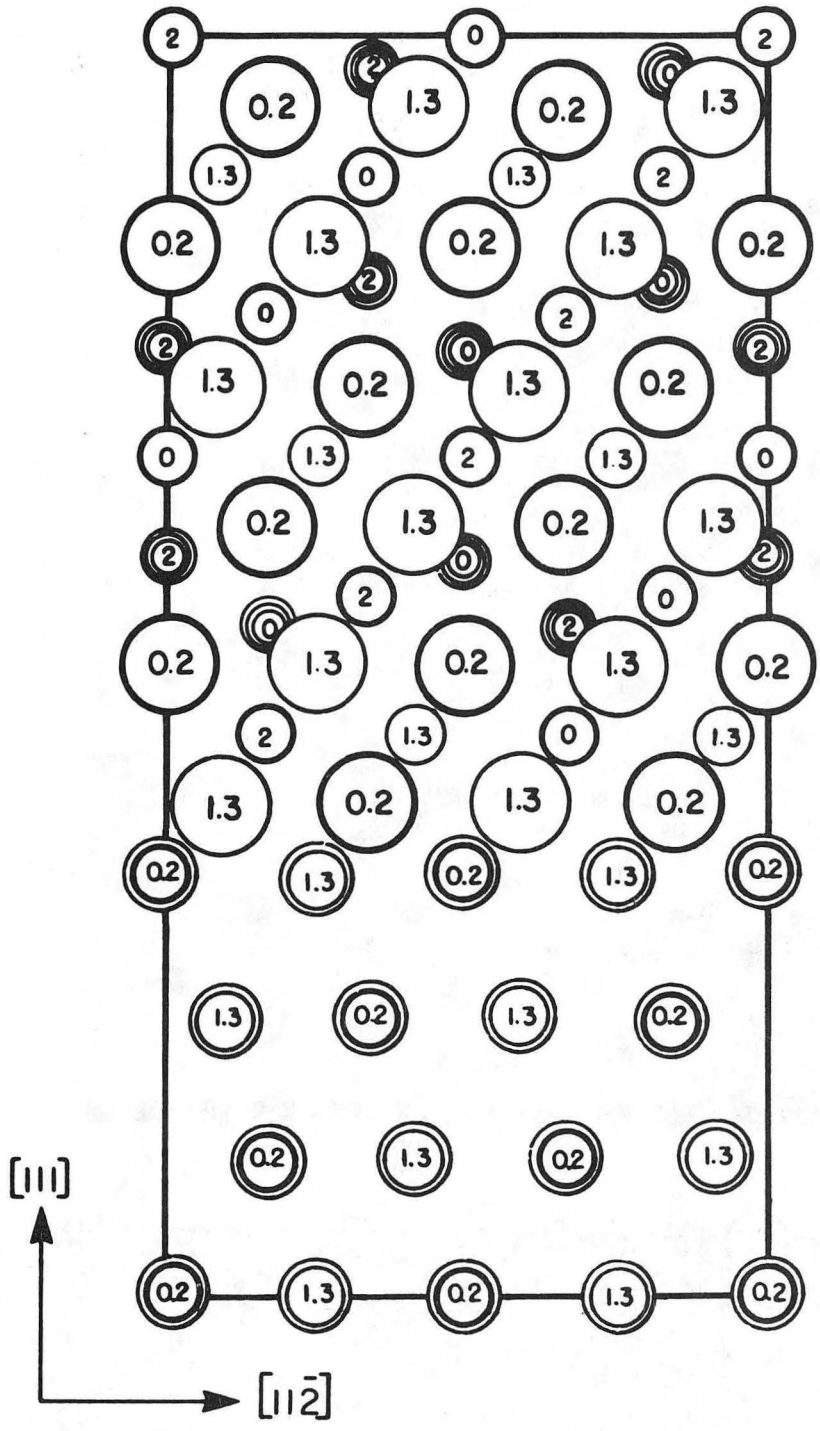

Fig. 36

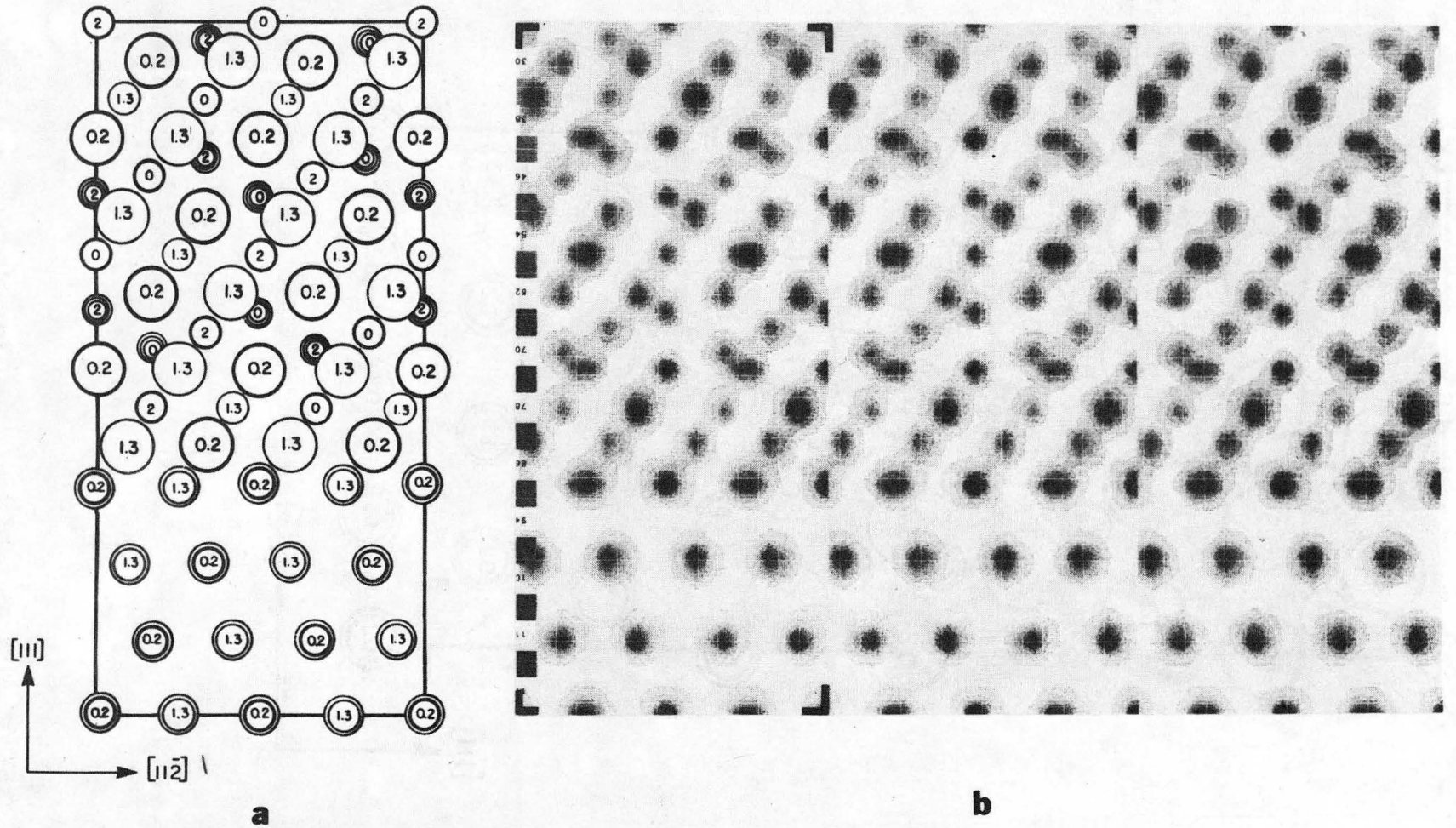

Fig. 37

XBB 857-5475

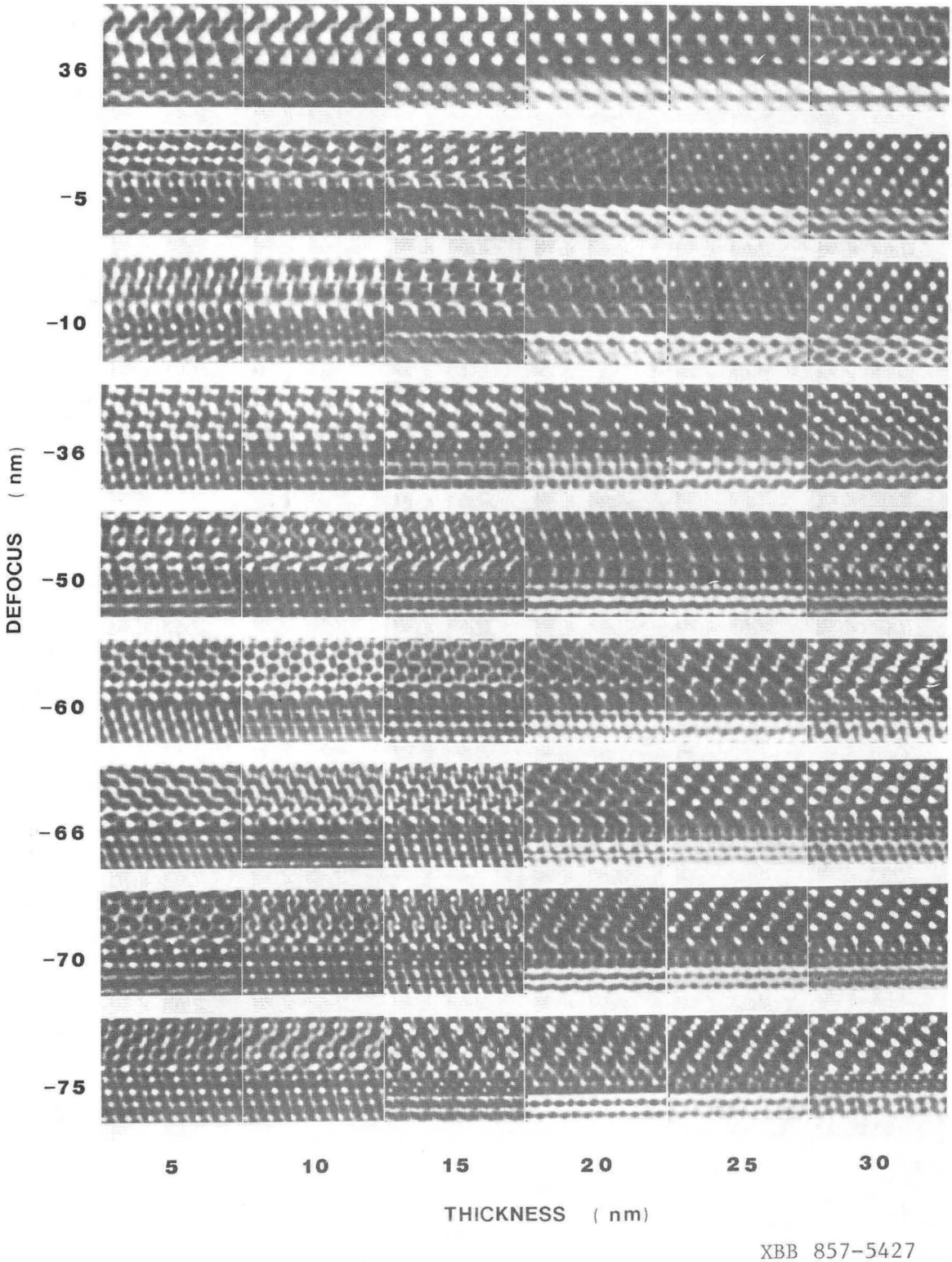

XBB 857-5427

Fig. 38 (a)

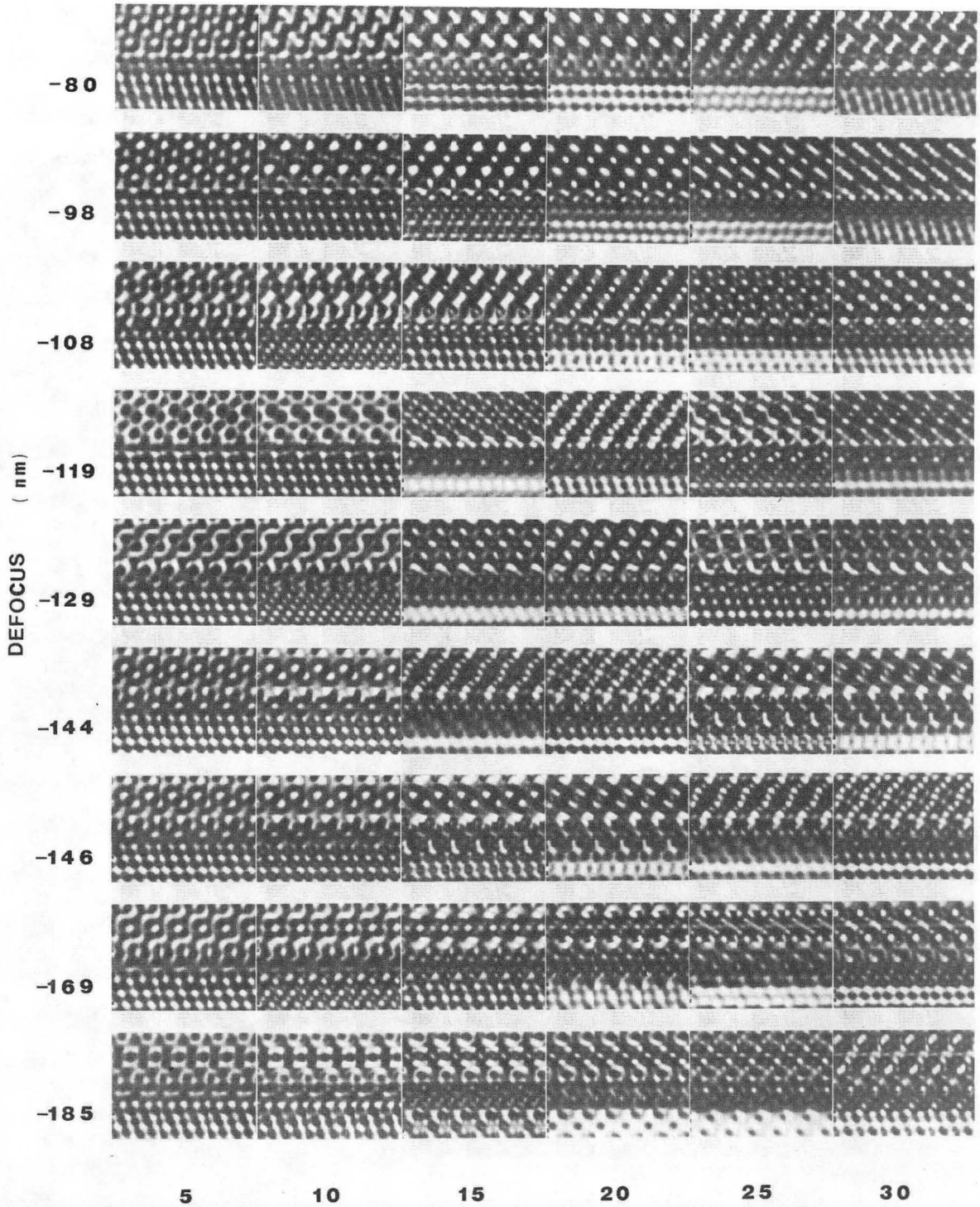

XBB 857-5426

Fig. 38 (b)

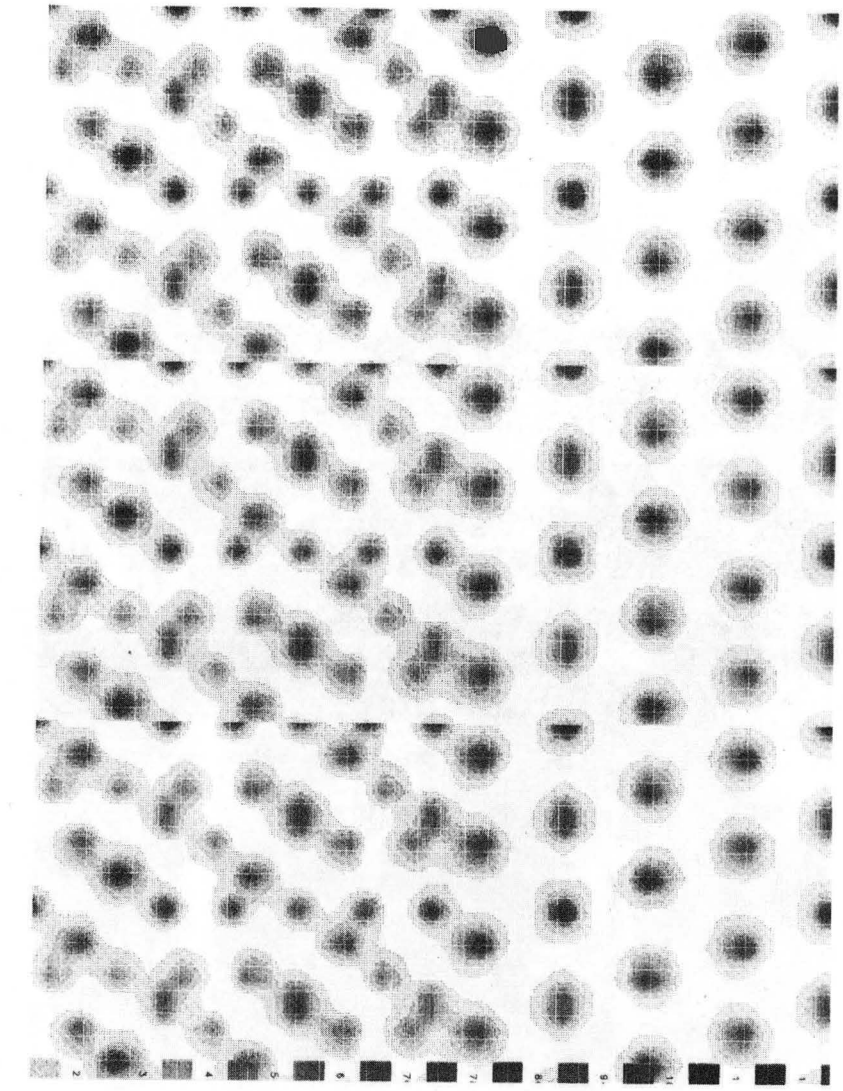

XBB 863-1453

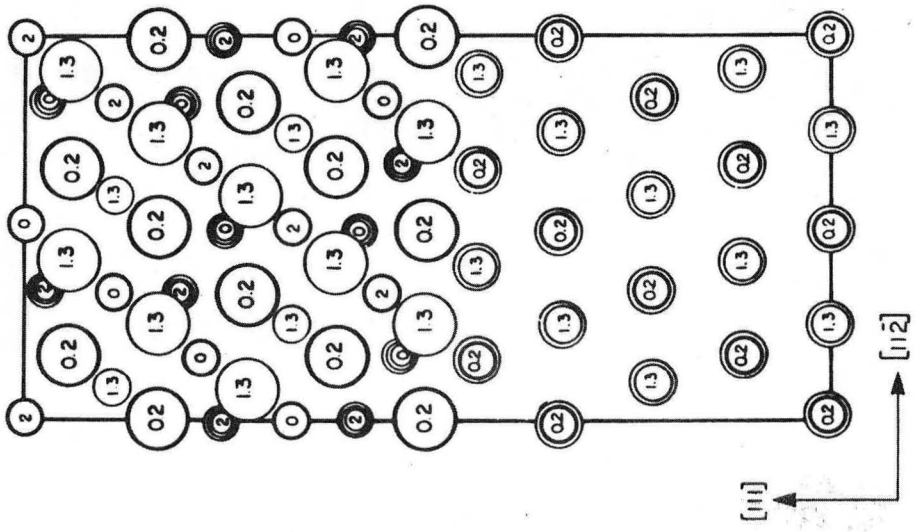

Fig. 39

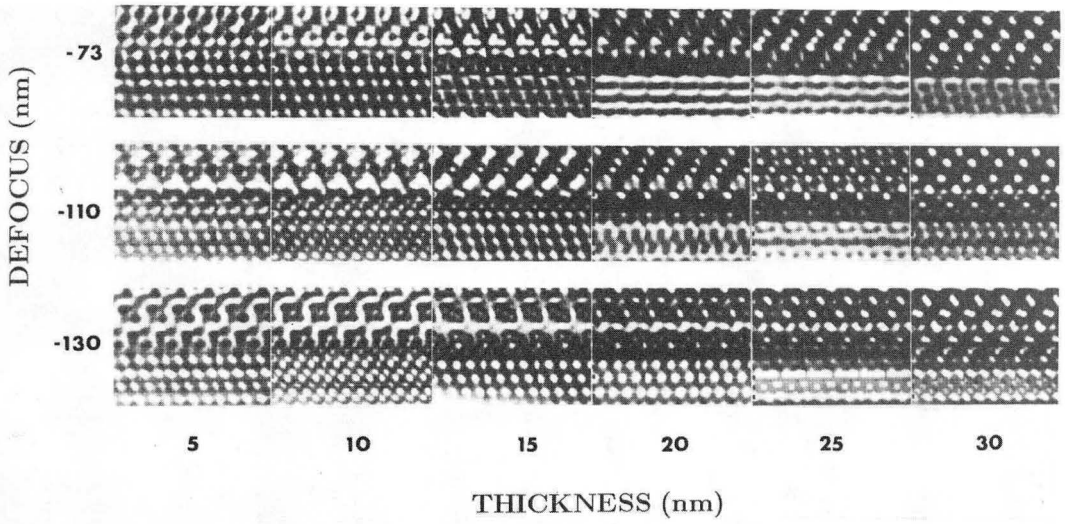

XBB 862-1414A

Fig. 40

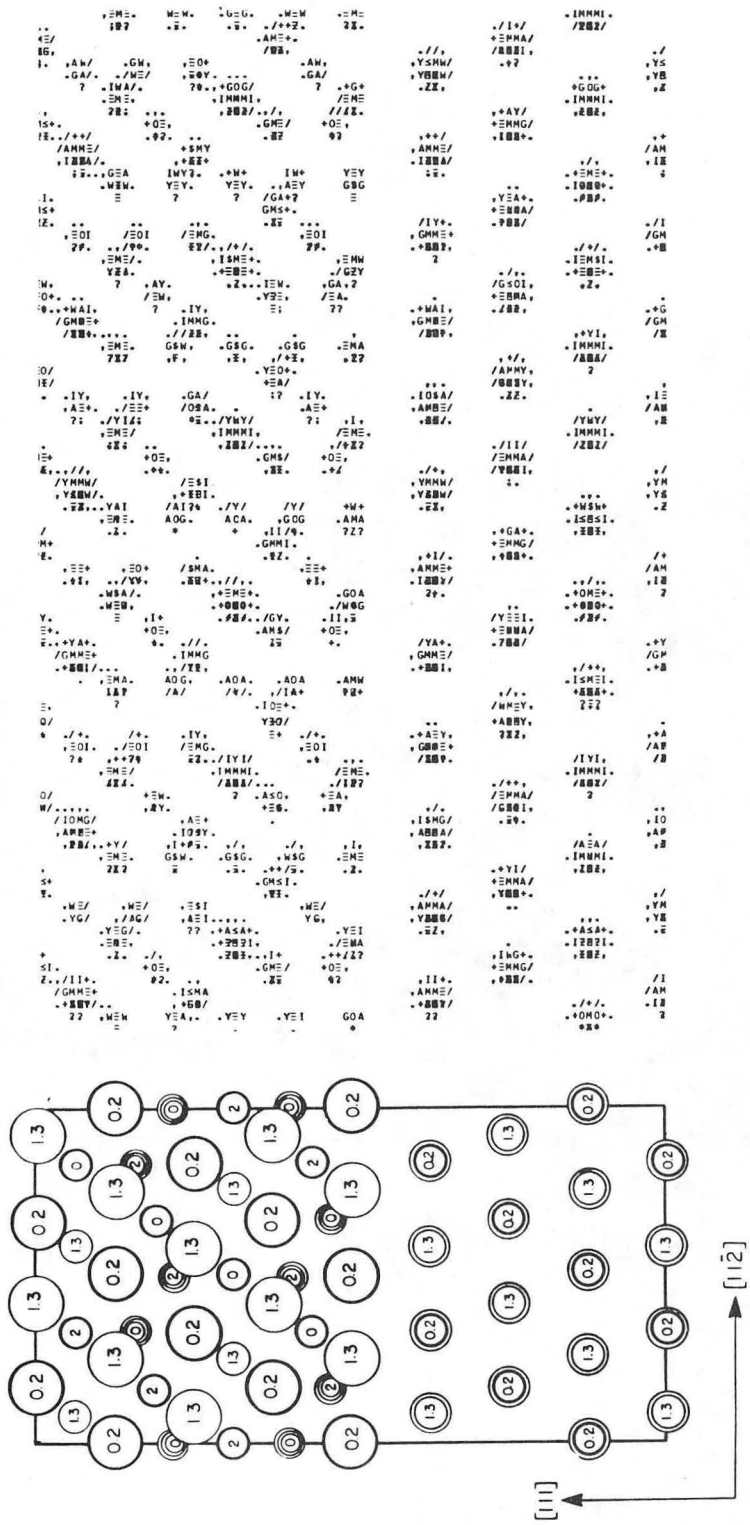

Fig. 41

XBL 863-996

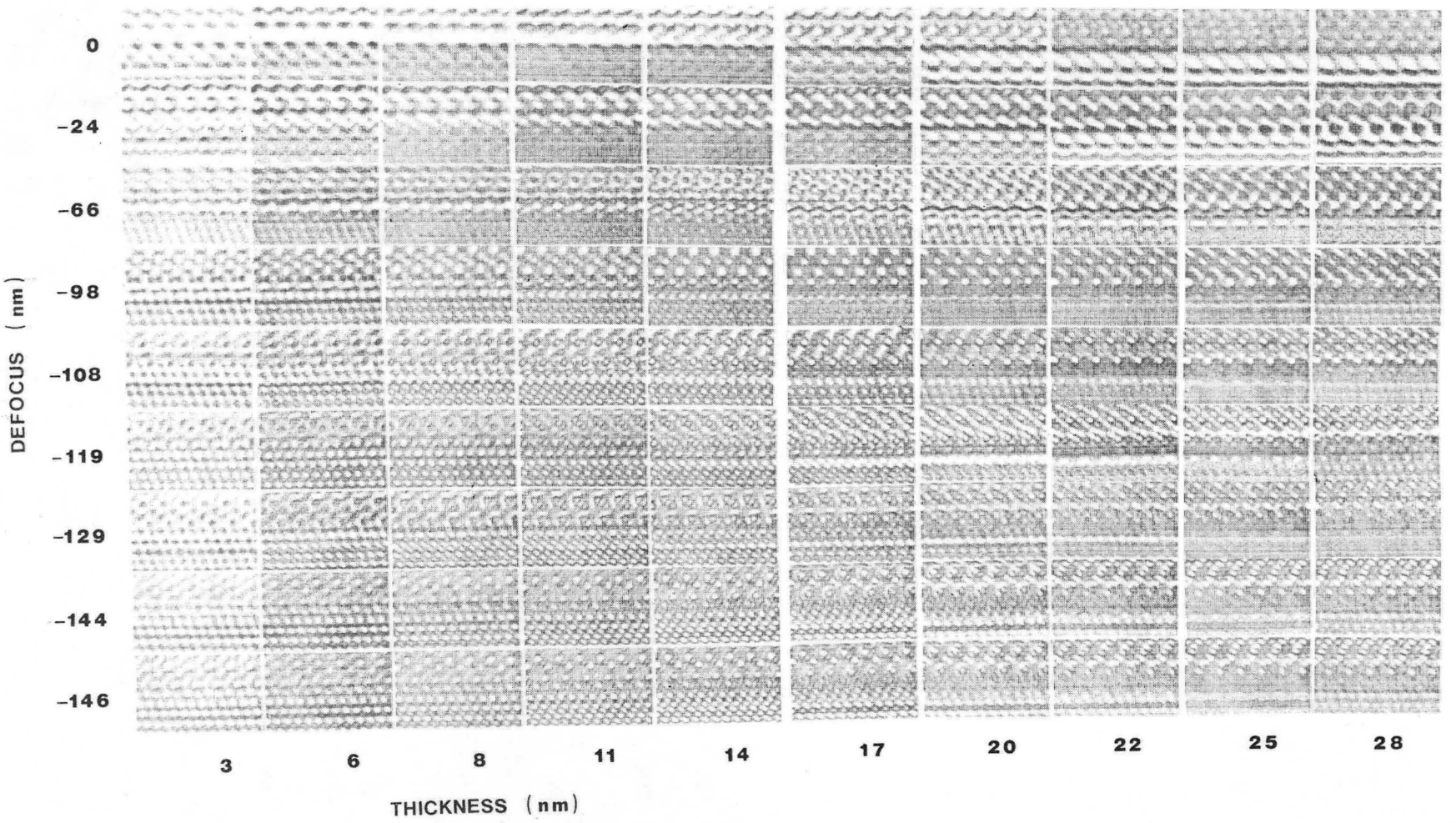

XBB 852-1699

Fig. 42

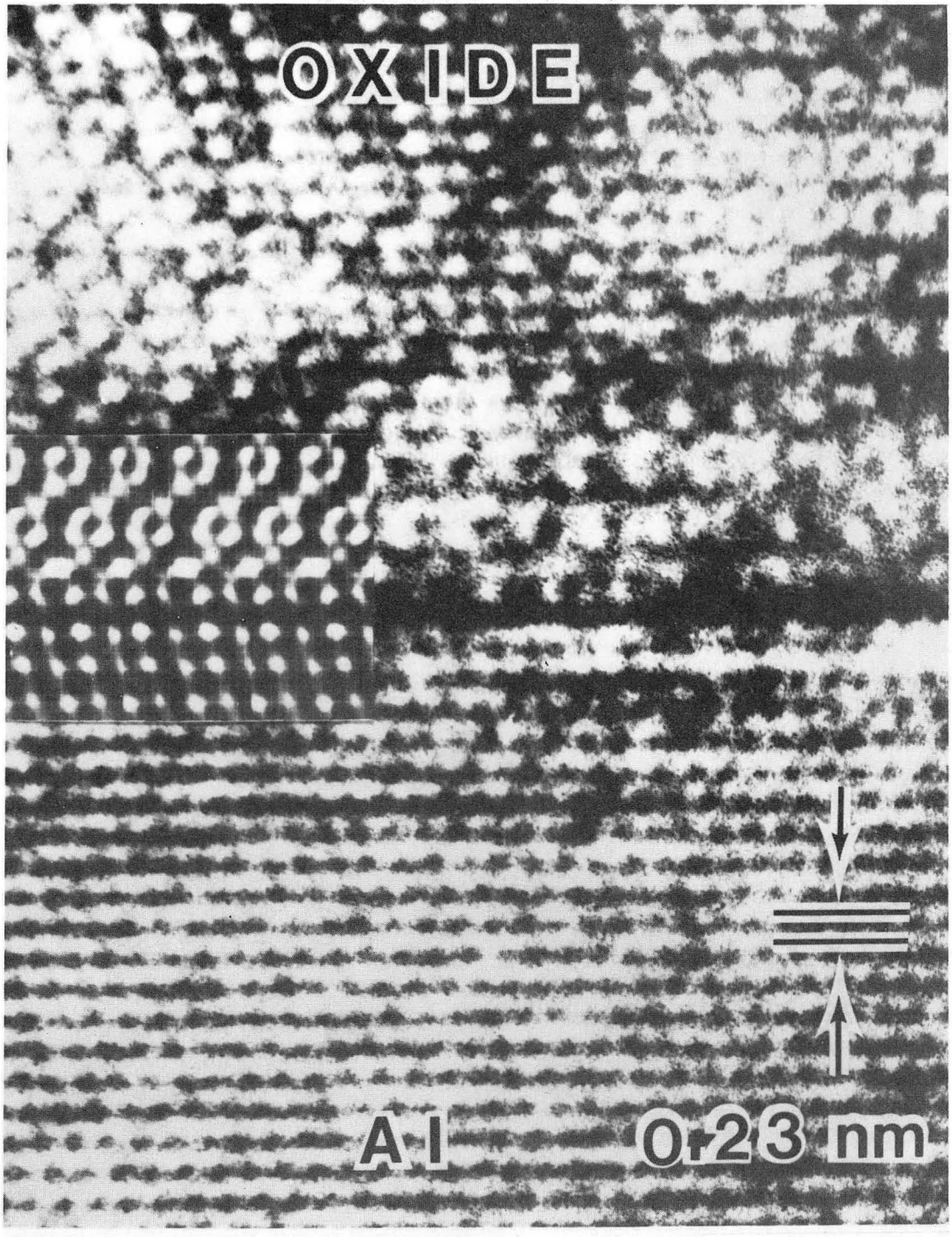

XBB 857-5346B

Fig. 43

Proposed transformation mechanism of Al to oxide structure with parallel orientation relationship

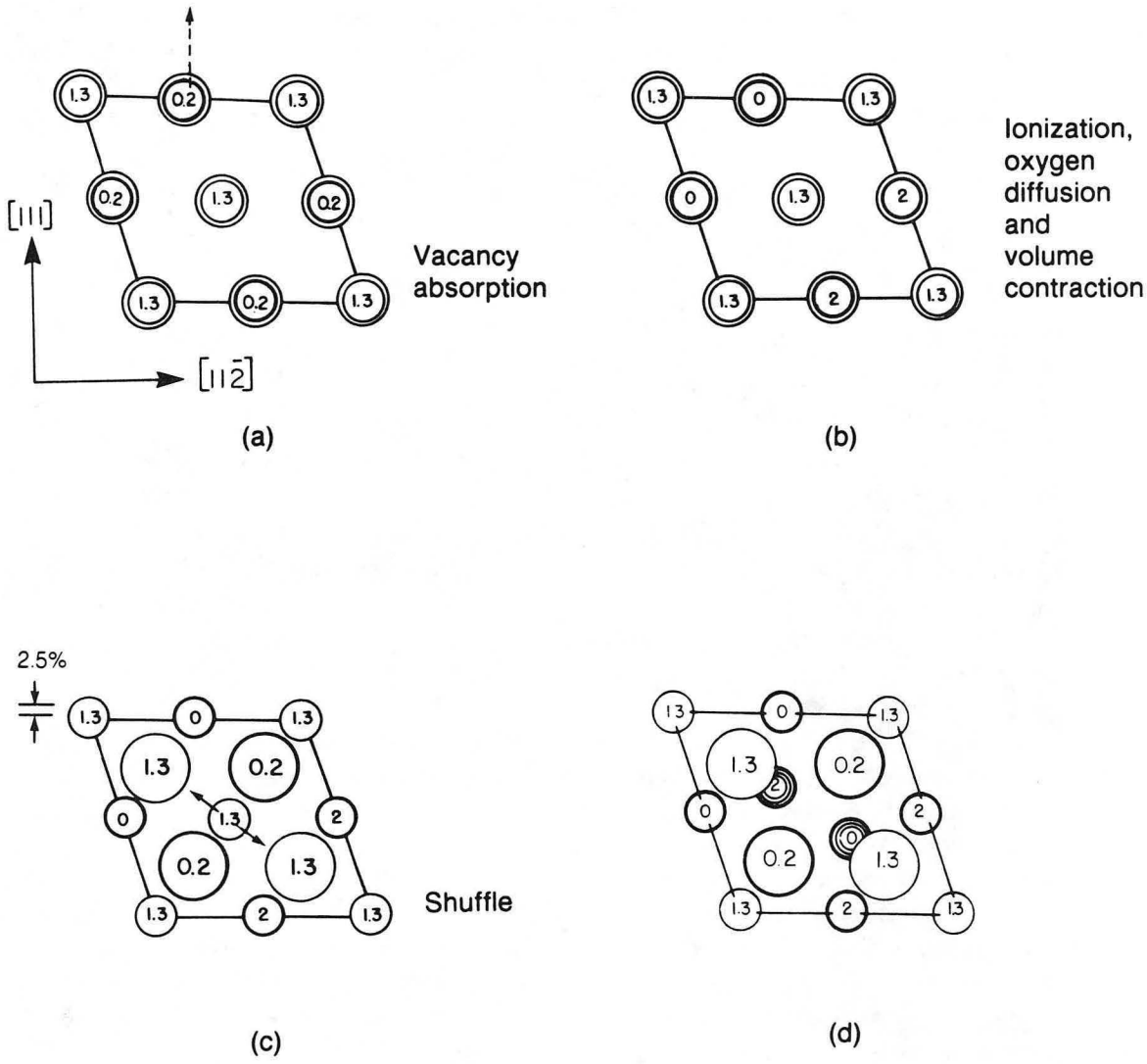

XBL 859-3953

Fig. 44

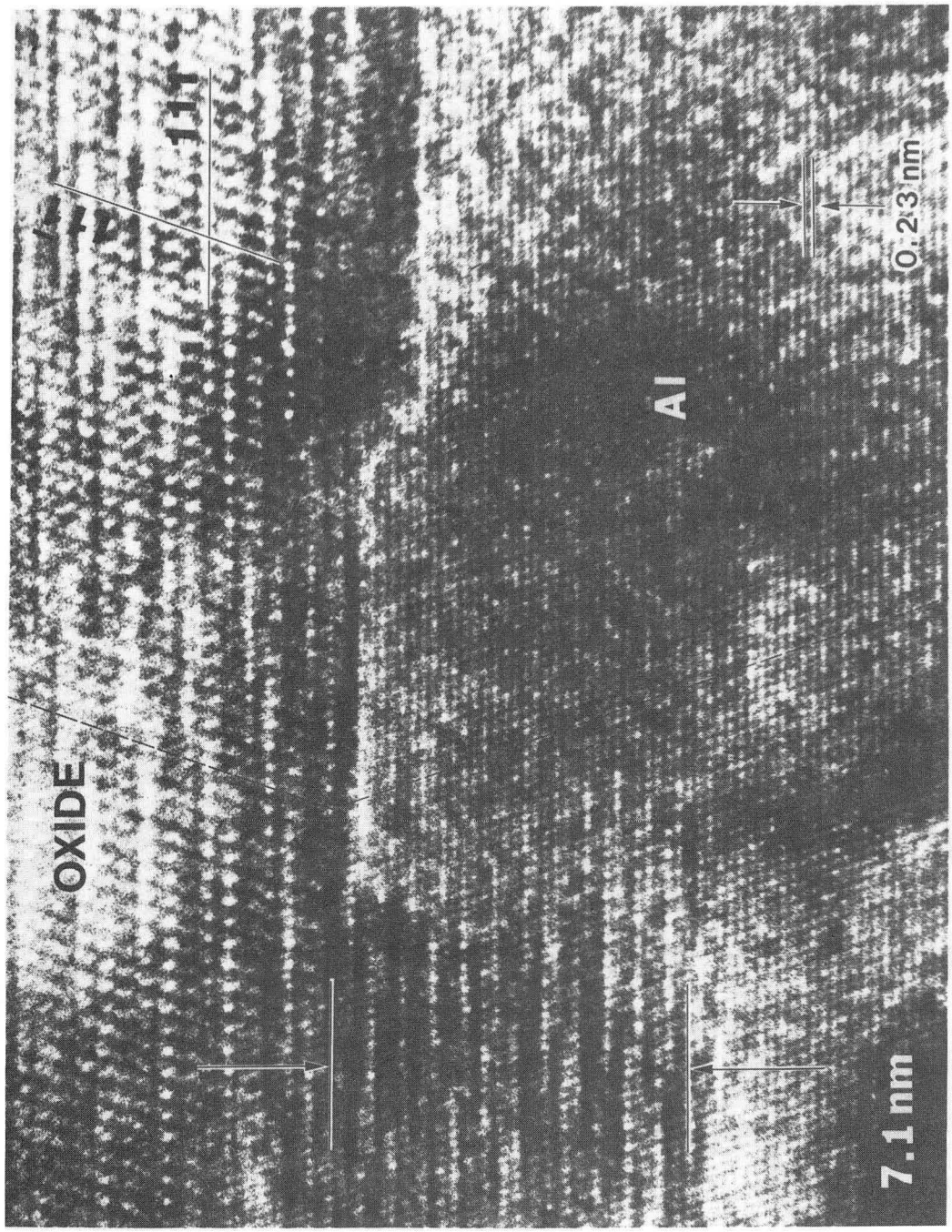

Fig. 45

XBB 852-1697

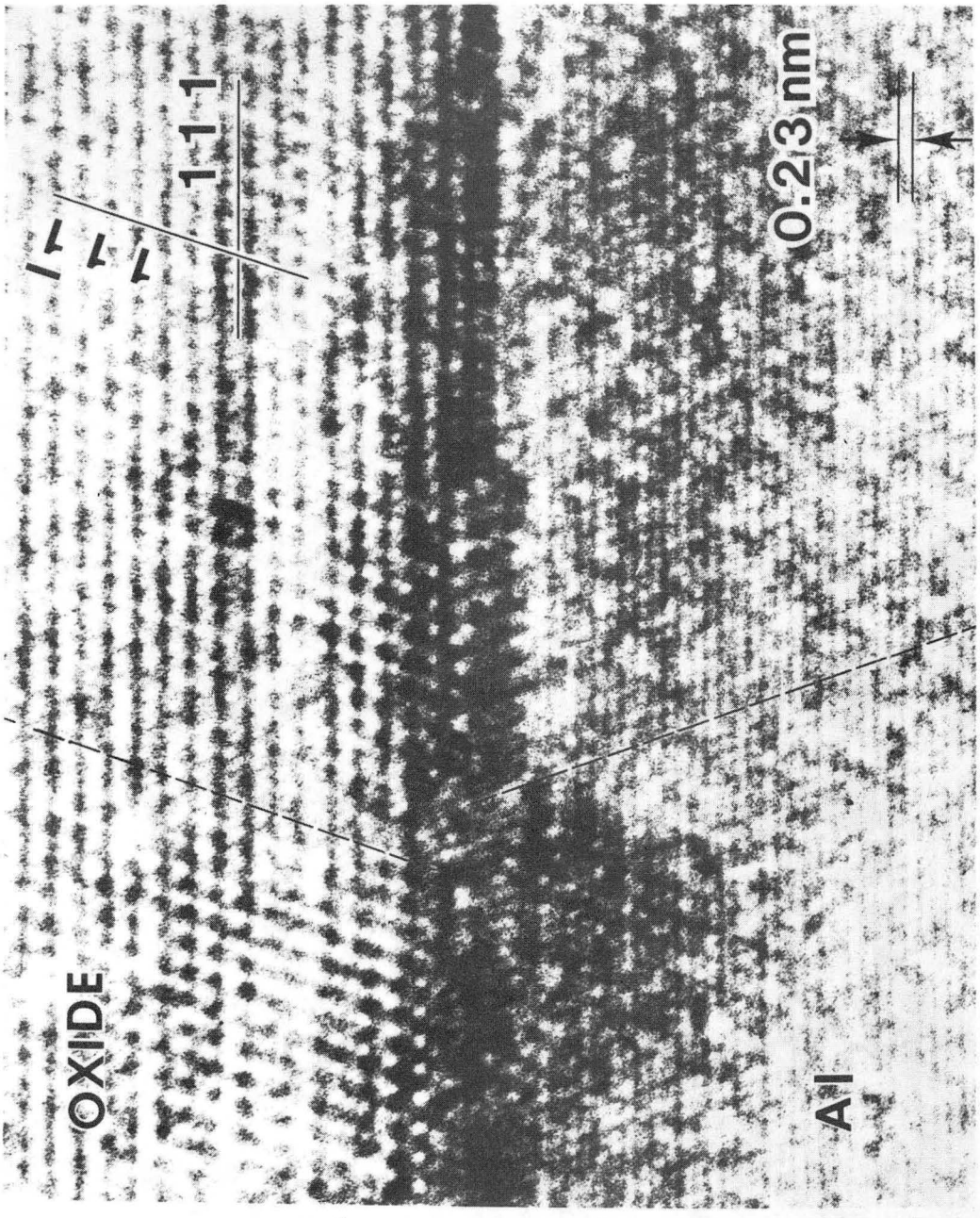

Fig. 46

XBB 859-7500

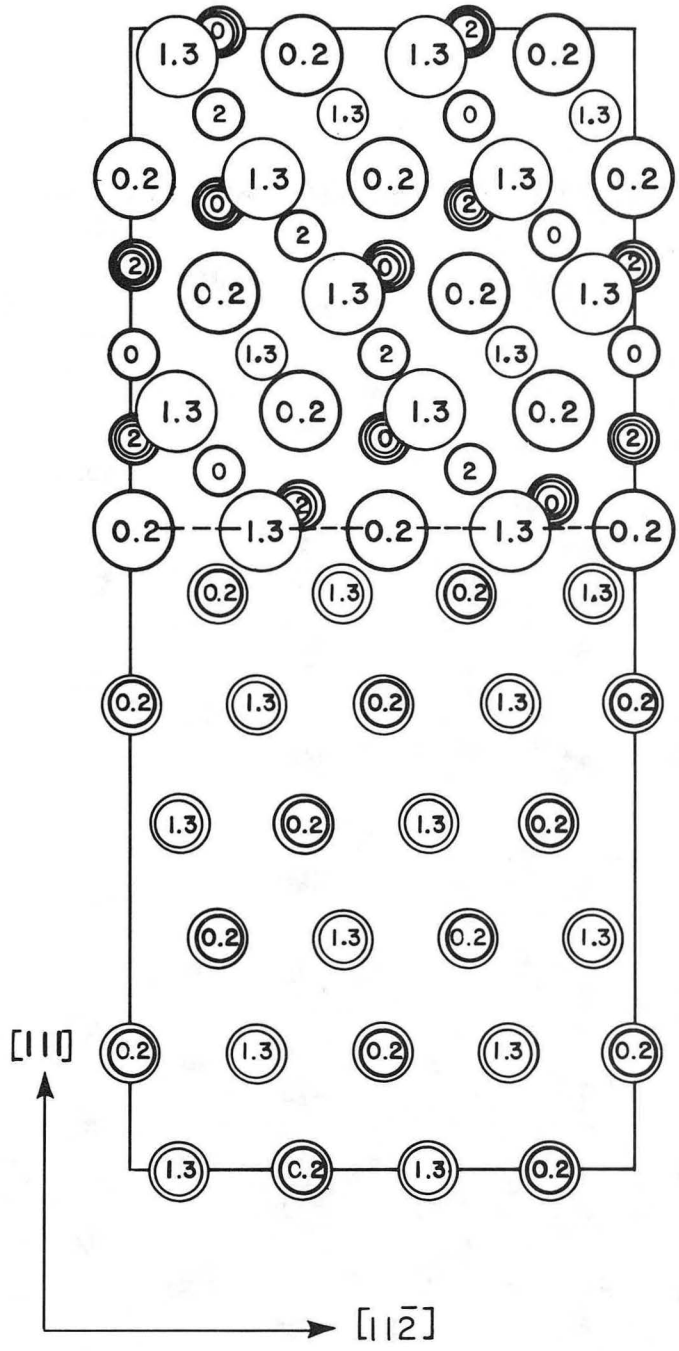

XBL 859-4021

Fig. 47

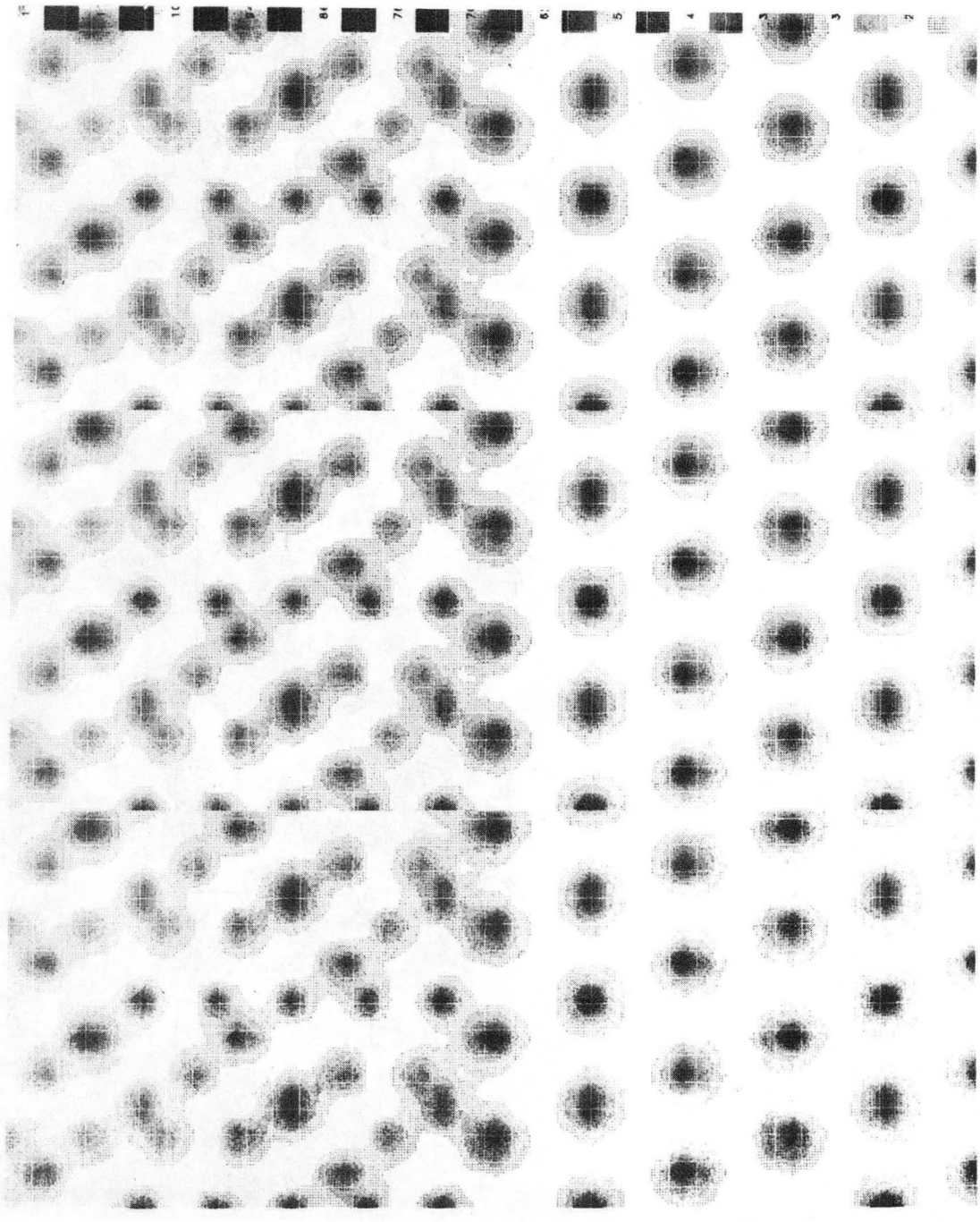

XBB 863-1454

Fig. 48

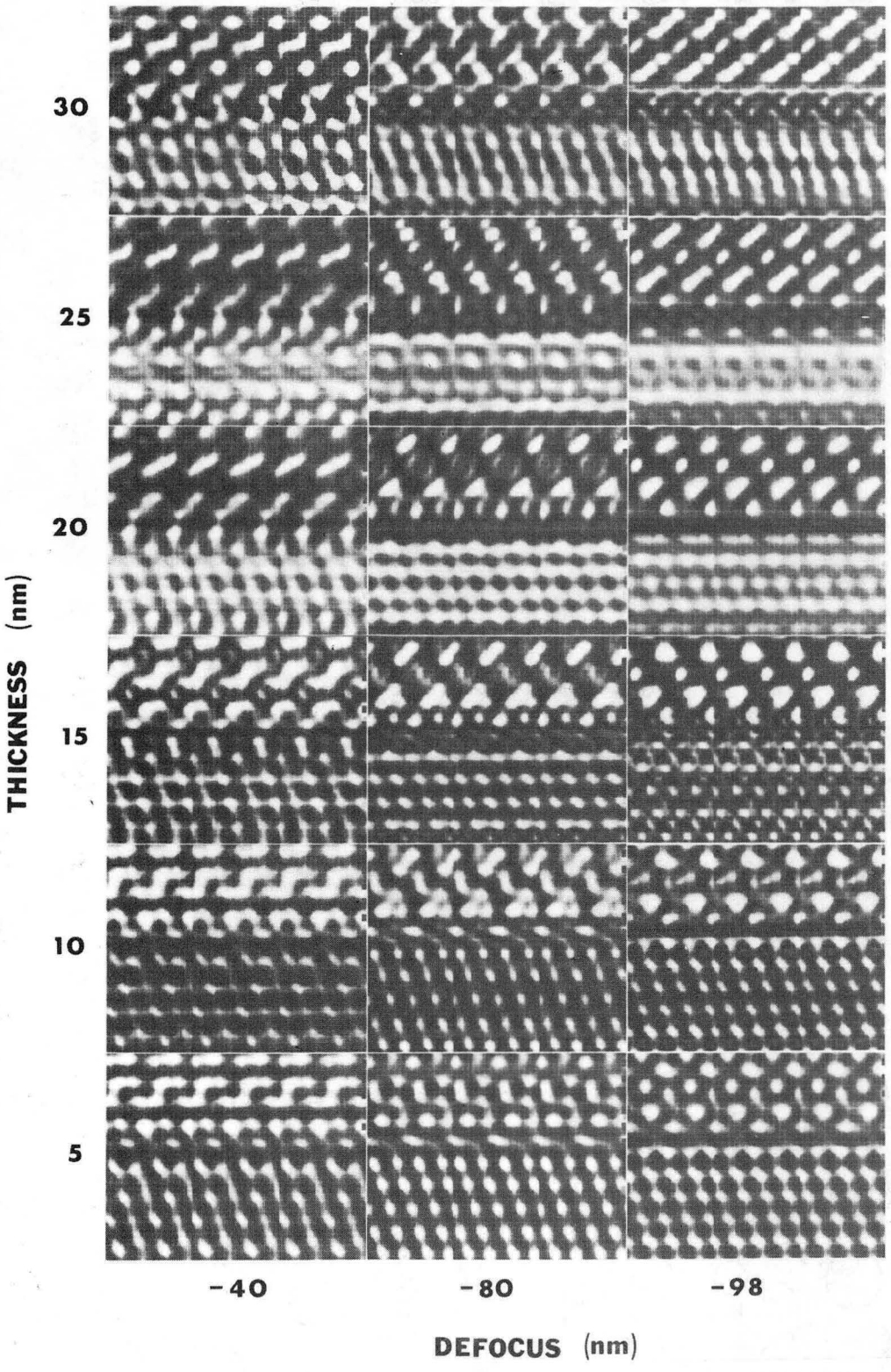

XBB 863-1650

Fig. 49

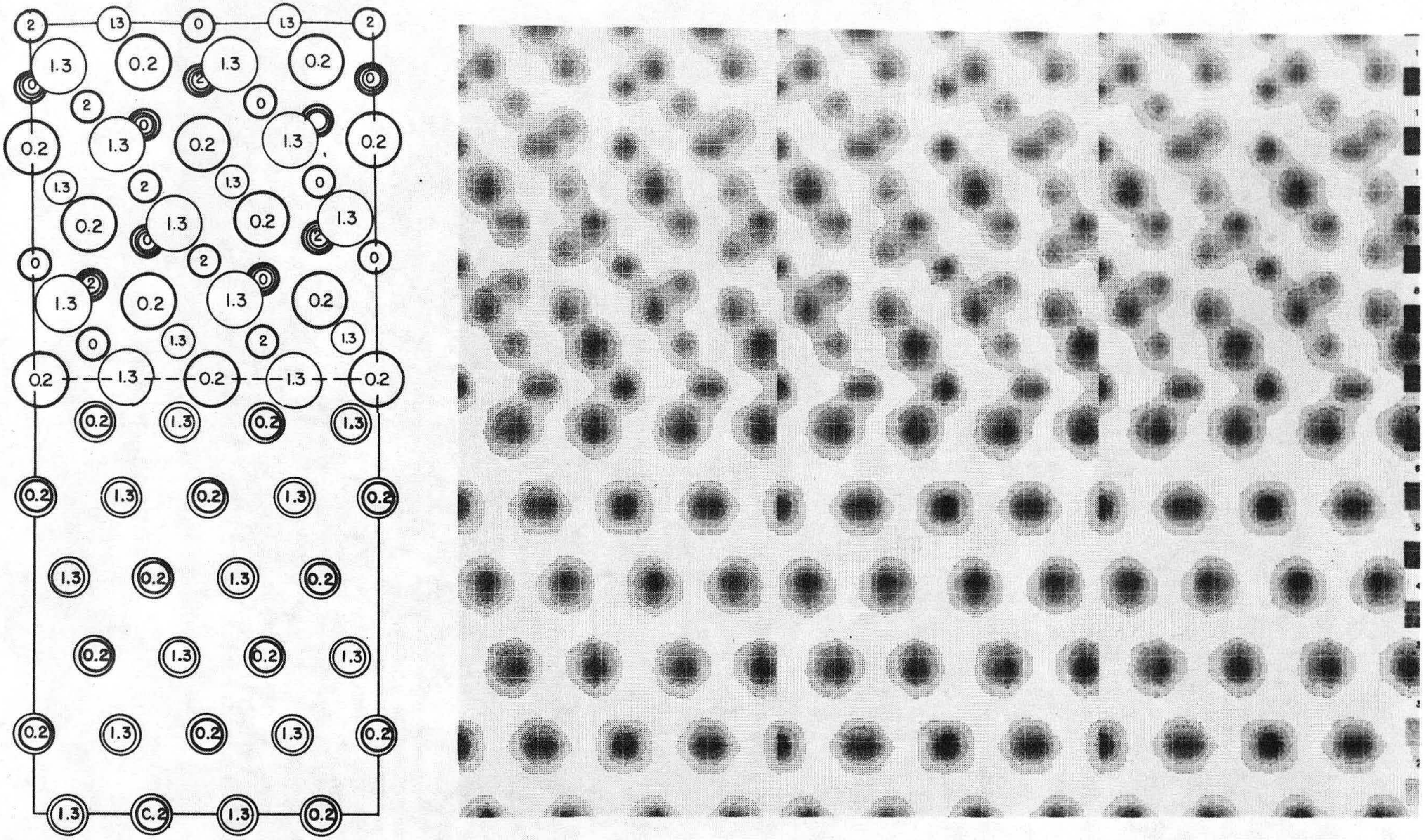

Fig. 50

XBB 863-1643

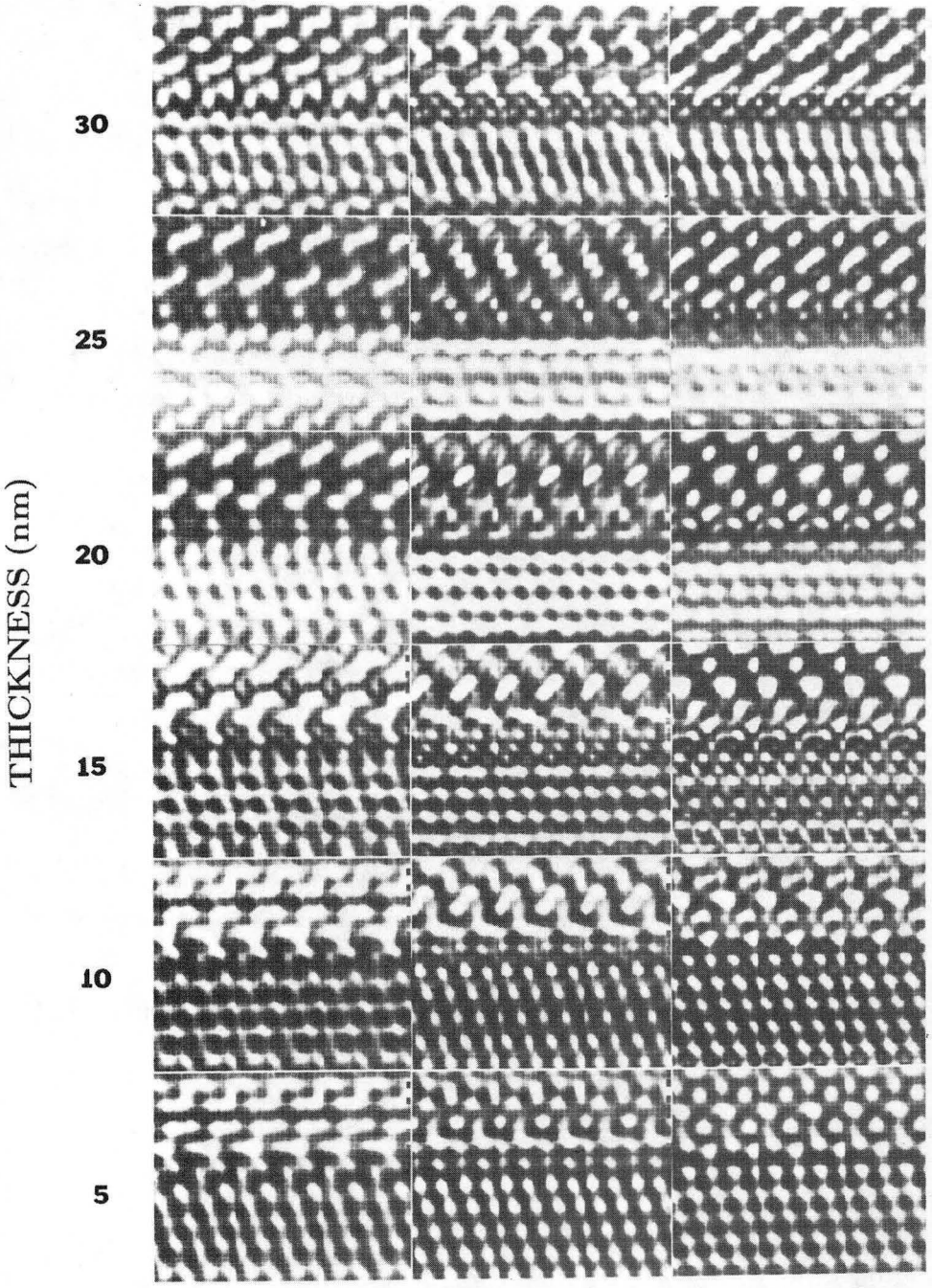

XBB 863-1557A

Fig. 51

Experimental and simulated images of Al/oxide interface with twin orientation relationship

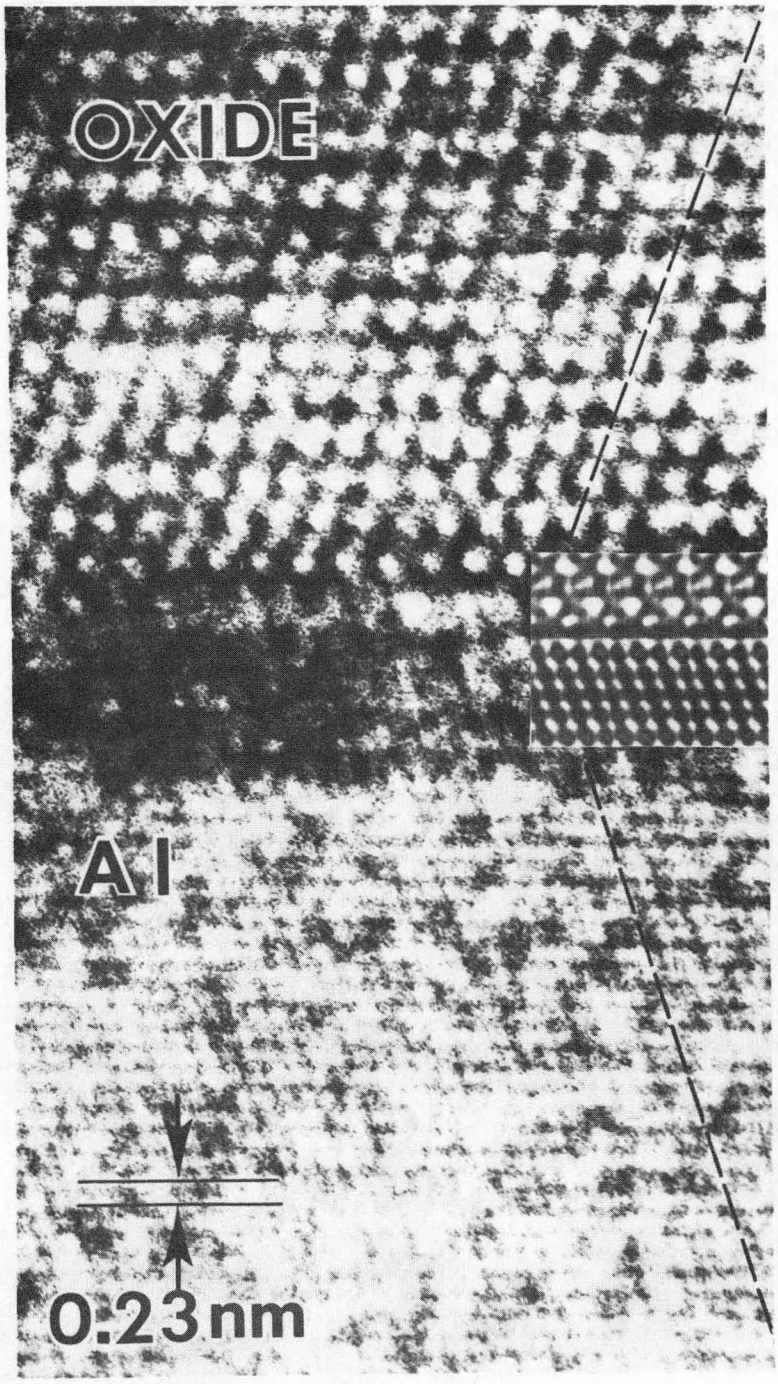

XBB 859-7501C

Fig. 52

Proposed transformation mechanism of Al to oxide structure with twin orientation relationship

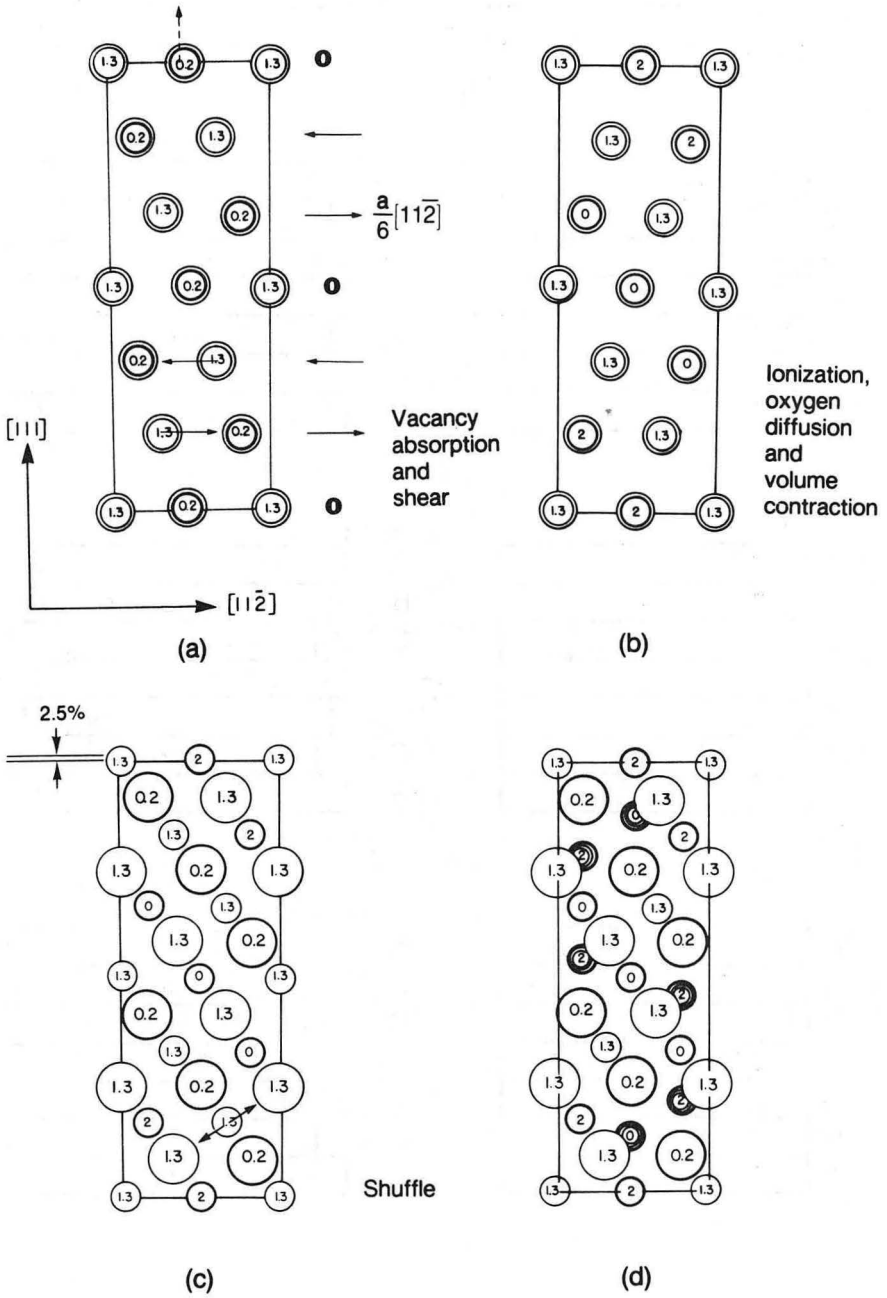

XBL859-3955

Fig. 53

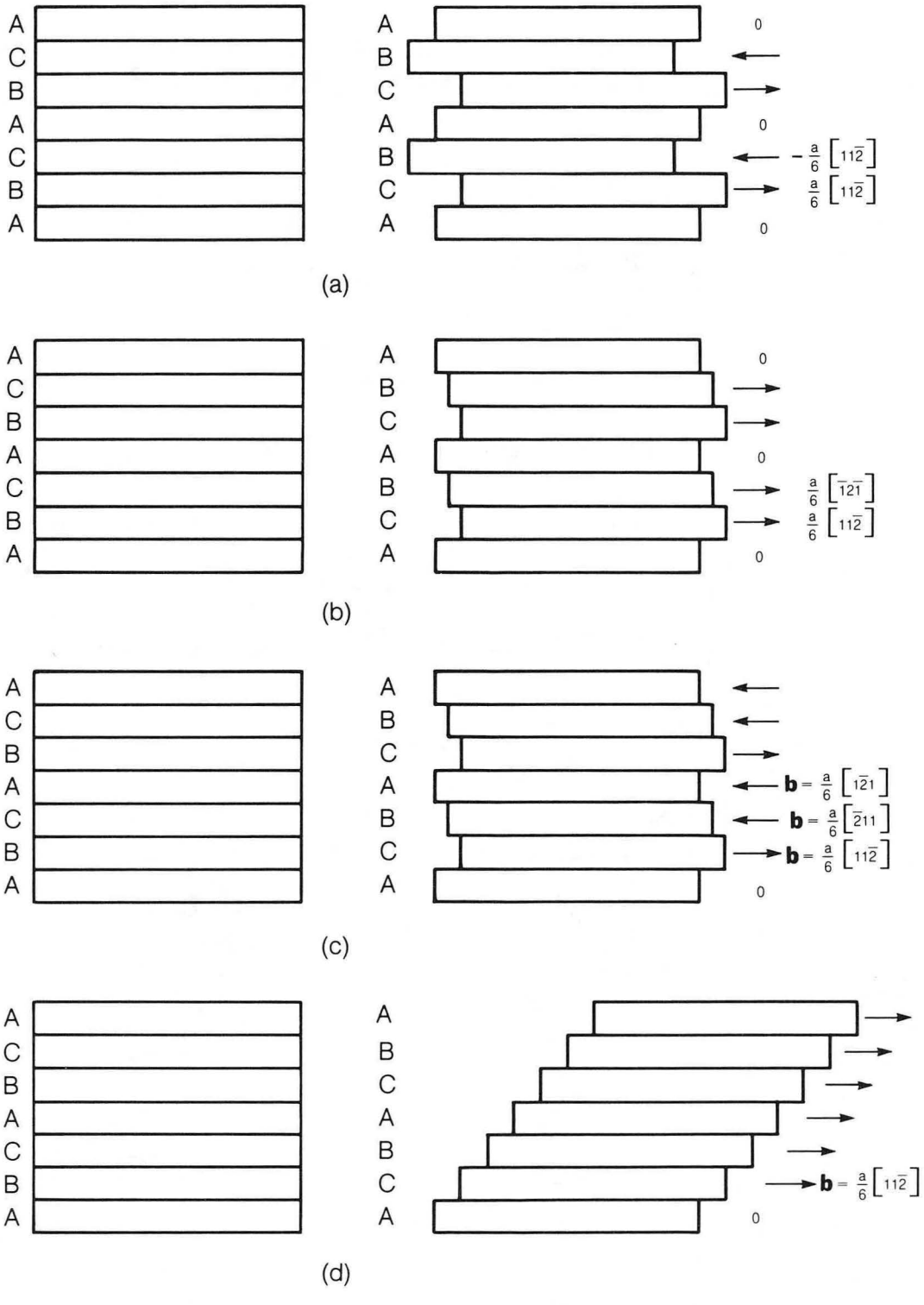
A
C
B
A
C
B
A
0
$-\frac{a}{6}[11\bar{2}]$
$\frac{a}{6}[11\bar{2}]$
(a)
$\frac{a}{6}[\bar{1}2\bar{1}]$
(b)
$\mathbf{b}=\frac{a}{6}[1\bar{2}1]$
$\mathbf{b}=\frac{a}{6}[\bar{2}11]$
$\mathbf{b}=\frac{a}{6}[11\bar{2}]$
(c)
(d)
XBL 864-1667

Fig. 54

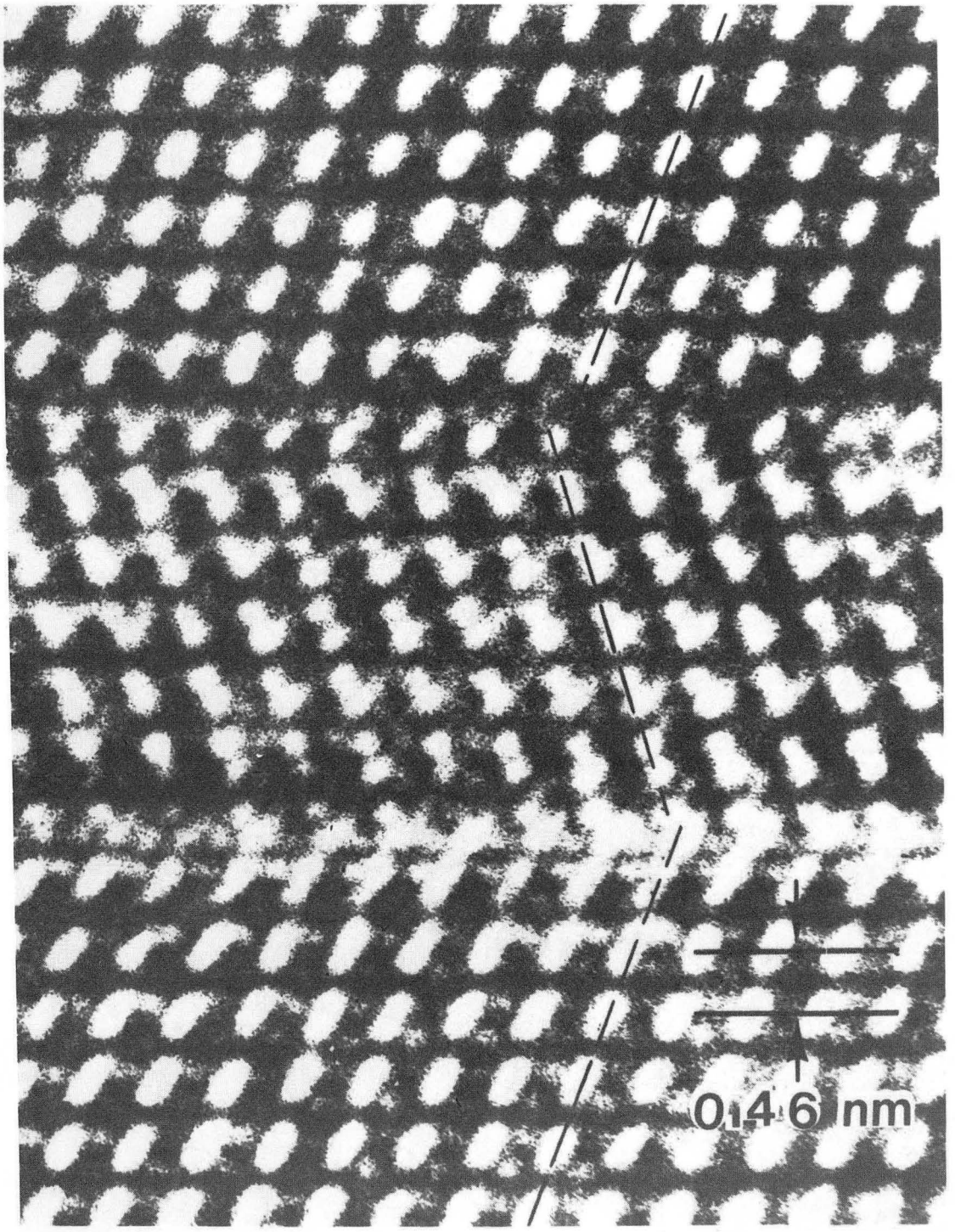

XBB 851-906

Fig. 55

Atomic model of an oxide twin boundary

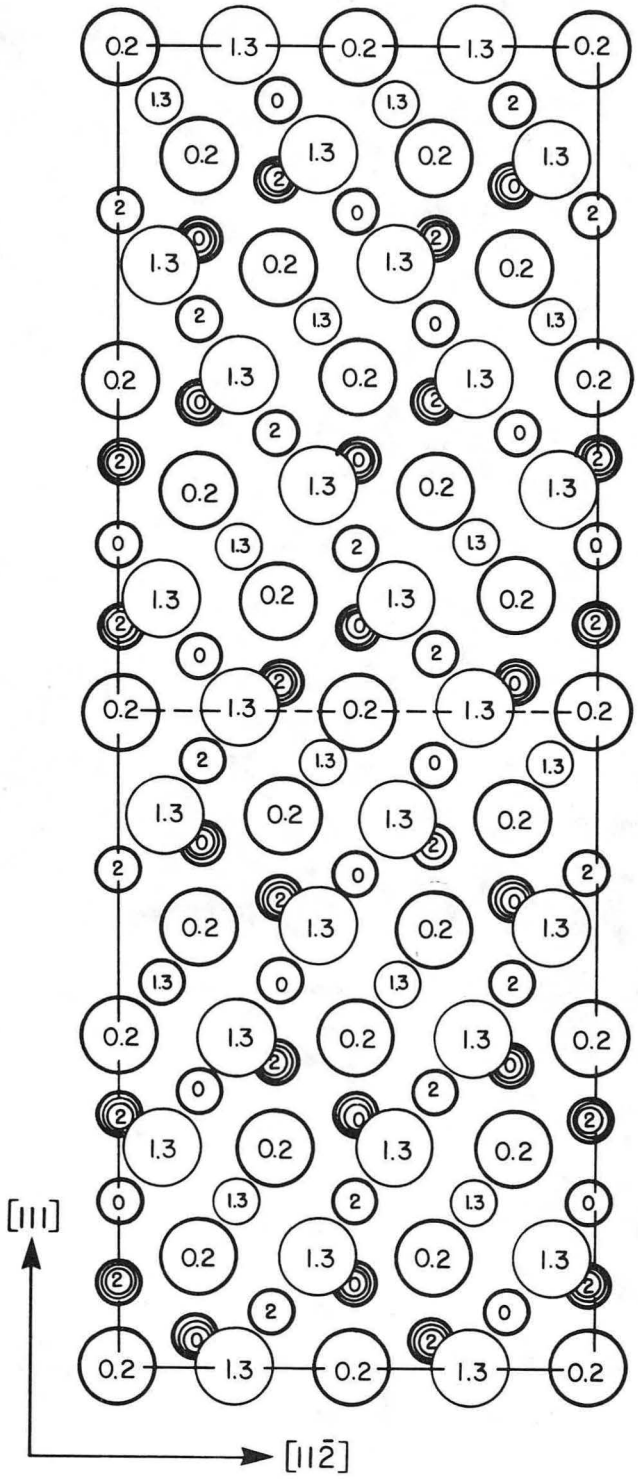

XBL. 852-10301

Fig. 56

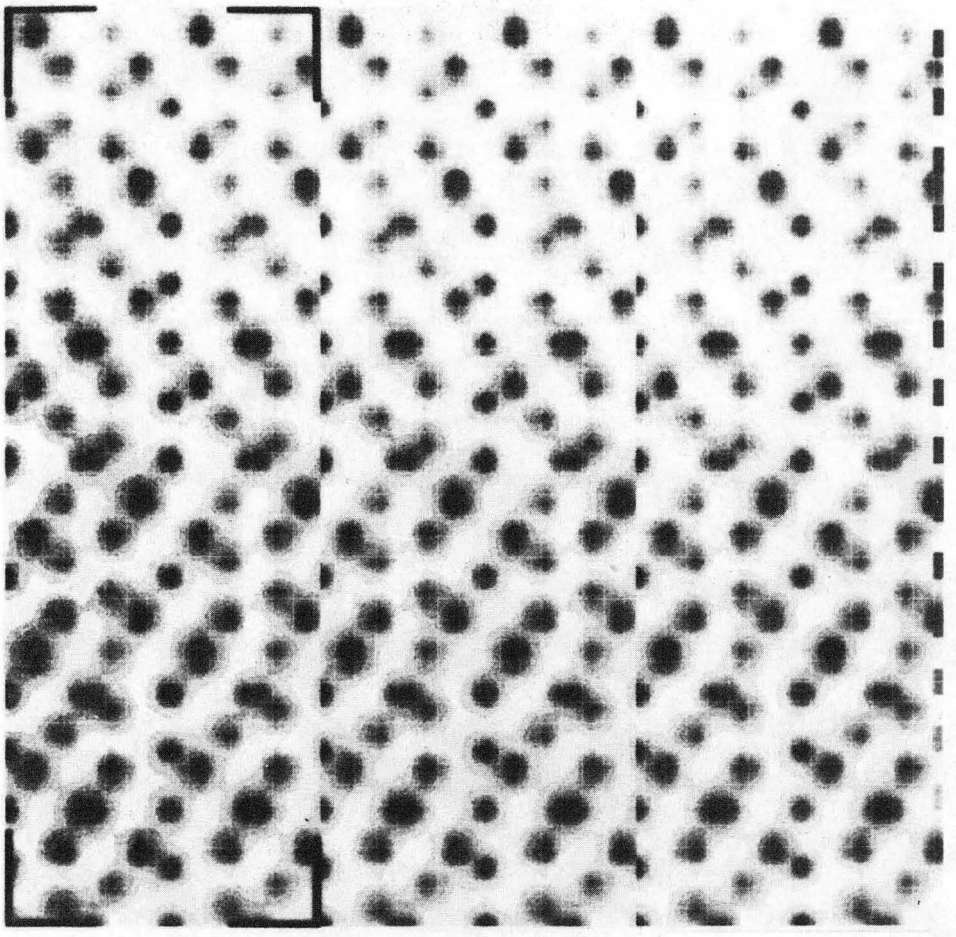

XBB 852-1553A

Fig. 57

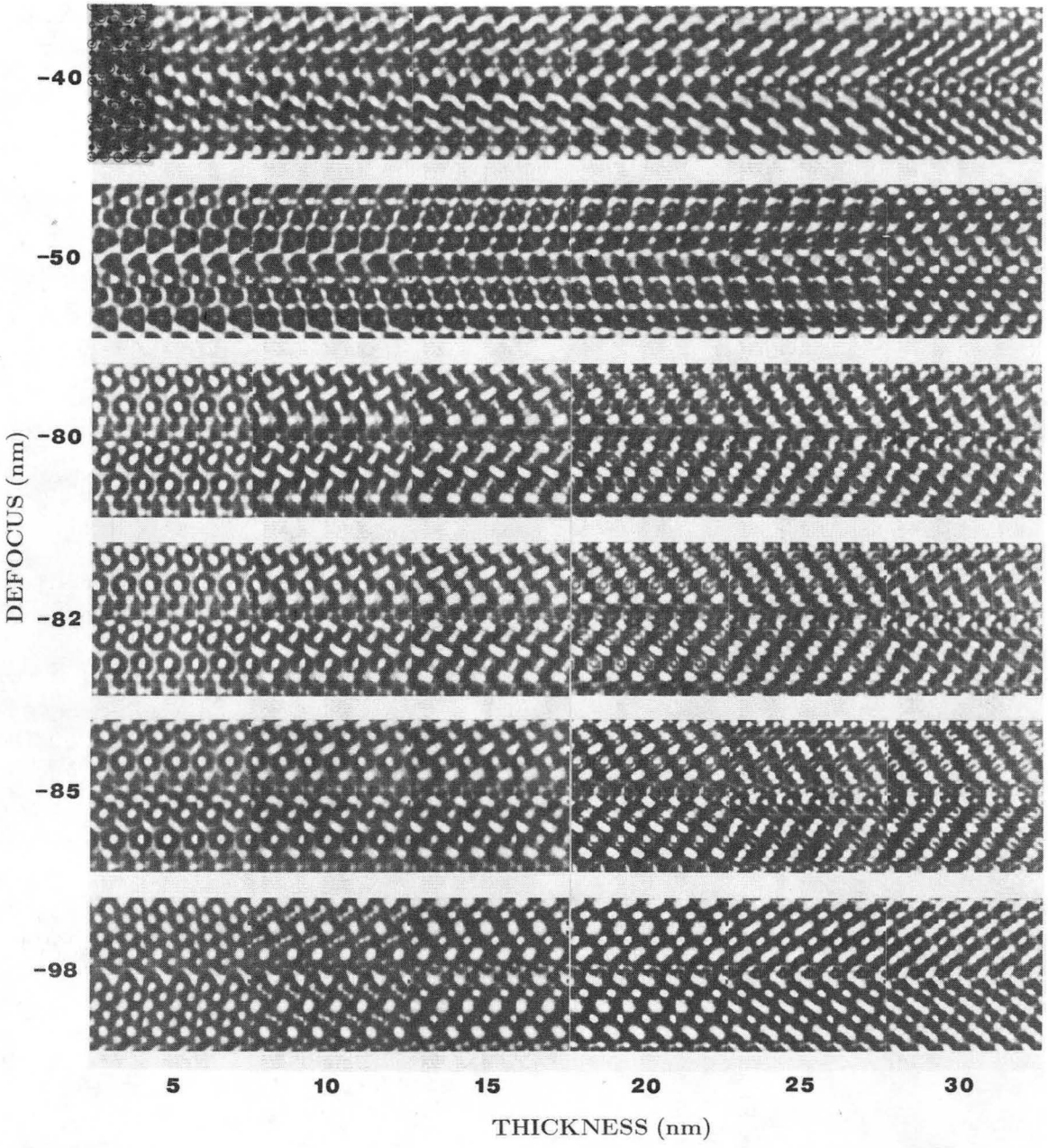

XBB 863-1648

Fig. 58

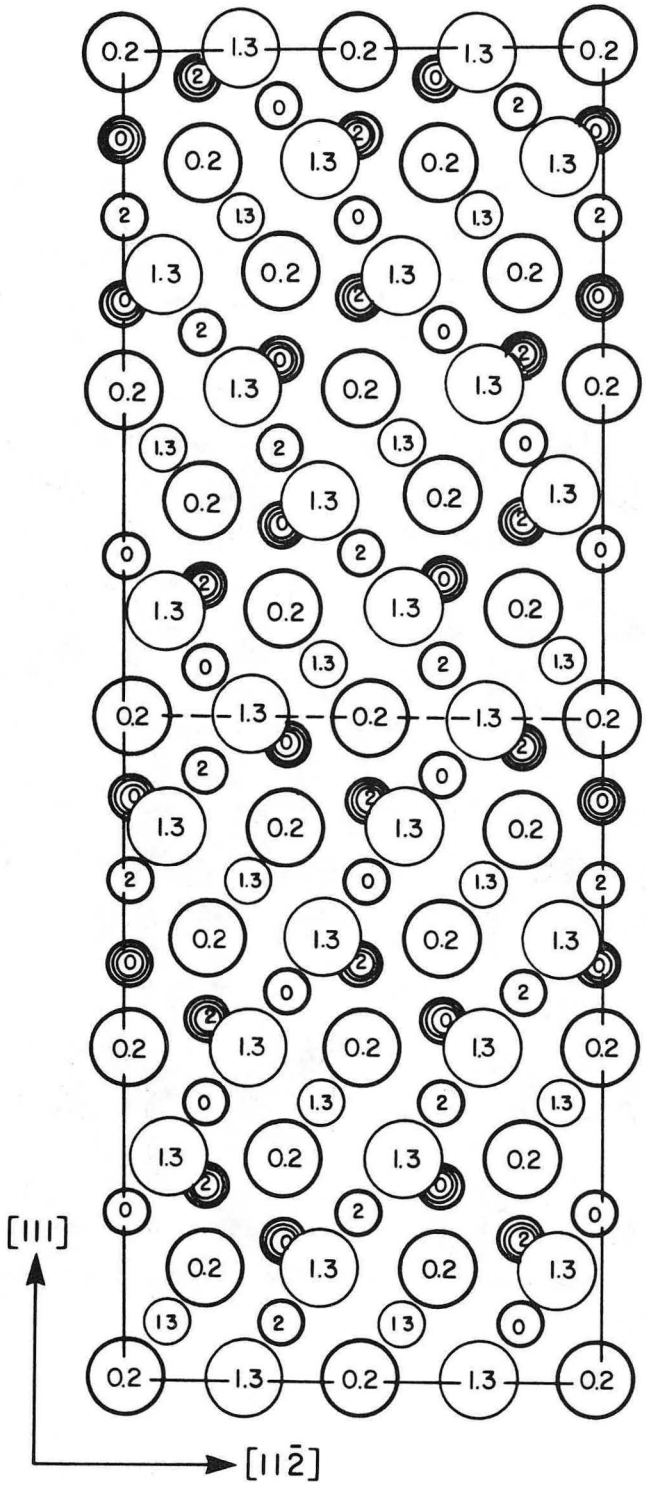

XBL 852-10299

Fig. 59

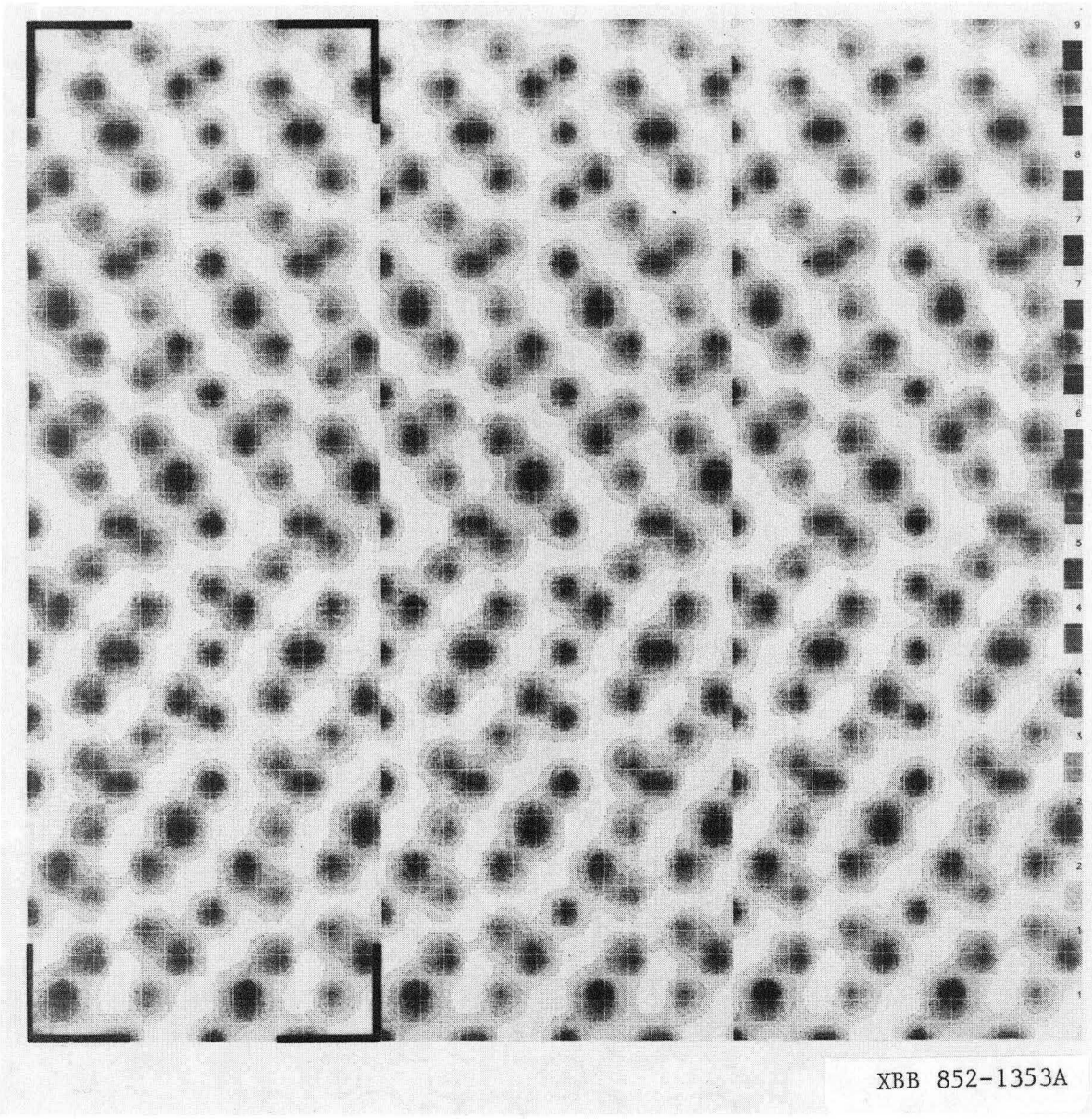

XBB 852-1353A

Fig. 60

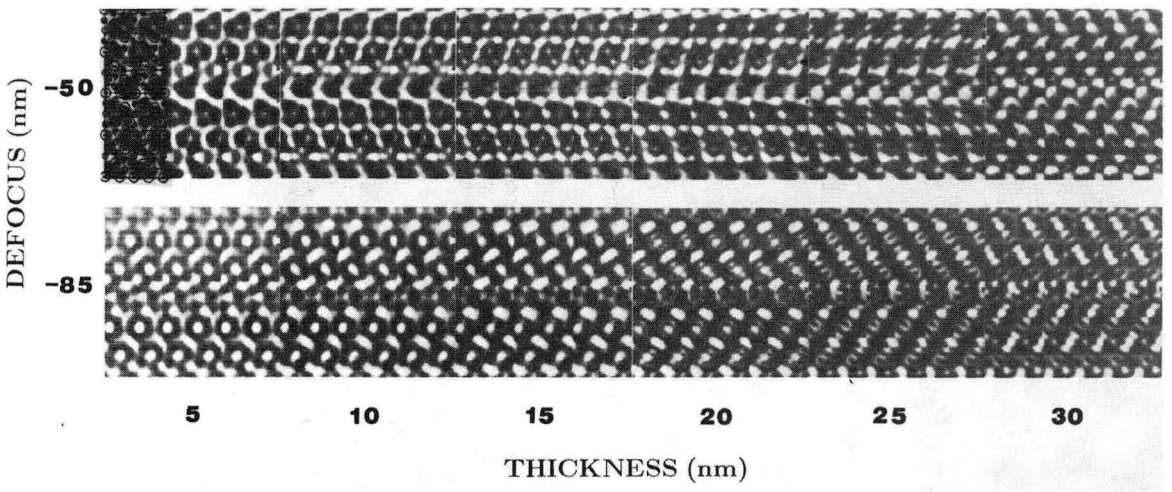

Fig. 61

Experimental and simulated images of an oxide twin boundary

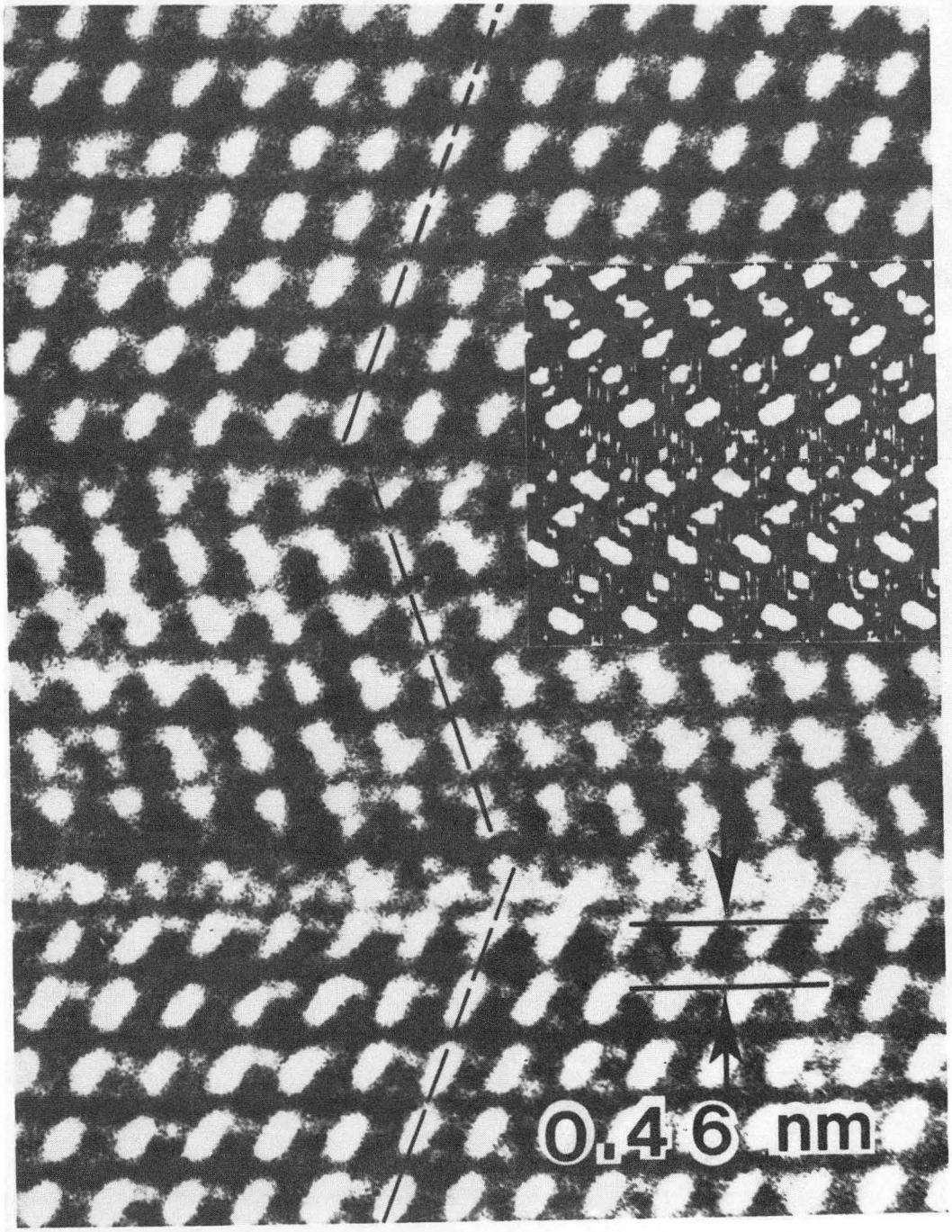

XBB 852-1069A

Fig. 62

Proposed mechanism for twin boundary formation in oxide

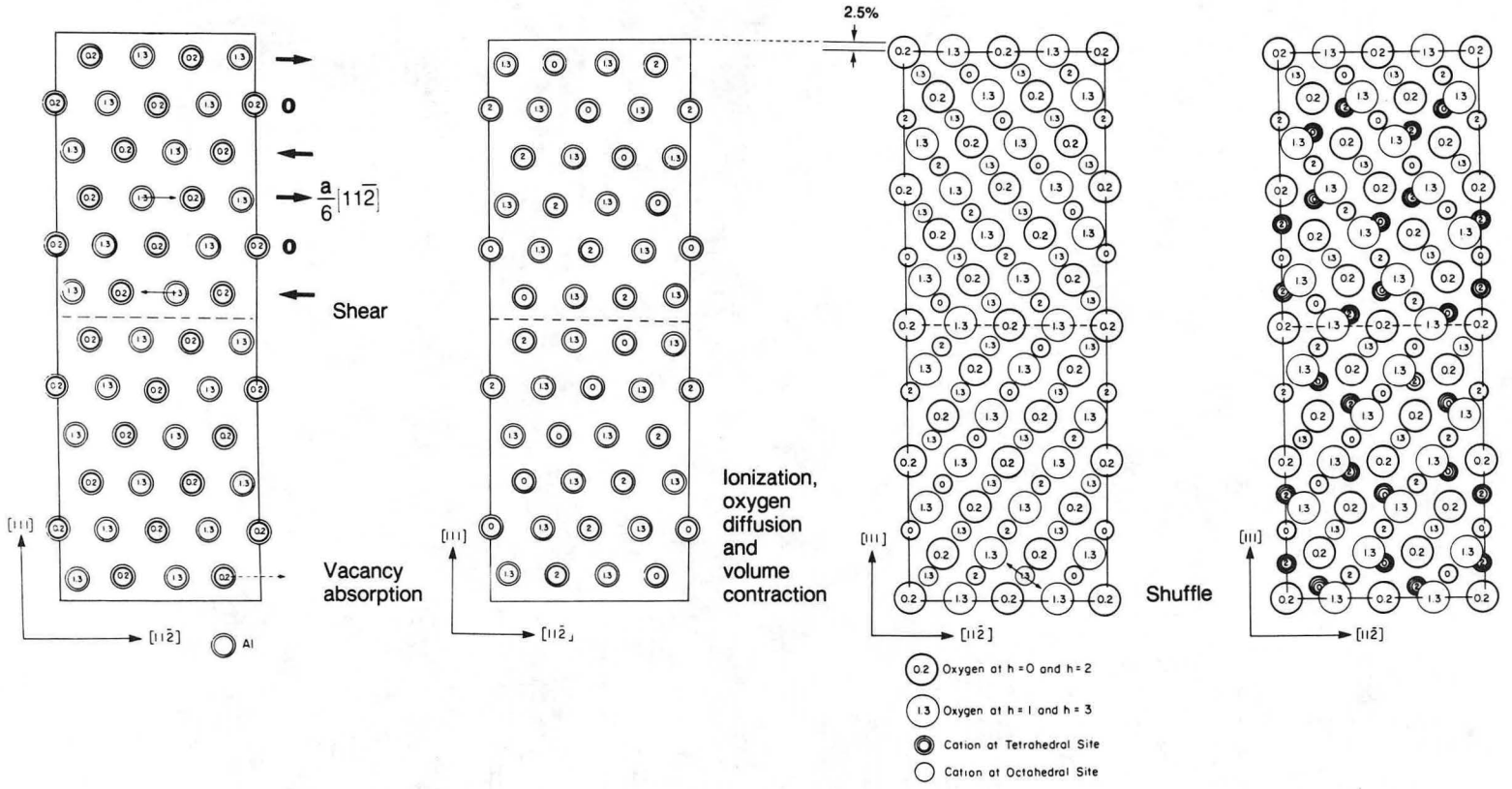

XBL 859-3956

Fig. 63

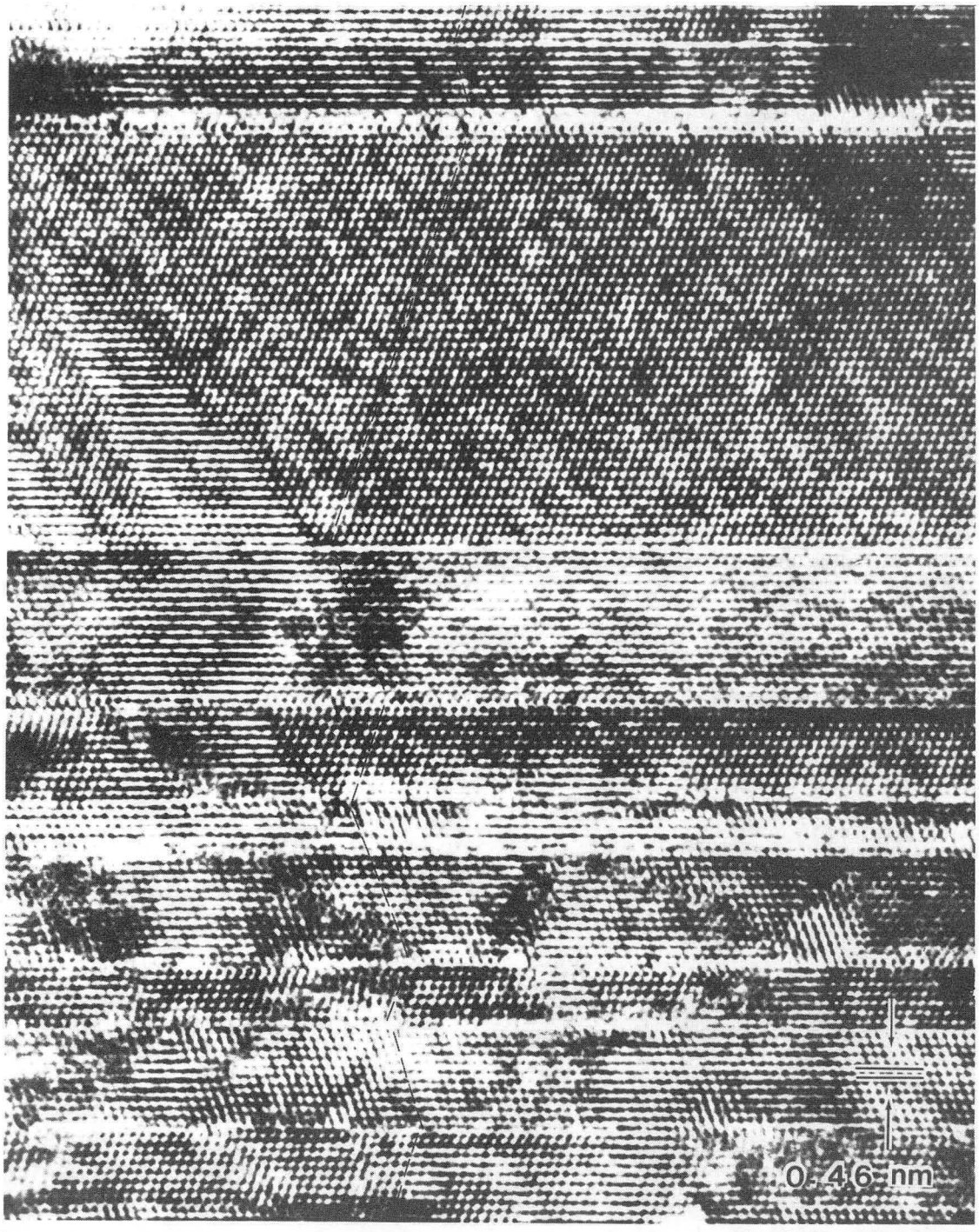

XBB 857-5424

Fig. 64

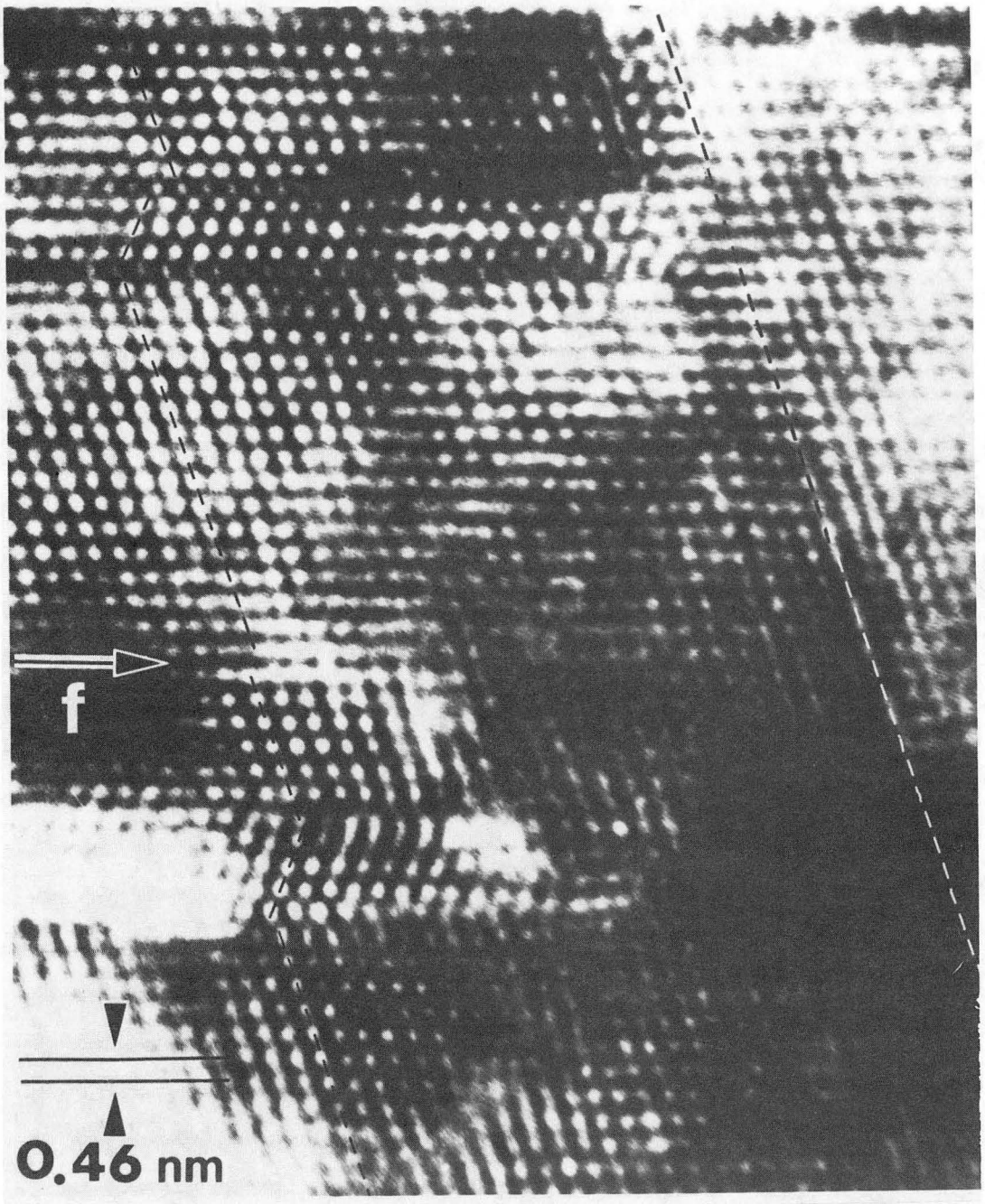

XBB 864-3060

Fig. 65

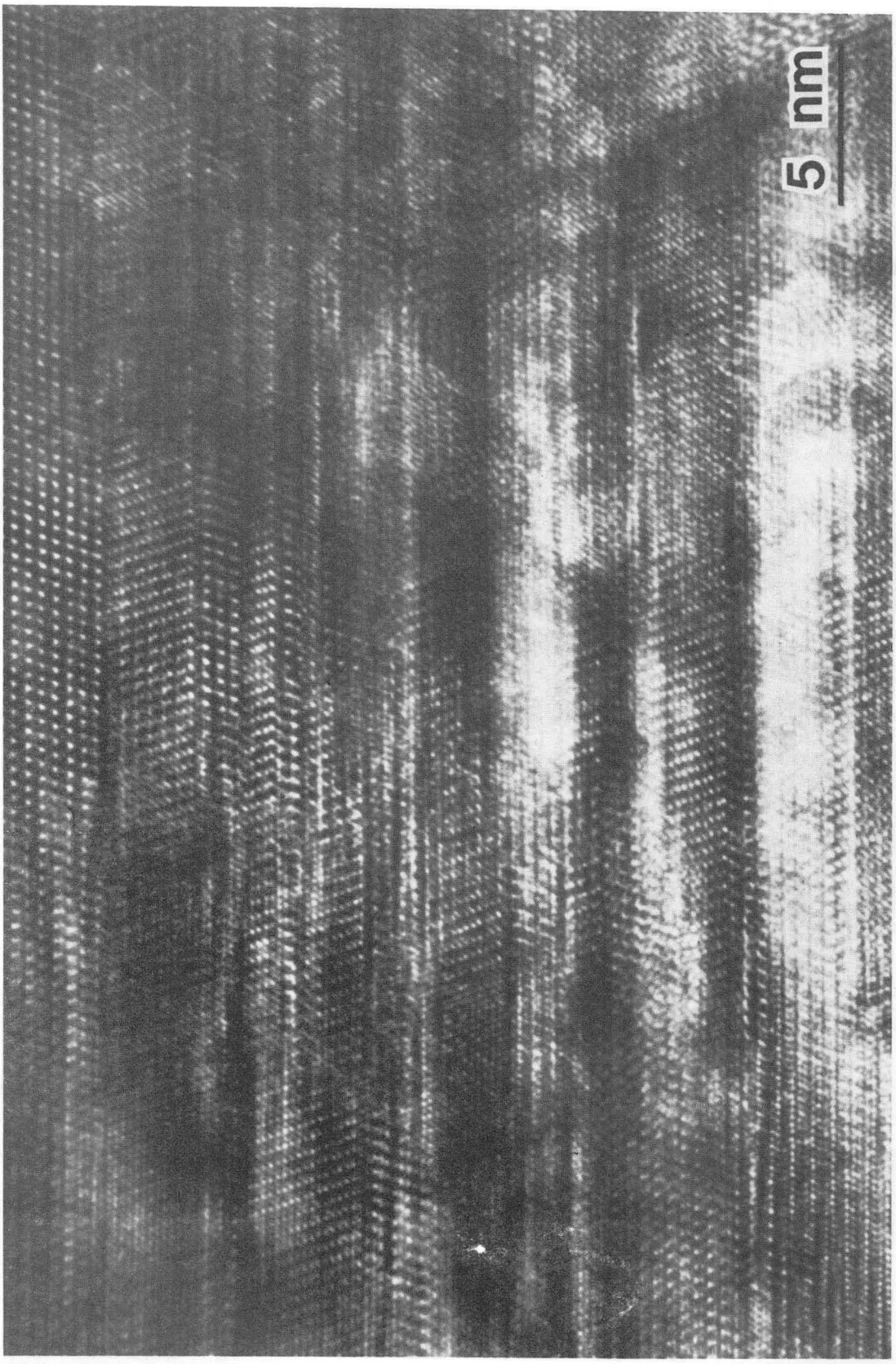

XBB 864-3084

Fig. 66

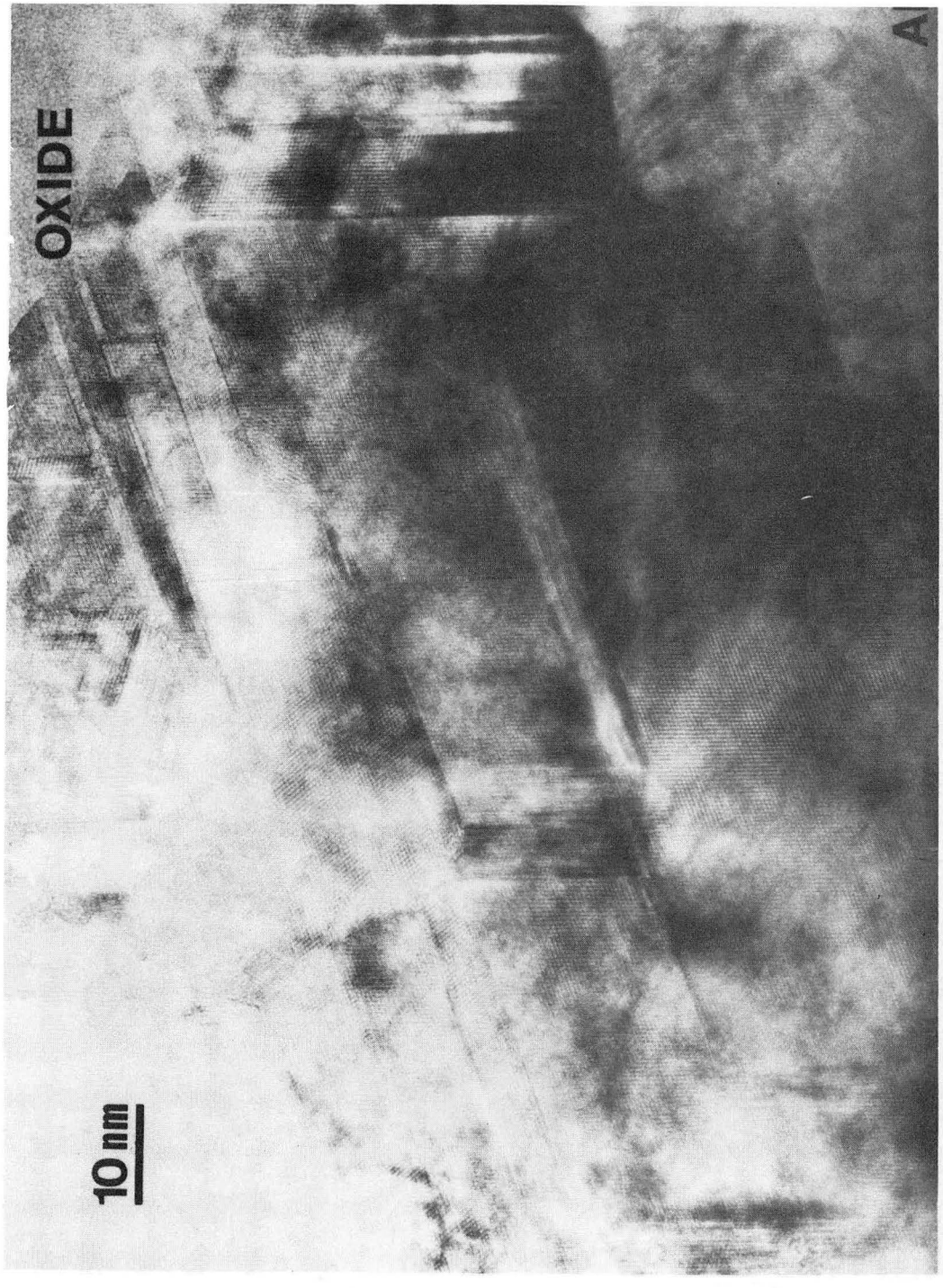

Fig. 67

XBB 852-1372

Multiple twinning in the oxide

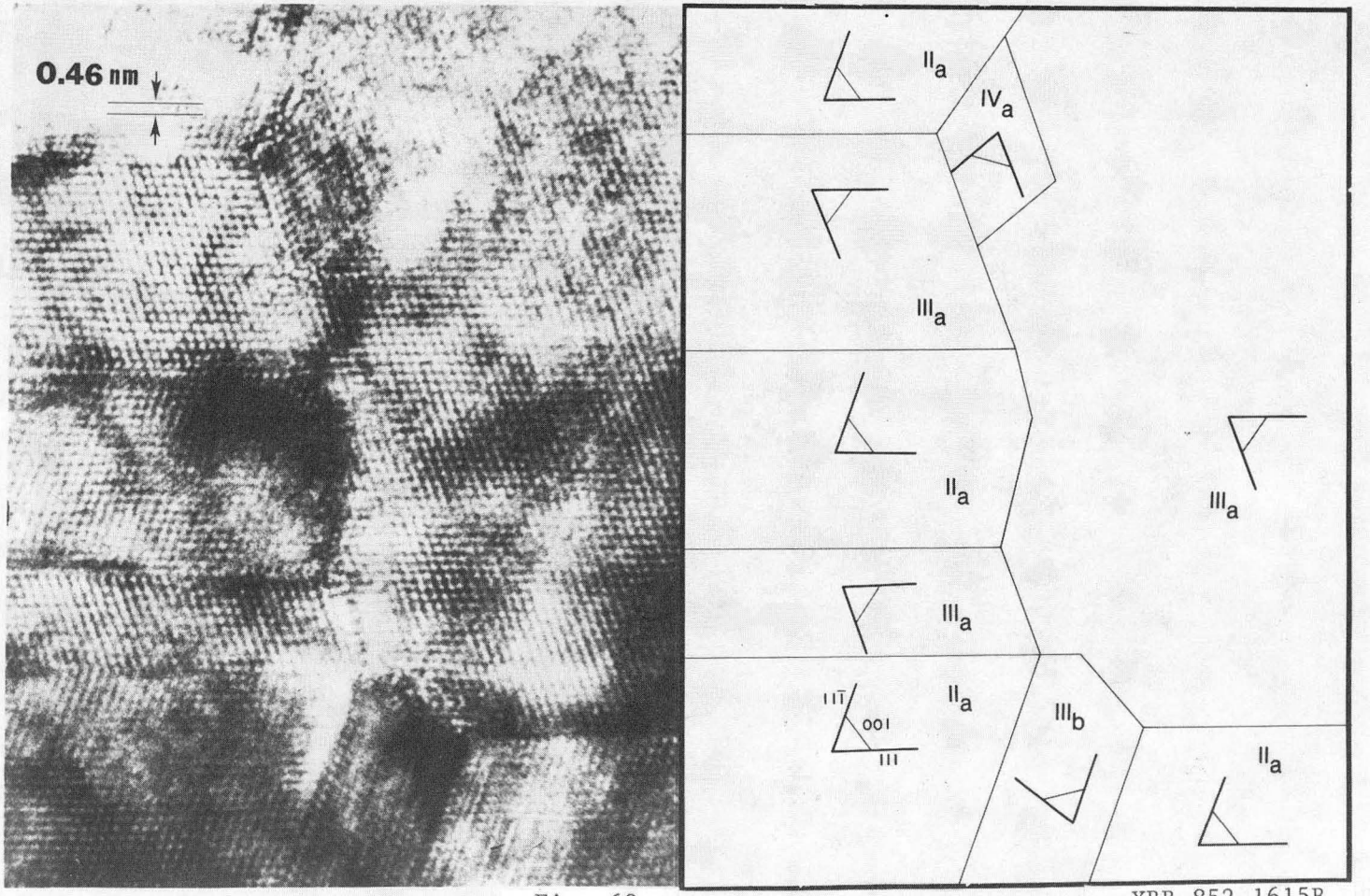

Fig. 68

XBB 852-1615B

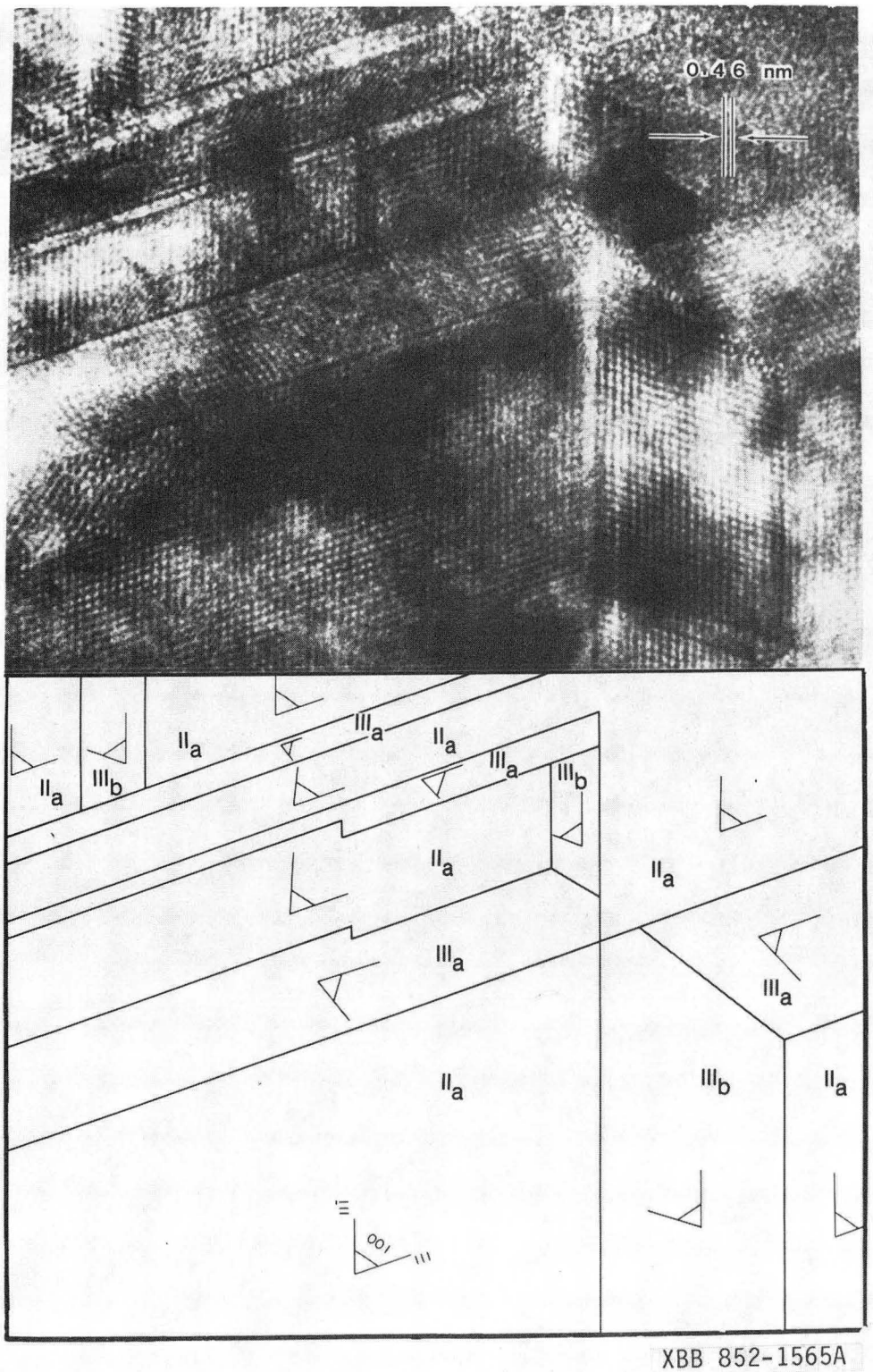
0.46 nm
II a
III b
III a
II a
III a
III b
II a
II a
III a
III a
II a
III b
II a
001
111
XBB 852-1565A

Fig. 69

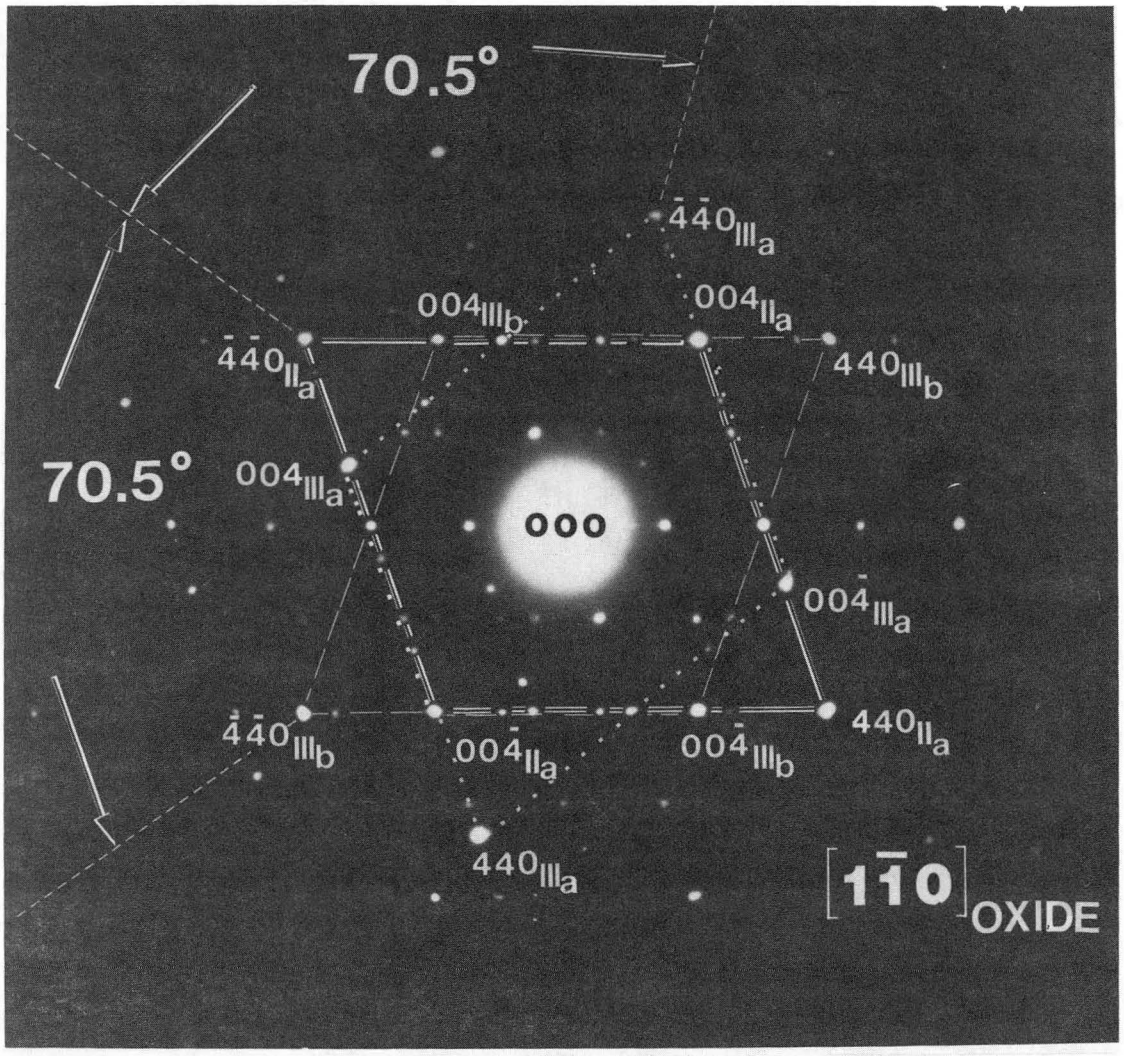

XBB 852-1621A

Fig. 70

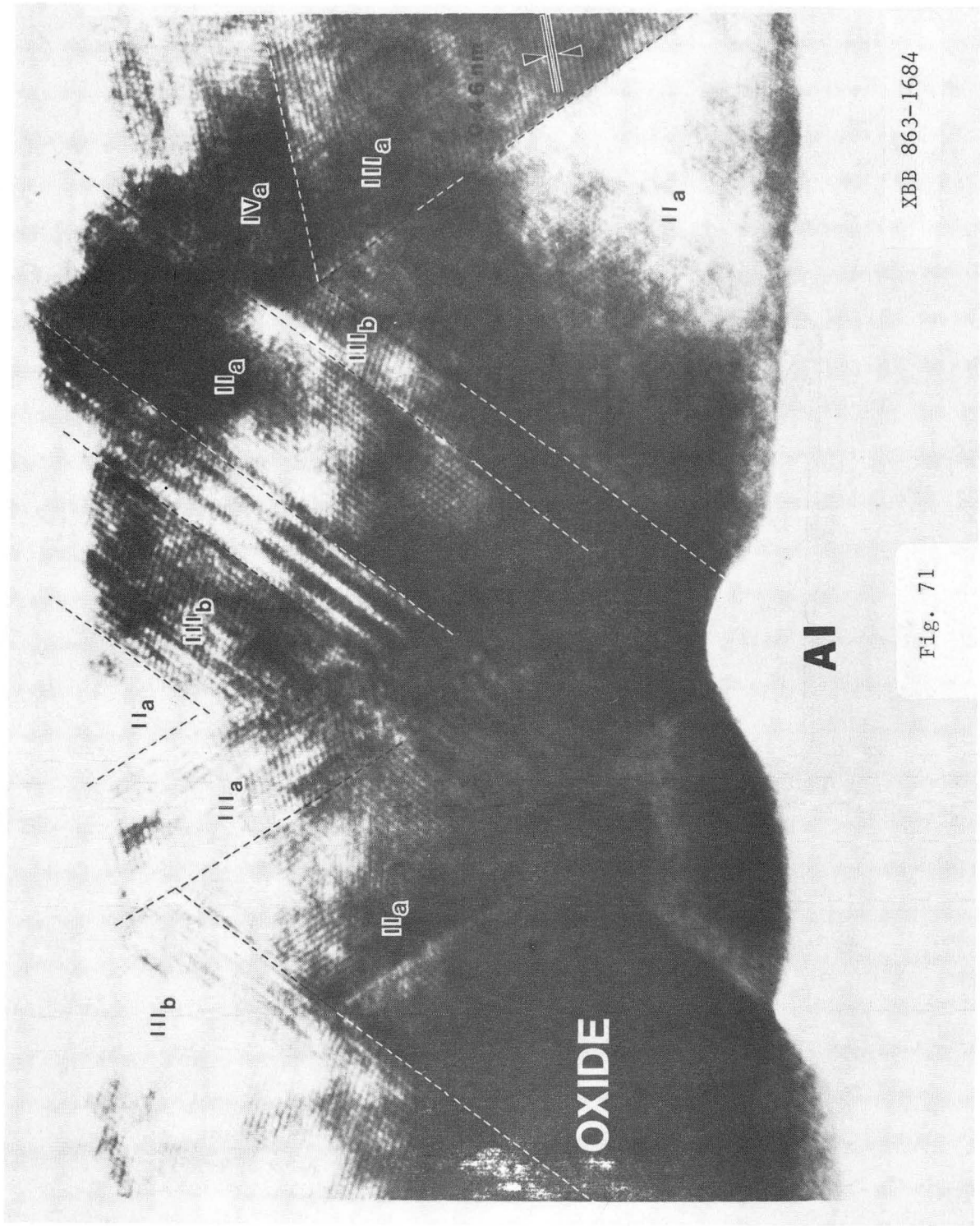

XBB 863-1684

Fig. 71

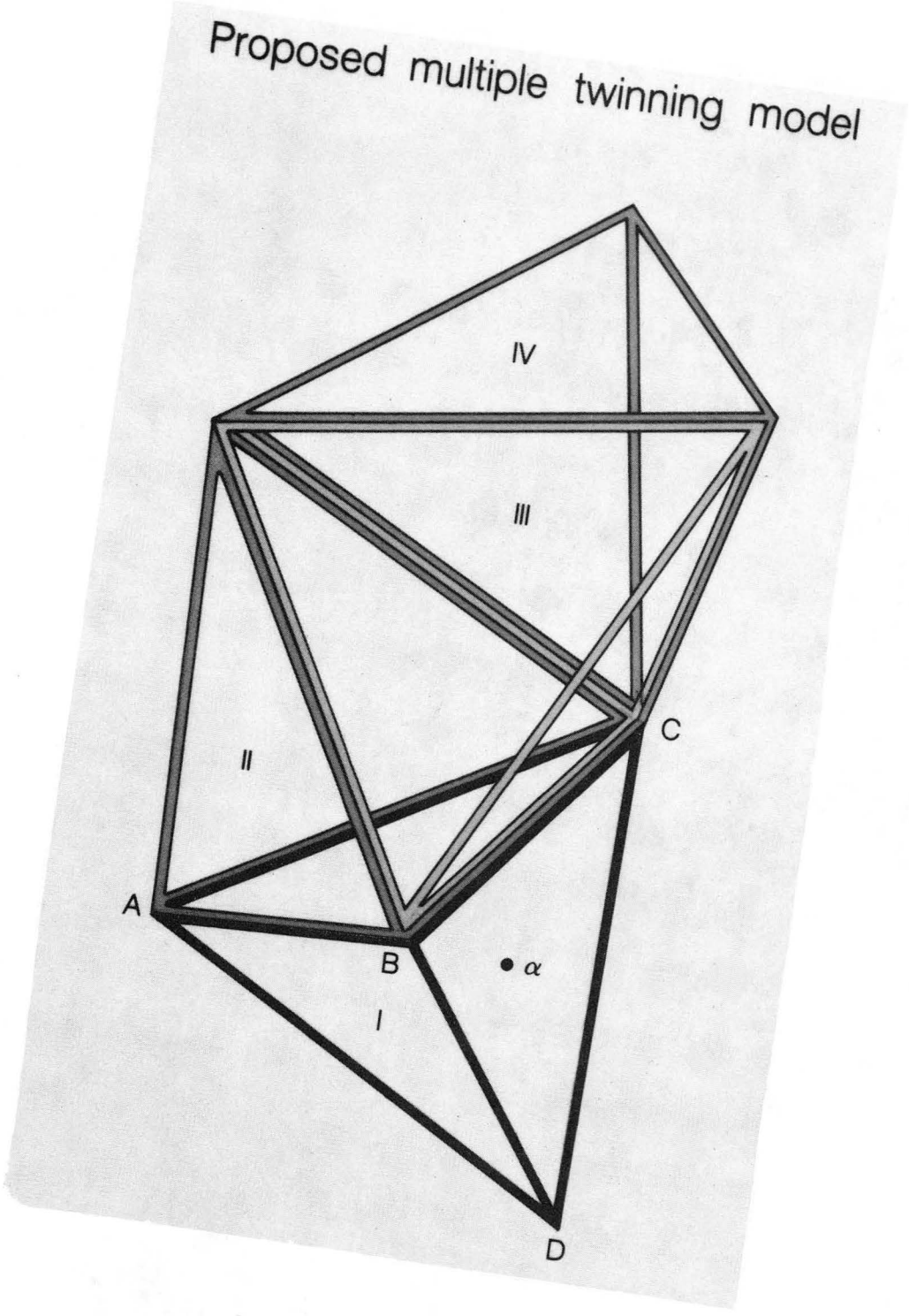

CBB 859-7380

Proposed Mechanism for New Grain Nucleation by Twinning

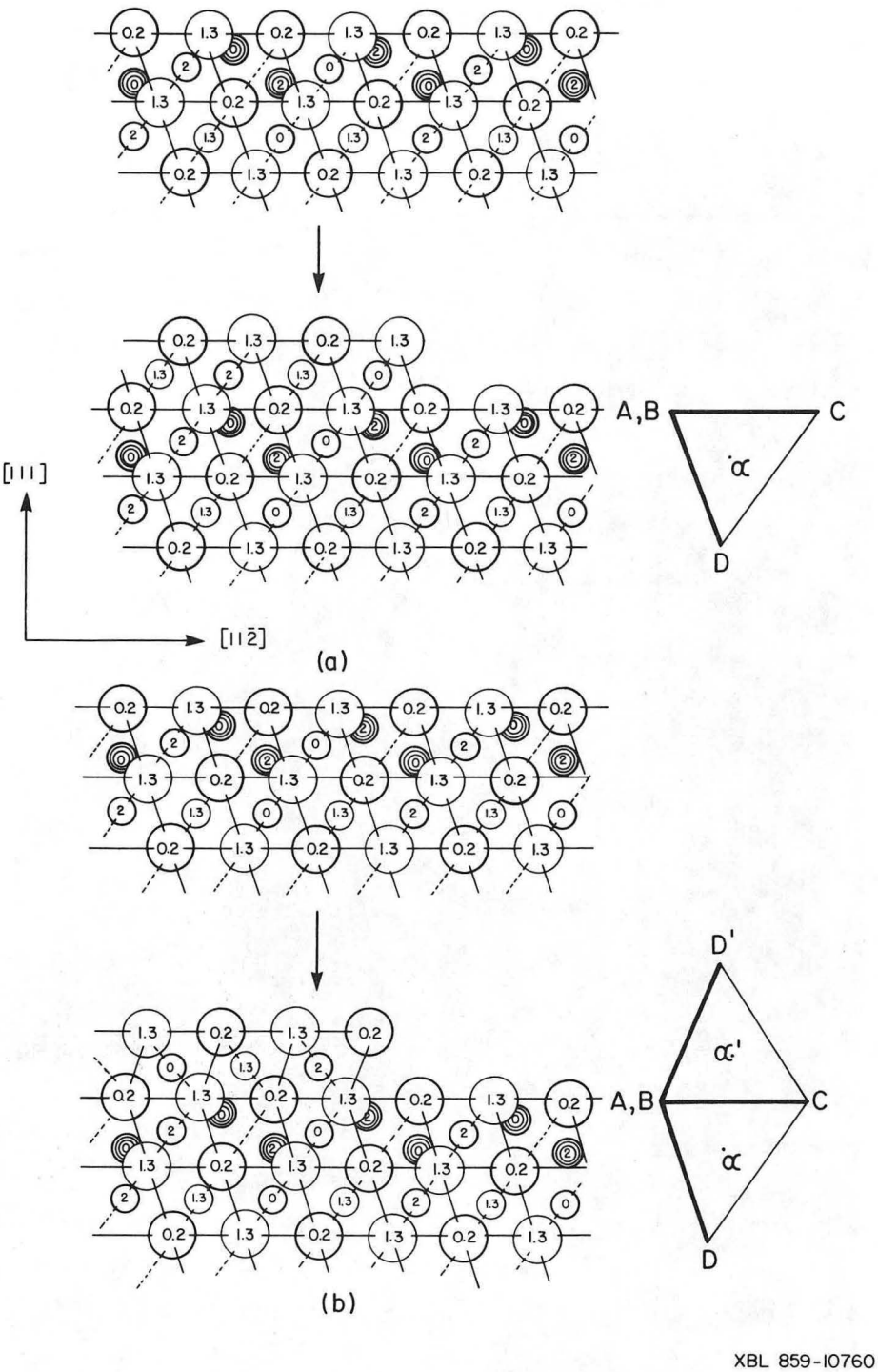

XBL 859-10760

Fig. 73

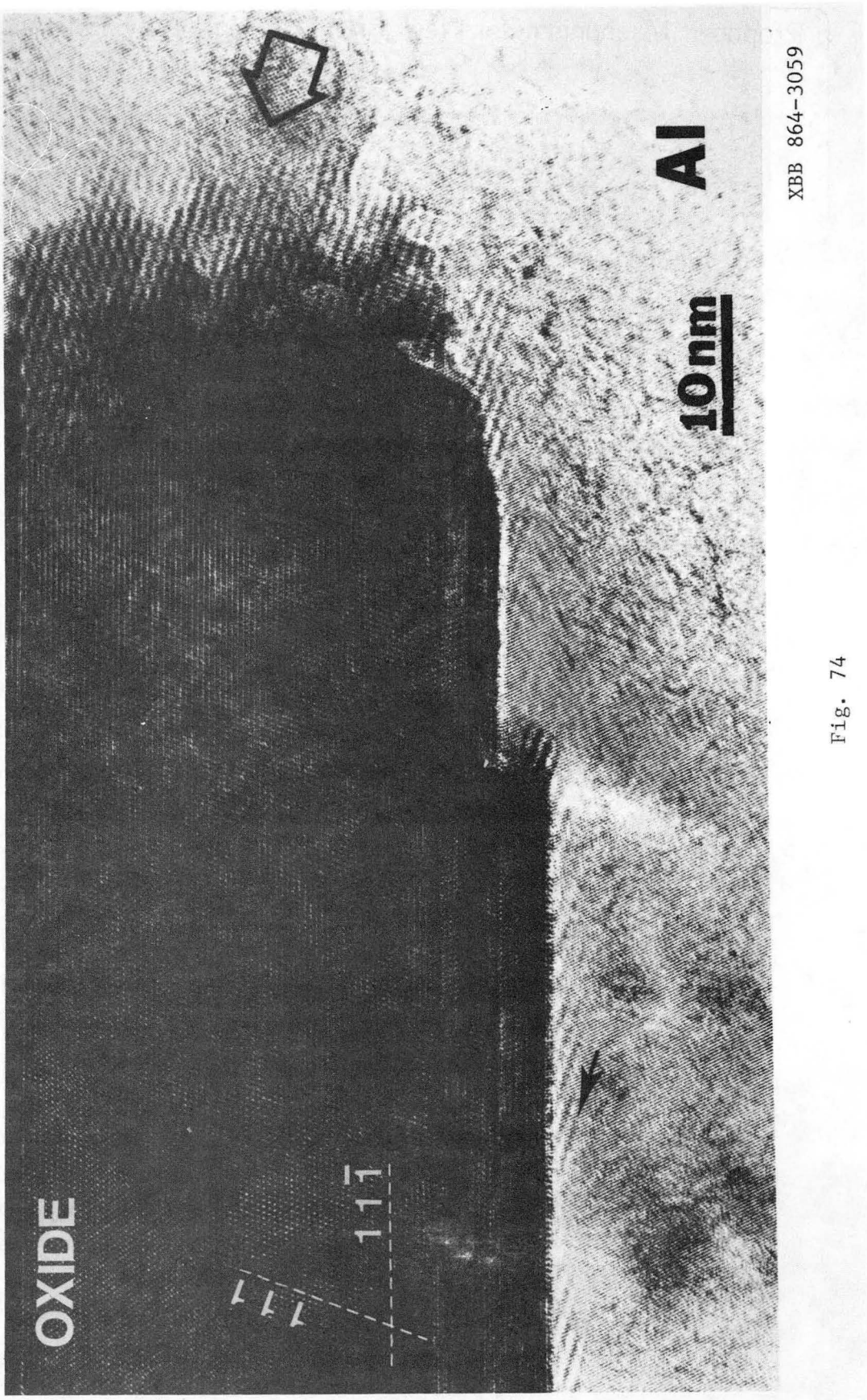

XBB 864-3059

Fig. 74

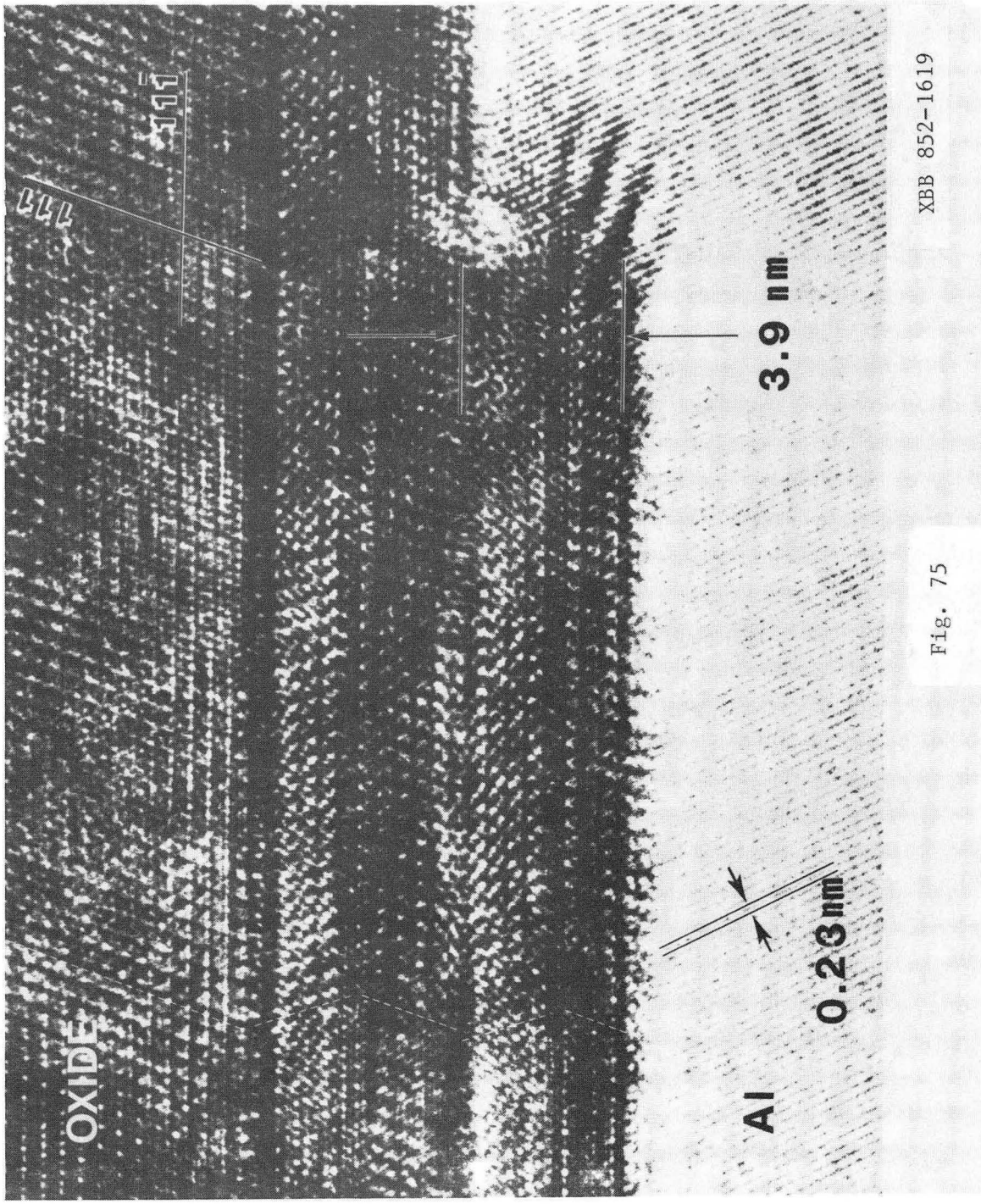

XBB 852-1619

Fig. 75

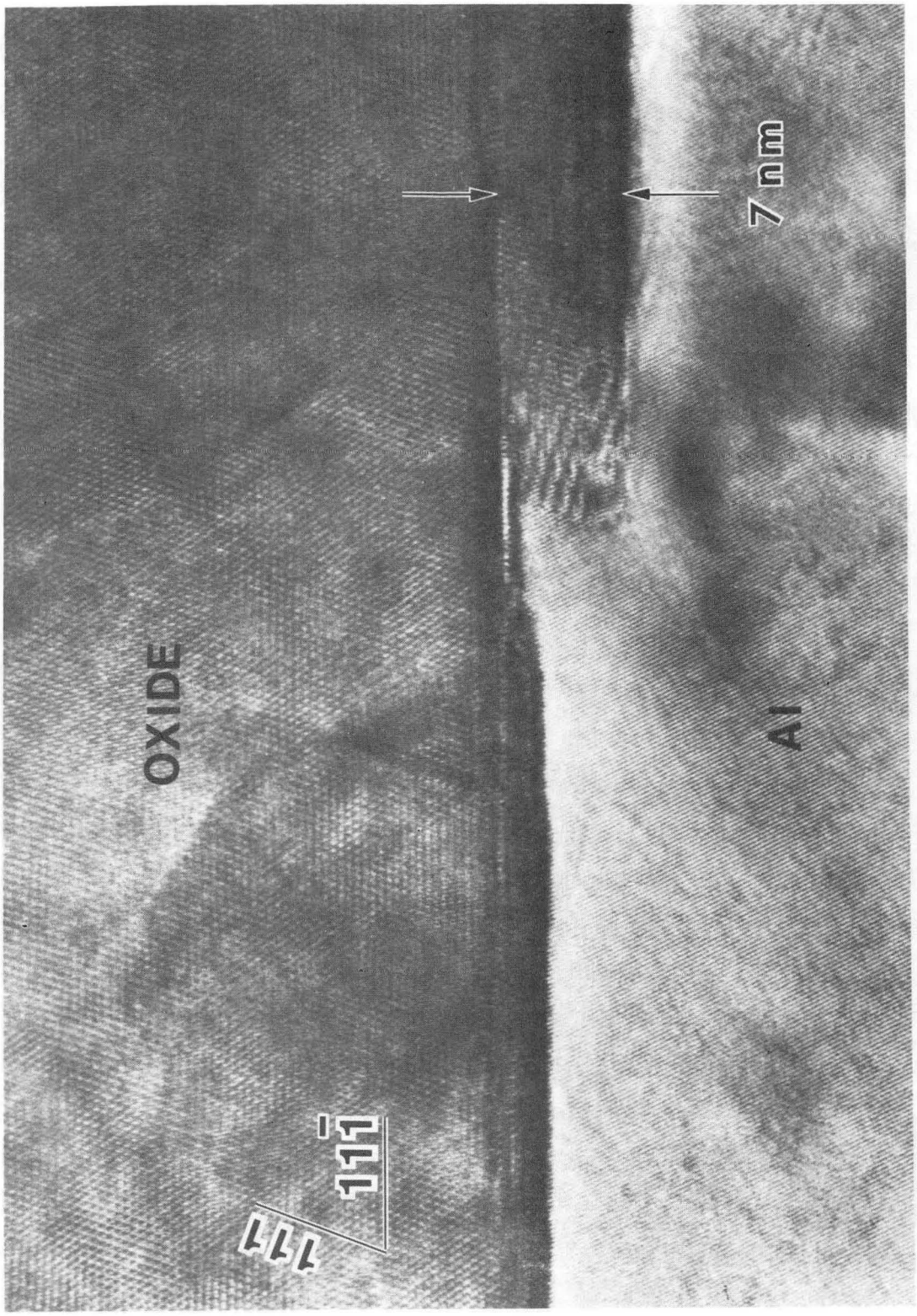

Fig. 76

XBB 864-3089

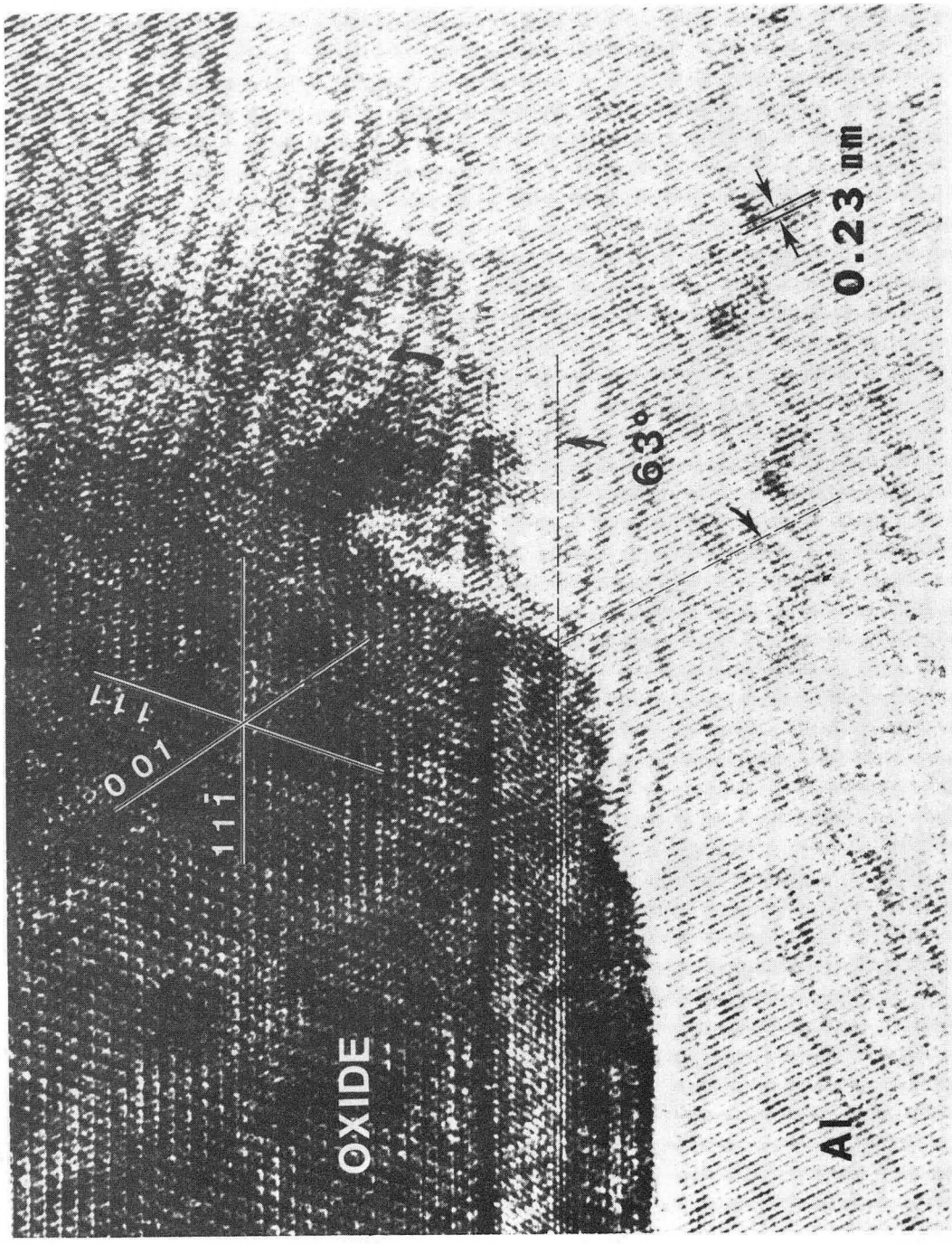

XBB 852-1620

Fig. 77

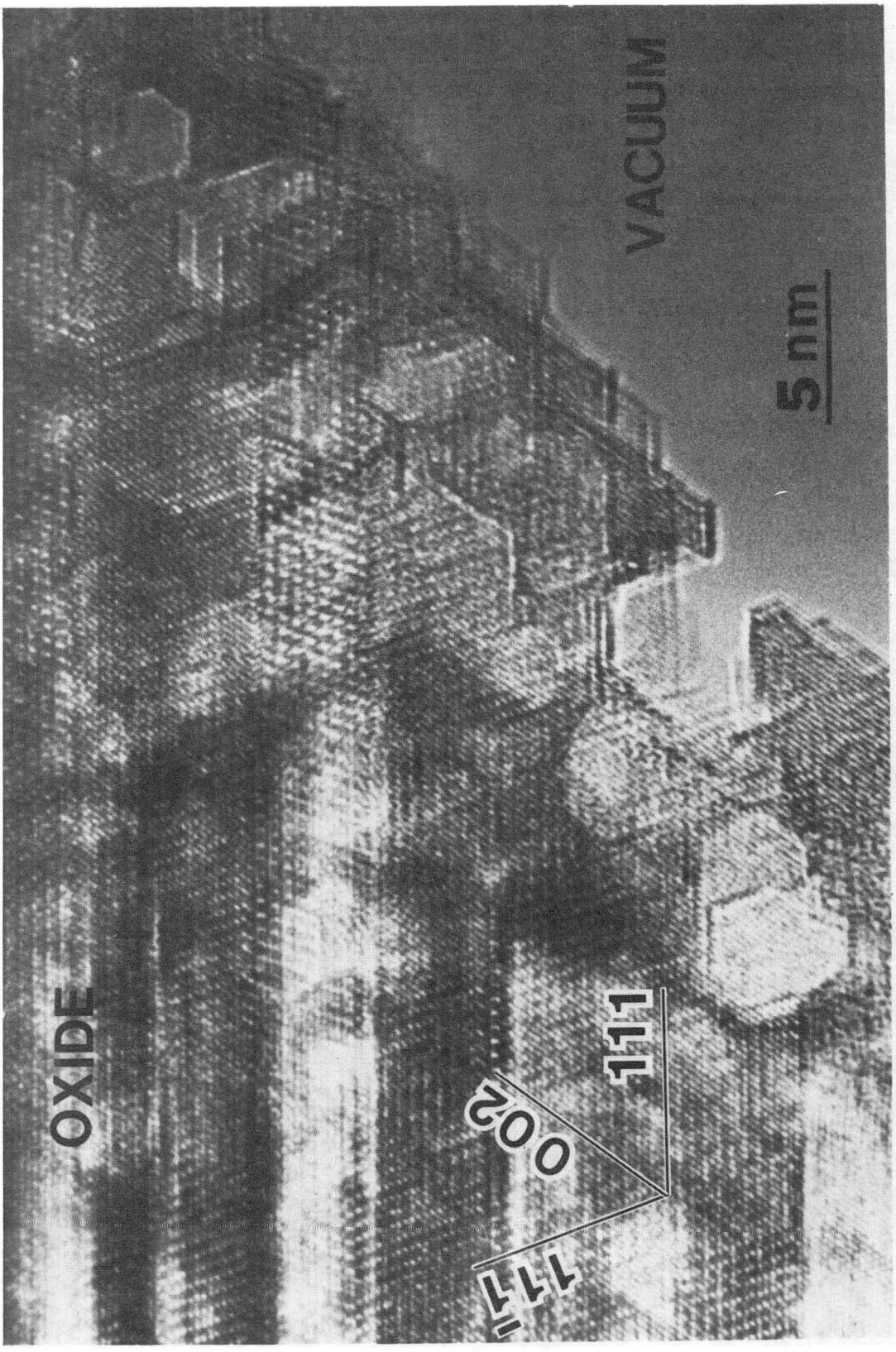

Fig. 78

XBB 864-3085

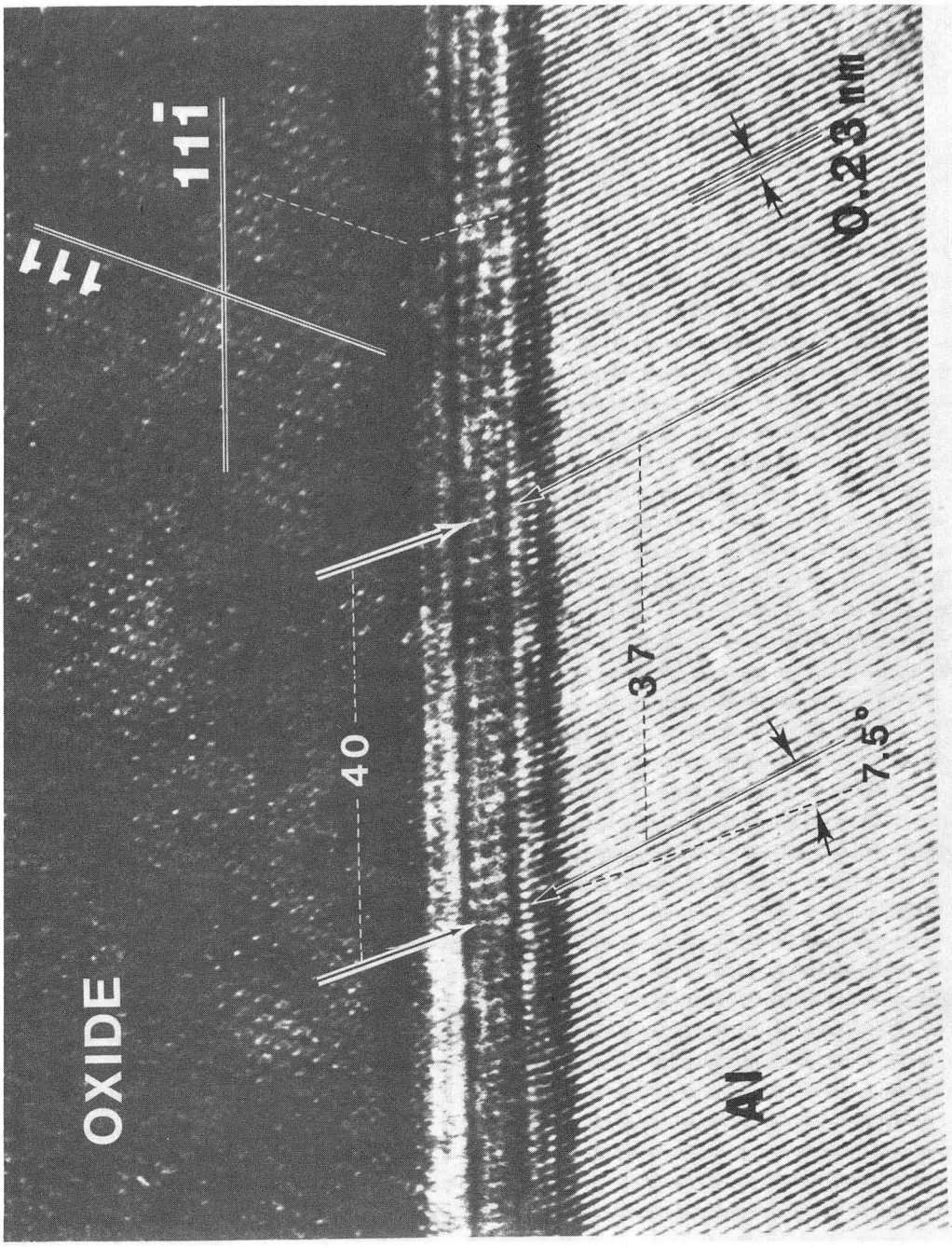

XBB 852-1696

Fig. 79

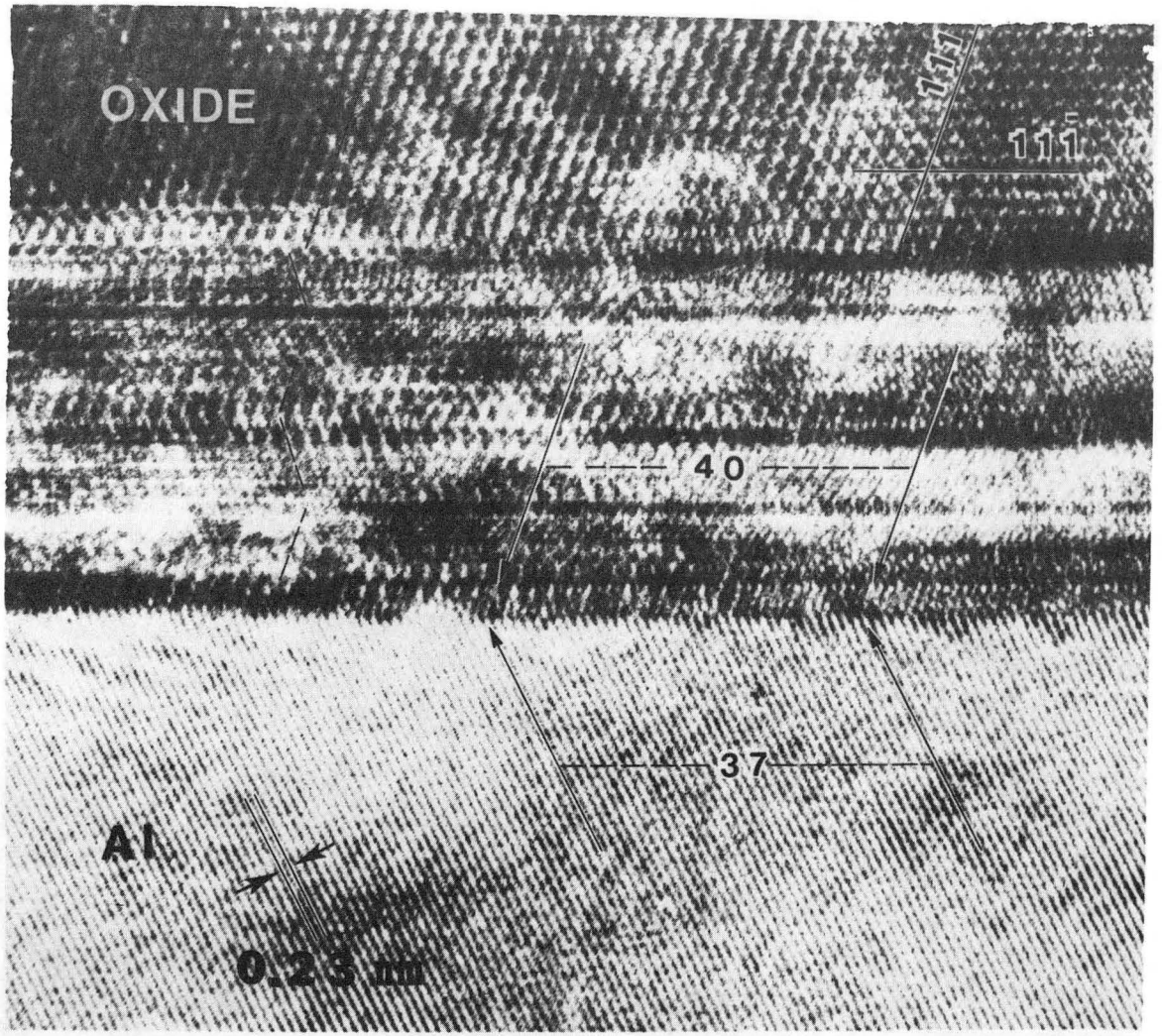

XBB 852-1695

Fig. 80

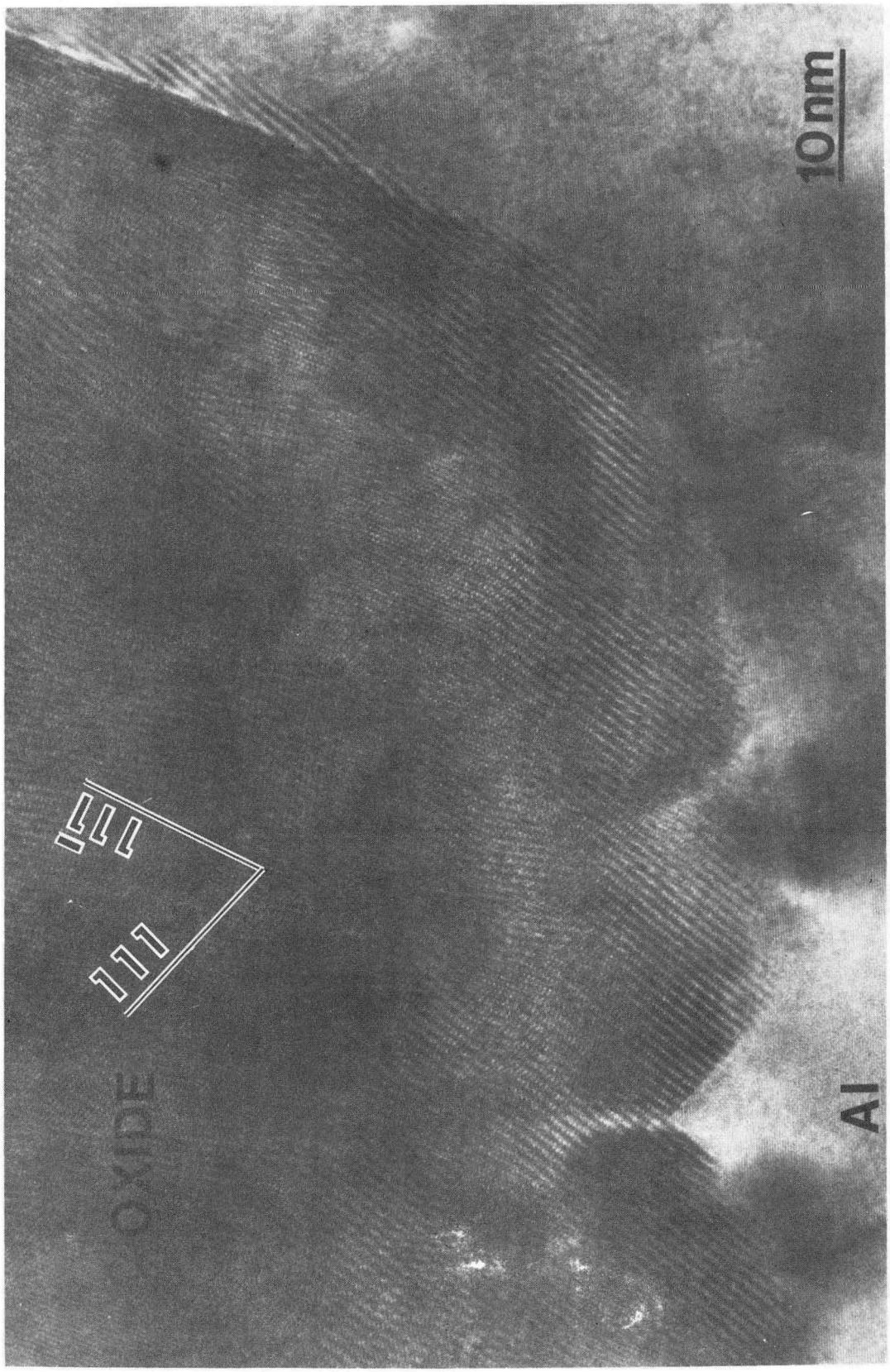

Fig. 81

XBB 864-3088

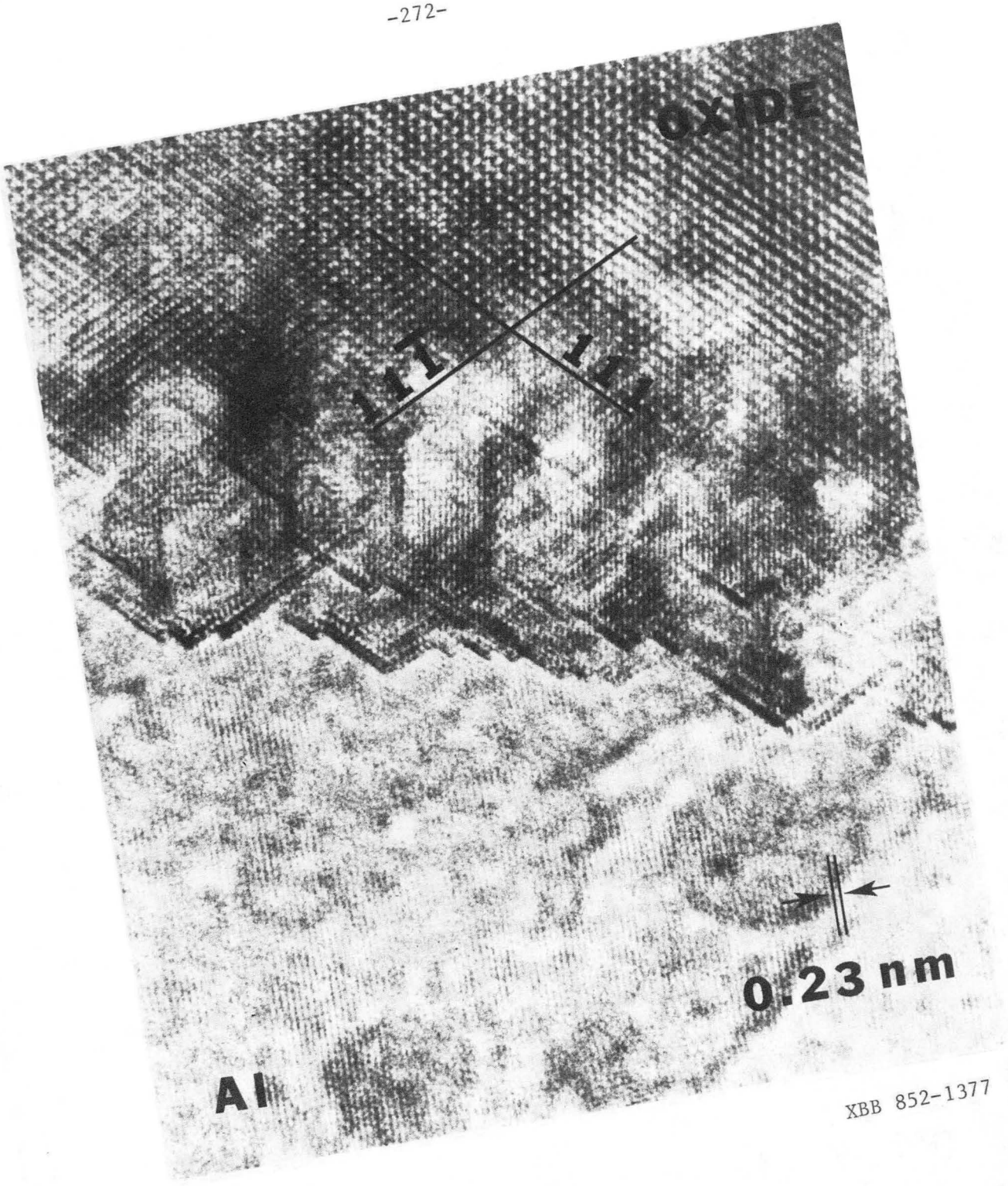

Fig. 82

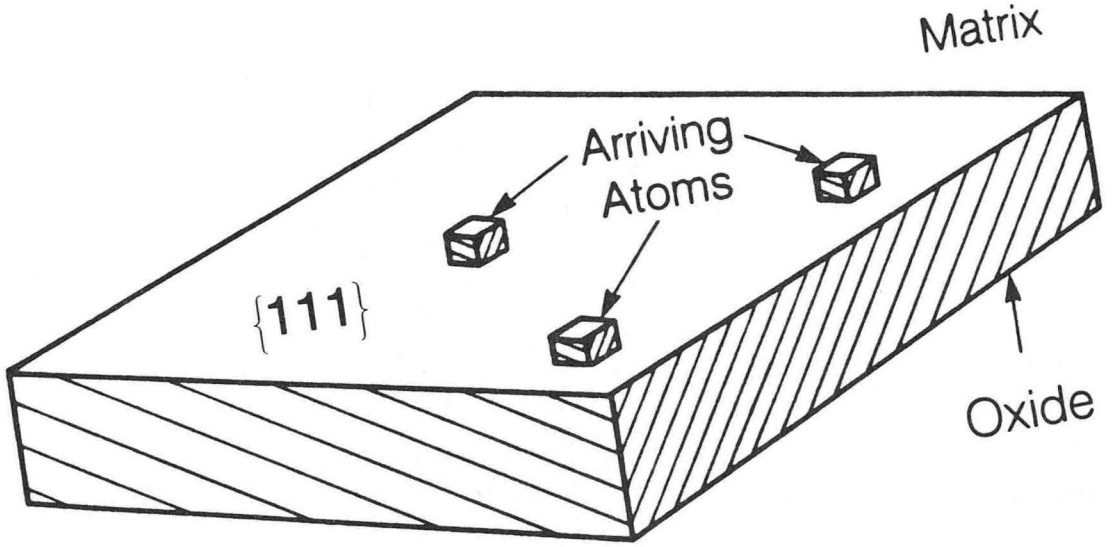

(a)

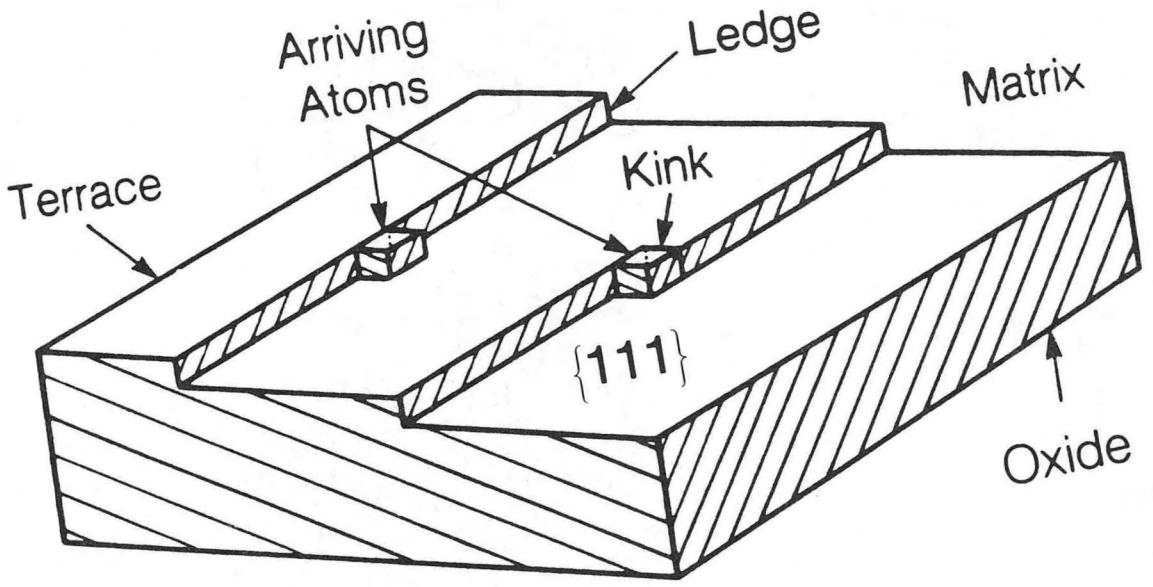

(b)

XBL 864-1548

Fig. 83

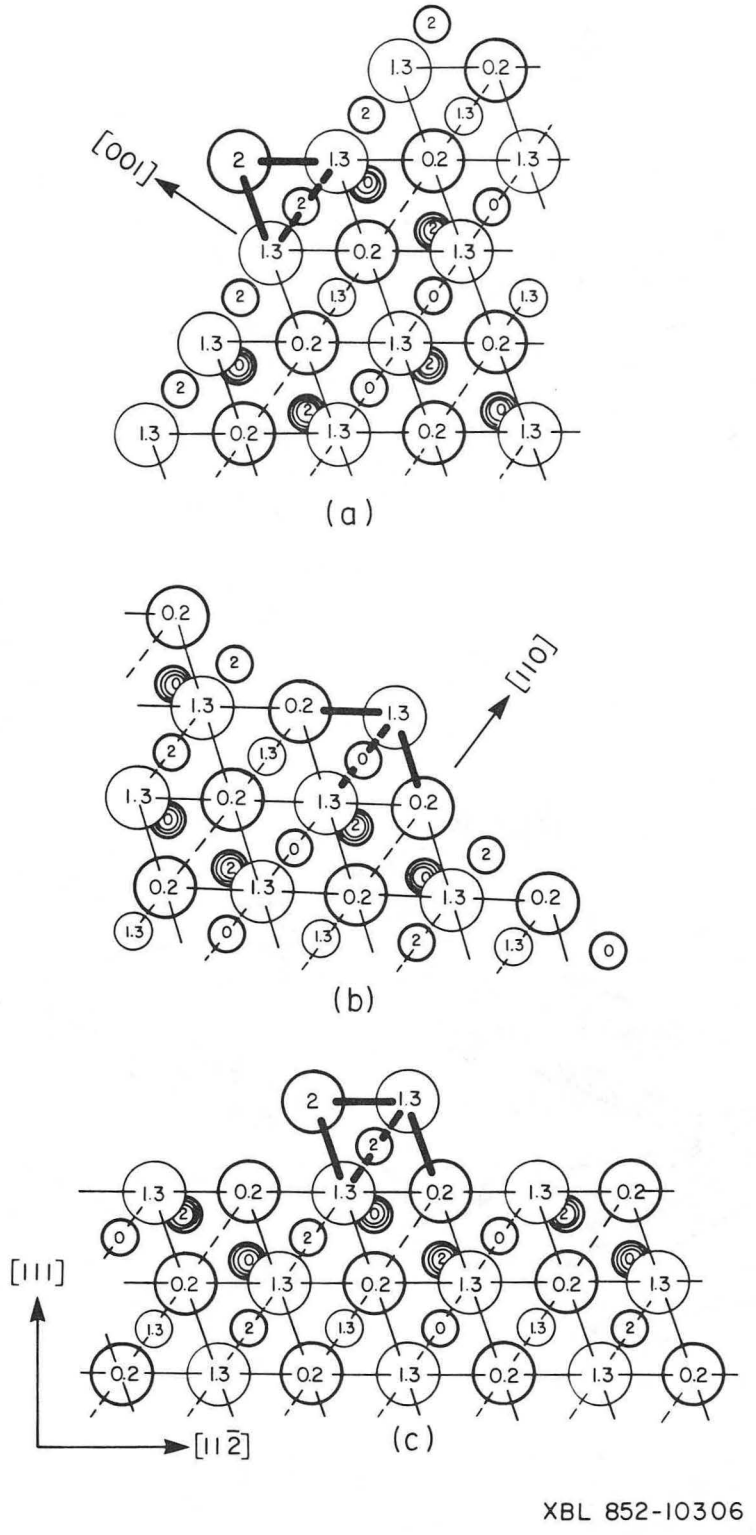

XBL 852-10306

Fig. 84

Proposed ledge mechanism of oxide growth

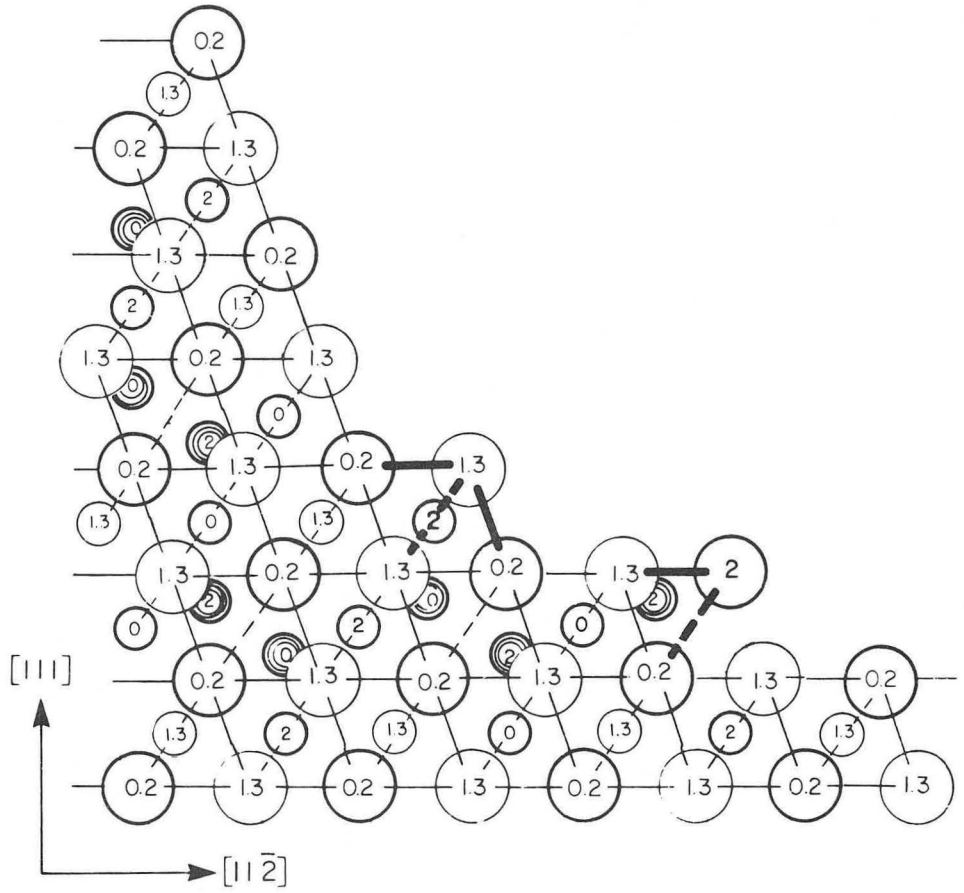

XBL 852-1440A

Fig. 85

LAWRENCE BERKELEY LABORATORY
TECHNICAL INFORMATION DEPARTMENT
UNIVERSITY OF CALIFORNIA
BERKELEY, CALIFORNIA 94720